INTERNATIONAL CONFERENCES
ON ADVANCED MATERIALS

7th International Workshop on Functional
and Nanostructured Materials
FNMA'10
16–20 July 2010, Malta

The International Symposium
on Trends in Continuum Physics
TRECOP 2010
16–20 July 2010, Malta

3rd International Conference and
7th International Workshop
on Auxetics and Related Systems
19–23 July 2010, Gozo & Malta

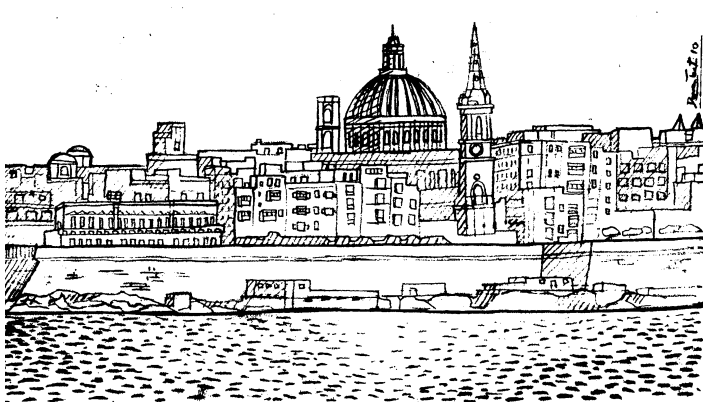

ABSTRACT BOOK

TITLE

International Conferences on Advanced Materials – Abstract Book:

Part 1
7^{th} International Workshop
on Functional and Nanostructured Materials
FNMA'10

Part 2
The International Symposium
on Trends in Continuum Physics
TRECOP 2010

Part 3
3^{rd} International Conference and
7^{th} International Workshop
on Auxetics and Related Systems

REVISED VERSION, 21.07.2010

EDITORS

Jarosław Rybicki, Bogdan T. Maruszewski and Joseph N. Grima

TECHNICAL EDITOR

Agnieszka Witkowska

TYPESETTING USING TEX

BOP s.c., www.bop.com.pl

THE PUBLICATION WAS SUPPORTED BY FUNDS
RECEIVED FROM THE ZACHODNIOPOMORSKIE VOIVODESHIP BUDGET

TASK PUBLISHING 2010
GDANSK, POLAND

ISBN 978-83-930549-1-6

7th International Workshop on Functional and Nanostructured Materials FNMA'10

ORGANISED BY

Department of Solid State Physics, Gdansk University of Technology, Poland
University of Malta, Msida, Malta
University of Athens, Greece
PWSZ im. Prezydenta St. Wojciechowskiego, Kalisz, Poland
University of Zielona Gora, Poland
Institute of Applied Mechanics, Poznan University of Technology, Poland

The International Symposium on Trends in Continuum Physics TRECOP 2010

ORGANISED BY

Institute of Applied Mechanics, Poznan University of Technology, Poland
Institute of Theoretical Physics, Technische Universität Berlin, Germany
Kielce University of Technology, Poland
University of Malta, Msida, Malta
Polish Academy of Sciences, Institute of Molecular Physics, Poznan, Poland
Foundation for Development of Poznan University of Technology, Poland
Polish Society of Theoretical and Applied Mechanics, Poland
Institute of Environmental Mechanics and Applied Computer Science, Kazimierz Wielki University, Bydgoszcz, Poland
Department of Solid State Physics, Gdansk University of Technology, Poland

3rd International Conference and 7th International Workshop on Auxetics and Related Systems

ORGANISED BY

University of Malta, Msida, Malta
Institute of Molecular Physics, PAS, Poznan, Poland

SPONSORS

Gdansk University of Technology
Gdansk, Poland

TASK Computer Centre
Gdansk, Poland

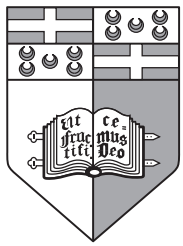

University of Malta
Msida, Malta

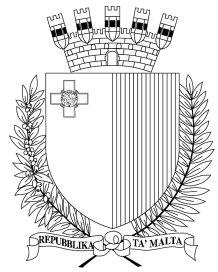

Ministry for Gozo
Gozo, Malta

University of Zielona Gora
Zielona Gora, Poland

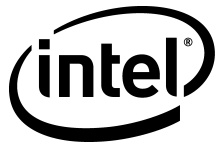

INTEL Technology Poland

Intitute of Applied Mechanics, PUT
Poznan, Poland

Polish Society of Theoretical
and Applied Mechanics

PWSZ im. Prezydenta
Stanisława Wojciechowskiego
w Kaliszu, Kalisz, Poland

Marshal's Office of
Zachodniopomorskie Voivodeship

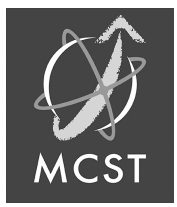

Malta Council
for Science & Technology

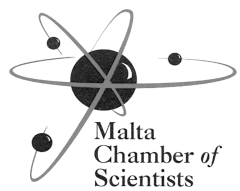

Malta Chamber
of Scientists

CONTENTS

PART 1
7th International Workshop on Functional and Nanostructured Materials, FNMA'10

PART 2
The International Symposium on Trends in Continuum Physics, TRECOP 2010

PART 3
3rd International Conference and 7th International Workshop on Auxetics and Related Systems

PART 1

7^{th} International Workshop on Functional and Nanostructured Materials FNMA'10

16–20 July 2010, Malta

Two Different Calcination Processes to Prepare Polycrystalline Bi-Based Superconductor with Improved Bi(2223) Phase

S. Memarzadeh[1], A. Amirabadizadeh[1a], N. Tajabor[2], Sh. Poormand[3], H. Farsi[4]

[1] *Department of Physics, Faculty of Science University of Birjand Birjand, Iran*

[2] *Department of Physics, Faculty of Science Ferdowsi University of Mashhad Mashhad, Iran*

[3] *Research Center of Kansaran Binalood Center Mashhad, Iran*

[4] *Department of Chemistry, Faculty of Science University of Birjand Birjand, Iran*

[a] *ahmadamirabadi@yahoo.com*

In this research two samples of a nominal composition of $(Bi\text{-}Pb)_2Sr_2Ca_{n-1}Cu_nO_x$ were prepared by the solid state reaction method, using two different routes. Codes A and B are used to refer to the samples. In preparing sample A, the standard calcination method was used, while in sample B, $SrCO_3$ and $CaCO_3$ were calcinated at 1100°C for 3 h. The calcination was done separately on $SrCO_3$ and $CaCO_3$ in order to eliminate CO_2. Then, after mixing and grinding, the powders in the mixture of Bi_2O_3, CuO, PbO, SrO and CaO were calcinated at 840°C for 70 h. The effects of this calcination on the structure and different superconducting phases (Bi-2212 and Bi-2223) were investigated by XRD, SEM and AC susceptibility. The results showed that the new calcination process helped increase rather the Bi-2223 phase than the 2212 one. The results were as follows:

(a) The volume fraction of the Bi(2223) and Bi(2212) phases was estimated by *X*-ray diffraction patterns. The XRD patterns showed that the new calcination favored the Bi(2223) phase formation.

(b) The SEM studies of the samples showed that the largest particle size would be increased when using the new calcination process.

(c) The AC susceptibility studies showed that by using new calcination process, the transition of the real part of the AC susceptibility for the intragranular component was sharper; indicating that the new calcination process improved the Bi(2223) phase formation.

High-Field Quantum Transport in Carbon Nanotubes

V. K. Arora

Division of Engineering and Physics, Wilkes University
Wilkes-Barre, PA18766, USA

Ibnu Sina Institute of Fundamental Sciences
Universiti Teknologi Malaysia
UTM Skudai 81310, Malaysia

vijay.arora@wilkes.edu

The charge carriers in nanowires (NWs), carbon nanotubes (CNTs), and those confined to a very high magnetic field have one-dimensional (1D) character as quasi-free propagation of electron waves with analog energy spectrum exists only in one direction. The energy spectrum is quantum (or digital) in other two cartesian directions where electron waves are standing waves. In the quantum limit, an electron (hole) occupies the lowest (highest) digital/quantized state giving it a distinct 1D character. The energy $E = v_F|k|$ in carbon-based devices is linearly dependent on the wave vector k, where $v_F \approx 10^6$ m/s. This is in direct contrast to parabolic character $E = \hbar^2 k^2/2m^*$ in solids with effective mass m^*, for example in silicon NWs. The probability of changing wavevector from $+ve$ to $-ve$ direction or vice versa is greatly reduced and hence high mobility is expected, especially at low temperatures. In this presentation, the crucial question to be answered is: Does a higher mobility leads to a higher ultimate saturation velocity? The distribution function in a high electric field E is then naturally asymmetrical affected by the energy $\pm qE\ell$ absorbed or emitted by a carrier of charge q during its ballistic flight in a mean free path ℓ. The ultimate drift in response to a high electric field results in unidirectional streaming of the otherwise randomly-oriented velocity vectors in equilibrium. The saturation velocity limited to the streamlined intrinsic velocity is an appropriate thermal velocity for non-degenerately-doped samples, increasing with the temperature, but independent of carrier concentration. However, this saturation velocity is the appropriate Fermi velocity for degenerately-doped samples, increasing with carrier concentration but independent of temperature. The high-field drift limited by the intrinsic velocity is ballistic unaffected by scattering-limited processes. The ultimate velocity is further limited by an emission of a quantum either in the form of an optical phonon or an emitted photon by an electron excited to the higher state by the applied electric field, not dependent on scattering parameters. This is in direct contrast to the findings of Monte Carloites who predict saturation velocity to be scattering-dominated. In a low-field and long (length $L \gg \ell$) samples, as is well-known, scattering processes play a dominant role and hence limit the mobility. Ballistic processes as a result of

reduction in length of a CNT or NW below the scattering-limited mean free path ℓ in the quasi-free direction are also discussed.

Acknowledgements
Work supported by the Brain Gain Fellowship of the Academy of Science Malaysia.

Ballistic Transport and Nano-CMOS Circuit Design

D. C. Y. Chek[1a], M. L. P. Tan[1,2], V. K. Arora[1,3]

[1] *Faculty of Electrical Engineering*
Universiti Teknologi Malaysia, UTM Skudai
Johor 81310, Malaysia

[2] *Electrical Engineering Division*
Engineering Department, University of Cambridge
9 J. J. Thomson Avenue, Cambridge CB3 0FA, UK

[3] *Division of Engineering and Physics, Wilkes University*
Wilkes-Barre, PA18707, USA

[a] *deschek2004@hotmail.com*

The scaling of channel length and width in a nanoscale n-type MOSFET (NMOS) and p-type MOSFET (PMOS) is examined in ballistic (B) nano-CMOS design. The ballistic process is predominant in a nanoscale device when channel length is shorter than the mean free path. Our predictive model agrees well with 45 nm experimental data from IBM. It is shown that the mobility is lower in the short channel device compared to the mobility in the long channel device due to the ballistic process.

The intrinsic velocity [1] for carriers in a 2-dimensional channel is given by $v_{i2} = v_{th2}\Im_{1/2}(\eta_{F2})/\Im_o(\eta_{F2})$, $v_{th2} = (\pi k_B T/2m_t^*)^{-1/2}$. Here $\Im_j(x)$ is the Fermi-Dirac integral of order j, T is the temperature, η_{F2} is the reduced Fermi energy and $m_t^* = 0.19m_o$ for an NMOS channel. For a PMOS channel, the appropriate effective mass that due to the heavy holes and quantization is given as $m^* = m_{hh}^* = 0.48m_o$. The low-field mobility $\mu_{\ell fe(h)} = q\tau_{ce(h)}/m_{e(h)}^*$ is controlled by quantum-confinement effect as well as by other scattering processes that may be present in the channel [2]. When channel length becomes smaller than the mean free path ℓ_o the mobility may be limited by the geometrical length $L_{e(h)}$ of the channel [3]. The ballistic mobility may also affect the nano-CMOS design. According to Rothwarf's mobility model [4], a 45 nm electron ballistic mobility is given by $\mu_{Le} = 0.036/(1 + (E_t/150.5 \cdot 10^{-6})^{0.666})$ where $\mu_{\ell fe(h)} = 0.036$ and $E_t = (V_{GS} + V_t)/(6t_{ox})$. $V_{GS} + V_t$ is the sum of gate and threshold voltage respectively while t_{ox} is the oxide thickness. On the other hand, the hole ballistic mobility is given by $\mu_{Le} = 0.005/(1 + (E_t/150.5 \cdot 10^{-6})^{0.666})$.

Both mobility model is incorporated in the *I-V* model of a 80 nm MOSFET [2] and verified against the IBM experimental data of a 45 nm NMOS and 45 nm PMOS [5]. The extracted experimental data from $V_G = 0.4$ V to 1.0 V has good agreement with the simulated current for both NMOS and PMOS as shown in Figure 1 and Figure 2, respectively. In order to achieve the comparable drain current in the CMOS design as shown in Figure 3, the NMOS and PMOS have to be scaled based on the velocity saturation and mobility ratios of both electrons and holes as well as length and width as shown in Table 2. This can be done by scaling of PMOS length about 4 times

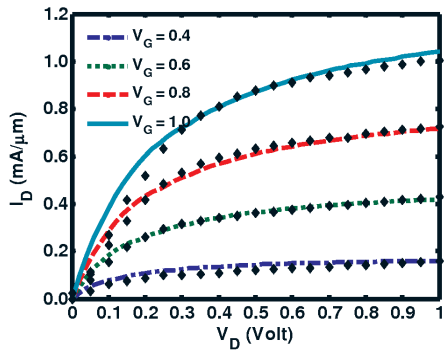

Figure 1: Simulated 45 nm NMOS (lines) *I-V* characteristic versus 45 nm IBM experimental data (symbol)

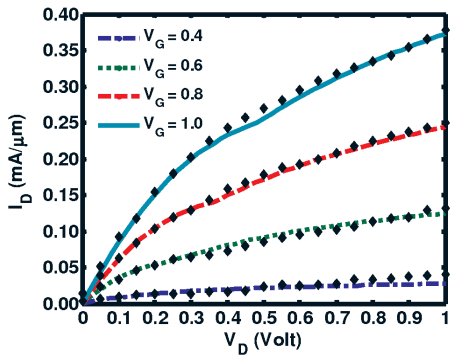

Figure 2: Simulated 45 nm PMOS (lines) *I-V* characteristic versus 45 nm IBM experimental data (symbol)

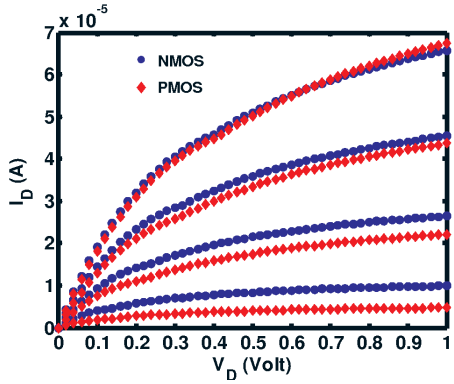

Figure 3: PMOS and NMOS *I-V* characteristic using ratio in Table 2 to achieve comparable saturation current. Initial V_{GS} at 0.4 V at 0.2 V spacing

Table 1: Device Model Specification NMOS & PMOS

Parameter	NMOS	PMOS
Effective Oxide Thickness, EOT [5]	1.2 nm	
Insulator Thickness, t_{ox}	2.1 nm	1.2 nm
Channel Length, L	45 nm	
Low Field Mobility, $\mu_{\ell f}$	0.036 m^2/V-s	0.005 m^2/V-s

Table 2: Device Model Specification for CMOS

Parameter	NMOS	PMOS
Channel Length, L	90 nm	22 nm
Channel Width, W	90 nm	108 nm
Length Ratio, L_p/L_n	0.24	
Width Ratio, W_p/W_n	1.20	
Ballistic mobility ratio μ_p/μ_n	0.11	
Saturation velocity ratio $v_{\rm satn}/v_{\rm satp}$	1.53	

smaller than NMOS while maintaining matching width for both devices. Both attain same drain current when at high gate voltage ($V_{GS} = 1.0$ V) as depicted in Figure 3. PMOS has an obvious lower mobility but higher velocity saturation than NMOS.

The models are verified with simulations and IBM 45 nm experimental data for NMOS and PMOS and are found to be in good agreement. The mobility model incorporated in the MOSFET model plays an important role in determining the modeling of CMOS device due to the predominant ballistic process. The new CMOS circuit design sets the width W_n of the NMOS and W_p of PMOS channels to be as close as possible ($W_p = 1.2W_n$) while length is scaled inversely proportional to the low-field mobility, of the channel. This promising design rule is shown to transform to $W_p/W_n = v_{\rm satn}/v_{\rm satp}$ with $L_p/L_n = \mu_{\ell fp}/\mu_{\ell fn}$ and push the performance limit of short channel CMOS device.

References

[1] V. K. Arora 2008 "Ballistic Quantum Transport in Nano Devices and Circuits", in 2nd *IEEE Int. Nanoelectronics Conf.*, Shanghai, People's Republic of China, 573–578

[2] V. K. Arora, M. L. P. Tan, I. Saad, R. Ismail 2007 *Appl. Phy. Lett.* **91** (Sep) 103510 (3 pages)

[3] J. Łusakowski, W. Knap, Y. Meziani, J.-P. Cesso, A. El Fatimy, G. Ghibaudo, F. Boeuf, T. Skotnicki 2005 *Appl. Phys. Lett.* **87** (July) 053507 (3 pages)

[4] A. Rothwarf 1987 *IEEE Electron Device Letters* **EDL-8** (10) 499–502

[5] V. Chan, R. Rengarajan, N. Rovedo, J. Wei, T. Hook, P. Nguyen, C. Jia, E. Nowak, C. Xiang-Dong, D. Lea, A. Chakravarti, V. Ku, S. Yang, A. Steegen, C. Baiocco, P. Shafer, N. Hung, H. Shih-Fen, C. Wann 2003 "High speed 45 nm gate length CMOSFETs integrated into a 90 nm bulk technology incorporating strain engineering", *IEEE Int. Electron Devices Meeting 2003*, Washington, DC, 3.8.1–3.8.4

Transit, L/R, and RC Time Delay for Reactive Elements in Series with a Micro/Nano-Resistor

V. K. Arora[1a,2], A. Manaf bin Hashim[2], D. C. Y. Chek[2], T. Saxena[3]

[1] *Division of Engineering and Physics, Wilkes University*
Wilkes-Barre, PA18707, USA

[2] *Faculty of Electrical Engineering*
Universiti Teknologi Malaysia, UTM Skudai
Johor 81310, Malaysia

[3] *Department of Physics, Indian Institute of Technology*
Bombay, Mumbai, India

[a] *vijay.arora@wilkes.edu*

The transient effects in a nano/micro-scale channel are severely affected by the resistance blow-up due to sublinear current-voltage characteristics leading to velocity and current saturation. This resistance blow-up effect increases the transit-time delay through the device that decreases as length of the conducting channel is decreased, but always larger than that predicted from the application of Ohm's law. RC time constant is shown to enhance dramatically while RL time constant decreases considerably over and above the predictions of Ohm's law. It is argued that the use of copper in place of aluminum for an interconnect and low-k dielectric for the parasitic capacitance may not necessarily lower the timing delay as intrinsic resistance rise is always present making optimization crucial. Also, the frequency response $f = 1/2\pi\tau$ will be affected as resistance blows up in a micro/nano-scale resistor. A higher capacitance extracted from RC time constants obtained from cutoff frequency is noted if $R = R_o$ (Ohmic) in place of blown-up resistance R is used. The critical voltage is $V_c \approx \infty$ for a macro-resistor. For example, with length $L = 1.0$ cm of a typical color-coded resistor used in an undergraduate laboratory, the critical voltage $V_c \approx \varepsilon_c L = 3.8$ kV is much larger than any value of the applied voltage. The experimentally measured critical electric field [1] for an InGaAs nano-resistor is $\varepsilon_c = 0.38$ V/μm. As the length of a resistor is reduced below micro/nano-regime, say $L = 1.0$ μm, $V_c \approx \varepsilon_c L = 0.38$ μm. A logic voltage of 5 V or even 1.8 V being considered in a modern-day very-large-scale-integrated (VLSI) nano-circuit exceeds the critical value ($V \gg V_c$). This onsets the sublinear behavior, making Ohm's law invalid [2]. All transients, including the transit-time τ_t, RC time constant $\tau_{RC} = RC$, and RL time constant $\tau_{RL} = L_{\rm ind}/R$ delay are sternly affected due to ensuing resistance blow-up effect [1]. The resistance (inverse slope of I-V characteristics) rises as linear Ohmic behavior transforms to sublinear one resulting in ultimate current saturation [2, 3]. R is the resistance of

a resistor in Ω, C the capacitance of a capacitor in F, and $L_{\rm ind}$ the inductance of an inductor in H. In this presentation, the transient phenomena as applied voltage switches from $V=0$ (low) to say $V=5$ V (high) is presented for applications. The critical voltage $V_c=\varepsilon_c L$ is then 0.38 V for a 1-μm length resistor, 1.9 V for a 5-μm resistor and 3.8 V for a 10-μm resistor.

The velocity response to an applied voltage $V=\varepsilon L$, where ε is the resultant electric field, in a nano/micro-scale device of arbitrary dimensionality is reported by Arora [3]:

$$v=v_{\rm sat}\,{\rm tgh}(\varepsilon/\varepsilon_c)=v_{\rm sat}\,{\rm tgh}(V/V_c)=\begin{cases}\mu_o\varepsilon & \varepsilon<\varepsilon_c\\ v_{\rm sat} & \varepsilon>\varepsilon_c\end{cases} \tag{1}$$

with μ_o the Ohmic mobility and $v_{\rm sat}$ the saturation velocity. The stochastic carrier motion in zero electric field (equilibrium) with zero average velocity is shown to streamline in a very high electric field resulting in velocity saturation [3]. The ultimate saturation velocity is the intrinsic velocity $v_{\rm sat}=v_i$ whose average value can be calculated from the Fermi-Dirac distribution function and the density of states [3] for a given dimensionality.

Figure 1 shows the current response to the applied electric field obtained from theoretical calculations that are consistent with the experimental data of Greenberg and del Alamo [1]. Figure 2 shows transit time delay as a fraction of $\tau_o=L/v_{\rm sat}$. The Ohmic transit time delay in $V>V_c$ regime is underestimated, but is not a serious factor in overall timing delay. Figure 3 shows the enhancement in RC switching delay that can be a serious factor as compared to transit-time delay. While transit time delay decreases with the length of the sample, the RC timing delay increase requiring optimization for the length of a conducting channel. Figure 4 shows the inductive coupling delay for which exact differential equation could be solved only by numerical means. However, an approximate analytical solution is consistent with the exact numerical solution. So, inductive coupling may not pose as much threat for frequency response in micro/nano-circuits as RC timing delay as length of a conducting channel is reduced.

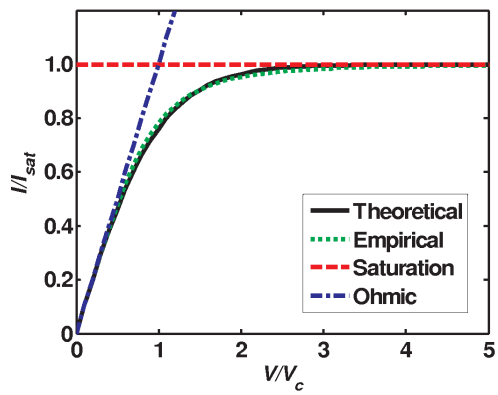

Figure 1: Theoretical and experimental I-V characteristics of a micro-resistor

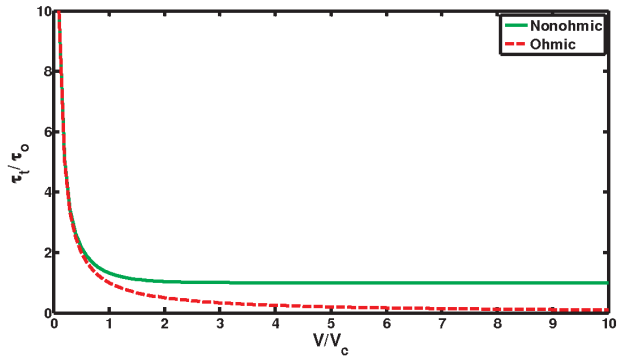

Figure 2: The normalized transit time delay as a function of normalized applied voltage

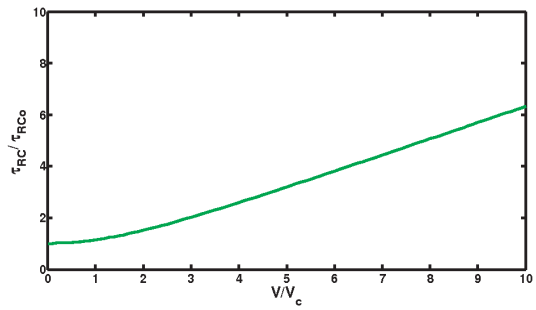

Figure 3: The normalized RC time delay as a function of normalized applied voltage

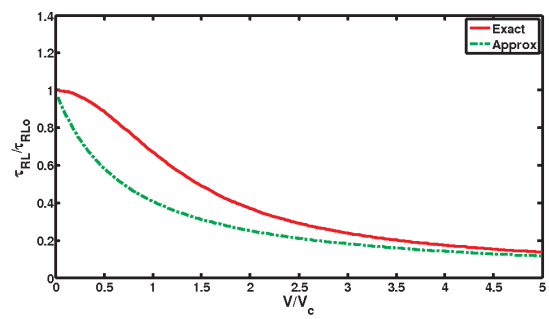

Figure 4: The normalized RL time delay as a function of normalized applied voltage

The blown-up resistance R as compared to its ohmic value R_o enhances as [3]:

$$\frac{R}{R_o} = \frac{V/V_c}{\text{tgh}(V/V_c)} \tag{2}$$

Equation (2) shows that in the Ohmic regime ($V < V_c$), $R/R_o \approx 1$. However, in the sublinear regime ($V > V_c$), $R/R_o \approx V/V_c$ rises linearly with the applied voltage. The

rise in the incremental resistance $r = dV/dI$ is even much higher affecting the propagation of analog signals.

References

[1] D. R. Greenberg, J. A. del Alamo 1994 *IEEE Trans. Electron Devices* **41** 1334–1339
[2] V. K. Arora 1984 *Phys. Rev. B* **30** 7297
[3] V. K. Arora 2009 *Current Nanoscience* (*CNANO*) **5** 227–231
[4] M. L. P. Tan, I. Saad, R. Ismail, V. K. Arora 2007 *NANO* **2** (4) 233–237

Magnetic Behaviour of Ni Nanoparticles Films Produced by Two Laser Irradiations in Vacuum

G. Ausanio[a], V. Iannotti, S. Amoruso, C. Hison, L. Lanotte

CNR-SPIN, Dip. to Sci. Fisiche, Univ. di Napoli Federico II
V. Tecchio 80, I-80125 Napoli, Italia

[a] *ausanio@na.infn.it*

Magnetic nanoparticles-assembled films are good candidates to obtain peculiar macroscopic magnetic properties which can be optimized for specific technological applications in a wide range of magnetomechanical and magnetoelectrical devices, by controlling the morphology and topology of the constituent nanoparticles (NPs). In fact, the physical properties of the systems of NPs associated to their small size and large surface-to-volume ratio can lead to peculiar properties that cannot be found in corresponding bulk materials [1, 2]. Despite the huge research efforts in the field of physical and chemical methods for the preparation of magnetic nanostructured systems – with reproducible narrow size distribution, controllable shape and proper NPs topology to tune suitable interplay between exchange and dipolar magnetic interactions – there is still a great need of simply, cost-effective synthesis techniques able to assure contemporaneously all the above mentioned characteristics.

Femtosecond pulsed laser deposition (fs-PLD) has been recently established to be an effective, versatile and reliable deposition technique for any material [3, 4]. The resulting films exhibit an enhanced purity and crystalline quality with respect to the conventional preparation techniques such as nanosecond pulsed laser deposition, dc/ac sputtering, etc. The morphological and topological peculiarities of the NPs-assembled films prepared by fs-PLD are: (i) the constituent NPs present a typical oblate shape, with the major axes parallel to the substrate surface, (ii) cauliflower-like aspect due to the NPs aggregates, made of non-coalescent, smaller primary NPs, with entrapped voids among them [5, 6].

In this work we study the possibility to modify the size and size distribution of the NPs produced by femtosecond pulsed laser deposition, by using the irradiation of the NPs plume with a secondary UV laser beam, and the consequent changes in the macroscopic magnetic behavior of the NPs systems.

The experimental setup used for the preparation of Ni NPs-assembled films is made of a chirped pulse amplification Nd:Glass laser system, delivering ultrashort laser pulses ($\approx$ 300 fs, 527 nm), a 99.9% pure Ni target mounted on a rotating holder and a silicon substrate located 30 mm away from the target surface and parallel to it, all placed in a vacuum chamber evacuated to a residual pressure of 10^{-10} bar. In order to modify the size of the NPs directly generated from the target by phase explosion and fragmentation mechanisms under the action of the fs laser pulses, a sheeted ultraviolet (UV) beam produced by a XeF excimer laser ($\approx$ 20 ns, 351 nm) was focused on the

expanding plume, in a perpendicular geometry. The appropriate adjustment of the temporal delay τ between the UV and fs laser pulse, using a delay generator, allows the UV beam to interact with different parts of the NPs plume. Subsequently, the NPs are collected onto the substrate and, due to suitable selected ablation-deposition parameters.

The morphological and topological characteristics of the NPs and NPs-assembled films was studied by an Atomic Force Microscope (AFM, Nanoscope IIIa Digital Instruments) on less than one layer deposits. The AFM was operating in tapping-mode, with scan size and rate of 1×1 μm and 1 Hz, respectively, using a sharpened AFM tip, with a very low curvature radius (2 nm) to minimize convolution effects. Moreover, all AFM images were corrected by deconvolution, in order to avoid tip size effect. *X*-ray Diffraction (XRD) was used for structural analysis. The magnetic behavior of the deposited films was investigated by a Vibrating Sample Magnetometer (VSM, Maglab 9T Oxford Instruments).

The comparative evaluation of the AFM images and of the corresponding size histograms of less than one layer deposits obtained without and with secondary UV laser irradiation, for two temporal delays (2.2 μs and 3.7 μs), shows a sensible decrease of the median value of the in-plane diameter (D) and height (d) up to $\approx 40\%$ and 80%, respectively of the NPs obtained by double laser irradiation with respect to those prepared only by fs-PLD. It has been established that plume NPs absorb the UV radiation, increase their temperature and partially vaporize, thus reducing their size. Moreover, the D and d size distributions exhibit a remarkable narrowing for the cases in which the secondary laser irradiation is active.

The normalized magnetization, M/M_s, versus magnetic field, $\mu_0 H$, cycles at 300 and 10 K show the dependence of the magnetic behavior of the Ni NPs-assembled films on their morphological and topological properties. The VSM measurements evidence an increase of the magnetic cycles squareness and a broader switching field distribution in the samples obtained using a secondary UV laser irradiation with respect to those prepared only by fs-PLD, while the saturation magnetic field and remanent magnetization ratio are almost constant.

The challenging task of solving the disadvantage of the fs-PLD technique, with respect to other preparation methods of NPs-assembled films, in what concern the broad size distribution of the deposited NPs has been accomplished by means of double laser irradiation in vacuum. The changes in the films morphology and topology, mainly characterized by NPs size decrease and size distribution narrowing, and consequently in their magnetic properties, can be controlled by properly modifying the time delay for the secondary UV laser irradiation that intercepts different regions of the NPs plume during its expansion from target to substrate, determining the NPs partial vaporization. The obtained results demonstrate that using this double laser irradiation in vacuum, the magnetic behavior of the NPs-assembled films can be efficiently and reproducibly tailored toward higher squareness of the magnetic cycles for specific applications in magnetic recording and magnetic micro/nano-electro-mechanical devices requiring hard magnetic materials.

Acknowledgements
This work was supported by the PRIN'07 Project of the Italian Ministry of Education, University and Research (MIUR), entitled "Magnetic Nanostructures with Coexistence of Magnetoresistive and Magnetostrictive Properties".

References

[1] Battle X, Labarta A 2002 *J. Phys. D: Appl. Phys.* **35** R15
[2] Sellmyer D, Skomski R (Eds.) 2006 *Advanced Magnetic Nanostructures* Springer
[3] Perez D, Lewis L J 2003 *Phys. Rev. B* **67** 184102
[4] Eliezer S, Eliaz N, Grossman E, Fisher D, Gouzman I, Henis Z, Pecker S, Horovitz Y, Fraenkel M, Maman S, Lereah Y 2004 *Phys. Rev. B* **69** 144119
[5] Ausanio G, Barone A C, Iannotti V, Scardi P, D'Incau M, Amoruso S, Vitiello M, Lanotte L 2006 *Nanotechnology* **17** 536
[6] Iannotti V, Ausanio G, Amoruso S, Barone A C, Campana C, Hison C, Lanotte L 2008 *Appl. Phys. A* **90** 653

New MEMS Technology Based on Nano-Structured Materials

M. Balucani[1a], P. Nenzi[1], C. Crescenzi[1], F. Palma[1], V. Bondarenko[2], A. Klyshko[2]

[1] *University „Sapienza" of Roma, Electronics Engineering Department*
Via Eudossiana, 18-00184 Roma, Italy

[2] *Belarussian State University of Informatics and Radioelectronics*
Micro- and Nanoelectronics Department
P. Brovki, 6, 220027 Minsk, Belarus

[a] *balucani@die.uniroma1.it*

Introduction. The testing step is a must in the industrial fabrication of integrated circuits. Alongside with the increasing complexity and performance of integrated circuits (ICs), the number of input and output pads is also increasing. As a result, the number of the test probes should increase at the same rate, but this is a challenging task due to the decreasing pad size and pad pitch [1, 2]. According to the ITRS, up to 2013 probe technologies must support peripheral staggered pad probes at effective pitches of 20–40 μm, 45 μm pitch for dual row, non-staggered probing on all die sides. Multi-site probing support is highly desirable.

The conventional needle probe card cannot fit to test higher pad-density ICs. Several alternative probe card technologies using the semiconductor fabrication techniques have been proposed [3, 4]. A membrane probe card for high-density ICs [5, 6] still has some limitations in use due to nonuniform contact force and high contact resistance [7–9]. A cantilever-type MEMS probe card developed by Zhang et. al. cannot endure or produce the force required to break the oxide on a pad surface [7].

Currently there is no available probe card technology on the market that would meet all of the technology requirements (such as low contact and low series resistances, high scalability, exact positioning of tips, versatile chip pattern, low cost per touchdown) simultaneously. Different technologies are used for different applications.

The new technology. The main idea of the proposed novel design of a probe card capable of further shrinking in dimensions is presented in Figure 1. A developed probe card is a compliant electrical contact structure. The technology is based on free standing metal wires embedded in a polymer matrix. The metal wires provide electrical contact; the polymer matrix supports the wires, adds mechanical stability and provides compliance with the assembly. The „compliance" of such an electric contact is determined totally by the polymer whose mechanical characteristics can be modulated.

A technology based on the silicon MEMS process was developed to obtain a developed structure. The contacting metal structures were lithographically patterned onto the carrier substrate. Lithography was used to define the wires and tips with a high

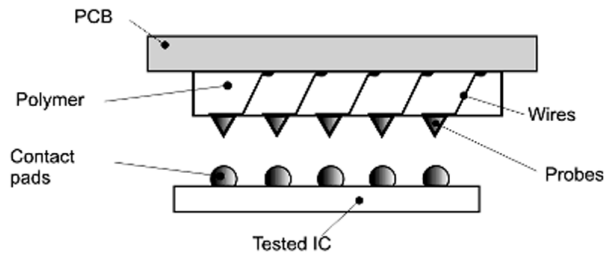

Figure 1: Proposed novel construction of the probe card

accuracy and shape to meet the pitch and electrical requirements. A combination of metal layers was then electroplated on the carrier substrate to obtain wires. At the assembly step the carrier substrate with probing structures was aligned with the alumina ceramic serving as a first level signal redistribution layer. Then, the structures were bonded face-to-face by means of solder in a thermo-compression process. Once bonded, the assembly was separated to release the metal wires from the carrier substrate and keep two substrates at a prescribed distance. A subsequent filling process was performed to fill the air gap with a liquid polymer. After the polymer had been cured the carrier substrate was etched releasing the probing tips.

Key processes. The technology relies on two key challenges: (i) the ability to increase and control the adhesion of thick metals onto silicon and (ii) on modulating the mechanical characteristics of the polymer. Nano-structured materials are used to fulfil both requirements. The adhesion is tuned changing the porosity of the nano-porous silicon structures. The fixed mechanical properties of the polymer (e.g. polydimethylsiloxane) are tuned nano-charging the polymer with nanoparticles (e.g. silica). Detailed investigations were performed in order to exploit these processes.

(i) The core of the proposed technology is a porous silicon layer. Porous silicon is a known material used in many applications as a sacrificial and active material. In the present technology a porous silicon matrix is used to increase and modulate adhesion of thick metal layers to the silicon wafer surface [10]. Such modulation is needed to keep metal wires on the carrier substrate during the preliminary step and allow their partial release without fracture at the assembly step. Samples of uniform porous silicon with different porosities were prepared and locally electroplated with copper in order to measure the porosity influence on the adhesion. The metal wires were then vertically pulled with a LLOYD LRX plus material testing machine. It was found that increasing the porosity of porous silicon led to a significant increase in the adhesion. The main reason for this is the penetration of metal into pores (Figures 2a and 2b), leading to an increase in the effective contact area between the metal layer and the silicon. Adhesion can be increased by increasing the porosity till the fragility of porous silicon becomes higher than the adhesion value.

(ii) The electronic application of organic polymers is becoming a very strong component in the design of devices. They are used in every step of the device fabrication process, starting from the substrate and ending with the packaging. This is explained by the widest spectra of the electrical, mechanical and chemical properties. In fact polymers have been usually employed as insulators and dielectrics, but now the de-

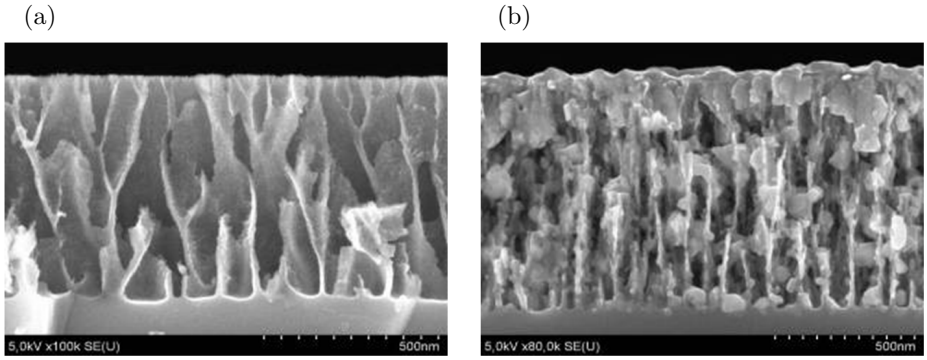

Figure 2: SEM cross section image of porous silicon as fabricated (a) and after metal deposition (b)

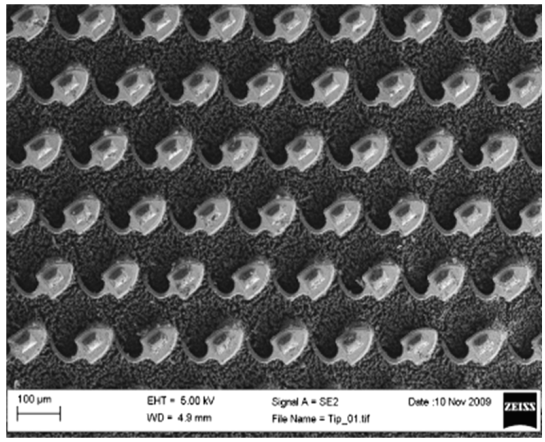

Figure 3: Compliant array configuration for probe card

velopment of new materials has broadened their utilization into areas where their semiconducting and conducting properties are utilized, such as in displays, corrosion resistant coatings, sensors, solar cells, capacitors. It is known that the mechanical properties of polymers are tunable by mixing of different types of resins, adding nano-powders, varying the curing time, out-gassing process, etc.

In the present application polymer was used to obtain a compliant structure composed of tip bars and a uniform layer containing all the suspended metal wires. The incorporation of nano-powder into the polymer was chosen as the process to tune the polymer properties. The polymer used was silicone RTV 90700AB (viscosity: 1000 mPa·sec, hardness Shore A 8, density 1.1 g/cm^3) and the nano-powder used was silicon dioxide with an average particle dimension of 10 nm. Notwithstanding the silicone's hyperelastic behavior, the elastic module of silicone increased from 3.5 MPa to 7 MPa loading with nano-powders. Furthermore, the polymer response to the rate strain was investigated. The tip bar height, the layer thickness and the mechanical properties of the nano-loaded polymer were among the critical parameters. Different

types of polymers with high mechanical strength, good behavior at fatigue stress and compliant strains were studied and tested. Detailed results of the mechanical properties of a polymer, mixed with nanoparticles, such as plasma etching behavior in different gas conditions, will be presented.

Conclusions. A new fabrication process was developed to produce a prototype of compliant MEMS. Such micro-compliant systems were applied for obtaining electric contacts for integrated circuit testing (e.g. array probe card, Figure 3), to replace the wire bonding technique for high power devices and for obtaining a THz band antennas array. The properties of familiar materials were modified by using nano-porous silicon and nanoparticles.

References

[1] S. Asai, K. Kato, N. Nakazaki, Y. Nakajima 1996 *IEEE Trans. Comp., Package. Manufat. Technol. A* **19** 258–267
[2] C. Barsotti, S. Tremaine, M. Bonham 1988 *Proc. ITC'88* 608–614
[3] R. Pandey, D. Higgins 1998 *IEEE ITC'98* 836–842
[4] T. Tada, R. Takagi, S. Nakao, M. Hyozo, T. Arakawa, K. Sawada, M. Ueda 1990 *IEEE ITC'90* 900–906
[5] J. Leung, M. Zargari, B. A. Wooley, S. S. Wong 1995 *IEDM'95* 424–429
[6] M. Beiley, J. Leung, S. S. Wong 1995 *IEEE Trans. Comp., Package. Manufat. Technol. B* **18** (1) 179–183
[7] Y. Zhang, Y. Whzng, R. B. Marcus 1999 *IEEE J. Microelectromechanical Systems* **8** 43–49
[8] B. H. Kim, S. J. Park, B. L. Lee, J. H. Lee, B. G. Min, S. D. Choi, D. I. Cho, K. J. Chun 2002 *The 14th IEEE Int. Conf. on MEMS* 368–371
[9] K. Kataoka, S. Kawamura, T. Itoh, T. Suga 2002 *The 15th IEEE Int. Conf. on MEMS* 364–367
[10] A. Klyshko, M. Balucani, A. Ferrari 2009 *Superlattices and Microstructures* **44** (4–5) 374–377

MR and Histological Evaluation of Acute Arterial Mesenteric Ischemia in Small Animals

D. Berritto[1], F. Somma[1], C. Cavaliere[1], M. Corona[2], N. Landi[1], R. Grassi[1]

[1] *Institute of Radiology, Neurological Sciences Department*
Second University of Naples
Piazza Miraglia, 80138, Naples, Italy

[2] *Cardarelli Hospital, Biotechnology Centre*
Via Cardarelli 9, 80131 Naples, Italy

Purpose: Mesenteric ischemia is an uncommon but often underestimated cause of nontraumatic acute abdomen and its global prevalence is around 0.1% of all hospital recoveries.

Despite our better knowledge and improved diagnostic techniques bowel infarction is still frequently a fatal disease, with reported mortality rates between 50% and 90%. This poor outcome has remained static for many decades and is associated with a variety of contributing factors. Of particular relevance is the late presentation, late or incorrect diagnosis, wrong therapies.

Thanks to a simple and versatile and inexpensive animal model, we reproduced this pathology, inducing intestinal ischemia without laparotomy. The aim of the study was to identify MR imaging patterns of lesions due to an acute occlusion of Superior Mesenteric Artery (SMA), relating these radiological findings to macroscopical monitoring and histology.

Methods and Materials: 30 *Sprague Dawley* rats were anesthetized, a laparotomy was performed, and the cranial mesenteric artery was isolated. In the first group of "control" animals ($n = 15$), the artery was directly occluded by a tight ligation, and, after 8 hours, the bowel was excised for a histological analysis. In the second group ($n = 15$), a loop (3-0 gut) was tied loosely around the vessel and the tips were exposed on the rat's back without occluding the artery. After 3 days from surgery, basal MR abdominal scans were collected for each rat. Afterwards the loop was tied by external tips to occlude the vessel and the MR session was repeated 4 and 8 hours later. The animals were then sacrificed and the entire intestinal package processed for a histological analysis on hematoxylineosin-stained sections.

Results: No animals died before the end of the study. One rat from the second group was excluded from the analysis because it showed SMA stenosis but not a complete occlusion at 8 h after ligation in the angio-MR sequences. Abdominal MR scans showed no gas in the abdominal cavity and no signs of bowel or mesentery irritation. The T2 MR sequences identified several injury signs of a vascular occlusion such as dilatation of loops, a decrease in the intestinal wall thickness and peritoneal fluid. These changes were paralleled by histological alterations as highlighted by ex-vivo

examination, with no significant differences in the histological analysis of the same intestinal tracts between the two groups.

Conclusion: This animal model could represent a useful and highly reproducible tool to evaluate by imaging the evolution of the intestinal ischemic lesion and to assess the effectiveness of new therapeutic modalities. Compared to the histological analysis, MR imaging can correctly identify morpho-functional alterations of intestinal ischemia due to an acute occlusion of SMA.

Mechanism of Metal Salts Reduction by Biradical Di-p-Xylylens

M. Bobrowski

Department of Solid State Physics, Gdansk University of Technology
Narutowicza 11/12, 80-233 Gdansk, Poland

TASK Computer Center, Gdansk University of Technology
Narutowicza 11/12, 80-233 Gdansk, Poland

In 2000 Jensen and coworkers [1] found that some metals and metal salts could quench the polymerisation of parylene-N and parylene-C. The inhibition of growth of parylene chains depends on the metal type used. On the other hand, it is well known that the polymerisation mechanism of parylenes in the gas phase is of a radical type [2, 3]. Recently it has been also found that there is a strong dependence between the thermodynamic barrier of metal salts reduction by radicals during polymerisation and the normal redox potential of appropriate reaction of reduction.

In this work I propose a mechanism of metal salts reduction by biradical di-p-xylylens. The calculations were performed by means of various *ab initio* DFT and semiempirical methods finding appropriate saddle points and energy profiles crossings depending on the spin symmetry of substrates and products. It turned out that in some cases the kinetic barriers were very low and depended on the value of the normal redox potential of an appropriate reaction of metal ion reduction while the anion type was less important.

Acknowledgements
The investigations were supported by STREP n 033201 (NMP3-CT-2006-033201) from the EC as well as by the Polish State Committee for Scientific Research. The calculations were carried out with the use of the resources and software of the Informatics Center of the Metropolitan Academic Network (IC MAN) at the Gdansk University of Technology and the Interdisciplinary Center for Mathematical and Computer Modeling (ICM) in Warsaw, Poland.

References

[1] K. M. Vaeth, K. F. Jensen 2000 *Chem. Mater.* **12** 1305–1313
[2] K. Smalara, A. Giełdon, M. Bobrowski, J. Rybicki, C. Czaplewski paper sent for publication to *J. Phys. Chem.*
[3] L. A. Errede, M. Szwarc 1958 *Q. Rev. Chem. Soc.* **12** 301 1

Photoelectron Spectra Induced by Broad-Band Chaotic Light from a Structured Continuum

V. Cao Long, W. Leoński, K. Q. Doan

Quantum Optics and Engineering Division, Institute of Physics
University of Zielona Gora
Prof. A. Szafrana 4a, 65-516 Zielona Góra, Poland

Different ionization processes of atoms in laser fields have been the center of interest in both theoretical and experimental research in atomic physics for a long time. One of the most interesting examples of those processes is the so-called laser induced autoionization in which a nontrivial structure of a continuum occurs due to the mixing of the ionizing states with the continuum. In this paper, we consider a model for laser-induced autoionization introduced before in [1]. Following [2] we assume that the laser light is decomposed into two parts: the deterministic (or coherent) part and the one which is a randomly fluctuating chaotic component, which is a correlated, Gaussian, Markov and stationary process (white noise). This model for the field is interesting by itself because it describes the electric field amplitude of the multimode laser, operating without any correlation between the modes. We solve a set of coupled stochastic integro-differential equations, describing a double Fano model for autoionization. We determine the exact photoelectron spectrum and compare it with our results obtained before in [1] and [2].

Our paper is organized as follows: After the introduction, in the second section some details of our model are described and the equation for atomic operators is derived. In the third part, our results are presented and discussed. Instead of presenting a rather complicated formula (some details of the calculations leading to that formula can be found in the appendix) we have restricted ourselves to just two most interesting physical limits: weak and strong fluctuations.

References

[1] W. Leoński, R. Tanaś, S. Kielich 1987 *J. Opt. Soc. Am. B* **4** 72
[2] V. Cao Long, M. Trippenbach 1986 *Z. Phys. B* **63** 267

Topographic Control of Neuronal Polarity: Shaping Adhesions into Stable Polarity States

M. Cecchini

NEST, Istituto Nanoscienze-CNR, Scuola Normale Superiore
Piazza San Silvestro 12, I-56126 Pisa, Italy

The interaction between differentiating neurons and the extracellular environment guides the establishment of cell polarity during nervous system development. The developing neurons read the physical properties of the local substrate in a contact-dependent manner and retrieve essential guidance cues. We engineered biocompatible nanostructured substrates designed for high-resolution live-cell microscopy by exploiting nanoimprint lithography techniques and cyclic olefin copolymers in order to unravel the mechanisms by which differentiating neurons read the local topography. Neuronal contact guidance, establishment of polarity, focal adhesion maturation, cell generated contractility, and active remodelling in differentiating PC12 cells sensing nanotopographies will be analysed and discussed. Finally, the role of different differentiation pathways in the regulation of neuronal polarization on nanogratings will be addressed.

Nano-Plasmonic for Single Molecule Detection and Nanomapping

F. De Angelis

NanoBioScience Laboratory, Italian Institute of Technology
via Morego 30, I-16163 Genova, Italy

francesco.deangelis@iit.it

The fields of plasmonics, Raman spectroscopy, and Atomic Force Microscopy experienced a huge but independent development in the last decades. The potential progress derived by unifying these different techniques is of primary importance for obtaining simultaneous and complementary information at level of single molecule detection. Here we propose and demonstrate that the convergence of those distant fields can open access to topographic, chemical and structural information on a spatial scale of few nanometers. We report on the design, fabrication and measurements of a photonic-plasmonic device that is fully compatible with atomic force microscopy and Raman spectroscopy. The physical mechanism exploited is the generation of surface plasmon polaritons by means of a tapered nanostructure that causes Raman excitation through an adiabatic concentration of electromagnetic field in a spatial region of few nanometers at the taper apex.

The device consists in a silver nano-cone acting as a plasmonic nanoantenna, placed at the centre of a photonic crystal (the device is fabricated on AFM cantilever). Surface imaging resolution and chemical sensitivity with a spatial resolution up to 7 nm were demonstrated. This new tool accesses to all of the information provided by the mentioned techniques, such as molecular structures, molecular interactions, force binding, local arrangement, surface topography and chemical nano-mapping also under physiological condition. It will provide an effective convergence between nano and bio technologies, where the understanding of how individual molecules behave has significant implications in Biology and Medicine.

Soft Magnetic Thick Films Electroless Deposited on Insulator Materials

E. Dimitriu[1], N. Lupu[2]

[1] *REGO COM*
Calea 13 Septembrie 115, 050716 Bucharest-5, Romania

[2] *National Institute of Research and Development for Technical Physics*
47, Mangeron Blvd., 700050 Iasi, Romania

The electroless deposition consists of the reduction reaction of nickel ions from a solution on activated substrates. An acid or a basic nickel plating solution, together with a reducing agent such as sodium hypophosphite, formaldehyde, dimethyl- or diethylborane, hydrazine, etc., are used [1–3]. During the reducing process some other metals or non-metals from the plating solution are included in the nickel deposit, and binary or ternary intermetallic compounds are obtained. These compounds modify some of the physico-chemical properties of pure nickel [1, 4–6].

In this paper, thick nickel films were chemically deposited on alumina and piezoceramic substrates. The substrate activation is based on the general tendency of ions in solutions to be reduced at zero-valent state in the presence of a metallic atom with a higher electronegativity value. For instance if Al or Mg is deposited on a dielectric substrate, with a suitable reducer and bath composition, the metallic ions from the solution, such as Ni^{+2} or Co^{+2}, are reduced and the film containing the metal from the solution is deposited on the substrate instead of Al or Mg [7]. The nickel was deposited in two stages. First the substrate was activated by an original method. A thin film of a metal with electronegativity values between 1.2 and 1.7 (Al and Mg, respectively) was evaporated in vacuum on the substrate. In the second stage the activated surfaces were introduced into alkaline nickel plating solutions, I and II, containing different amounts of sodium hypophosphite as the reducing agent: 0.5 wt. % and 1.5 wt. % solution (with the $NiCl_2$/sodium hypophosphite ratio of 1/1 and 1/3, respectively.) The pH values of the nickel plating solution were 8–9.5, and the deposition temperature range was 368–371 K.

The XRD spectrum of nickel layers chemically deposited on alumina from solutions with composition I and II is characterized by broad and weak diffraction peaks, indicating the presence of small amorphous particles and traces of crystalline Ni grown in the (111) plane. The diffuse maximum at $2\theta = 44.5°$ is attributed to the amorphous phase $Ni_{1-x}P_x$. The structural order degree of the Ni-P phase can be semi-quantitatively defined by the width, ΔNiP, at half maximum of the principal diffuse peak at $2\theta = 44.5°$ (Table 1). The amorphous phase gradually crystallizes during annealing for 1 h at 673 K and 1053 K in hydrogen atmosphere. The increase in the crystalline nickel concentration during annealing is estimated by the height ratio between the Ni [111] line and the amorphous peak contribution at the same angle, and

Table 1: Crystalline parameters of $Ni_{1-x}P_x$ compounds

Plating solution	T_a (K)*	Δ NiP	R_1	R_2
I	–	5.6	0.25**	0
I	673	5.6	>1.31	6.23
II	–	7.0	0.32**	0
II	1053	7.0	0.77	8.10

* Annealing temperature (1 h in H_2)
** Superposition of Ni [111] on the weak peak of the Al_2O_3 substrate

is denoted as R_1 (the Ni_{Cryst}/Ni_{amorph} ratio). Cubic Ni_7P_3 and traces of hexagonal Ni_5P_4 were present in the films deposited from solution I. In the annealed films prepared from solution II, hexagonal Ni_5P_2 was evidenced. The wt. % P concentration of the layers prepared from solutions I and II was 11.05 and 11.95 respectively, and corresponded to the approximate formula $Ni_{80}P_{20}$. Therefore, a mixture of the Ni and Ni_7P_3 phases (with a small amount of Ni_5P_2) looked reasonable. All the phases showed a preferred orientation of the crystallites with respect to the alumina substrate plane. The appearance of the Ni_xP_y phases upon annealing is described in Table 1 by the ratio, R_2, between the line maximum with $d = 1.94$ Å (mainly due to Ni_7P_3 and Ni_5P_4) and the diffuse halo height taken at $2\theta = 46.6°$ ($R_2 = NiP_{Cryst}/NiP_{amorph}$).

The thickness of electroless nickel layers is very important for the electrical properties: amorphous layers with thicknesses over 8–12 μm are good conductors of electricity, while those with the thickness less than 1 μm are resistive. The electrical resistivity of an amorphous Ni layer is about 800 $\mu\Omega$cm at room temperature, i.e. very large compared with that of pure Ni (6.9 $\mu\Omega$cm) [8]. The electrical resistivity of an amorphous Ni layer is almost constant over a large temperature range (300–77 K). For the samples annealed in hydrogen at 673 K, the electrical resistivity decreases at about 190 $\mu\Omega$cm at room temperature, since the metallic behaviour of the nickel layers is improved. The resistivity ratio ($\varrho_{300\ K}/\varrho_{77\ K}$) increases from about 1.05 to 4.20 for annealed samples. The linear dependence of the resistivity as a function of temperature, $\varrho(T)$ for both samples suggests that the phonon contribution to the carrier scattering is dominant.

The magnetic properties of as-deposited amorphous samples on alumina and Nb-doped PZT substrates were measured. The results are presented in Table 2 and Figure 1.

Whilst $Ni_{1-x}P_x$ films deposited on alumina show typical soft magnetic behaviour, the magnetic hysteresis loops of $Ni_{1-x}P_x$ films deposited on Nb-doped PZT ceramic

Table 2: Magnetic characteristics of amorphous $Ni_{1-x}P_x$ layers

Sample / substrate	Coercivity, H_c (G)	Magnetic moment at 1400 G M_{1400} (emu)	m_r/m_{1400}
$Ni_{1-x}P_x$/alumina	49	$84.6 \cdot 10^{-6}$	0.23665
$Ni_{1-x}P_x$/PZT-Nb $R_{sq} = 0.2\ \Omega$	64	$459.1 \cdot 10^{-6}$	0.13978
$Ni_{1-x}P_x$/PZT-Nb $R_{sq} = 0.4\ \Omega$	64	$461.3 \cdot 10^{-6}$	0.13766

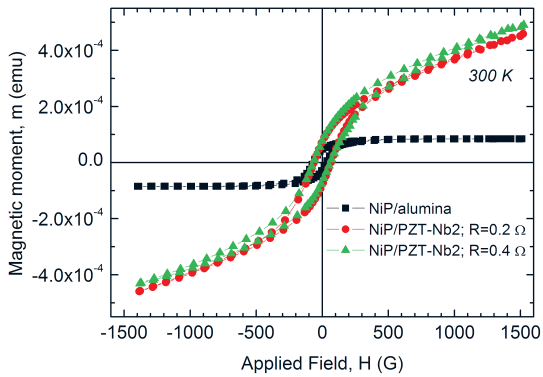

Figure 1: Magnetization curves for $Ni_{1-x}P_x$ films deposited on alumina and Nb-doped PZT ceramic substrate

substrates consist of two superposed components (Figure 1): the ferromagnetic component is the response of the $Ni_{1-x}P_x$ film, and the paramagnetic one is the contribution of the substrate. A slight shifting of the magnetic moment curve *vs.* the applied magnetic field is observed for the films deposited on a PZT substrate, too. We assume that the magnetic moment is influenced by the conductivity of the $Ni_{1-x}P_x$ deposit, depending in its turn on the film thickness. The ferromagnetic properties described above are in good agreement with the results from the literature for $x < 14$ wt. % [9].

The same activation method can be used for Ni-Fe-P alloy deposition on dielectric substrates.

In conclusion, the nickel layers chemically deposited by this method are amorphous and contain 11–12 wt. % P. The layers crystallize during heat treatment, with formation of metallic nickel and a mixture of nickel phosphides: cubic Ni_7P_3, hexagonal Ni_5P_4, hexagonal Ni_5P_2. The heat treatment of the Ni-P chemically deposed layer decreases the resistivity values by several times. The prepared thick Ni films, characterized by a good adherence on the substrate and chemical stability together with their electrical properties, are suitable as electrodes on insulator materials.

References

[1] Gawrilov G C 1974 *Chemische (Stromlose) Vernicklung* Eugen G. Leuze Verlag, Saulgau Wurtt
[2] Mononobe S and Ohtsu M 2007 *Jpn. J Appl. Phys.* **46** (9B) 6258
[3] Kim K M, Lee J H, Yoon S M, Lee H C, Lee Y K, Choi J Y 2006 *J. Electroceramics* **17** 339
[4] Gylienė O, Vaskelis A, Tarozaitė R, Jagminienė A 2007 *Chemija* **18** (1) 1
[5] Mendoza-Zelis L, Thomé L, Brossard L, Chaumont J, Królas K, Bernas H 1982 *Phys. Rev. B* **26** 1306
[6] Chiriac H, Moga A E, Urse M, Paduraru I, Lupu N 2004 *J. Magn. Magn. Mater.* **272–276** 1678
[7] Dimitriu E 1995 Patent No. RO 109905 C1
[8] 1996/1997 *Goodfellow Catalogue*, Goodfellow Cambridge Limited, Cambridge, England
[9] Bakonyi I, Burgstaller A, Socher W, Voitländer J, Toth-Kadar E, Lovas A, Ebert H, Wachtel E, Willmann N, Liebermann H H 1993 *Phys. Rev. B* **47** (22) 14961

Luminescence and Excited State Dynamics of $(Lu_{1-x}Gd_x)_2SiO_5$ Solid Solutiuon Crystals Doped with Dy^{3+} Ions

G. Dominiak-Dzik[1a], W. Ryba-Romanowski[1], R. Lisiecki[1], P. Solarz[1], M. Berkowski[2]

[1] *Institute of Low Temperature and Structure Research Polish Academy of Sciences Okólna 2, 50-950 Wrocław, Poland*

[2] *Institute of Physics, Polish Academy of Sciences Al. Lotników 32/46, Warsaw, Poland*

[a] *G.Dominiak-Dzik@int.pan.wroc.pl*

Lutetium and gadolinum oxyorthosilicates, Lu_2SiO_5 (LSO) and Gd_2SiO_5 (GSO), belong to monoclinic structure, however, they differ in the space group ($C2/c$ and $P2/c$, respectively). Recently, they have been of great interest owing to their unique thermal and optical properties. Co-doped with Ce^{3+}, they offer such applications as detectors in positron emission tomography or efficient phosphors. Both crystals possess the ability to accommodate rare earth ions thereby emerging as valuable materials for the design of new laser systems. Doped with Dy^{3+} ions, they can make laser materials emitting in the visible range. However, a disadvantage of the LSO crystal is its high melting point of 2050°C that is very close to the breakdown temperature of an iridium crucible. An alternative is the growing of mixed $(Lu_{1-x}Gd_x)_2SiO_5$ (LGSO) solid solution crystals with lower melting points comprising between 2050°C (LSO) and 1770°C (GSO).

The $(Lu_{1-x-z}Gd_xDy_z)_2SiO_5$ ($x = 0.2,\ 0.4,\ 0.6,\ 0.8,\ z = 0.04$) single crystals were grown by the Czochralski method. It was found that the growth behaviour of the Dy:LGSO crystals was similar to that of Dy:LSO and the melt temperature decreased monotonously from 2000°C for $(Lu_{0.8}Gd_{0.2})_2SiO_5$:Dy to 1835°C for $(Lu_{0.2}Gd_{0.8})_2SiO_5$:Dy. The X-ray results revealed that the LGSO:Dy solid solution crystals exhibited an LSO type structure ($C2/c$) even for the sample with 80% of Gd^{3+} replacing Lu^{3+} ions in the structure.

The emission bands exhibited the nature of a Dy:LSO crystal. However, the spectral lines were quite broadened and their crystal-field structure was poorly resolved what implied a considerable structural disorder. The visible luminescence from the $^4F_{9/2}$ state was observed at 574 nm (yellow emission) and at 484 nm (blue emission). It was found that the luminescence intensities of Dy^{3+} in the $(Lu_{1-x}Gd_x)_2SiO_5$ compounds were higher than those of the Dy:LSO [1] or Dy:GSO [2] crystals. The experimental lifetimes of the $^4F_{9/2}$ state in the Dy:LGSO solid solutions were close to those in Dy:LSO ($\tau_{\mathrm{mean}} \approx 63\ \mu$s in LGSO:4% Dy, $\tau_{\mathrm{mean}} = 202\ \mu$s in LSO:5% Dy) and substantially longer than those in GSO:5% Dy ($\tau_{\mathrm{mean}} = 118\ \mu$s).

The laser potential related to the $^4F_{9/2} \rightarrow ^6H_{13/2}$ emission in the Dy:LGSO materials was assesed based on evaluation of the emission cross section values and compared with those of the Dy:LSO and Dy:GSO crystals.

References

[1] R. Lisiecki, G. Dominiak-Dzik, P. Solarz, W. Ryba-Romanowski, M. Berkowski, M. Głowacki 2010 *Appl. Phys. B* **98** 337–346
[2] G. Dominiak-Dzik, W. Ryba-Romanowski, R. Lisiecki, P. Solarz, M. Berkowski *Appl. Phys. B* DOI 10.1007/s00340-009-3852-x

Multiphoton Nanolithography of Functional Materials Towards Applications of MEMS/NEMS

X.-M. Duan

Laboratory of Organic NanoPhotonics, Technical Institute of Physics and Chemistry, Chinese Academy of Sciences
Beijing, China

Zhongguancun Beiyitiao, Haidian
Beijing 100190, China

xmduan@mail.ipc.ac.cn

Introduction. In the past few years, the research on nanolithography has attracted significant attention and interest. Among various techniques, multiphoton nanolithography (MPN) has emerged as a powerful tool, which might hold the key to complex 3D structures fabrication with nanometer scale precision [1]. The spatial resolution of MPN becomes one of the key issues for its application in nanolithography. With laser direct writing technique, the spatial resolution is difficult to achieve at nanometer scale due to the diffraction limit of light. MPN provides the potential to break the diffraction limit and realize the fabrication resolution under nanometer scale [2]. Here, we report the latest progresses on improvement of MPN resolution with multiphoton polymerization (MPP) of organic photoresist, functionalization of materials suited for MPP, and the applications for MEMS/NEMS.

Spatial Resolution in MPP. Here, we define the spatial fabrication resolution (SFR) as the area size of the spatial volume where the multiphoton absorption occured. In MPN, SFR depends on the distribution of laser intensity of at lateral focus plane and on the propagation direction. Fig. 1 shows the isophotes of light intentisty calculated using a objective lens with NA of 1.45 [3]. SFR can be expressed as lateral and axial spatial resolution (LSR and ASR).

Using fs pulse laser ($\lambda = 800$ nm) and high speed scanning mode, we obtained the LSR of 50 nm on the surface of substrate as shown in Fig. 2(a) [3], which indicated that the area of MPP is limited to nanometer scale. Moreover, we also achieved the highest LSR of 15 nm when the cured polymer line was fabricated as suspended line between two supports as shown in Fig. 1(b) [4], in which shrinkage of cured polymers with low polymerization degree was effective for reducing the LSR. Utilizing asymmetric shrinkage of cured polymer allows us to obtain polymer lines with low aspect ratio [3], which is of importance for fabrication of photonic devices.

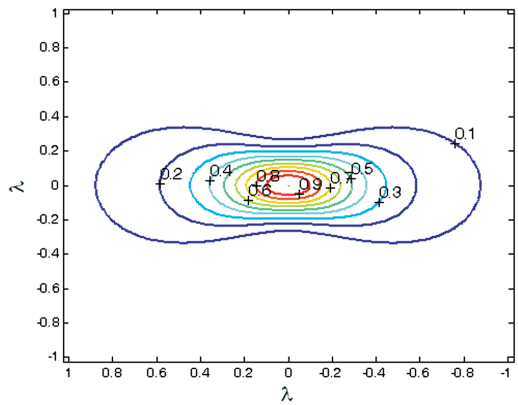

Figure 1: Isophotes of light intensity calculated using a objective lens with NA of 1.45 in MPN

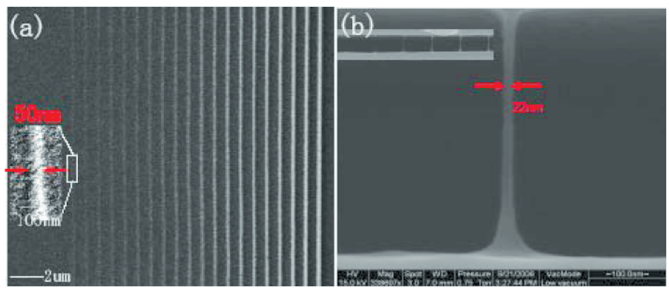

Figure 2: SEM images of cured polymer lines by MPP; (a) the highest LSR of 50 nm cured on surface of substrate; (b) LSR of 22 nm cured as suspended line

3D Lithography for MEMS/NEMS

Photonic Devices. For improving the functions of 3D microstructures, we proposed a method suited for MPP fabrication of 3D microstructures of nanocomposites [5]. Recently, we developed the concept of size control of nanoparticles in composites with tuning the crosslinking networks of polymer [6]. Using this concept, we successfully

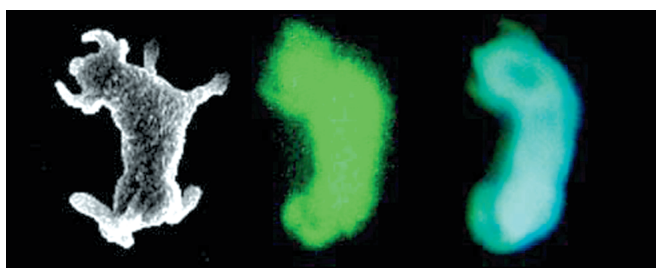

Figure 3: Multicolored microbulls of CdS-polymer nanocomposites with tunable CdS nanoparticle sizes fabricated by combination of in situ synthesis and MPP

fabricated various 3D microstructures with the polymer nanocomposites with different sizes of nanoparticles [7, 8], and obtained multicolor 3D microstructures (Fig. 3).

We used dendrimer to modify laser dyes and improved the dye concentration upto 5.5 wt % in photoresist. This photoresist was used to fabricate a 3D micro/nanometer-scaled resonator, which was composed of a series of suspended polymerized fibers supported by cuboids arrays. The fabricated 3D resonator contained nanofibers exhibited the lasing phenomenon as shown in Fig. 4 [9]. The lasing at 556 nm was observed with a ultralow threshold of 0.30 μJ/pulse. It was indicated that the polymeric suspended nanofibers plays a critically important role in constructing this microresonator.

3D MEMS. In order to realize the application of MPP, improving fabrication speed is important for mass fabrication of micromachines and microdevices. Recently, we developed a new technique for fabricating assembled 3D microstructures using a designable multiple beams [10], which could efficiently simplify the assembling process. Using this technique, we successfully fabricated various sets of 2D & 3D microstructures as shown in Fig. 5. The method can be expected in the applications for the practical fabrication of micro/nanoscale MEMS.

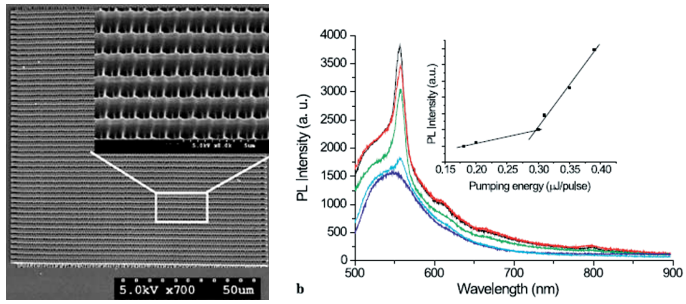

Figure 4: (a) SEM image of cuboids arrays with suspended fibers; (b) Emission spectra of the cuboids arrays with suspended fibers

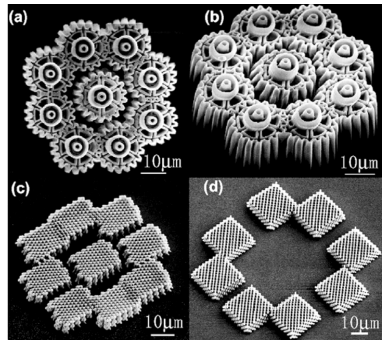

Figure 5: Top (a) and side (b) views of assembled microgear set; sets of 3D PhCs with hcp (c) and diamond structures (d)

Conclusion. Multiphoton nanolithography techniques, including multiphoton polymerization and photoreduction, have exhibited the capability as a potential tool for the application in fabrication of nanostructures and nanodevices, since it could break the diffraction limit and obtain the nanoscale resolution with direct laser writing technique. The resolutions of 50 nm and 120 nm have been achieved in MPP and MPR, respectively. With funtional materials such as nanocomposites, luminescent polymers as well as nobel metals, various nanostructures have been demonstrated as functional devices for the applications in photonics.

References

[1] S. Kawata et al. 2001 *Nature* **412** 697
[2] J.-F. Xing et al. 2007 *App. Phys. Lett.* **90** 131106
[3] X.-Z. Dong, Z.-S. Zhao, X.-M. Duan 2008 *App. Phys. Lett.* **92** 091113
[4] D. Tan et al. 2007 *App. Phys. Lett.* **90** 061106
[5] X.-M. Duan et al. 2004 *Thin Solid Films* **453–454** 518
[6] Z.-B. Sun et al. 2008 *Adv. Mater.* **20** 914
[7] Z.-B. Sun et al. 2007 *Chem. Lett.* **36** 156
[8] Z.-B. Sun et al. 2007 *Appl. Phys. A* **86** 427
[9] C.-F. Li et al. 2007 *Appl. Phys. A* **89** 145
[10] X.-Z. Dong, Z.-S. Zhao, X.-M. Duan 2007 *App. Phys. Lett.* **91** 124104

Elastic Response of Magnetic Viscous Materials Subjected to Resonance Magnetic Field

M. R. Dudek[1], N. Guskos[2,3]

[1] *Institute of Physics, University of Zielona Gora*
Szafrana 4a, 65-069 Zielona Góra, Poland

[2] *Solid State Physics Section, Department of Physics, University of Athens*
Panepistimiopolis, 15 784 Zografos, Athens, Greece

[3] *Institute of Physics, West Pomeranian University of Technology*
Al. Piastów 17, 70-310 Szczecin, Poland

It is shown that magnetic viscoelastic materials with a magnetic component consisting of magnetic nanoparticle agglomerates can have different elastic responses to different values of the external dc magnetic field, $H_{\rm dc}$. In the particular case of magnetic resonance taking place at the resonance field, $H_{\rm dc} = H_r$, the elastic deformation

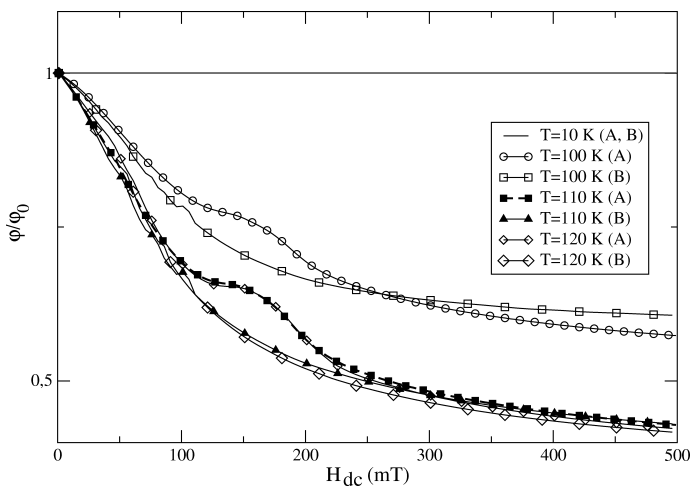

Figure 1: Dependence of average angle, $\varphi = \frac{1}{N}\sum_{i=1}^{N}\varphi_i$, formed by the magnetic anisotropy axis and the direction of $H_{\rm dc}$ on $H_{\rm dc}$ strength for different temperatures; φ_0 represents the initial angle at which the magnetic nanoparticle is pinned elastically to its nonmagnetic surrounding. Sample A denotes the results for a cluster of $N = 30$ magnetic nanoparticles with the majority of magnetic anisotropy axes aligned with the direction of the external dc magnetic field, Hdc. Sample B represents a cluster of $N = 30$ magnetic nanoparticles with all magnetic anisotropy axes which are oriented at random with respect to the direction of $H_{\rm dc}$. The values of $H_{\rm dc}$ where the maximum discrepancy of φ/φ_0 between samples A and B is observed correspond to the resonance magnetic field, H_r

of the surrounding of magnetic nanoparticles can be much larger than the deformations corresponding to the values of H_{dc} close to H_r. The magnetic anisotropy axes of the magnetic nanoparticles undergo orientation ordering after the external magnetic field, H_{dc}, is switched on. The reorientation processes of magnetic nanoparticle agglomerates strongly depend on the viscoelasticity of the materials in which they are dispersed. It is especially important for the deformation phenomena driven by a low concentration of magnetic nanoparticles in a non-magnetic matrix. Some physical properties of such a matrix could change positively for their application state [1, 2]. A theoretical study of the viscoelastic materials and their temperature dependence could give a better understanding of the orientation processes of the spin correlating systems in transforming the physical properties of a new generation of magnetic materials.

There is a narrow range of temperatures where the magnetic resonance can be detected from the deformation strength of the surrounding of magnetic nanoparticles. A simple theoretical model of a single cluster consisting of N magnetic nanoparticles in an elastic polymer matrix is introduced to show the magnetic resonance effect on the deformation of the nonmagnetic nanoparticle surrounding through magnetic-elastic coupling. The model is based on the stochastic version of the Lifshitz-Landau equation for nanoparticle magnetization. The role of the viscosity temperature dependence on the absorption lines in the FMR experiment (ferromagnetic resonance experiment) has been discussed by the authors recently [3].

Acknowledgements
Publication of this paper was realised with partial financial support from the budget resources of the West Pomeranian Voivodeship.

References

[1] Maryniak M, Guskos N, Typek J, Guskos A, Gorący K, Rosłaniec Z, Kwiatkowska M 2009 *Polimery* **54** 546
[2] Guskos N, Typek J, Padlyak B V, Gorelenko Yu K, Pełech I, Narkiewicz U, Senderek E, Guskos A, Rosłaniec Z, submitted to *J. Non-Cryst. Solids*
[3] Dudek M R, Guskos N, Senderek E, Rosłaniec Z, submitted to *J. Comp. and Alloys*

Nanostructure-Based Biosensors

X. Chen, S. Roy, Z. Gao[a]

Institute of Bioengineering and Nanotechnology
31 Biopolis Way, Singapore 138669

[a] *zqgao@ibn.a-star.edu.sg*

Electrical detection schemes for the quantification of DNA using nanostructure-based sensor arrays are proposed in this work. The prime objective is to develop a novel sensing procedure, based on the electrical transduction mechanism, which would mitigate the problems intrinsic to nanostructure-based biosensing devices. Design considerations of the sensor array take into account the feasibility of mass production in a cost-effective way by using standard silicon microfabrication technologies.

Two nanostructures, namely silicon nanowires and nanogaps, are discussed. Arrays of highly ordered n-type silicon nanowires (SiNW) are fabricated using complementary metal-oxide semiconductor compatible technology and their applications in biosensors are investigated. Peptide nucleic acid (PNA) capture probe-functionalized SiNW arrays show a concentration-dependent resistance change upon hybridization to complementary target DNA that is linear over a large dynamic range with a detection limit of 10 fM. As with other SiNW biosensing devices, the sensing mechanism can be understood in terms of the change in charge density at the SiNW surface after hybridization, the so called "field effect".

The second type of sensor array is based on nanogaps. The sensing mechanism relies on bridging the nanogap upon hybridization of the two termini of a target DNA with two different surface-bound capture probes, followed by a simple metallization step. About two orders of magnitude enhancement in conductance, as referred to a clean background (< 1.0 pS), was obtained in the presence of as little as 1.0 fM target DNA. A linear relationship between the conductance and DNA concentration was obtained from 1.0 fM to 1.0 pM with an exceptional signal intensity of $2.1 \cdot 10^4\%$ change per unit concentration. This change in conductivity is so large that it can unambiguously detect the concentration of DNA quantitatively and may obviate the need for target amplification used in current DNA tests.

Thermo Mechanical Metamaterials

J. N. Grima

Faculty of Science, University of Malta
Msida MSD 2080, Malta

auxetic@um.edu.mt

Most materials we encounter have a tendency to get thinner when stretched (i.e. exhibit a positive Poisson's ratio). Nevertheless, not all materials behave like this and it is possible for materials and structures to get fatter when stretched (i.e. exhibit a negative Poisson's ratio). Such materials are commonly referred to as auxetic, a word which derives from the Greek word $\alpha\upsilon\xi\varepsilon\tau o\sigma$.

Auxeticity, despite being uncommon, is a highly desirable property since materials with a negative Poisson's ratio are known to exhibit several beneficial or enhanced properties when compared to their conventional counterparts. These include an increased resistance to indentation, enhanced vibration absorption properties and a natural ability to adopt dome shaped surfaces.

In this paper we present some recent advances made in the field of auxetic materials. In particular we review some of the models which are currently in use to explain the Poisson's ratio (both positive and negative) in various classes of materials and show that new materials can be produced to exhibit this anomalous property. We also discuss materials and structures which exhibit negative thermal expansion (i.e. shrink when heated) and negative compressibility (i.e. expand in size when they are subjected to positive hydrostatic pressure), and show that some systems can exhibit more than one of these negative properties.

Nanocomposites Based on PCL/MWCNT for Application In Nanosensors

A. Grozdanov[1], A. Buzarovska[1], M. Avella[2], M. E. Errico[2], G. Gentile[2]

[1] *Faculty of Technology and Metallurgy*
Rugjer Boskovic 16, 1000 Skopje, R. Macedonia

[2] *Institute for Chemistry and Technology of Polymers – CNR*
Fabricato Oliveti 70, Pozzuoli, Napoli, Italy

Carbon nanotubes (CNTs) exhibit unique electronic, metallic and structural properties compared to other materials. For that reason, researchers have focused on utilizing these characteristics for engineering applications such as actuators, hydrogen storage, chemical sensors and nanoelectronic devices. Several papers have been published utilizing CNTs as the sensing material in pressure, flow, thermal, gas, optical, mass, strain, stress, chemical and biological sensors [1, 2]. Amongst many of their superior electro-mechanical properties, it is the piezoresistive effect in CNTs that is attractive for designing strain sensors. When CNTs are subjected to mechanical strain, a change

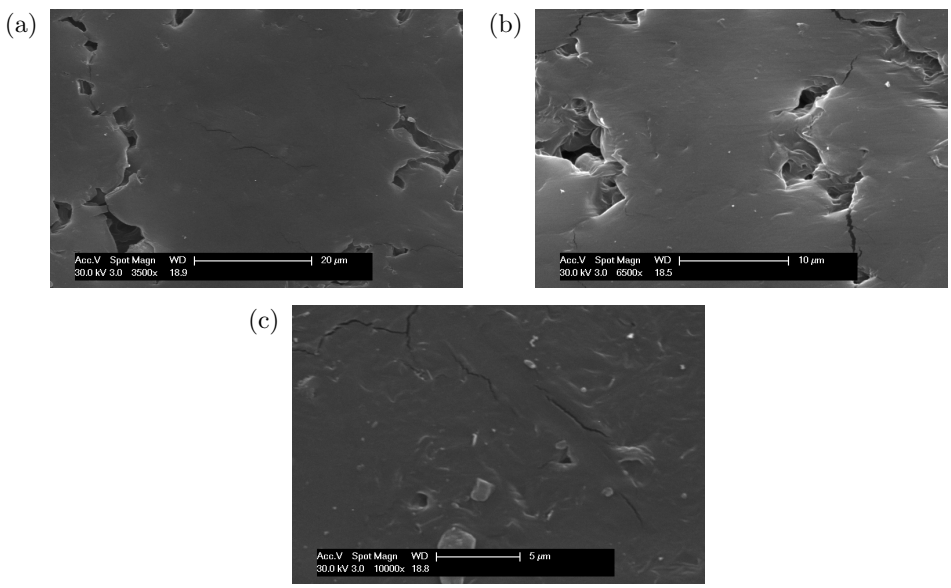

Figure 1: SEM microphotographs of prepared PCL/CNT nanocomposites; (a) PCL-neat (×3500), (b) PCL/0.5% CNT (×6500), (c) PCL/1% CNT (×10000)

in their chirality leads to a modulation of their conductance. In this paper, a novel carbon nanotube/biopolymer nanocomposite was used to develop a piezoresistive strain bio-nanosensor. A biocompatible polymer matrix was used to provide good interfacial bonding between carbon nanotubes. MWCNTs ($d = 30$–50 nm, purity $> 95\%$) were used for preparation of polycaprolactone based nanocomposites, PCL/MWCNT. The PCL/MWCNT nanocomposites were prepared by mixing of the MWCNT and PCL in a tetrahydrofuran solution for 24 h. The PCL/MWCNT nanocomposite films were characterized by DSC, TGA, FTIR and SEM.

The characteristic morphology of the prepared nanocomposites is presented in Figure 1 (a: PCL-neat, b: PCL/0.5% CNT, c: PCL/1% CNT).

References

[1] P. Dharap, Z. Li, S. Nagarajaiah, E. V. Barrera 2004 *Nanotechnology* **15** 379
[2] R. Shandas, C. Lanning 2003 *Med. Biol. Eng. Comp.* **41** 416

Temperature Dependence of Magnetic Anisotropy of Nanocrystalline $0.90(Fe_2O_3)/0.10(ZnO)$ Studied by FMR

N. Guskos[1,2], S. Glenis[1], G. Żołnierkiewicz[2], J. Typek[2], D. Sibera[3], U. Narkiewicz[3]

[1] *Solid State Section, Department of Physics, University of Athens Panepistimiopolis, 15 784 Zografos, Athens, Greece*

[2] *Institute of Physics, West Pomeranian University of Technology Al. Piastów 48, 70-311 Szczecin, Poland*

[3] *Institute of Chemical and Environmental Engineering West Pomeranian University of Technology Al. Piastów 17, 70-310 Szczecin, Poland*

A nanocrystalline $0.90(Fe_2O_3)/0.10(ZnO)$ sample was prepared by the coprecipitation and calcination method. The phase composition of the sample was determined by *X*-ray diffraction. It was dominated by the Fe_2O_3 and ZnO phases and also a very small concentration of the $ZnFe_2O_4$ phase was identified. The ferromagnetic resonance (FMR) of the $0.90(Fe_2O_3)/0.10(ZnO)$ nanopowder was investigated in the temperature range from liquid helium to room temperature (Figure 1). An asymmetrical and very intense magnetic resonance line was recorded at all temperatures.

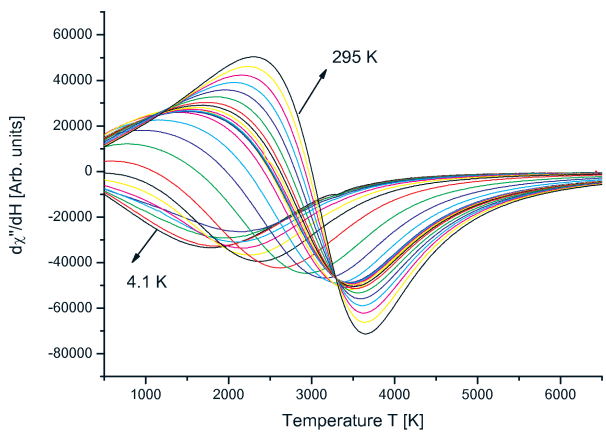

Figure 1: Registered FMR spectra of $0.90(Fe_2O_3)/0.10(ZnO)$ at different temperatures

A significant shift of the FMR spectra towards low magnetic fields with decreasing temperature was observed. Very good fitting by two Lorentzian functions was

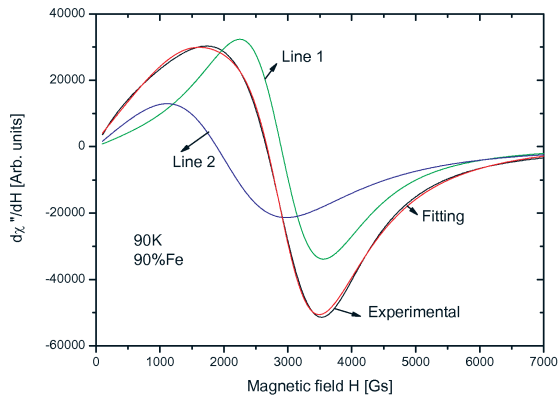

Figure 2: $0.90(Fe_2O_3)/0.10(ZnO)$ FMR spectrum decomposition registered at 90 K

achieved which suggests the existence of a strong anisotropic magnetic interaction. The $0.90(Fe_2O_3)/0.10(ZnO)$ FMR spectrum decomposition registered at 90 K on two components is shown in Figure 2. The temperature dependence of the resonance fields (left panel), linewidths (middle panel) and FMR signal amplitudes (right panel) for the two component lines of the $0.90(Fe_2O_3)/0.10(ZnO)$ sample is presented in Figure 3. Certain similarities could be observed in the temperature dependence of the FMR parameters registered previously for the $0.95(Fe_2O_3)/0.05(ZnO)$ sample, but the measured values were essentially different. The temperature shift of the resonance field $\Delta H_r/\Delta T$, the resonance line broadening as well as the FMR signal amplitude changed more strongly with temperature in comparison to the $0.95(Fe_2O_3)/0.05(ZnO)$ nanopowder. The following $\Delta H_r/\Delta T$ gradient values were obtained for the $0.90(Fe_2O_3)/0.10(ZnO)$ sample: 16.7(1) Gs/K and 20.7(1) Gs/K for temperatures above 60 K (for $0.95(Fe_2O_3)/0.05(ZnO)$ it was 3.7(1) Gs/K and 8.3(1) Gs/K [1]) while below 40 K the values were 41.5(1) Gs/K and 56.0(1) Gs/K (in contrast to 40.5 Gs/K and 49.6 Gs/K for $0.95(Fe_2O_3)/0.05(ZnO)$ [1]). Thus the reorientation processes were more intense in the $0.90(Fe_2O_3)/0.10(ZnO)$ sample, especially at high temperatures.

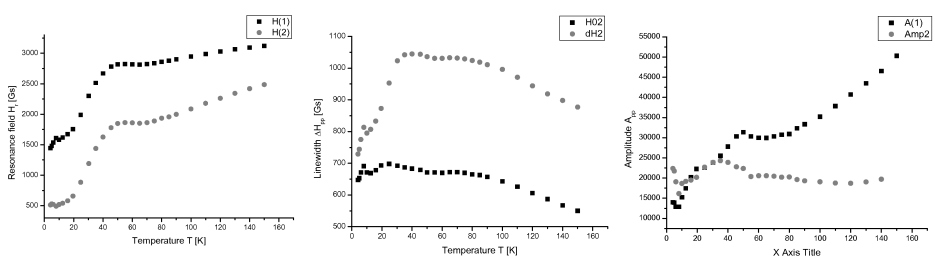

Figure 3: Temperature dependence of resonance fields (left panel), linewidths (middle panel) and FMR signal amplitudes (right panel) for two component lines of $0.90(Fe_2O_3)/0.10(ZnO)$ sample

Acknowledgements
Publication of this paper was realised with partial financial support from the budget resources of the West Pomeranian Voivodeship.

References

[1] N. Guskos, S. Glenis, G. Żołnierkiewicz, J. Typek, D. Sibera, J. Kaszewski, D. Moszyński, U. Narkiewicz, W. Łojkowski, submitted for publication in *J. All. Comp.*

Spin Reorientation Processes in Nanocrystalline 0.95(MnO)/0.05(ZnO)

N. Guskos[1,2], S. Glenis[1], G. Żołnierkiewicz[2], J. Typek[2], D. Sibera[3], U. Narkiewicz[3]

[1] *Solid State Section, Department of Physics, University of Athens Panepistimiopolis, 15 784 Zografos, Athens, Greece*

[2] *Institute of Physics, West Pomeranian University of Technology Al. Piastów 48, 70-311 Szczecin, Poland*

[3] *Institute of Chemical and Environmental Engineering West Pomeranian University of Technology Al. Piastów 17, 70-310 Szczecin, Poland*

A nanocrystalline 0.95(MnO)/0.05(ZnO) sample was prepared by the coprecipitation and calcination method. According to the XRD analysis the dominating phases are Mn_3O_4 and $ZnMn_2O_4$ [1]. The electron paramagnetic/ferromagnetic resonance (EPR/FMR) investigation was carried out in the temperature range from liquid helium to room temperature (RT). The registered spectra at different temperatures are presented in Figure 1. An almost symmetric, very broad and intense magnetic resonance line was recorded in the high temperature range ($T > 60$ K) and a very asymmetric line in the low temperature range ($T < 40$ K).

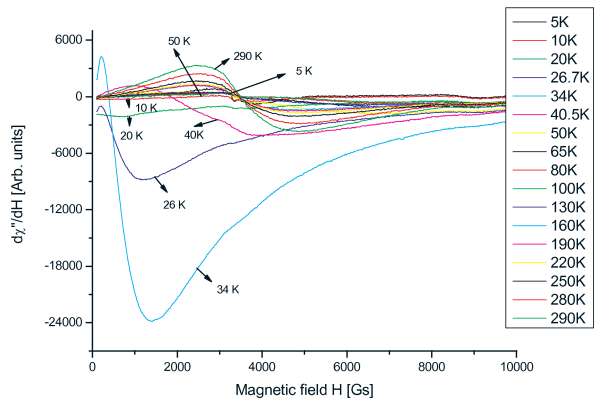

Figure 1: EPR/FMR spectra of nanocrystalline 0.95(MnO)/0.05(ZnO) at different temperatures

A resonance line due to the Mn_3O_4 phase dominated in the high temperature range while the signal from the $ZnMn_2O_4$ phase prevailed at low temperatures. Therefore, a significant change of the magnetic resonance spectrum was observed with the

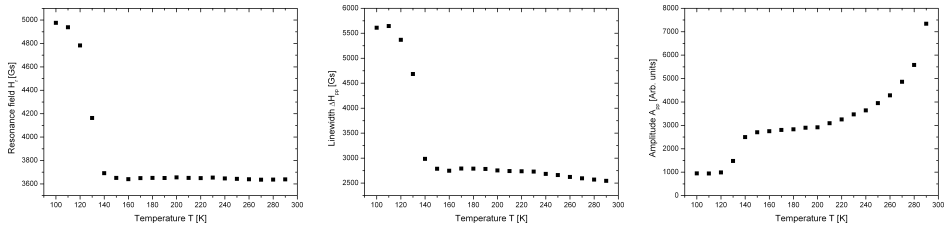

Figure 2: Temperature dependence of the resonance field (left panel), linewidth (middle panel), and signal amplitude (right panel) obtained from the high temperature spectra

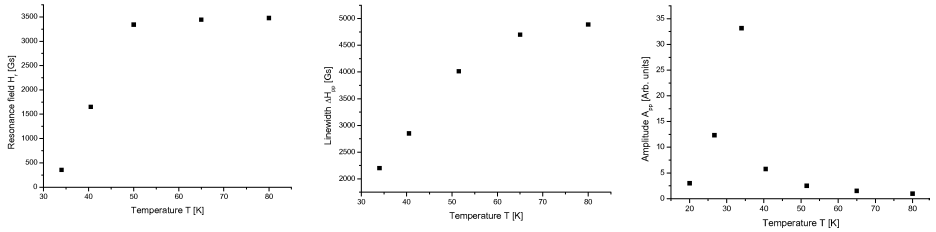

Figure 3: Dependence of the resonance field (left panel), linewidth (middle panel), and signal amplitude (right panel) obtained from the low temperature spectra

temperature decreasing from RT. It resulted in a strong temperature dependence of the magnetic resonance parameters (resonance field, linewidth, signal amplitude). In Figure 2 the temperature dependence of these parameters, obtained from the high temperature spectra, is presented while in Figure 3 a similar dependence for the low temperature range is shown. Magnetic ordering processes (of the antiferromagnetic type) in Mn_3O_4 nanoparticles are assumed to be responsible for the disappearance of the high temperature magnetic resonance line. The observed temperature dependence of the magnetic resonance parameters is connected with the magnetic interaction between nanoparticles during the correlated spin system formation. The magnetic resonance line amplitude in the low temperature range reaches a maximum value at 20 K probably after formation of a strongly correlated spin system with ferromagnetic ordering. The temperature dependence of the resonance line is also characteristic for a strongly correlated system with ferromagnetic ordering [2].

Acknowledgements
Publication of this paper was realised with partial financial support from the budget resources of the West Pomeranian Voivodeship.

References

[1] N. Guskos, G. Żołnierkiewicz, J. Typek, D. Sibera, U. Narkiewicz submitted for publication in *Rev. Adv. Mat. Sci.*
[2] U. Narkiewicz, N. Guskos, W. Arabczyk, J. Typek, T. Bodziony, W. Konicki, G. Gąsiorek, I. Kucharewicz, E. Anagnostakis 2004 *Carbon* **42** 1127

Photoacoustic Response of Green and Red Leaves of Ficus Benjamina Plant

N. Guskos[1,2], J. Majszczyk[2], J. Typek[2], J. Rybicki[3,4], A. Guskos[2]

[1] *Solid State Section, Department of Physics, University of Athens*
Panepistimiopolis, 15 784 Zografos, Athens, Greece

[2] *Institute of Physics, Pomeranian University of Technology*
Al. Piastów 17, 70-310 Szczecin, Poland

[3] *Department of Solid State Physics, Faculty of Applied Physics and Mathematics*
Gdansk University of Technology
Narutowicza 11/12, 80-233 Gdansk, Poland

[4] *Institute of Mechatronics, Nanotechnology and Vacuum Techniques*
Koszalin University of Technology
Racławicka 5–17, 75-620 Koszalin, Poland

Leaves of Ficus benjamina were prepared in a thick film form to study the photoacoustic (PA) response. Two absorption bands in the visible range at about 398 nm and 670 nm for the green leaf and 544 nm and 570 nm for the red leaf were registered. Absorption bands from the $\pi \rightarrow \pi^*$, $\pi \rightarrow n$ charge transitions were detected in the ultraviolet range. The visible PA spectra strongly depended on the leaf colours. The absorption band at 670 nm could be connected with photosynthesis processes [1, 2].

Figure 1: Ficus benjamina leaves in November 2009 on the University of Athens Campus

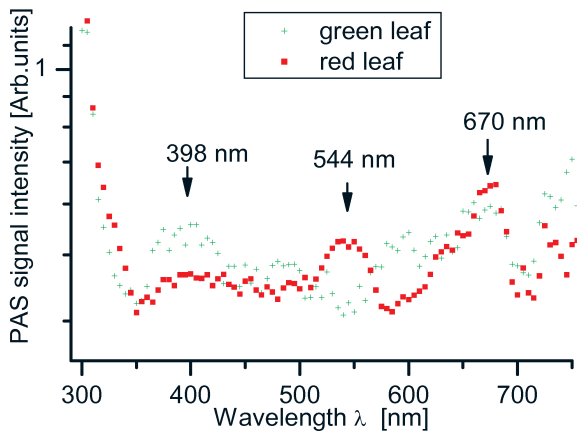

Figure 2: PA spectrum of green and red Ficus benjamina leaves

The observed absorption band at 398 nm for the green leaf disappeared for the red one, but a new band appeared at 544 nm. The above absorption bands in the PA spectrum were very similar to an earlier obtained spectrum of another living organism [3, 4]. The absorption band near 544 nm was similar to the one obtained for spermidine, an important compound involved in the information transfer to DNA [5]. The results obtained are significant, confirming experimentally that the red leaf absorption is particularly strong in that part of the solar radiation spectrum where water is transparent.

Acknowledgements
Publication of this paper was realised with partial financial support from the budget resources of the West Pomeranian Voivodeship.

References

[1] C. Buschman 1989 *Phil. Trans. R. Soc. Lond. B* **323** 423
[2] H. Kojima, M. Tawata, T. Takabe, H. Shimajama 2000 *IEICE Trans. Electron. E* **83** 1142
[3] N. Guskos, K. Aidnis, G. J. Papadopoulos, J. Majszczyk, J. Typek, J. Rybicki 2008 *Optical Materials* **30** 814
[4] N. Guskos, J. Majszczyk, J. Typek, J. Rybicki, I. Kruk, A. Guskos, G. Żołnierkiewicz, E. A. Anagnostakis, C. Aidinis 2010 to appear in *Rev. Adv. Mat. Sci.*
[5] N. Guskos, J. Typek, J. Majszczyk, M. Maryniak, E. Grech, B. Kołodziej 2007 *Rev. Adv. Mat. Sci.* **14** 97

Transport Properties of $Ni_2MV_3O_{11}$ (M=Cr and Fe) and $M_3Fe_4(VO_4)_6$ (M=Mg and Mn) Compounds

N. Guskos[1,2], J. Typek[2], K. Karkas[1], A. Guskos[2], A. Błońska-Tabero[3], M. Bosacka[3]

[1] *Department of Physics, University of Athens*
Panepistimiopolis, 15 784 Zografos, Athens, Greece

[2] *Institute of Physics, West Pomeranian University of Technology*
Al. Piastów 48, 70-311 Szczecin, Poland

[3] *Department of Inorganic and Analytical Chemistry*
West Pomeranian University of Technology
Al. Piastów 17, 70-310 Szczecin, Poland

The transport properties of the multicomponent vanadates, $Ni_2MV_3O_{11}$ (M = Cr and Fe) and $M_3Fe_4(VO_4)_6$ (M = Mg and Mn), were investigated by electrical conductivity measurements. All the compounds exhibited semiconducting behavior. The two former samples showed better conductivity of many orders of magnitude (over

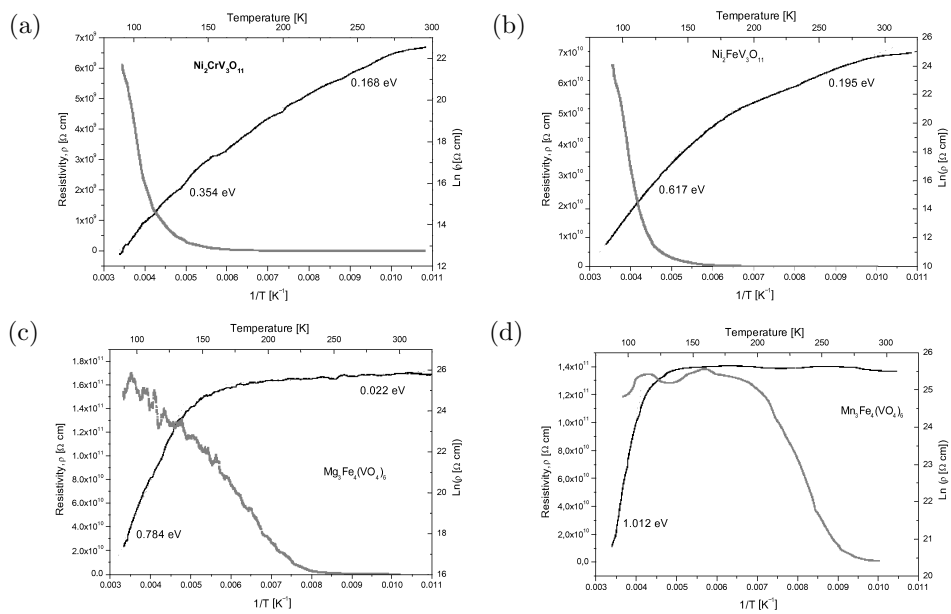

Figure 1: Temperature dependence of resistivity for four different multicomponent vanadates

10^5 times at RT) than the later two ones (see Figure 1). Replacement of the magnetic Cr(III) cation with a magnetic Fe(III) ion in $Ni_2MV_3O_{11}$ resulted in a significant increase in its electrical conductivity at RT and an increase in the activation energy. Very low conductivity was registered in the $M_3Fe_4(VO_4)_6$ compounds in which replacement of the non-magnetic Mg(II) ion with a magnetic Mn(II) ion caused a strong decrease in conductivity. The $M_3Fe_4(VO_4)_6$ compounds had a few sublattices with magnetic ions and displayed the presence of competing magnetic interactions and were thus susceptible to drastic changes of their transport properties by replacement of ions.

Acknowledgements
Publication of this paper was realised with partial financial support from the budget resources of the West Pomeranian Voivodeship.

Magnetic, Elastomagnetic and Elastoresistive Behaviour of Nanoparticles-Assembled Films Produced by fs-PLD

V. Iannotti[1a], S. Amoruso[2], G. Ausanio[1], C. Campana[1], E. Espsosito[3], C. Hison[1], V. Pagliarulo[1], G. Pepe[1], L. Lanotte[1]

[1] *CNR-SPIN, Dip.to di Scienze Fisiche*
Università degli Studi di Napoli "Federico II"
P. le V. Tecchio 80, I-80125 Napoli, Italy

[2] *CNR-SPIN, Dip.to di Scienze Fisiche*
Università degli Studi di Napoli "Federico II"
Complesso Universitario di Monte S. Angelo, I-80126 Napoli, Italy

[3] *CNR-ICIB, Istituto di Cibernetica "Eduardo Caianiello", Comprensorio "A. Olivetti"*
Via Campi Flegrei 34, I-80078, Pozzuoli (NA), Italy

[a] *iannotti@na.infn.it*

Material synthesis using femtosecond pulsed laser deposition (fs-PLD) is an important application because an interesting by-product of the process is the automatic generation of nanometer scale particles during ablation. In the first part of this lecture the related phenomenology will be presented, the nanoparticles (NPs) identified by their structureless continuum optical emission, and the advantages will be showed in comparison with other techniques. From a theoretical point of view, the different models and simulations are based on two important points: (i) the heat transfer from the laser pulse to the target occurs almost at solid density with respect to nanosecond pulses with comparable fluence because the energy is delivered before any significant thermal conduction into the target's bulk can occur and (ii) the subsequent rapid expansion and cooling of the irradiated material result in NPs generation trough mechanisms like phase explosion and fragmentation [1, 2, 3]. These mechanisms, regulated by suitable laser fluence values, determine the splitting of the ejected plume in two main components: a cloud of fast atomic species and a slower one, mainly composed of NPs [4, 5]. Comparing with ablation techniques that use longer laser pulses, namely ns-PLD, where the presence of a high-pressure gas is necessary to obtain NPs [6], in this production system the NPs are produced directly through material decomposition with the ejection of clusters of material of different sizes down to individual atom dimension [1, 7]. Therefore the Nps are spontaneously obtained during the ablation process, the volume fraction can be controlled independently of the NP size and the NPs can come into direct contact.

An important issue is the actual shape of the deposited NPs. They have systematically a disk-like, instead of a sphere-like shape, indicative of a liquid or at least plastic state of the particle impinging on the substrate with a kinetic energy sufficient

to give rise to particle deformation which produces the final observed shapes and an aspect ratio value that depends on the ablation-deposition parameters (e.g. laser intensity, wavelength, etc.). This is of special interest in the case of magnetic materials since these shapes could potentially give rise to anisotropies characteristic of these morphologies [8, 9, 10]. It was observed that the NPs do not coalesce but retain a distinct boundary, even at high NPs volume fractions, though the precise nature of the interface remains uncertain, and an exchange interaction is active among the nearest NPs [11]. Moreover, the films are characterized by an ordinate disposition of the NPs with the major cross-section parallel to the deposition substrate [12].

For all these reasons, fs-PLD is an interesting emergent technique for the fabrication of magnetic nanostructures with a wide size range and exhibiting interesting geometries.

fs-PLD is accomplished by irradiation of a rotating target with high-intensity (10^{12}–10^{14} W/cm^2) ultrashort laser pulses (typically ≈250 fs, 527 nm), in high vacuum (the typical pressure is in the 10^{-7} to 10^{-3} mbar range). The ablated material was collected on suitable substrates placed at a distance of few centimetres from the target surface, and analyzed by microscopy techniques (AFM and SEM). Less than one layer deposits have been used to characterize the NPs shape and size distribution, while collection of a large number of NPs leads to the deposition of a NPs-assembled film. *X*-ray Diffraction (XRD) was used for structural analysis, while the chemical composition of the prepared films was determined by micro-Energy Dispersive *X*-ray Spectroscopy (mEDXS). The magnetic characterization of the deposited films was performed by means of a Vibrating Sample Magnetometer (VSM, Maglab 9T Oxford Instruments).

Exchange-coupled monocomponent (Fe, Co, Ni,) and bicomponent (NiSi, CoCu, FeAg) magnetic films constituted of disk-shape nanoparticles, produced by fs-PLD in vacuum, will be showed together with their magnetic properties. The strict correlation between the NPs morphology (i.e. particles aspect ratio), their ordinate disposition without coalescence, and the macroscopic magnetic behaviour of the fs-PLD NPs films it has been confirmed by the behaviour of the hysteresis loop and initial magnetization curve. The as-deposited films present a high in-plane remanence ratio, relatively low values of the saturation and coercive fields and a steep slope near coercivity at a volume fraction above the magnetic percolation threshold. This appears related to the fact that the nanoparticles, connected by exchange interactions, are effectively single domain and single grain NPs, as observed comparing AFM and *X*-ray size evaluations. Consequently, the fs-PLD films are substantially composed by randomly oriented single domain magnetic NPs without significant textures, coupled through the exchange interactions caused by moderate aggregation of the NPs due to free volume inclusion. The single domain character is also confirmed by the first magnetization curves of the corresponding films.

Subsequently it will be evidenced that the exchange interaction between hard magnetic nanoparticles (Terfenol-D) and soft magnetic nanoparticles (Iron) is active in the fs-PLD film, giving a cumulative magnetic response resulting from an average of the properties of the two component phase (exchange-spring magnets).

The mEDXS measurements demonstrate that the prepared films have the same composition of the target, within an accuracy of ≈5%.

In prospective the striking properties of these nanoparticles-assembled films appear very promising for potential application as nanocomposite permanent magnets and in data storage technology, by tailoring the deposition parameters.

However, for fs-PLD to become of relevance in a near future as a standard technique for the fabrication of magnetic nanostructure, a few aspects need to be improved, especially concerning the particle size distribution. In order to reach this goal, that is to say Nps with a monodisperse small size, we exploited the technique based on the irradiation of the NPs produced by fs-PLD, in flight prior to deposition, with a second, appropriately delayed nanosecond UV beam. By selecting the time delay from the fs laser ablation pulse, one allows vaporizing laser pulse to interact with different parts of the NPs plume. In particular, for time delays $\approx$1–2 μs the vaporizing beam intercepts the most of the NPs plume, while only the trailing edge of the ablated NPs is irradiated at longer time delays. In brief NPs which absorb the UV radiation increase their temperature and are partially vaporized, thus reducing their mean size and the size distribution.

In the second part of this lecture the elastomagnetic and elastoresistive effects in $Co_{50}Fe_{50}$ films produced by fs-PLD, will be showed. In particular, this investigation is focused on the influence of the novel structural conditions on the coupling between strain and magnetization, and/or strain and resistivity, in $Co_{50}Fe_{50}$ NP films deposited on Kapton substrate. Due to the NP nature of the films, these couplings are substantially different from standard magnetostrictive and piezoresistive effects. Magnetization and resistivity versus applied strain were studied [13], thus evidencing novel elastoresistive and elastomagnetic functionalities and evaluating their relative sensitivities.

Room-temperature micro and nano electromechanical devices technology will can benefit by further in-depth studies about these innovative materials.

Finally, in view of the development of cost-effective, innovative, patterned magnetic systems for magnetic random access memories (MRAM), magnetic media for recording density up to 1 Tb·in^{-2} and nanomagnetic logic devices, we have starting to study the possibility to use, together with fs-PLD, the Electron Beam Lithography (EBL) as a high resolution method for fabricating advanced magnetic nanostructures. Preliminary results concerning the elastoresistive effect in $Co_{50}Fe_{50}$ microwires, produced by micrometric photolithography, and the magnetoresistance in $Ni_{84}Fe_{16}$ nanowires containing two constrictions about 100 nm width, produced by EBL, will be presented.

Acknowledgements
This work was supported by the PRIN'07 Project of the Italian Ministry of Education, University and Research (MIUR), entitled "Magnetic Nanostructures with Coexistence of Magnetoresistive and Magnetostrictive Properties".

References

[1] Perez D and Lewis L J 2002 *Phys. Rev. Lett.* **89** 255504
[2] Glover T E 2003 *J. Opt. Soc. Am. B* **20** 125
[3] Amoruso S, Bruzzese R, Wang X, Nedialkov N N, Atanasov P A 2007 *J. Phys D: Appl. Phys.* **40** 331
[4] Amoruso S, Bruzzese R, Spinelli N, Velotta R, Vitiello M, Wang X, Ausanio G, Iannotti V, Lanotte L 2004 *Appl. Phys. Lett.* **84** 4502
[5] Grojo D, Hermann J, Perrone A 2005 *J. Appl. Phys.* **97** 063306

[6] Perrière J, Millon M, Chamarro M, Morcrette M, Andreazza C 2001 *Appl. Phys. Lett.* **78** 2949
[7] Lorazo P, Lewis L J, Meunier M 2003 *Phys. Rev. Lett.* **91** 225502
[8] Cebollada A, García Martín J M, Clavero C, Balcells Ll, Estradé S, Arbiol J, Peiró F, Smith C, Clarke R, Martínez L, Huttel Y, Román E, Telling N D, van der Laan G 2009 *Phys Rev. B* **79** 014414
[9] Iannotti V, Aruta C, Ausanio G, Barone A C, Campana C, Amoruso S, Lanotte L 2008 *J. Phys. D: Appl. Phys.* **41** 195006
[10] Iannotti V, Ausanio G, Campana C, D'Orazio F, Hison C, Lucari F, Lanotte L 2008 *J. Magn. Magn. Mater.* **320** e594
[11] Ausanio G, Barone A C, Iannotti V, Scardi P, D'Incau M, Amoruso S, Vitiello M, Lanotte L 2006 *Nanotechnology* **17** 536
[12] Ausanio G, Barone A C, Iannotti V, Lanotte L, Amoruso S, Bruzzese R, Vitiello M 2004 *Appl. Phys. Lett.* **85** 4103
[13] Ausanio G, Campana C, Iannotti V, Amoruso S, Wang X, Lanotte L 2010 *IEEE Trans. Magn.* **46** 479

The Effect of Surface Nano-Architecture of Polyterpenol Thin Films on Bacterial Retention

K. Bazaka[1], M. V. Jacob[1],
Vi Khanh Truong[2], R. J. Crawford[2], E. P. Ivanova[2a]

[1] *Electronic Materials Research Lab*
School of Engineering and Physical Sciences, James Cook University
Townsville QLD 4811, Australia

[2] *Faculty of Life and Social Sciences, Swinburne University of Technology*
PO Box 218, Victoria 3122, Australia

[a] *eivanova@swin.edu.au*

The nanometer scale surface topography of a solid substrate is known to influence the extent of bacterial attachment and their subsequent proliferation to form biofilms. Previous studies on the effect of surface roughness on the attachment behavior and production of extracellular polymeric substances for the Gram-positive coccoid pathogen, *Staphylococcus aureus* CIP 68.5, and Gram-negative rod shaped bacterium, *Pseudomonas aeruginosa* ATCC 9027, have shown that both pathogens exhibit a greater propensity for adhesion to surfaces that are "nanosmooth", resulting in elevated cellular metabolic activity, augmented production of extracellular polymeric substances, and increased number of bacterial cells undergoing attachment.

In this context, the present study is an extension of our previous work on the development of a novel organic polymer coating for the prevention of growth of medically significant bacteria on three-dimensional solid surfaces. In this study, the effect of surface encapsulation on the adhesion and proliferation tendencies of *S. aureus* and *P. aeruginosa* were examined. The surface of substrat was encapsulated with a polyterpenol thin film prepared from terpinen-4-ol using radio frequency plasma enhanced chemical vapor deposition. Terpinen-4-ol is a constituent of tea-tree oil and its monomer (liquid) form is known to inhibit growth of broad range of bacteria. The resulting polyterpenol thin films were first characterized using X-ray photoelectron spectroscopy (XPS), water contact angle measurement, atomic force microscopy (AFM) and 3-D interactive visualization and statistical approximation of the topographic profiles. AFM studies showed that application of the coating decreased the substrate surface roughness from approximately 2.1 nm to 0.4 nm.

The extent of bacterial attachment and extracellular polymeric substances (EPS) production was then analyzed using scanning electron microscopy (SEM) and confocal scanning laser microscopy (CSLM). The CSLM and SEM analyses clearly demonstrated that *S. aureus* and *P. aeruginosa* presented notably different patterns of attachment in response to the presence of the surface film, where the amount of attachment, EPS production and cell proliferation on the encapsulated surface was found to be greatly reduced compared to that obtained on the unmodified surface. This work

suggests that the antimicrobial and antifouling coating could be effectively integrated into medical and other clinically relevant devices to prevent bacterial growth and to minimize bacteria-associated adverse host responses.

Selective Functionalization of Singlewalled Carbon Nanotubes via Chemical Treatment

A. Jędrzejewska[1], M. H. Rümmeli[2], X. Chen[1],
R. J. Kaleńczuk[1], E. Borowiak-Paleń[1]

[1] *Institute of Chemical and Environment Engineering*
West Pomeranian University of Technology
Pułaskiego 10, 70-322 Szczecin, Poland

[2] *IFW Dresden*
P.O. Box 270116, 01171 Dresden, Germany

Depending on the geometry, single-walled carbon nanotubes (SWNTs) can be either metallic or semiconducting. So far this is the only known material to possess this unique property. For electronic applications it is of vital importance to separate the two electronic components. Selective chemical functionalization can support the separation of semiconducting from metallic SWNTs. Therefore, we performed functionalization of SWNTs via H_2O_2 what led to the preferential removal of the semicionducting tubes hence enrichment of metallic tubes concentration in the bulk sample. The starting material was synthesized in a catalytic process using Pt:Rh:Re as the catalyst in laser ablation (LA). The samples have been characterized via high resolution transmission electron microscopy (HR-TEM), optical absorption spectrosacopy (OAS) and Raman spectroscopy.

Reduction Process of Iron Catalyst for Ammonia Synthesis Doped with Lithium Oxide

R. Jędrzejewski, I. Jasińska, W. Arabczyk

Institute of Chemical and Environmental Engineering
West Pomeranian University of Technology
Al. Piastów 17, 70-310 Szczecin, Poland

The reduction of fused iron catalyst doped with calcium oxide (2.94 wt %), aluminum oxide (2.31 wt %), silicon oxide (0.42 wt %) and potassium oxide (0.53 wt %) or lithium oxide (1.67 wt %) with different ion ratio Fe^{2+}/Fe^{3+} higher then 0.5 was studied. The ICP-AES, in situ XRD, TGA and selective etching methods were used. Potassium oxide doesn't form solid solution with iron oxide and it is located in the intergranular spaces. Lithium oxide occurs in two forms: the solid solution with magnetite and as $Li_2Fe_3O_4$ phase.

During the reduction process of catalyst doped with potassium oxide, the reduction of iron (II) oxide was observed from 350–400°C and the magnetite reduction started from the temperature of 400°C. Reduction of the catalyst doped with lithium oxide is slower than that observed for the catalyst doped with potassium oxide. The magnetite phase with dissolved lithium oxide was reduced first. As a result of reduction, elemental iron as well as a solid solution $Li_2O \cdot x\mathrm{FeO}$ where $x > 3$ are formed. The $Li_2Fe_3O_4$ and $Li_2O \cdot x\mathrm{FeO}$ phases are reduced slower then magnetite. Lithium oxide coming from reduction wets the iron surface and forms a glass phase with silicon oxide.

Femtonewton Force Sensing Using SiC Nanoelectromechanical Resonance at Room Temperature

J. H. Cho[1], W. Kim[1], J. S. Shin[2],
I. S. Song[2], X. M. H. Huang[3], S. C. Jun[1]

[1] *School of Mechanical Engineering, Yonsei University*
Seoul 120-749, Korea

[2] *Communication Lab, Samsung Advanced Institute of Technology*
Yongin-Si, Gyeonggi-Do, 449-712, Korea

[3] *Department of Mechanical Engineering and Nanoscale Science and Engineering Center, Columbia University*
New York, NY 10027, USA

Nanoelectromechnical resonators are promising in various new applications. Their resonance frequency can be made as high as GHz [1], and femtogram-level mass detection has been achieved with a gold-coated silicon cantilevers resonating at about 2 MHz with Q factors around 25, photothermally actuated by a 4 mW diode laser [2]. Possibility of attogram detection has been shown using nano-beams of higher Q factors 10^3 to 10^4 [3, 4]. Also, force sensing by measuring the detection of piezoresistive cantilevers have been achieved at pN [5] and even at aN [6] level for the forces perpendicular to the surface at 4.8 K, or at the nN level for the lateral forces [7].

This paper presents femtonewton-level force sensing using a nanoelectromechanical doubly-clamped beam with magnetomotive transduction in moderate conditions.

SiC has been considered to be a versatile material for high-frequency resonator. Due to high Young's Modulus, low density (high tensile-strength-to-density) and high

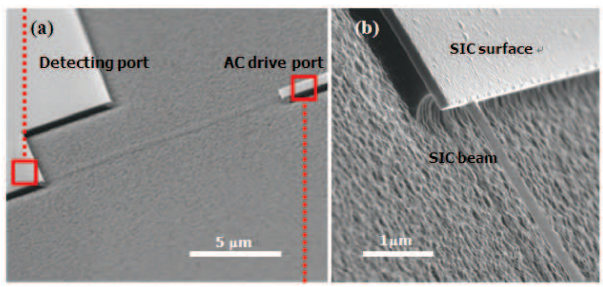

Figure 1: A schematic view of the nano-beam. (a) AC driving ports; (b) Fully suspended structure

acoustic velocity, SiC-based resonators provide high Q factors [8], high resonant frequencies, and high sensitivity.

Although SiC has high rigidity, it does not have electrical conductivity and current density high enough. Therefore, Al has been selected as a conducting layer. Since Al's low density does not significantly reduce resonator's sensitivity or resonance frequency, Al is suitable for a sacrificial layer to increase the electrical conductivity with the minimal weight increase.

Two types of beams are fabricated with the Al capped 3C-SiC film and AuPd on a silicon wafer, which undergo E-beam (electron-beam) lithography and liftoff processes [9]. The device pattern is made on top of the film using E-beam lithography, followed by evaporation and liftoff of Al. DRIE (deep reactive ion etching) process etched away the Si substrate. A schematic view of the nano-beam is presented in Figure 1. The length of the beam is 12 μm and width of 100 nm with SiC thickness of 30 nm and with varying Al thicknesses from 10 to 100 nm. In this work, a room temperature apparatus in Figure 2 (a) is constructed, which is composed of PCB connection to minimize frequency loss. The conceptual diagram of NEMS doubly-clamped beam readout is shown in Figure 2 (b).

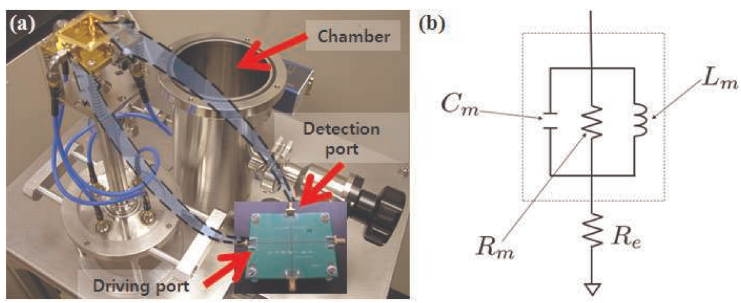

Figure 2: Room-temperature test equipment. (a) A moderate vacuum (≈ 1 Torr) chamber with a permanent magnet (0.8 T); (b) Conceptual diagram of NEMS doubly-clamped beam readout

The oscillation of the doubly-clamped beam can be viewed as a displacement $y(t)$ of a damped harmonic oscillator with an effective mass m, damping coefficient c, and spring constant k under the driving force $F(t)$:

$$m\frac{d^2y}{dt^2} + c\frac{dy}{dt} + ky(t) = F(t). \tag{1}$$

The induced emf in the electrode can be written as $V_{\text{emf}}(t) = \xi L_e B dy/dt$ where B is the strength of the magnetic field, L_e is the length of the electrode and ξ is the constant that can be obtained by integrating the fundamental mode shape along the length of the electrode. Since the driving force can be written as $F(t) = L_b B I_d(t)$, taking Fourier transform of the equations yields:

$$V_{\text{emf}}(\omega) = \frac{i\omega\omega_0^2 \xi L_e L_b B^2/k}{\omega_0^2 - \omega^2 + i\gamma\omega} |I_d(\omega)|. \tag{2}$$

By defining the quality factor $Q = \omega_0/\gamma$, the average motion-induced emf in the electrode to the driving current I_d can be represented as the following Lorentzian curve:

$$|V_{\text{emf}}(\omega)| = V_0 \frac{\omega_0 \omega / Q}{\sqrt{(\omega_0^2 - \omega^2)^2 + (\omega_0 \omega / Q)^2}} |I_d(\omega)|, \tag{3}$$

where $V_0 = \omega_0 \xi L_e L_b B^2 Q I_d / k$ denotes the amplitude $|V_{\text{emf}}(\omega_0)|$ at the resonance frequency ω_0.

The resonance frequency ω_0 of a rectangular doubly clamped beam under zero stress is:

$$\omega_{0,0} = 2\pi 1.03 \frac{w}{L_b^2} \sqrt{\frac{E}{\rho}}, \tag{4}$$

and under stress σ, this increases to:

$$\omega_{0,\sigma} = \omega_{0,0} \sqrt{1 + \frac{\sigma L_b^2}{3.4 E w^2}}. \tag{5}$$

The resonance frequency of the beams range from 12.9 to 9.5 MHz and Q factors range from 5000 to 4000. Calculated stress range from 185 to 95 MPa as shown in Figure 3 (a). Theoretical simulation results using COMSOL yield the maximum stress 168 MPa which value is fairly close (about 5–9% difference) to the value extracted from the measurements.

From Equation (5), we can obtain the stress responsivity equation $\delta\omega_0/\delta\sigma$ or the inverse:

$$\frac{\delta\sigma}{\delta\omega_{0,\sigma}} = \frac{2\omega_{0,\sigma}}{\omega_{0,0}^2} \frac{3.4 E w^2}{L_b^2}. \tag{6}$$

This equation denotes stress sensitivity per unit frequency. We have obtained force sensing limit down from 25 to 54 fN per unit frequency. Furthermore, minimum detectable frequency shift of the coupled resonator/transducer system is $\delta\omega_0 = \omega_0/Q 10^{-(\text{DR}/20)}$ [3] where DR is the dynamic range (dB), defined to be the ratio

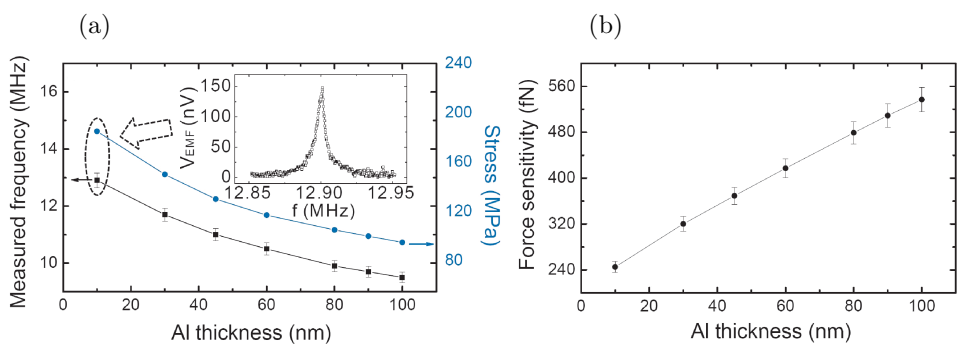

Figure 3: (a) Measured resonance frequency f_f and stress computed using Equation (5) show similar tendency. Inset is the readout of resonance (freq vs. amp of induced emf) showing a frequency response of a harmonic oscillator of Al thickness of 10 nm; (b) Force and stress sensitivity with varying thickness of Al show inversed tendencies

of 1 dB compression point to the noise amplitude at the resonance. Stress sensitivity, $\delta\sigma$, can be roughly obtained from the inverse of stress responsivity times the minimum detectable frequency shift, $\delta\omega$, which is $\delta\sigma \approx |\delta\sigma\delta\omega_0|\delta\omega_0$. This equation let us estimate the stress sensitivity with the experimental parameters of $Q \approx 4500$, DR ≈ 63 dB. It is obvious that force sensitivity can be calculated by multiplying the cross sectional area of doubly-clamped beam resonator by stress sensitivity. Based on the equations, minimum sensing of force is estimated to be hundreds order of fN as shown in Figure 3 (b). The trend of graph shows that as Al thickness gets thinner the force sensitivity decreases, which means that minimum detectable force gets lower. If we ignore geometrical dominancy, assuming increase in areal geometry is relatively small (square of nano meter scale) and is negligible, values of force sensitivity slightly decrease from 368 to 248 fN which correspond to stress sensitivities.

In conclusion, we have investigated the possibility of femtonewton force sensing using doubly-clamped nanoelectromechanical resonator by magnetomotive transduction in moderate conditions. In addition, geometrical dependencies of force sensitivity is calculated using derived equations. This paper promotes further researches regarding operation of nanoelectromechanical resonator in moderate conditions and indicates that detection below femtonewton force sensing may be possible with higher Q factor resonator or with material combinations of different conductance layer and rigid SiC layer.

Acknowledgements
This work was partially supported by the National Research Foundation of Korea (NRF) funded by the Ministry of Education, Science and Technology (2010).

References

[1] Huang X M H, Zorman C A, Mehregany M, Roukes M L 2003 *Nature* (London) **421** 496
[2] Lavrik V, Datskos P G 2003 *Appl. Phys. Lett.* **82** (16) 2697
[3] Ekinci K L, Huang X M H, Roukes M L 2004 *Appl. Phys. Lett.* **84** (22) 4469
[4] Ilic B, Craighead H G, Krylov S, Senaratne W, Ober C, Neuzil P 2004 *J. Appl. Phys.* **95** (7) 3694
[5] Gel M, Shimoyama I 2004 *J. Micromech. Microeng.* **14** 423
[6] Stowe T D, Yasumura K, Kenny T W, Botkin D, Wago K, Rugar D 1997 *Appl. Phys. Lett.* **71** (2) 288
[7] Duc T C, Creemer J F, Sarro P M 2006 *Micromech. Microeng.* **16** S102
[8] Perisanu S, Vincent P, Ayari A, Choueib M, Purcell S T, Bechelany M, Cornu D 2007 *Appl. Phys. Lett.* **90** 043113
[9] Jun S C, Cho J H, Kim W K, Jung Y M, Hwang S J, Shin S C, Kang J Y, Shin J, Song I, Choi J Y, Lee S Y, Kim J M 2009 *IEEE Electron Device Lett.* **30** (10) 1042

Tailoring of Carbon Nanotubes Structure Grown from Ferromagnetic and Non-Ferromagnetic Catalysts via CVD

R. J. Kaleńczuk, A. Jędrzejewska, E. Borowiak-Paleń

Center of Knowledge Based Nanomaterials and Technologies
Institute of Chemical and Environment Engineering
West Pomeranian University of Technology
Pułaskiego St. 10, 70-322 Szczecin, Poland

The catalytic growth of different carbon nanotubes by chemical vapor deposition (CVD) using ferromagnetic catalyst particles (such as iron) and non-ferromagnetic catalyst particles (such as copper or platinum) will be presented. A study of the effect of the metal-support interaction by employing iron particles supported on magnesium oxide (MgO) nanopowder in an alcohol-CVD process for single-walled carbon nanotubes growth is presented. Three main observations were made upon prolongation of the process time: (i) a decrease in the mean nanotube diameter, (ii) a reduction in the diameter distribution by the factor of two, (iii) an increase in the relative purity of samples. In this work detailed studies were also conducted showing that catalysts with fully filled d orbital (e.g. Cu) can be a source of a bulk scale synthesis of single-walled or multi-walled carbon nanotubes using the same catalyst mix (viz. equal molar ratio of metal or non-metal to magnesia) but with different experimental setups and conditions. A detailed analysis of the samples is supported by electron transmission microscopy observations, the energy dispersive *X*-ray spectroscopy mode, *X*-ray Diffraction and Raman spectroscopy.

Quantum Size Effect, Energy Transfer and Tunability in Luminescent Materials: Semiconductor Nanoparticles and Tb(III) Ions Immobilized on Silica Xerogel

A. M. Kłonkowski, M. Zalewska, B. Lipowska-Łastówka

Faculty of Chemistry, Universisty of Gdańsk
Gdansk, Poland

Nanoparticles of such broad band semiconductors as ZnO, ZnS, CdS, WO_3, TiO_2 and $SrTiO_3$ were used to enhance luminescence emission intensity of terbium(III) ions embedded on oxide matrices. Both the optically active components were incorporated onto xerogels by impregnation of the xerogel samples immersed firstly in $SrTiO_3$ sol and subsequently in solution with Tb(III). The effect related to the semiconductor nanoparticles of various sizes immobilized in silica matrix influences on band shifting and changes of the emission intensity of the nanostructures. Similar phenomenon is observed for emitting Tb(III) ions in presence of the nanosized semiconductors, if both the components are immobilized on silica matrix.

Photoluminescence studies allow to describe a plausible mechanism of the enhanced Tb(III) emission that could be attributed to energy transfer from the excited silica support *via* semiconductor nanoparticles to Tb(III) ions. It is observed that shifting of emission bands of the semiconductors is due to quantum size effect and it is manifested in this case for size of the nanostructures larger than quantum dots. Simultaneously, with the shift effect related to the semiconductor nanostructures is demonstrated shift of the Tb(III) emission bands [1, 2].

Acknowledgements
Financial support by the National Center of Research and Development (Grant 15 029/06/2009) is gratefully acknowledged.

References

[1] A. M. Kłonkowski, M. Zalewska, B. Kościelska 2006 *J. Non-Cryst. Solids* **352** 4183
[2] M. Zalewska, A. M. Kłonkowski 2008 *Opt. Mater.* **30** 725

Synthesis, Defects and Magnetic Properties of Ni-Al Ferrite Nanopowders

A. V. Kopayev[1], Yu. N. Tafiychuk[1], D. L. Zadnieprianniy[1], B. V. Padlyak[2,3a], O. O. Smyrnov[3], A. Drzewiecki[3]

[1] *Vasyl Stefanyk PreCarpathian National University, Physical-Technical Faculty*
57 Shevchenko Str., 76-000, Ivano-Frankivsk, Ukraine

[2] *Institute of Physical Optics*
23 Dragomanov Str., 79-005, Lviv, Ukraine

[3] *University of Zielona Góra, Institute of Physics*
Szafrana 4a, 65-516 Zielona Góra, Poland

[a] *B.Padlyak@proton.if.uz.zgora.pl; bohdan@mail.lviv.ua*

Ni-Al ferrites possess record low conductivity and represent perspective materials for magneto-electronic devices. In addition, the magnetization values of Ni-Al ferrites are changed in a wide range up to a compensation point in the dependence on their chemical composition and conditions of thermal annealing [1]. These properties are instrumental in their usage in microwave frequency devices and as magnetic components of electromagnetic composite materials.

Ferrites of the $NiAl_xFe_{2-x}O_4$ composition were obtained using a nanotechnology process by the sol-gel auto-combustion method. According to the X-ray analysis results, the obtained powders of Ni-Al ferrites consisted of one phase with a spinel structure. The size of blocks of coherent scattering was in the 20–50 nm range. According to the XANES (X-ray Absorption Near Edge Structure) method, iron is incorporated into the crystal lattice of Ni-Al ferrites in the trivalent state. Both the structural and surface defects were investigated in the obtained nanopowders of Ni-Al ferrites. The high specific surface of particles resulted in formation of magnetic poles on the surface. This led to the creation of demagnetizing fields in the Ni-Al ferrite nanopowders which were determined and analysed using two experimental techniques: magnetic susceptibility measurements at low frequencies and ferromagnetic resonance (FMR) spectroscopy in the microwave range.

The obtained data showed that the technological conditions of the sol-gel auto-combustion synthesis of the Ni-Al ferrite nanopowders led to changes in the size of particles. The magnetic susceptibility of the Ni-Al ferrite nanopowders showed linear dependence on the sizes of particles which correlated with the calculated data. The X-band FMR spectra of the Ni-Al ferrite nanopowders were investigated and analysed. The lineshape and maxima position of the FMR absorption curves for all the investigated Ni-Al ferrite nanopowders were closely similar to the corresponding calculated data. The crystalline structure defects were closely associated with the magnetic structure parameters which were investigated by the Mossbauer spectroscopy method. Particularly, it was shown that the area and parameters of the $^{57}Fe^{3+}$ paramagnetic

doublet, which was observed in the background of the $^{57}Fe^{3+}$ sextet of magneto-ordered phase, depended on the technological conditions of nanopowder preparation.

The obtained results are interpreted and discussed in the framework of the modern theory of nanosized antiferromagnetics.

References

[1] Kopayev A V, Ostafiychuk B K, Yaremiy I P and Vylka I Y 2007 *Journal of Surface Investigation, X-ray, Synchrotron and Neutron Techniques* (10) 79

Electrovariable Nanoplasmonics and Self-Assembling Smart Mirrors

A. A. Kornyshev

Department of Chemistry, Imperial College
London, SW7 2AZ, United Kingdom

a.kornyshev@imperial.ac.uk

The areas of research in electrovariable optics, which include electrowetting based adjustable lenses and addressable mirrors [1–4], light driven and field-controlled molecular machines, optical filters based on stark effect in quantum dots [5, 6], and nanoplasmonic systems [7] are important to consider.

Electrovariable nanoplasmonics launched recently in [7] will be the central part of the talk. It allows electrically tunable reflection of light at an interface of two immiscible electrolytic solution or a solid ITO electrode/liquid electrolyte interface. Its operation principle relies on voltage controlled localization of metal (Plasmon-active) nano-particles at the corresponding interfaces or removal of these nanoparticles to the bulk of the solution [8]. At the interface, nanoparticles perform a coherent reflection of light; in the bulk, if their concentrations are minute (just as much as needed to cover the surface) they 'optically' disappear. For appropriate sizes and charges of the nanoparticles, and concentration of the electrolytes, about half a volt potential bias may be sufficient to reversibly convert the system from a transparent window to a mirror.

As this function can be performed without a passage of electrical current, there are no Ohm losses involved, and these devices can be used for energy saving building technologies in countries with hot climate. Specifically this windows will be polarized to reflect light when no one is inside the room, or adjust light penetration into at direct sunlight exposure when the room is occupied. This will help to save energy spend on air conditioning, as well as create a more comfortable, adjustable lighting.

Various other applications of electrovariable nanoplasmonic systems, e.g. related to surface enhanced Raman scattering will be briefly discussed, in the context of new kind of sensors or molecular electronics.

References

[1] A. A. Kornyshev, A. R. Kucernak, C. W. Monroe, A. E. S. Sleightholme, M. Urbakh 2010 *J. Phys. Chem. C* (in press)
[2] C. W. Monroe, M. Urbakh, A. A. Kornyshev 2009 *J. Electrochem. Soc.* **156** P21-P28
[3] C. W. Monroe, M. Urbakh, A. A. Kornyshev 2007 *J. Phys. Cond. Matter* **19** # 375113
[4] C. W. Monroe, L. I. Daikhin, M. Urbakh, A. A. Kornyshev 2006 *Phys. Rev. Lett.* **97** # 136102
[5] M. E. Flatté, A. A. Kornyshev, M. Urbakh 2009 *Faraday Discuss.* **143** 109–115

[6] M. E. Flatté, A. A. Kornyshev, M. Urbakh 2008 *Proc. Natl. Acad. Sci USA*, **105** 18212–18214
[7] M. E. Flatté, A. A. Kornyshev, M. Urbakh 2010 *J. Phys. Chem. C* **114** 1735–1747 (feature article)
[8] M. E. Flatté, A. A. Kornyshev, M. Urbakh 2008 *J. Phys. Cond. Matter* **20** # 073102

XAS Investigations of Nitrided NbN-SiO_2 Sol-Gel Derived Films

A. Witkowska, B. Kościelska[a]

Faculty of Applied Physics and Mathematics
Gdansk University of Technology
Narutowicza 11/12, 80-233 Gdańsk, Poland

[a] *basia@mif.pg.gda.pl*

In recent years much attention has been paid to nitride and oxynitride thin films. These materials are interesting because of their attractive characteristics such as high hardness, corrosion resistance and thermal stability. In particular, NbN is a hard coating material with many commercial applications related to its high melting point, hardness, chemical stability at high temperatures and high electrical conductivity. Interest in NbN layers is also focused on their superconducting properties. Niobium nitride with the superconducting critical temperature ranging between 14 and 18 K, high critical current density, low r. f. surface resistance and good mechanical properties is one of the leading materials in superconducting microelectronic applications.

This work presents the results of a structural analysis of xNbN-$(100-x)SiO_2$ (where $x = 100$, 80, 70 mol %) thin films. The films were prepared by thermal nitridation with ammonia of sol-gel derived xNb_2O_5-$(100-x)SiO_2$ coatings. The nitridation process of the coatings led to the formation of weakly disordered structures, with NbN metallic grains dispersed in the matrix of insulating SiO_2. Moreover, it was clearly noted that superconducting properties in this kind of a layer strongly depended on the NbN/SiO_2 molar ratio. The origin of this behaviour is not clear and for this reason some structural investigations were performed using *X*-ray absorption spectroscopy (XAS). Several unique features of the XAS technique, such as atomic selectivity, local structure sensitivity and sensitivity on extremely low photoabsorber concentration, allowed us to correlate the studied films stoichiometry with the geometric and electronic structure of Nb ions.

Elastic Properties of Three-Dimensional Polydisperse Hard Dimers: a Monte Carlo Study

M. Kowalik[a], K. W. Wojciechowski[b]

Institute of Molecular Physics, Polish Academy of Sciences
Mariana Smoluchowskiego 17, 60-179 Poznań, Poland

[a] *kowalik@ifmpan.poznan.pl,* [b] *kww@man.poznan.pl*

Systems interacting *via* hard-body potential (infinite when any particles overlap, and zero otherwise) constitute very interesting class of model systems. Not only they are able to mimic many phenomena encountered in real physical system, but (being entropy driven) exhibit many striking, counterintuitive properties. For example, it was shown that, both in two [1, 2] and three [3] dimensions, hard homonuclear dimers – molecules consisted, respectively, of two adjacent discs or spheres of diameter σ – freeze into, so called, *degenerate crystal* (DC). In such a phase neither molecular positions nor their orientations exhibit any kind of periodicity although the atoms (at close packing limit) form translationally invariant crystalline lattice (triangular in 2D, and fcc or hcp in 3D).

Nowadays, when industry demand on so called *smart materials* (i.e. materials exhibiting special and sometimes unusual features) is steadily increasing, it is essential to analyze how various microscopic mechanisms may affect properties of system at macroscopic level. Hard dimer system can be used as convenient model to study how various kinds of disorder at molecular level influence macroscopic properties of the system, e.g. its elastic properties, which are important for both fundamental research and practical applications.

Elastic properties of the hard homonuclear dimer DC were already investigated in two [4] and three dimensions [5]. However, man-made micro-, mezo-, and macroparticles usually are not perfectly identical. Thus, model systems including polydispersity of atomic sizes seem to be better equipped to describe or predict properties of such man-made systems. But the question, how the polydispersity will affect the elastic properties of the hard dimer DC remains open and the aim of this work is to fill this gap.

Acknowledgements
This work was partially supported by the MNiSW grant NN202 261438. Part of the simulations was performed at the Poznań Supercomputing and Networking Center (PCSS).

References

[1] Wojciechowski K W, Frenkel D, Brańka A C 1991 *Phys. Rev. Lett.* **67** (6) 3168
[2] Wojciechowski K W, Brańka A C, Frenkel D 1993 *Phys. Lett. A* **196** 519
[3] Vega C, MacDowell L G, McBride C 2004 *J. Mol. Liquids* **113** 37
[4] Tretiakov K V, Wojciechowski K W 2006 *J. Non-cryst. Solids* **352** (40-41) 4221
[5] Kowalik M, Wojciechowski K W 2005 *Phys. Stat. Sol. (b)* **242** (3) 626

Spectroscopy and Low-Dimensionality in Carbon Nanotubes

C. Kramberger[1], M. Knupfer[2], E. Einarsson[3], S. Maruyama[3], J. Fink[4], S. Huotari[5], T. Pichler[1]

[1] *University of Vienna, Faculty of Physics*
Strudlhofgasse 4, A-1090, Vienna, Austria

[2] *IFW Dresden*
Helmholtzstraße 20, D-01069 Dresden, Germany

[3] *The University of Tokyo, Dept. of Mechan. Engineering*
7-3-1 Hongo, Bunkyo-ku, Tokyo 113-8656, Japan

[4] *BESSY*
Albert-Einstein-Straße 15, D-12481 Berlin, Germany

[5] *European Synchrotron Radiation Facility*
Boîte Postale 220, F-38043 Grenoble Cedex 9, France

The diameter of an individual nanotube is only on the order of one to a few nm but its length may be in the mm range. This enormous aspect ratio spans the entire length scale from molecular to bulk physics. From that point of view carbon nanotubes maybe envisaged as a chimaera consisting of a periodic quantum dot on the one side and a one dimensional solid on the other side. The narrow nanoscopic confinement on the width, or more precisely to the circumference, of a nanotube gives rise to quantized states, analogous to the quantized orbitals in atoms or molecules. Along its axis a nanotube resembles a quasi-infinite regular periodic crystal, which renders it a unique showcase example of a strictly one-dimensional solid. The comprehensive description of carbon nanotubes requires two different fields of physics, namely quantum dot and solid state physics. Here we focus on momentum and energy dispersive loss-spectroscopies, utilizing either *X*-rays or relativistic electrons [1, 2]. The high energy methods are compared to optical absorption [3]. The combination of the spectroscopic techniques allows to identify and clearly distinguish confined and itinerant features in the excitation spectrum of single-walled carbon nanotubes.

Acknowledgements
E. E. acknowledges support from the *Global Center of Excellence for Mechanical Systems Innovation* by the Japanese Ministry of Education, Culture, Sports, Science and Technology; T. P. acknowledges the DFG 440/3/5 and the FWF P21333-N20.

References

[1] C. Kramberger, R. Hambach, C. Giorgetti, M. H. Rummeli, M. Knupfer, J. Fink, B. Buchner, L. Reining, E. Einarsson, S. Maruyama, F. Sottile, K. Hannewald, V. Olevano, A. G. Marinopoulos, and T. Pichler 2008/May *Phys. Rev. Lett.* **100** (19) 196803

[2] C. Kramberger, E. Einarsson, S. Huoatri, T. Thurakitseree, S. Maruyama, M. Knupfer, T. Pichler 2010 *Phys. Rev. B* **81** 205410
[3] Y. Murakami, E. Einarsson, T. Edamura, S. Maruyama 2005/March *Phys. Rev. Lett.* **94** (8) 087402

RF MEMS and MMIC Process Integration on GaAs and GaN Substrates

C. Lanzieri

SELEX-SI s.p.A., Engineering Division
Via Tiburtina Km 12.400, 00131 Rome, Italy

RF MEMS switches have exhibited a very attractive performance at microwave frequencies using different topologies (cantilever, rotary and membrane) and could be represent a valid solution to overcome the limitation exhibited by conventional RF devices, enabling circuits with new levels of performance not otherwise achievable. In particular, RF-MEMS represents a feasible solution to obtain very low power dissipation and insertion loss, high isolation and linearity respect to "solid state" technologies (pin-diode, FET-switches).

For such reasons, the feasibility to integrate MEMS and HEMT in a single fabrication process plays a key role in the implementation of the future generation of Transmit/Receive modules. MMICs fabrication on GaN/SiC and GaN/Si substrates utilises active devices (HEMT) and passive components (transmission lines, resistors, inductances and capacitors), requiring metallic thin film deposition, thick plating metallization, dielectric deposition and chemical wet and dry etching. Such manufacturing steps are also used in RF-MEMS fabrication, although process optimizations are required to improve switch mechanics and device reliability. In this presentation, we demonstrate the possibility to fully integrate the process fabrication of RF-MEMS switches in the GaAs-PHEMT and GaN-HEMT manufacturing steps in order to develop a RF-MEMS/MMIC prototype.

Catalytic Ammonia Decomposition on Cobalt and Iron Catalysts

Z. Lendzion-Bieluń[a], W. Arabczyk

West Pomeranian University of Technology
Institute of Chemical and Environment
Engineering, Pułaskiego 10, 70-322 Szczecin, Poland

[a] *zosi@zut.edu.pl*

The catalytic reaction of ammonia decomposition is considered to be an ideal source of pure hydrogen for fuel cells [1, 2]. The development of high performance solid catalysts is essential for the supply of such hydrogen from ammonia.

The rate of catalytic ammonia decomposition depends on many factors such as, for example, gas phase composition [3], morphology and composition of the surface of the catalyst [4] on which the reaction proceeds.

The aim of the present study was to analyze the kinetics of catalytic ammonia decomposition on cobalt and iron catalysts. The obtained results were interpreted on the basis of the adsorption range model [5].

A nanocrystalline iron catalyst, promoted with Al_2O_3 (3.3 wt. %), CaO (2.8 wt. %) and K_2O (0.65 wt. %) was studied. The chemical composition of the cobalt catalyst, regarding the content of promoters, was similar to the composition of the iron catalyst.

The kinetics of catalytic ammonia decomposition was investigated using an analytical installation equipped with a flow tubular differential reactor with a gas phase composition analyzer and that made it possible to conduct thermogravimetric measurements.

The ammonia decomposition process was preceded by a reduction of the analyzed samples of the catalysts. The reduction process temperature under atmospheric pressure for the iron and cobalt catalysts was 500 and 600°C, respectively.

The catalytic ammonia decomposition reaction was investigated under an atmosphere of ammonia-hydrogen mixtures, under atmospheric pressure. The ammonia concentrations, as well as the nitriding potentials, were changed gradually from 0 to 100% at the reactor inlet. The temperature was changed in the range of 400–500°C.

The ammonia conversion degree was calculated (α_{NH_3}) on the basis of the gas phase inlet and outlet composition:

$$\alpha_{NH_3} = \frac{X_{H_2} F^0 - F^0_{H_2}}{F^0_{NH_3}(1.5 - X_{H_2})}$$

where: F^0 – the total molar flow rate of the inlet stream, $\mathrm{mol \cdot s^{-1}}$; $F^0_{H_2}$ and $F^0_{NH_3}$ the hydrogen and ammonia molar flow in the inlet stream, respectively, $\mathrm{mol \cdot s^{-1}}$; X_{H_2} – the molar concentration of hydrogen in the reactor, $\mathrm{mol \cdot mol^{-1}}$.

The ammonia decomposition reaction rate, r_{decomp}, was calculated from the equation:

$$r_{\mathrm{decomp}} = \alpha_{\mathrm{NH_3}} F^0_{\mathrm{NH_3}}$$

The changes in the gas reactant concentrations and the resultant partial pressures changes resulted in changes of the nitriding potential defined as:

$$P = \frac{p_{\mathrm{NH_3}}}{p^{3/2}_{\mathrm{H_2}}}$$

The ammonia decomposition process on the iron catalyst proceeded concurrently with the α-Fe nitriding reaction. The nitriding degree dependence and the ammonia decomposition rate as a function of the nitriding potential at 475°C is shown in Figure 1.

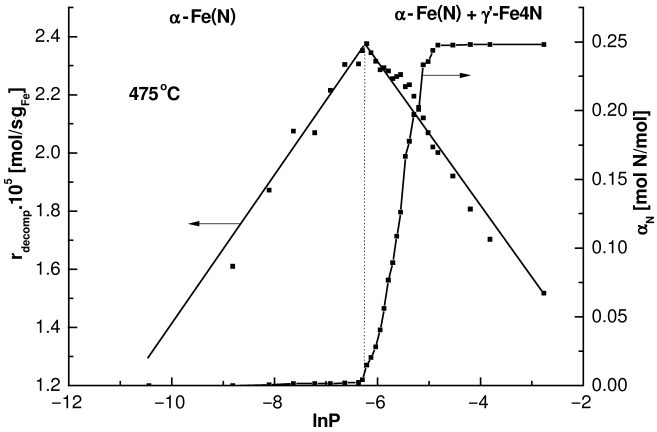

Figure 1: Dependence of ammonia decomposition reaction rate and iron catalyst nitriding degree on nitriding potential logarithm (ammonia-hydrogen mixtures at reactor inlet)

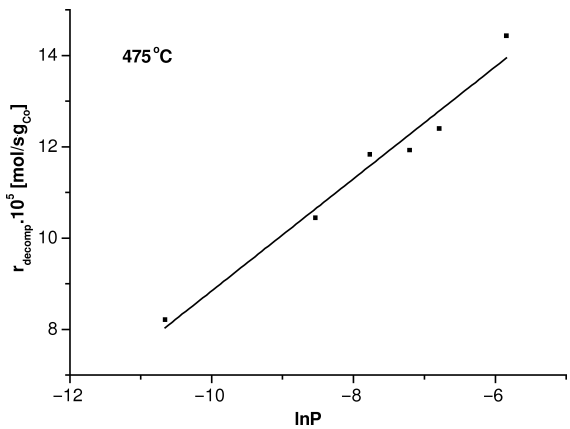

Figure 2: Dependence of ammonia decomposition reaction rate on cobalt catalyst on nitriding potential logarithm (ammonia-hydrogen mixtures at reactor inlet)

From the plot in Figure 1 it can be seen that the ammonia decomposition reaction rate depends linearly on the nitriding potential logarithm. When the nitriding potential was increasing the catalytic ammonia decomposition rate on α-Fe(N) was increasing, too. However, the decomposition reaction rate was decreasing with the increasing nitriding potential.

The cobalt nitriding process was not found in the examined conditions of temperature, pressure and nitriding potential. The ammonia decomposition rate dependence on the nitriding potential logarithm for the cobalt catalyst is shown in Figure 2.

Comparing the ammonia decomposition rates on the cobalt and iron catalysts it was found that ammonia decomposition reaction proceeded at a significantly higher rate on the cobalt catalyst.

References

[1] T. V. Choudhary, C. Sivadinarayana, D. W. Goodman 2001 *Catal. Lett.* **72** 197
[2] A. S. Chellappa, C. M. Fischer, W. J. Thomson 2002 *Appl. Catal. A* **227** 231
[3] W. Arabczyk, J. Zamłynny, D. Moszyński, K. Kałucki 2005 *Polish J. Chem.* **79** 1495
[4] W. Arabczyk, D. Moszyński, U. Narkiewicz, R. Pelka, M. Podsiadło 2007 *Catal. Today* **124** 43
[5] W. Arabczyk, R. Wróbel 2003 *Solid State Phenomena* **94** 185

Electromagnetically Induced Ionization from Double Autoionizing Levels with Lorentzian Continuum

W. Leoński, V. Cao Long, T. Bui Dinh

Quantum Optics and Engineering Division
Institute of Physics, University of Zielona Gora
Prof. A. Szafrana 4a, 65-516 Zielona Góra, Poland

Systems comprising autoionizing (AI) levels can behave in a diverse and nontrivial way leading to the occurrence of various interesting physical phenomena. They can be, for instance, quantum interferences discussed in [1, 2] (and the references quoted therein), electromagnetically induced transparency or light slowdown modifications [3], or the quantum anti-Zeno effect [4].

In this communication we shall concentrate on a system of two AI levels (labeled by $|1\rangle$ and $|2\rangle$), coupled to the structured continuum, $|\omega)$, of the Lorentzian shape, with the width equal to Γ_L. All these states are excited and coupled to some discrete ground level $|0\rangle$ by an external coherent electromagnetic field. In fact, the Lorentzian shaped continuum is equivalent to (and can be replaced by) both: the flat continuum $|\omega\rangle$ and the third AI level $|3\rangle$ – *c*oupled thereto (see Figure 1). Such replacement can be described in terms of the *Fano profiles* theory [5, 6].

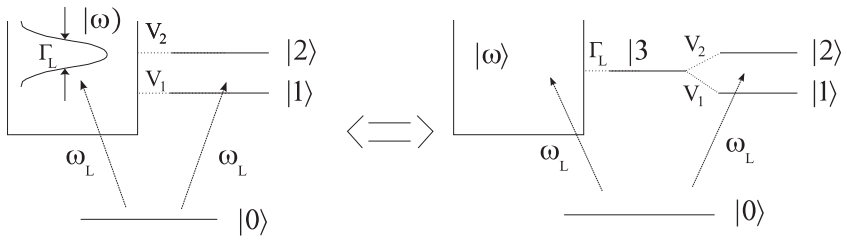

Figure 1: Atomic level scheme with Lorentzian shaped continuum $|\omega)$ (left) and two AI states $|1\rangle$ and $|2\rangle$ coupled thereto. These excited states are coupled to the ground state $|0\rangle$ by an external electromagnetic field with a frequency of ω_L. The Lorentzian width is equal to Γ_L. This model is equivalent to that with a flat continuum $|\omega\rangle$ and a single discrete level, $|3\rangle$, (right) coupled thereto.

Our system is assumed to be initially in the ground state $|0\rangle$ and then it is irradiated by an external laser field with a constant amplitude. We assume that all radiative transitions are of a dipole nature and the field is tuned closely to the positions of both the AI levels ($|1\rangle$ and $|2\rangle$). Moreover, these two states are sufficiently far

from the ionization threshold, so we can neglect all the threshold effects. The interaction strength of the two AI levels with the structured continuum, $|\omega)$, is described by matrix elements denoted by V_i $\{i = 1, 2\}$.

For such a model, we calculate long-time photoelectron spectra. We show that a Lorentzian structure can affect such spectra considerably as we compare them with those derived from the model with a flat continuum and two AI levels [1]. For instance, we can observe enhancement of the discussed system's sensitivity for interaction with an external electromagnetic field. In consequence, the Autler-Townes doublet can be visible in the spectrum even for a weak external field case. Moreover, according to the quantum interferences present in our model, such a doublet (and other peaks visible, as well) can be affected considerably leading also to the *confluence of coherences* effect [1, 7].

References

[1] Leoński W, Tanaś and Kielich S 1987 *J. Opt. Soc. Am. B* **4** 72
[2] Leoński W and Tanaś 1988 *J. Phys. B:At. Mol. Opt. Phys.* **21** 2835
[3] Raczyński A, Rzepecka M, Zaremba J and Zielińska-Kaniasty S 2006 Opt. Commun. **266** 552
[4] Lewenstein M and Rzążewski K 2000 *Physical Review A* **61** 022105
[5] Fano U 1961 *Phys. Rev.* **124** 1866
[6] Durand Ph, Paidarová I and Gadéa F X 2001 *J. Phys. B: At. Mol. Opt. Phys.* **34** 1953
[7] Rzążewski K and Eberly J H 1981 *Phys. Rev. Lett.* **47** 408

Synthesis and Dielectric Properties of Double Tungstates in Crystal and Nanocrystalline Form

L. Macalik[1a], B. Macalik[1], A. Majchrowski[3], J. Hanuza[1,2]

[1] *Institute of Low Temperature and Structure Research*
Polish Academy of Sciences
Okólna 2, 50-422 Wrocław, Poland

[2] *Department of Bioorganic Chemistry*
Faculty of Industry and Economics, Wrocław University of Economics
Komandorska 118/120, 53-345 Wrocław, Poland

[3] *Institute of Applied Physics, Military University of Technology*
Kaliskiego 2, 00-908 Warsaw, Poland

[a] *l.macalik@int.pan.wroc.pl*

Double potassium and rare earth tungstates with a monoclinic structure have an important position among laser host materials. Yb-doped $KY(WO_4)_2$ or $KGd(WO_4)_2$ crystals have been applied as diode-pumped and femtosecond lasers due to their large absorption and emission cross-section. Double sodium and rare earth tungstates with a tetragonal structure seem to be particularly promising in generating femtosecond pulses due to their uniaxial optical nature and effective energy transfer. The Ln^{3+} absorption and emission bands of their spectra are broadened as a result of the inhomogeneous crystal field [1, 2]. Moreover, it has been revealed that powder samples of the double tungstate family might be used as phosphors for visual display and solid-state lighting [3]. Although the optical properties of these scheelite-type crystals have been widely studied, only a few investigations of other physical properties have been reported.

In the present work sodium (potassium) and Gd^{3+} or Y^{3+} double tungstates doped with trivalent europium or ytterbium ions were studied. Their properties were compared in the micro- and nanocrystalline states. Single crystals of $KY(WO_4)_2$, $KGd(WO_4)_2$ and $NaY(WO_4)_2$ were grown by the low-gradient Czochralski technique. On the other hand, samples in the nanocrystalline form were obtained by the hydrothermal method from solutions of rare earth nitrates and alkali metal tungstate.

The dielectric properties of the obtained materials were measured in the temperature range from 370 to 1070 K with a step of 20 K at a frequency range from 10^{-1} to 10^5 Hz for the bulk crystal and nanocrystallite samples. The obtained complex dielectric permittivity data were analysed taking into account relaxation and conductivity processes. The activation energy for direct current conductivity and relaxation were calculated and mechanisms responsible for these processes were proposed.

References

[1] A. Méndez-Blas, M. Rico, V. Volkov, C. Cascales, C. Zaldo, C. Coya et al. 2004 *J. Phys: Condens Matter* **16** 2139
[2] J. Liu, J. M. Cano-Torres, F. Esteban-Betegón, M. D. Serrano, C. Cascales, C. Zaldo et al. 2007 *Optics & Laser Technology* **39** 558
[3] S. Neeraj, N. Kijima, A. K. Cheetham 2004 *Chem. Phys. Lett.* **387** 2

Synthesis and Properties of $Bi_2W_2O_9$ and $BaBi_2Ta_2O_9$ Aurivillius Phases

M. Mączka[1a], M. Ptak[1], L. Kępiński[1], P. E. Tomaszewski[1], L. Macalik[1], K. Hermanowicz[1], J. Hanuza[1,2]

[1] *Institute of Low Temperature and Structure Research*
Polish Academy of Sciences
P.O.Box 1410, 50-950 Wrocław 2, Poland

[2] *Department of Bioorganic Chemistry, Faculty of Industry and Economics*
University of Economics
Komandorska 118/120, 53-345, Wrocław, Poland

[a] *m.maczka@int.pan.wroc.pl*

Bismuth layered compounds (Aurivillius family), of general formula:

$$(Bi_2O_2)(A_{m-1}B_mO_{3m+1}),$$

where A = Na, K, Ca, Sr, Ba, Pb etc., and B = W, Ta, Nb, Ti etc. [1] have received much attention for device applications [1, 2]. In particular, $BaBi_2Ta_2O_9$ (BBT) has been shown to be a prospective material for fabrication of ferroelectric nonvolatile random access memories because of its excellent resistance to polarization fatigue [3]. This material exhibits also relaxor properties [4]. Recently, $Bi_2W_2O_9$ (BWO) has been found to be a photocatalytic material for H_2 and O_2 evolution as well as for photodegradation of organic compounds [5]. It has also been found to be a promising material for microwave applications [6].

BBT has been synthesized by many methods such as conventional solid state reaction, the co-precipitation technique and milling in a vibratory mill [4, 7–9]. These studies have shown that a pure BBT phase synthesis by solid state reaction requires heating for a long time at temperatures of about 1000°C with intermediate regrinding to complete the reaction [4, 7]. The co-precipitation method or milling in a vibratory mill has allowed obtaining BBT at a shorter time and lower temperatures. Thus, the grain size could be lowered to about 100 and 400 nm in the first and second case, respectively.

The literature data on $Bi_2W_2O_9$ concerns preparation of this material mainly by conventional solid state reaction [6, 10, 11] Preparation of a pure phase of $Bi_2W_2O_9$ using this method is difficult since samples synthesized below 700°C contain mainly the Bi_2WO_6 phase. Preparation of nearly pure $Bi_2W_2O_9$ requires prolonged firing at high temperatures, 800–860°C, and this material decomposes into Bi_2WO_6 and WO_3 above 870°C [6]. Recent reports on the synthesis of this material through a complex organic precursor and the Pechini method have shown that these methods allow obtaining $Bi_2W_2O_9$ at lower temperatures, 720–750°C [5, 12]. However, the synthesized samples were not completely pure and contained a small admixture of Bi_2WO_6.

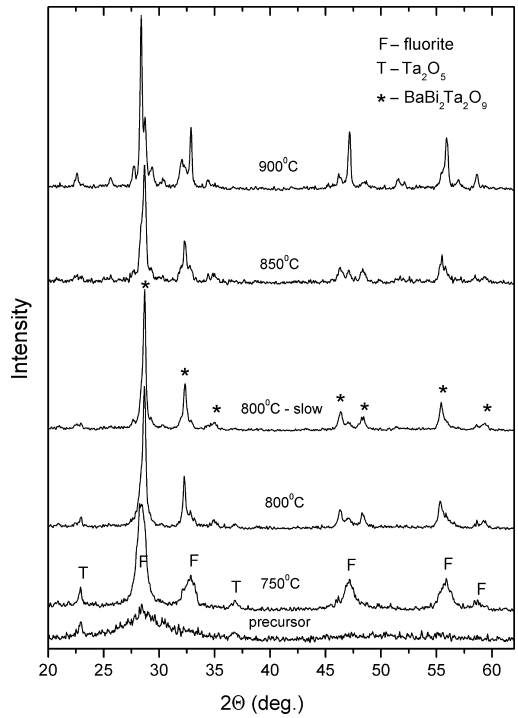

Figure 1: XRD patterns of BBT amorphous precursor prepared by milling in planetary ball mill, and that precursor annealed at different temperatures for 2 h

The above presented information shows that it is difficult to obtain pure phases of BBT and BWO, especially in the nanometric size of crystallites. A synthesis of samples with small sized crystallites is however important from the application point of view, since it is well known that a change in the crystallite size may lead to significant changes of various properties. For instance, a decrease in the crystallite size is expected to lead to enhancement of the photocatalytic properties of BWO since a good photocatalyst should have a large surface area and good crystallinity at the same time.

Here, we report the preparation of BBT and BWO by annealing of precursors, which were prepared by milling in a planetary ball mill. BBT was also obtained by the Pechini method. The aim of this study was to obtain information on the crystallization mechanism of BBT and BWO and the properties of the thus obtained crystallites which were studied using scanning and transmission electron microscopy, *X*-ray diffraction, Raman and IR spectroscopes and diffuse reflectance. We will show that the mechanochemical synthesis allows obtaining a BBT phase in a much shorter time than the Pechini method. Materials obtained by both methods have also significantly different properties. Interestingly enough, in both methods crystallization occurs *via* an intermediate fluorite phase (see Figure 1). In case of BWO, the mechanochemical method allows further lowering of the crystallization temperature, with respect to the Pechini method or the solid state reaction which in turn results in a smaller grain

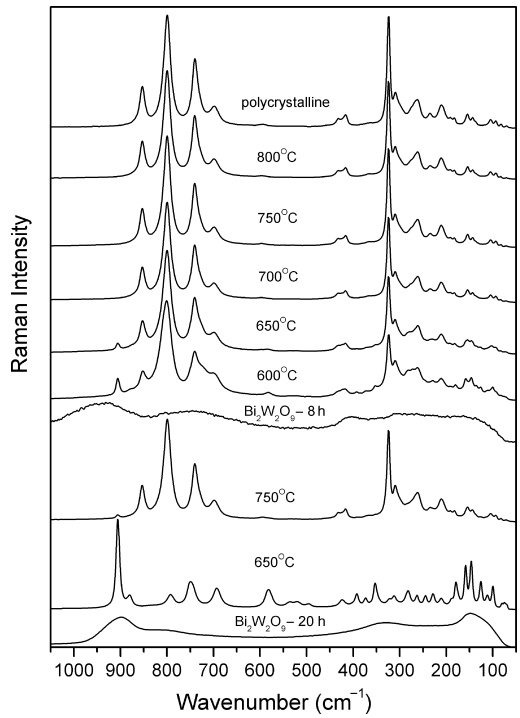

Figure 2: Raman spectra of BWO amorphous precursors prepared by milling of Bi_2WO_6 and WO_3 in ball mill for 8 or 20 h, and those precursors annealed at different temperatures

size, and thus, in a larger surface area. Our results also show that the milling time has a very significant impact on the mechanism of crystallization (see Figure 2).

References

[1] M. S. Islam, S. Lazure, R. N. Vannier, G. Nowogrocki, G. Mairesse 1998 *J. Mat. Chem.* **8** 655
[2] Y. Noguchi, K. Murata, M. Miyayama 2006 *Appl. Phys. Lett.* **89** 242916
[3] C. A. Paz de Araujo, J. D. Cuchiaro, L. D. McMillan, M. C. Scott, J. F. Scott 1995 *Nature* **374** 627
[4] C. Miranda, M. E. V. Costa, M. Avdeev, A. L. Kholkin, J. L. Baptista 2001 *J. Eur. Ceram. Soc.* **21** 1303
[5] A. Martinez-de la Cruz, S. O. Alfrao, L. M. Torres-Martinez, I. J. Ramirez 2008 *J. Ceram. Proc. Res.* **9** 490
[6] A. Feteira, D. C. Sinclair 2008 *J. Am. Ceram. Soc.* **91** 1338
[7] Y. Li, G. Chen, H. Zhang, Z. Li, J. Sun 2008 *J. Solid State Chem.* **181** 2653
[8] S. R. Dhage, R. Pasricha, A. Vadivel Muruga, V. Ravi 2006 *Mat. Chem. Phys.* **98** 344
[9] M. Senna, T. Kinoshita, Y. Abe, H. Kishi, C. Ando, Y. Doshida, B. Stojanovic 2007 *J. Eur. Ceram. Soc.* **27** 4301
[10] Y. Bando, A. Watanabe, Y. Sekikawa, M. Goto, S. Horiuchi 1979 *Acta Cryst. A* **35** 142
[11] J. Tang, J. Ye 2005 *J. Mater. Chem.* **15** 4246
[12] M. Mączka, M. Ptak. L. Kępiński, P. E. Tomaszewski, J. Hanuza 2010 *Vib. Spectrosc.* **53** 199

Applications of Nanomaterials in Nanoelectronics and Biosensing

G. Maruccio

University of Salento, CNR-Institute of Nanoscience
Via per Arnesano, 73100 Lecce, Italy

Due to the fundamental limitations of the top-down approach, nano- and molecular electronics [1, 2] have been proposed as alternative routes for a future (post-silicon) electronics. Because of their unique characteristics such as atomic-like spectra and wavefunctions [3–5], semiconductor quantum dots (QDs) and colloidal nanocrystals (NCs) are promising materials for optoelectronics, nanoelectronics and biosensing although the influence of their coupling with the environment needs to be deeply investigated [5]. In particular, colloidal nanoparticles can be finely tailored by tuning their size, shape, and composition opening new opportunities for nanoelectronics and spintronics since spin dependent transport in magnetic nanostructures is expected to exhibit novel phenomena, because of the interplay of single electron tunneling (SET) and spin dependent tunneling. Here the fabrication of nanoscale spin devices based on magnetic nanoparticles is described. Three different device layout are investigated, from multilayer structures to nanojunctions fabricated by electron beam lithography or through non-conventional approaches (e.g. by the selective wet-etching and oxidation of an AlGaAs/GaAs quantum well structure), with the final target to reduce a functional spin device to a single NP or molecule [6–10]. In such devices, the coexistence of single electron and spin polarized tunneling is observed.

Additionally, the availability of functional nanomaterials opens up new opportunities for robust electrical detection of few (down to single) biorecognition events within economical nanoarray. As a proof of concept, a sensor for DNA sequencing is reported, in which targets are oligonucleotides conjugated to gold nanoparticles. As a consequence of target-probe binding events, a conductive bridge forms between two electrodes, resulting in a quantized change in conductivity. This approach can be applied also to other binding events (like specific interactions between proteins, antibodies, ligands and receptors). Moreover, target amplification techniques (such as PCR) are no longer necessary, while microfluidic modules can be integrated for the injection and movement of biomaterials, drugs and physiological samples.

References

[1] Joachim C, Gimzewski J K, Aviram A 2000 *Nature* **408** (6812) 541–548
[2] Maruccio G, Cingolani R, Rinaldi R 2004 *J. Mater. Chem.* **14** (4) 542–554
[3] Maltezopoulos T et al. 2003 *Phys. Rev. Lett.* **91** (19) 196804
[4] Maruccio G et al. 2007 *Nano Lett.* **7** (9) 2701–2706
[5] Maruccio G et al. 2009 *Small* **5** (7) 808–812
[6] Maruccio G et al. 2005 *Adv. Mater.* **17** (7) 816–822

[7] Maruccio G et al. 2003 *Nano Lett.* **3** (4) 479–483
[8] Maruccio G et al. 2007 *Small* **3** (7) 1184–1188
[9] Maruccio G et al. 2009 *Analyst* **134** (12) 2458–2461
[10] Baadji N et al. 2009 *Nat. Mater.* **8** (10) 813–817

Scaled Silicon Nanoelectromechanical Functional Systems

H. Mizuta[1a], J. Ogi[2], Y. Tsuchiya[1], S. Oda[2]

[1] *NANO Group, School of Electronics and Computer Science*
University of Southampton
Southampton SO17 1BJ, U.K.

[2] *Quantum Nanoelectronics Research Center*
Tokyo Institute of Technology
Tokyo, Japan

[a] *hm2@ecs.soton.ac.uk*

Silicon VLSI technology developed and matured over the past decades has been fully exploited to build the vast technology area of micro-electromechanical systems (MEMS). Along with a rapid expansion of the MEMS market, there have also been continuous efforts at making the MEMS smaller in order to boost the operating frequency to GHz and beyond. The appearance of high-speed nano-electromechanical systems (NEMS) is tempting enough for us to consider the hybridization of the NEMS and conventional silicon electronic devices ('More than Moore') because we expect such hybrid systems enhance scaling of functional density and performance while simultaneously reducing the power dissipation beyond the conventional CMOS-based systems. A number of new hybrid NEM-CMOS devices have recently been studied for advanced switch, memory and sensing applications. As for the memory applications, we proposed two types of novel highspeed and nonvolatile NEM memory devices to go beyond conventional Flash memory. The bistable floating gate (FG) NEM memory features a buckled SiO_2 FG with embedded Si nanodots as single-electron storage. The other one is a suspended gate (SG) Si nanodot memory (SGSNM) in which the SG is pulled in to the FG only when we programme and erase the information. As for the sensing applications, a new in-plane resonant NEM sensor has recently been studied based on a mass-detection principle. This nanosensing device features a silicon resonant-suspended-gate and an in-plane MOSFET co-integrated on an ultrathin SOI platform and enables sub-attogram-level mass detection.

By downscaling the NEMS towards a 100-nm-regime and even smaller, we may explore a novel hybrid system of NEMS and single-electron transistors (SETs). There are a number of new phenomena associated with strong coupling of single-electron tunneling and low-dimensional phonons, such as phonon blockade and single-electron quantum shuttle, which may be exploited to develop novel 'Beyond CMOS' information devices. A suspended quantum dot (QD) SET (Figure 1) is particularly attractive to investigate the interaction between single electrons and phonons confined in suspended QDs. Recent study of the single-electron tunneling current for

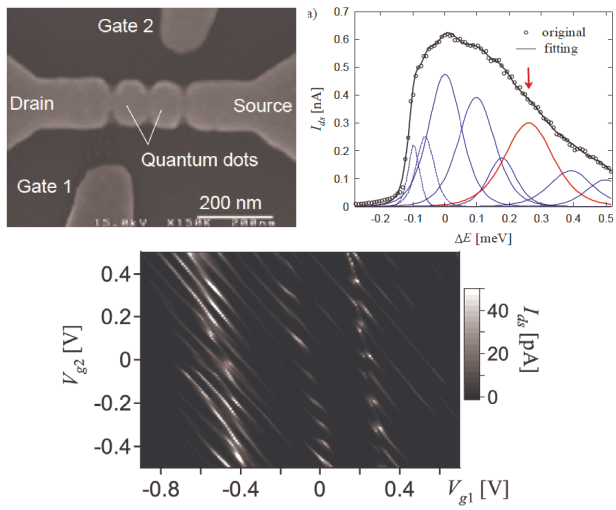

Figure 1: Suspended DQD-SET, Ids-Vg1-Vg2 curves at 120 mK and current peaks around the charge triple point

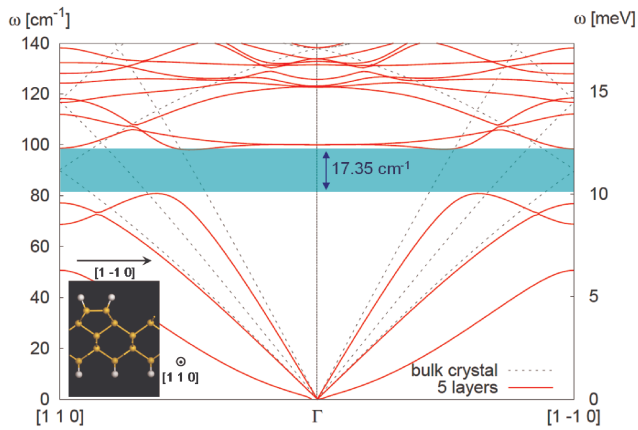

Figure 2: *Ab-initio* simulation of nanophononic spectra for a hydrogen-terminated ultrathin Si film of 5 atomic layers in thickness. A phonon bandgap of 17.35 cm^{-1} is formed both in the (110) and (1–10) directions

the double QDs suspended SET reveals the existence of multiple current peaks associated with inelastic tunneling mediated by confined phonons. These results allow envisaging the future possibility of tailoring the electron-phonon interaction in such suspended QDs systems. Extremely-scaled NEM systems will eventually exploit electro-mechanical properties of atomically-controlled Si nanostructures. The *ab-initio* simulation of 'nanophonons' has recently been conducted for the H-terminated free-standing ultrathin Si films of just a few atomic layers in thickness, and remarkabke phonon bandgaps have been demonstrated caused by the Si(001) 2×1 surface dimers

(Figure 2). Such nanophononic properties are quite different from those for bulk silicon and may be exploited as one of approaches to nanoscale thermal management and novel energy transfer interactions.

Acknowledgements

The authors are very grateful to Prof. K. Uchida, T. Nagami of Tokyo Institute of Technology and M. A. G. Ramirez, F. A. Hassani and M. A. Ghiass of University of Southampton for their contributions to the present work. This work is partly supported by SORST JST (Japan Science and Technology).

Phase Composition and Surface Properties of Cobalt Molybdenum Nitrides Modified by Chromium

D. Moszyński, W. Arabczyk

West Pomeranian University of Technology
Pułaskiego 10, 70-310 Szczecin, Poland

Cobalt molybdenum nitrides, particularly Co_3Mo_3N, are considered as good catalysts for many chemical reactions [1–4]. Theoretical studies have indicated that this compound is potentially the most active catalyst for ammonia synthesis and it has been proved experimentally that catalysts based on cobalt molybdenum nitride can be more active in that reaction than industrial iron catalysts as well as promoted ruthenium [5, 6]. The active phase is obtained by ammonolysis of a precursor and it has a nanocrystalline structure with a relatively high surface area. The addition of some cesium and potassium compounds to the cobalt molybdenum nitride results in an increase in its catalytic activity despite decreases in its surface area [7, 8]. The influence of cesium and potassium compounds resembles their effect on the industrial iron catalyst for ammonia synthesis, which also has a metallic, nanocrystalline structure in its active form [9]. One of the main parameters characterizing a good catalyst is a developed surface area. It is dependent on a relatively complex interaction of several effects from which it is the chemical composition and the preparation procedure that are worth noting here. Considering a similarity between the iron catalyst and the cobalt molybdenum catalyst it is supposed that an addition of some compounds can

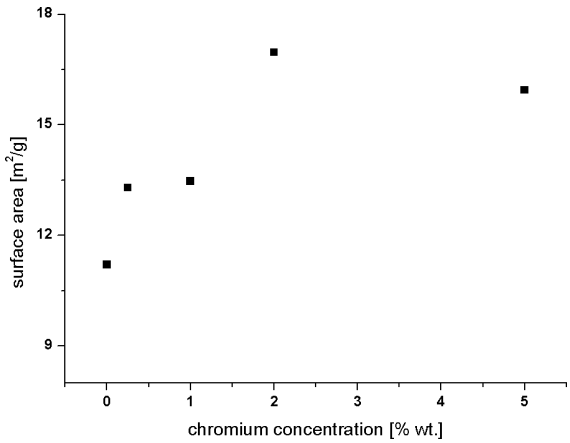

Figure 1: Surface area of cobalt molybdenum samples modified by chromium

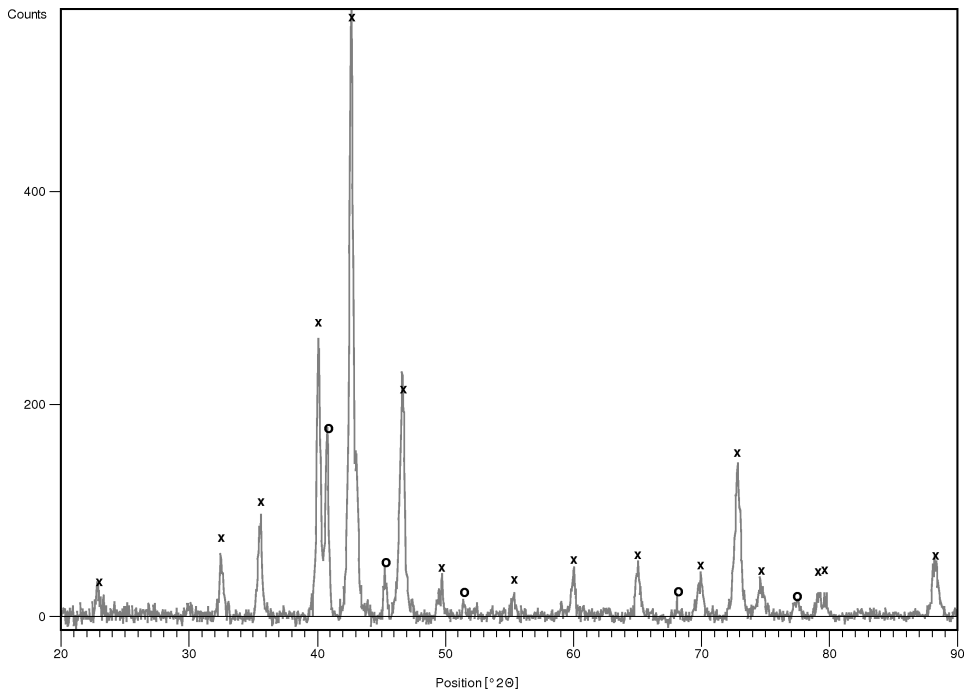

Figure 2: *X*-ray diffractogram for sample containing 0.25% wt. of chromium; identified phases: × – Co_3Mo_3N, ○ – Co_2Mo_3N

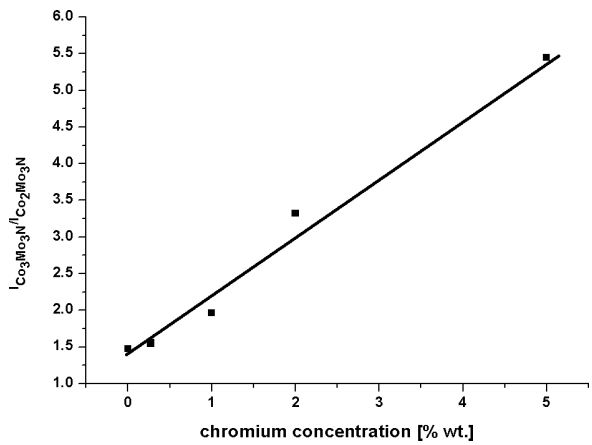

Figure 3: Intensity ratio, $I_{Co_3Mo_3N}/I_{Co_2Mo_3N}$, for two XRD peaks characteristic for Co_3Mo_3N and Co_2Mo_3N phases

substantially influence the structural and surface properties of cobalt molybdenum nitrides. The effect of chromium compounds is described herein.

The catalyst precursor, cobalt molybdenum oxide, $CoMoO_4$, was obtained by pre-

cipitation from water solutions of cobalt nitrite and ammonium molybdate. The precursor was then impregnated in a chromium nitrate solution so as to prepare samples containing different loads of chromium. Finally the impregnated precursor was exposed to pure gaseous ammonia to prepare an active phase, cobalt molybdenum nitrides. The phase composition of the received samples was characterized by means of *X*-ray diffractometry (XRD) and their surface area was measured using a volumetric method utilizing the BET model.

The surface area of cobalt molybdenum nitrides changes notably with a variation of the chromium concentration (Figure 1). The initial substrate, containing no chromium, has the surface area of about 11 m^2/g and with an increase in the chromium concentration the surface area rises up to about 16 m^2/g for the sample with 2% wt. of Cr. A further increase in the chromium admixture does not change the surface area substantially.

In all samples two different phases of cobalt molybdenum nitrides were identified: cubic Co_3Mo_3N and cubic Co_2Mo_3N. The diffractogram of the nitrided sample containing 0.25% wt. of chromium is shown in Figure 2. No distinct phases containing chromium atoms were found, though up to 5% wt. of chromium atoms was present in the samples. It suggests that chromium atoms dissolve homogeneously in cobalt molybdenum phases, forming no separated phases. However, a relative amount of Co_3Mo_3N and Co_2Mo_3N differs from sample to sample. A ratio of two prominent peaks for each phase was taken as a measure of the sample composition. The peaks at position 40.07° for Co_3Mo_3N and at position 40.77° for Co_2Mo_3N, respectively, were chosen.

Their intensity ratio, $I_{Co_3Mo_3N}/I_{Co_2Mo_3N}$, is shown in Figure 3. The amount of Co_2Mo_3N drops substantially with the increasing chromium concentration. The relatively good linear correlation between the chromium concentration in the cobalt molybdenum nitrides and $I_{Co_3Mo_3N}/I_{Co_2Mo_3N}$ is seen. It indicates that the presence of chromium atoms increases the stability of Co_3Mo_3N leading to the formation of a Co_2Mo_3N-lean mixture. There is also a certain correlation between the phase composition of cobalt molybdenum samples and their surface area. The samples with prevailing concentration of the Co_3Mo_3N nitride have a relatively better developed surface area. It can be supposed that the complete removal of the Co_2Mo_3N phase from the mixture would lead to even higher values of the surface area. It seems that a further addition of chromium should not lead to this effect, however, it may be supposed that it can be achieved by an alteration of the preparation procedure.

References

[1] Hada K, Nagai M, Omi S 2001 *J. Phys. Chem. B* **105** 4084–4093
[2] Hada K, Tanabe J, Omi S, Nagai M 2002 *J. Catal.* **207** 10–22
[3] Logan J W, Heiser J L, McCrea K R, Gates B D, Bussell M E 1998 *Catal. Lett.* **56** 165–171
[4] Shi C, Zhu A M, Yang X F, Au C T 2004 *Catal. Lett.* **97** (1–2) 9–16
[5] Jacobsen C J H, Dahl S, Clausen B S, Bahn S, Logadottir A, Norskov J K 2001 *J. Am. Chem Soc.* **123** 8404–8405
[6] Kojima R, Aika K-i 2001 *Appl. Catal. A: General* **215** 149–160
[7] Kojima R, Aika K-i 2001 *Appl. Catal. A: General* **218** 121–128
[8] Kojima R, Aika K-i 2001 *Appl. Catal. A: General* **219** 157–170
[9] Arabczyk W, Narkiewicz U, Moszyński D 1999 *Langmuir* **15** (18) 5785

Structural Features in Molten Ni_xBi_{1-x} before Peritectic Reaction

S. Mudry, I. Shtablavyi, A. Korolyshyn

Physics of Metals Department, Ivan Franko National University of Lviv
Kyrylo and Mephodii 8, 79005 L'viv, Ukraine

Information on the structure of melts whose phase diagram reveals peritectic reactions is sparse because these alloys, in comparison with eutectic ones with low melting temperatures, have found less application in various areas. Nevertheless, one can suppose that structural changes can occur at the cooling of a melt whose concentration corresponds to the peritectic point before reaction with a solid phase of some definite concentration.

In order to check this assumption that is important for the understanding of physical-chemical processes in solid-liquid metallic mixtures, an *X*-ray diffraction investigation of molten Ni-Bi alloys, containing 10, 12, 15 and 22 at % of Ni was carried out. The structure factors (SF) obtained at different temperatures at cooling and pair correlation functions (PCF) calculated therefrom were analyzed. It was found that the SFs for the melts under investigation showed a profile closer to that of liquid Bi, but the principal peak was smaller at height while the shoulder on its right side was more pronounced. Similar features were also observed in the temperature dependence of the PCFs.

The experimental data for the melts were compared with those for intermetallic phases, formed in peritectic reactions. The comparison resulted in a supposition about the dominant role of the chemical ordering in the structure formation process before reaction of the melt with the crystalline phase. The chemical ordering in some aspects was similar to the crystalline structure of intermetallics, as a product of the peritectic reaction.

Influence of Disorder on Elastic Properties of the Degenerate F.C.C. Crystal of Soft Polydisperse Dimers at Zero Temperature

J. W. Narojczyk[a], K. W. Wojciechowski[b]

Institute of Molecular Physics, Polish Academy of Sciences
Mariana Smoluchowskiego 17, 60-179 Poznań, Poland

[a] *jwn@ifmpan.poznan.pl*, [b] *kww@man.poznan.pl*

Modern technology often requires designing materials of special properties which are not commonly seen in nature. This work is focused on materials showing unusual elastic properties, i.e. exhibiting anomalous (negative) Poisson's ratio. Recently, such materials, called *auxetics*, have been a subject of increasing interest [1]. Effective design of such materials would be much easier if various mechanisms controlling properties of elastic media are identified and understood. Studies of simple model systems constitute an important step in this direction.

This work is aimed to extend our knowledge on the influence of atomic size polydispersity on the macroscopic elastic properties of three-dimensional system of soft dimers. The dimers, built of soft spheres (atoms), interact through atom-atom, soft, purely repulsive, nearest-neighbour interactions. Although the atomic centres form almost perfect f.c.c. structure, the dimers do not show any periodicity and, thus, they form a degenerate crystalline (DC) phase [2]. An efficient method [3] for studying the elastic constants of static model systems (i.e. systems at zero temperature) by computer simulations is applied in the present work.

The choice of the dimer system is, amongst other reasons, related to the fact that behaviour of polydisperse dimers of fixed distance between the centres of soft spheres [4] was found to be different from that observed for other systems [5–9]. Namely, a typical effect of rising particle size polidyspersity is the increase of the Poisson's ratio [5–9], in both the isotropic and anisotropic systems. However, recent studies indicated that (at least) for some three-dimensional systems of cubic symmetry crystalline directions exist, along with the Poisson's ratio decreases with an increase of size polydispersity of the particles [4, 10]. In particular, in the case of the soft polydisperse spheres forming a f.c.c. solid phase [10] such a decrease of the Poisson's ratio, with increasing polydispersity, was observed for soft interactions only. In the case of the DC phase of polydisperse dimers, however, the Poisson's ratio was found to decrease (down to *negative* values) in a certain direction also when the interaction potential became very hard [4]. This surprising result encourages one to study polydisperse dimers with dispersion of the distances between centres of spheres forming them and binary mixtures of dimers. Both those systems are studied in this work.

Acknowledgements
This work was partially supported by the MNiSW grant NN202 261438. Part of the simulations was performed at the Poznań Supercomputing and Networking Center (PCSS).

References

[1] Remillat C., Scarpa F., Wojciechowski K. W. 2009 *Phys. Stat. Sol. (b)* **246** 2007–2009 and references cited in that issue
[2] Wojciechowski K. W., Frenkel D., Brańka A. C. 1991 *Phys. Rev. Lett.* **67** (6) 3168
[3] Narojczyk J. W., Wojciechowski K. W. 2007 *Phys. Stat. Sol. (b)* **244** 943–954
[4] Narojczyk J. W., Wojciechowski K. W. 2010 *J. Non-Cryst. Sol.*, in print
[5] Wojciechowski K. W., Narojczyk J. W. 2006 *Rev. Adv. Mat. Sci.* **12** 120–126
[6] Narojczyk J. W., Wojciechowski K. W. 2006 *Mat. Sci. Pol.* **24** 921–927
[7] Narojczyk J. W., Wojciechowski K. W. 2006 *J. Non-Cryst. Sol.* **352** 4292–4298
[8] Narojczyk J. W., Wojciechowski K. W. 2008 *Phys. Stat. Sol. (b)* **245** 2463–2468
[9] Narojczyk J. W., Alderson A., Imre A. R., Scarpa F., Wojciechowski K. W. 2008 *J. Non-Cryst. Sol.* **354** 4242–4248
[10] Narojczyk J. W., Wojciechowski K. W. 2008 *Phys. Stat. Sol. (b)* **245** 606–6013

Magnetic Properties and FMR Spectra of Ni/C Nanoparticles in Sodium Borosilicate Porous Glass

N. Guskos[1,2], M. R. Dudek[3], B. V. Padlyak[3a,4], G. Żołnierkiewicz[2], Yu. K. Gorelenko[5], E. Rysiakiewicz-Pasek[6], I. Pełech[7], U. Narkiewicz[7]

[1] *Solid State Physics Section, Department of Physics, University of Athens Panepistimiopolis, 15 784 Zografos, Athens, Greece*

[2] *Institute of Physics, West Pomeranian University of Technology Al. Piastów 17, 70-310 Szczecin, Poland*

[3] *Institute of Physics, University of Zielona Gora Szafrana 4a, 65-516 Zielona Góra, Poland*

[4] *Institute of Physical Optics Dragomanov Str. 23, 79-005 L'viv, Ukraine*

[5] *Department of Chemistry, Ivan Franko National University of Lviv Kyryla & Mefodiya Str. 6, 79-005 L'viv, Ukraine*

[6] *Institute of Physics, Wroclaw University of Technology Wyb. Wyspiańskiego 27, 50-370 Wrocław, Poland*

[7] *Institute of Chemical and Environmental Engineering West Pomeranian University of Technology Al. Piastów 17, 70-310 Szczecin, Poland*

[a] *B.Padlyak@proton.if.uz.zgora.pl*

The static magnetic susceptibility and FMR spectra of nickel nanoparticles of the face-centered cubic (fcc) phase, covered by carbon (Ni/C), embedded in the two types of sodium borosilicate porous glass were investigated and analyzed. The Ni/C nanoparticles with the average size of 20 nm were obtained through decomposition of

Table 1: Parameters of porous glass texture

Parameters	Glass of type B	Glass of type D
specific area, m^2/g	28.9	5,9
pore volume, cm^3/g	0.44	0.47
pore average diameter, nm	46	320
porosity, %	50	48

ethylene on nanocrystalline Ni at 700°C according to [1]. Two porous glass samples (B and D type) were obtained from one sodium borosilicate basic glass with 92% SiO_2-7% B_2O_3-1% Na_2O composition according to the technology described in [2]. For the phase separation B and D type glasses the basic glass was heated at 490°C for 165 hours and at 650°C for 100 hours, respectively. All the obtained porous glass samples were etched in hydrochloric acid and rinsed in deionized water. Then, both types of glasses were immersed in KOH. The parameters of the porous B and D type glass texture were essentially different (Table 1).

Rectangular porous glass plates sized $10 \times 10 \times 0.5$ mm^3 were filled with Ni/C nanoparticles which were introduced from a water suspension according to the technological condition developed by the authors. A few nanoparticles on the glass surface are shown in Figure 1.

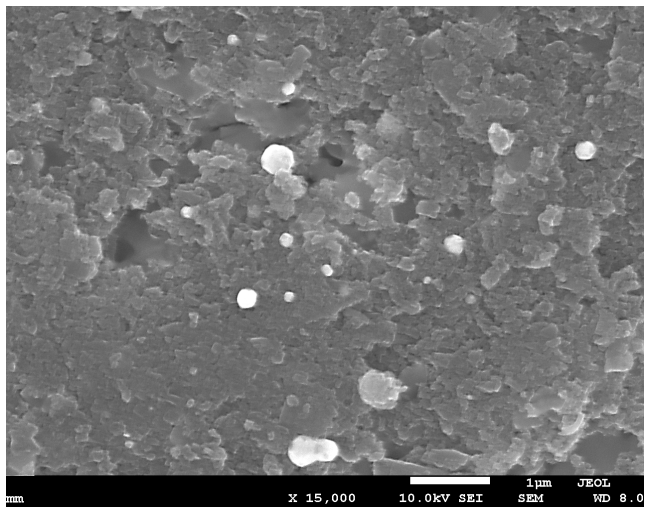

Figure 1: SEM image of carbon coated Ni nanoparticles on sodium borosilicate porous glass surface

The static magnetic susceptibility, measured by the balance Faraday technique and X-band FMR spectra of glass samples of the B and D types, containing Ni/C nanoparticles with different concentration were investigated in the 90–300 K temperature range. Both the glass samples with low and high Ni/C concentration showed a linear dependence of the static magnetic susceptibility on the reciprocal values of the magnetic field which was evidence of their superparamagnetic properties. The temperature dependence of the magnetic susceptibility for both the investigated samples was similar to the corresponding dependence for the bulk Ni sample. The X-band FMR spectra consisted of intense symmetrical FMR signals centered at $H_r = 300(3)$ mT (peak-to-peak linewidth, $\Delta H_{pp} = 61.5$ mT) and $H_r = 297.8(3)$ mT ($\Delta H_{pp} = 72.1$ mT) at $T = 300$ K in samples with lower and higher Ni/C concentration, respectively. It should be noted that the observed FMR line intensities for both samples decreased with decreasing temperature and they disappeared below $T = 90$ K as a result of broadening processes. A simple theoretical model of N magnetic nanoparticles dis-

persed in a porous nonmagnetic matrix is introduced in order to explain the properties of the FMR spectra. It is based on the Lifshitz-Landau equation for nanoparticle magnetization.

Acknowledgements
Publication of this paper was realised with partial financial support from the budget resources of the West Pomeranian Voivodeship.

References

[1] Guskos N, Maryniak M, Typek J, Podsiadły P, Narkiewicz U, Senderek E, Rosłaniec Z 2009 *J. Non-Cryst. Solids* **355** 1400
[2] Rysiakiewicz-Pasek E, Lukaszewski P, Bogdańska J 2000 *Opt. Appl.* **XXX** 173

A General Formula for the Transmission Coefficient Through Any Barrier

G. J. Papadopoulos

Department of Physics, Solid State Physics Section, University of Athens
Panepistimiopolis, 15 784 Zografos, Athens, Greece

A general formula providing the transmission coefficient through a given barrier is presented in terms of the incoming carrier energy and the logarithmic wave function derivative at the start of the barrier. The derivation bears a certain relation to the analytical transfer methodology. However, the procedure, employed, is simpler in that the parameters, involved, beyond the incoming energy are limited to logarithmic derivative which is obtained via an appropriate Riccati equation. On account of the facility provided for obtaining the transmission coefficient we proceeded obtaining the characteristic for a quantum dot carved barrier which exhibits a region of extremely large negative differential resistance together with a highl peak to valley ratio. Under the circumstances, the possibility of developing a nanostructure switch utilizing a small variation in the applied bias exists.

Purification of Multi-Walled Carbon Nanotubes – Influence of Hydrogenation and Oxidation on Removal of Metal Particles

I. Pełech[a], U. Narkiewicz

Institute of Chemical and Environmental Engineering
West Pomeranian University of Technology
Pułaskiego 10, 70-310 Szczecin, Poland

[a] *ipelech@zut.edu.pl*

Multi-walled carbon nanotubes can be synthesized by three dominant techniques: arc discharge, laser ablation, chemical vapor deposition. The last of these methods is the most interesting one because of its low production costs, and therefore it is very attractive for large scale production of nanotubes. CVD involves catalyst-assisted decomposition of hydrocarbons (methane, acetylene, ethylene, benzene, propylene). The best results are obtained with iron, nickel and cobalt nanoparticles used as catalysts. As-synthesized CNTs prepared by the above method inevitably contain metal catalyst particles and carbon impurities in the form of amorphous carbon or carbon nanoparticles. The separation of CNTs from catalyst traces is most often carried out using hydrofluoric, hydrochloric, sulfuric or nitric acids. The oxidation method is applied to purify carbon nanotubes from carbon impurities. Amorphous carbon can be eliminated by chemical oxidation including gas phase oxidation using air or steam or by liquid phase oxidation using potassium permanganate, hydrogen peroxide, nitric acid.

In our work multi walled carbon nanotubes were obtained by chemical vapor deposition and ethylene was applied as the carbon source and nanocrystalline iron with an addition of a small amount of CaO and Al_2O_3 was used as a catalyst. The role of the promoter oxides was to stabilize the nanocrystalline iron structure at elevated temperatures. The mean crystallite size of iron determined using an *X*-ray diffraction method (Philips X'Pert) and calculated using the Scherrer's equation was equal to 17 nm.

The purification procedure was carried out in two stages. In order to remove amorphous carbon the material was treated under hydrogen or air atmosphere at 500 and 550°C, respectively. The carbon removal degree depended on the experimental conditions and equaled from 10 to 70%. The as prepared material was refluxed in 1 or 5 M nitric and 1 or 5 M hydrochloric acid for 60 and 300 minutes. After this treatment, the metal amount was decreased to ≈1 wt %.

Different methods were employed to characterize CNTs. The phase composition of the samples was studied using an *X*-ray diffraction method (X'Pert). Transmission electron microscopy (High Resolution Transmission Electron Microscopy Jeol JEM 3010TEM) was used to determine the type of carbon nanotubes and to verify the structures. Thermogravimetric analysis (TGA) was employed to determine metal in the samples.

Temperature Dependence of FMR Spectra of γ-Fe_2O_3 Agglomerates in Organic Matrix

N. Guskos[1,2], G. Żołnierkiewicz[2], J. Typek[2], A. Guskos[2], D. Petridis[3]

[1] *Solid State Section, Department of Physics, University of Athens Panepistimiopolis, 15 784 Zografos, Athens, Greece*

[2] *Institute of Physics, West Pomeranian University of Technology Al. Piastów 48, 70-311 Szczecin, Poland*

[3] *NCSR "Demokritos", Aghia Paraskevi, Attikis Athens, Greece*

Two samples containing an extended free radical network derived from a condensation of cyanuric chloride with p-phenylenediamine and containing a small amount of magnetic agglomerates were prepared. Both samples produced asymmetric, very intense ferromagnetic (FMR) spectra (Figures 1a and b). The temperature dependence of FMR lines was measured in the 80–290 K temperature range. The FMR spectra were fitted by two Lorentzian functions (Figures 1c and d). The following

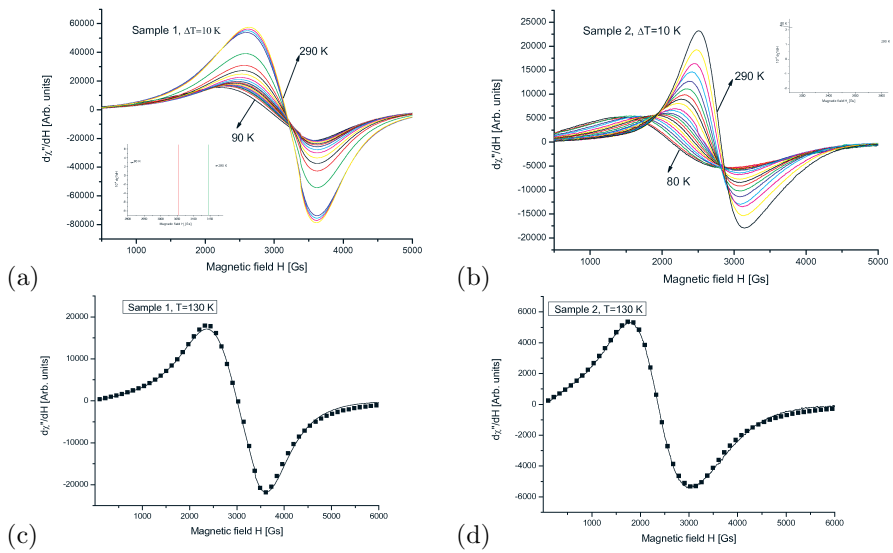

Figure 1: FMR spectra for sample 1 (a), sample 2 (b) and fitted spectra at 130 K for sample 1 (c), and for sample 2 (d)

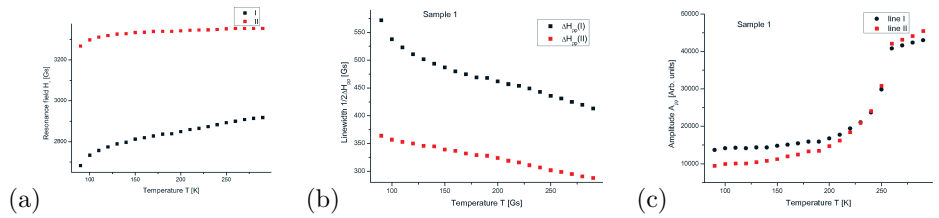

Figure 2: Temperature dependence of component resonance fields (a), linewidths (b) and amplitudes (c) for sample 1

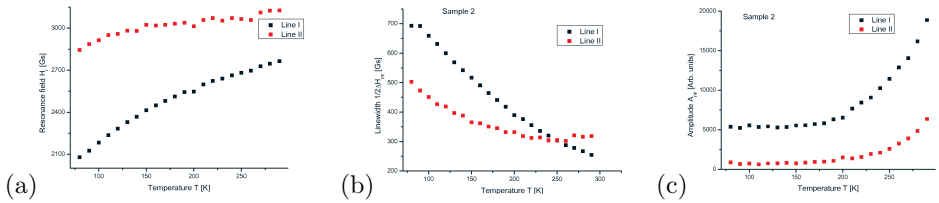

Figure 3: Temperature dependence of component resonance fields (a), linewidths (b) and amplitudes (c) for sample 2

values of the resonance fields and linewidths for the component lines were obtained: $H_r(I) = 3354(1)$ Gs ($g_{eff}(I) = 2.017(1)$), $H_r(II) = 2918(1)$ Gs ($g_{eff}(II) = 2.315(1)$) with linewidths $\Delta H_{pp}(I) = 815(2)$ Gs, $\Delta H_{pp}(II) = 573(2)$ Gs for sample 1, and $H_r(I) = 3124(1)$ Gs ($g_{eff} = 2.170(1)$), $H_r(II) = 2768(1)$ Gs ($g_{eff}(II) = 2.436(1)$) with linewidths $\Delta H_{pp}(I) = 573(2)$ Gs, $\Delta H_{pp}(II) = 630(2)$ Gs for sample 2. The ultra low concentration of magnetic agglomerates in similar matrices showed very different behavior [1]. In both samples the resonance lines shift to lower magnetic fields, the linewidths increase, and the amplitudes decrease with decreasing temperature (Figures 2 and 3). Low concentrations of magnetic nanoparticles in nanocomposite matrices behave in a similar way [2], while the average positions of the resonance lines essentially change at room temperature. The following values of resonance fields temperature gradients were measured: $\Delta H_r/\Delta T(I) \approx 0.26(3)$ Gs/K, $\Delta H_r/\Delta T(I) \approx 0.92(3)$ Gs/K, for sample 1, and $\Delta H_r/\Delta T(II) \approx 1.31(3)$ Gs/K, $\Delta H_r/\Delta T(II) \approx 3.34(3)$ Gs/K, for sample 2. The magnetic iron oxide clusters could produce an internal magnetic field which could be associated with reorientation processes of the spin system. The magnetic anisotropy as well as the reorientation processes strongly depend on the concentration of the magnetic centers.

Acknowledgements
Publication of this paper was realised with partial financial support from the budget resources of the West Pomeranian Voivodeship.

References

[1] N. Guskos, G. Żołnierkiewicz, J. Typek, A. Guskos, D. Petridis 2008 *J. Non-Cryst. Solids* **354** 4211
[2] N. Guskos et. al. 2006 *J. Appl. Phys.* **99** 084307; 2008 *J. Nanosci. Nanotech.* **8** 2127

Removal of SO_2 from Gases on Carbon Nanotubes

A. Pietrasz, I. Pełech, U. Narkiewicz

Institute of Chemical and Environment Engineering
West Pomeranian University of Technology
Pułaskiego 10, 70-322 Szczecin, Poland

Sulphur dioxide is emitted mainly as a component of exhaust gases from vehicles, industrial or power plants. To lower the level of this toxic gas, various absorption, adsorption and catalytic methods are applied. The catalytic methods are the most useful, because they generate a useful, commercial product – sulphuric acid.

In this work the studies on an elimination of sulphur dioxide from gases on modified nanocarbons (carbon nanotubes containing iron) were performed.

The following materials were used in the studies:

1) Nanocarbon – material marked as NC, synthesised through decomposition of ethylene on nanocrystalline iron. The material contains mainly multi walled carbon nanotubes ended with iron carbide crystallites and amorphous carbon. The specific surface area measured by using BET method is about 43 m^2/g. This value is lower than that given in the literature [1, 2] for pure carbon nanotubes, but in the case of the material under the study the nanotubes contain iron (the mass ratio of carbon to iron is $m_C/m_{Fe} = 6.5$), then the density of such a material is higher and the specific surface area – lower than that of pure CNTs.

2) Material marked as NCH, obtained after the reduction of material NC under a flow of hydrogen (20 dm^3/h) at the temperature of 550°C. The reduction was carried out to remove amorphous carbon and also to remove the graphitic layer from iron carbide crystallites, with an expectation of an increase of activity. The reduction resulted in removal of amorphous carbon and decomposition of iron carbide to iron and methane. Then, the NCH material contained multi walled carbon nanotubes ended with crystallites of metallic iron (diameter of about 40 nm). The specific surface area of this material was a little bit higher than that of nanocarbon as synthesised and amounted to about 54 m^2/g. Under the oxidising conditions of the sulphur dioxide removal process, the metallic iron was subsequently oxidised to iron oxide.

The process was carried out by passing 10.6 dm^3/h of a gas mixture of SO_2, O_2, N_2, containing various concentrations of SO_2 (close to 0.18 or to 0.3 vol.%) at the temperature of 30–200°C. The activity of nanocarbon reduced with hydrogen (NCH) was studied at higher temperatures – 200–450°C. The flow of the gas mixture was fixed using mass flowmeter. For studies at lower temperatures (up to 80°C) the volume of 10 ml of a sample was put in the reactor with water jacket and the temperature was fixed with a thermostat. The height of the catalyst bed was 140 mm. In the case of the experiments carried out in the temperature range of 100–450°C, the glass reactor was heated by an electric furnace, the volume of a sample was 5 ml and the height of the catalyst bed – about 20 mm.

Figure 1 shows a dependence of the outlet relative SO_2 concentration (referred to the inlet concentration of SO_2) on time for the NC sample. The inlet concentration of SO_2 was 0.31 vol. %. In the temperature range of 30–80°C, the efficiency of the process increases with temperature and the best results were obtained at 80°C. The adsorption capacity of the nanocarbon disappears after 50 min.

Figure 2 presents a dependence of the outlet relative SO_2 concentration (referred to the inlet concentration of SO_2) on time for the NC sample. The inlet concentra-

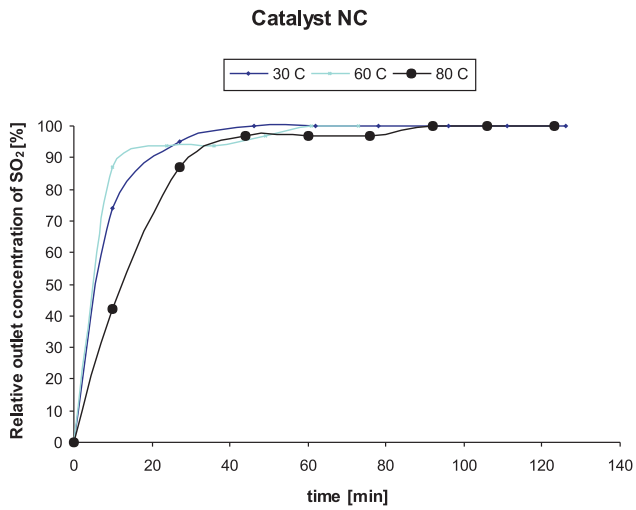

Figure 1: Changes of outlet SO_2 concentration in the temperature range 30–80°C for NC catalyst

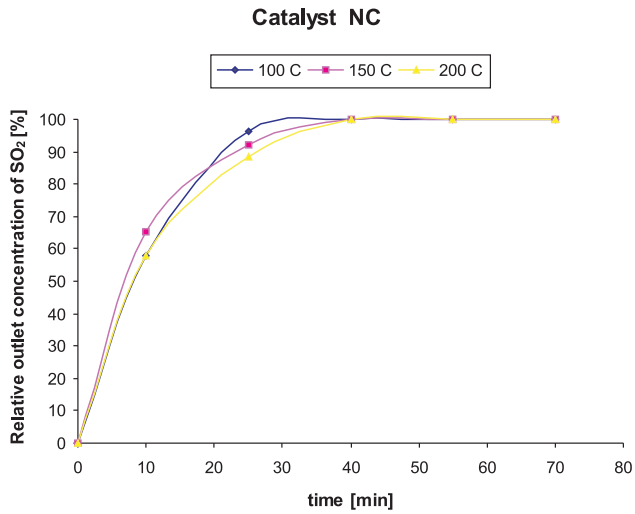

Figure 2: Changes of outlet SO_2 concentration in the temperature range 100–200°C for NC catalyst

tion of SO_2 was 0.26 vol. %. In the temperature range of 100–200°C, the efficiency of the process increases slightly with temperature. The adsorption capacity of the nanocarbon disappears, as at lower temperatures, after 50 min.

Figure 3 presents a dependence of the outlet relative SO_2 concentration on time for the NCH (nanocarbons after a hydrogen treatment) sample. The inlet concentration of SO_2 was 0.18 vol. % and the process was studied in the temperature range of 200–450°C. The efficiency of the process increases with temperature and the best results were obtained at 450°C.

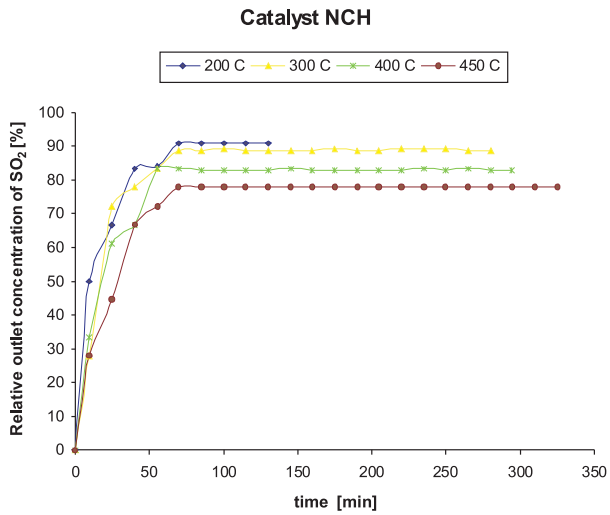

Figure 3: Changes of outlet SO_2 concentration in the temperature range 200–450°C for NCH catalyst

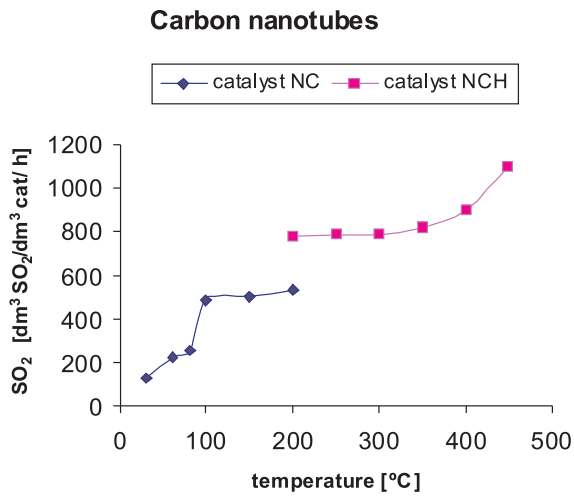

Figure 4: Dependence of the adsorption capacity of nanocarbons NC and NCH on temperature

To compare the obtained results, the volume of the eliminated SO_2 was referred to the corresponding volume of a catalyst and a unit of time. The efficiency of SO_2 removal expressed in $dm^3_{SO_2}/dm^3_{cat}/h$ as a function of temperature is shown in Figure 4.

For the sample NC at 200°C, the efficiency of SO_2 removal amounts to 536 $dm^3_{SO_2}/dm^3_{cat}/h$, whereas for the sample NCH – 780 $dm^3_{SO_2}/dm^3_{cat}/h$. Then, the reduction of carbon deposit under hydrogen results in an increase of efficiency in SO_2 removal of 1.5 times.

Acknowledgements
This work was supported by the European Union within the European Social Fund.

References

[1] J. Xie, N. Zhang, V. K Varadan 2006 *Smart Mater. Struct.* **15** S5–S8
[2] A. Peigney, Ch. Laurent, E. Flahaut, R. R. Bacsa, A. Rousset 2001 *Carbon* **39** 507–514

Controlled Electrospinning and Novel Nanofibers

D. Pliszka[1], T. Velmurugan[1], S. Neubert[1], T. Krishnamoorthy[2], S. S. Al-Deyab[3], E.-R. Kenabi[3], S. Ramakrishna[1a,3,4]

[1] *National University of Singapore, Singapore*

[2] *Nanyang Technology University, Singapore*

[3] *King Saud University, Saudi Arabia*

[4] *Institute of Materials Research and Engineering, Singapore*

[a] *seeram@nus.edu.sg*

Among other nanotechnology techniques electrospinning is a simple and versatile method for fabrication of polymer based fibers [1]. Currently it is the only method for fabrication of continuous fibers in the nanometer range [2]. The simplicity of the process has caused increased interest among numerous scientific groups. A basic electrospinning setup consists of a polymer solution delivery system with an orifice connected to a high voltage power supply. Fibers are deposited on a grounded collector (see Figure 1A).

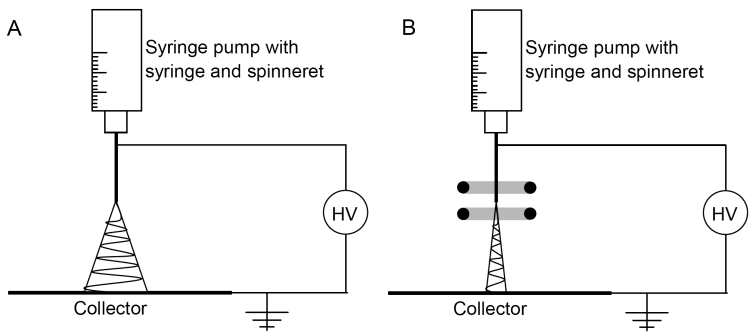

Figure 1: Classic electrospinning setup (A), modified electrospinning setup (B)

Due to the nature of the electrospinning, it is especially the self inducted chaotic bending modes of the electrospinning jet that lead to quite a large deposition spot size. Usually, it is about 10 cm and above, depending on the setup geometry and the collector size. The resulting nonwoven membranes have found numerous applications in bioengineering, environmental engineering, microelectronics and energy technology [3–7].

The development of the basic electrospinning may be divided into two mainstreams.

One is based on development and improvement of the process to control fiber deposition. Initially works were focused on the collector area modification. Due to

the electric field's nature, the introducing of patterned collectors has resulted in the fabrication of aligned nanofiber patterns. The fiber collection method on the high speed rotating edge [8] which was developed in our lab allowed obtaining highly aligned unidirectional fibrous structures. Recently an improved method to deposit aligned fibers with a 90 nm diameter size has been developed.

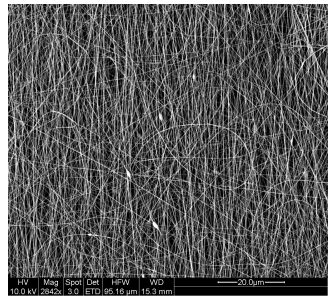

Figure 2: Aligned (80% of alignment) TiO_2 nanofibers

It has been achieved by using custom designed air-shields reducing the influence of air turbulences on the very fine fibers. Other approaches for electrospinning control incorporate additional electrodes placed between the spinneret and the collector (see Figure 1B). The potential of such an approach has been shown by [9] and [10] allowing the deposition spot size to be decreased and the fiber deposition to be controlled more precisely to some extent. It has been shown in our lab that it is possible to decrease the deposition size spot down to 5 mm using a simple setup with a few additional electrodes and only one additional power supply. Though this improvement seems to be rather far from very precise deposition of electrospun fibers it has brought reduction in terms of the fiber deposition time and the polymeric solution wastage. Presently works in our lab are focused on the development of a device for precise deposition of fibers in a highly controlled way.

The second mainstream are materials used for fiber fabrication. Polymer is the most widely used material for electrospinning, but there is no limitation to polymeric materials. Recently, ceramic fibers have meet with interest of research groups due their unique electrical properties. In such case polymer carriers are blended with the precursor, for example titanium (IV) isopropoxide in case of TiO_2 fibers [7]. In the post process samples are sintered in an oven and the polymer matrix is removed leaving pure ceramic fibers. A similar approach is used in case of carbon fibers where a phenolic resin precursor is used [11]. The carbonization process during sintering in an inert atmosphere causes again removal of the polymeric component, leaving carbon fibers. Other materials explored recently are conductive fibers [12] as well as photoluminescent fibers [13].

References

[1] Reneker D H and Chun I 1996 *Nanotechnology* **7** 216–223
[2] Doshi J and Reneker D H 1995 *J. Electrost.* **35** 151–160
[3] Sundarrajan S and Ramakrishna S 2007 *J. Mater. Sci.* **42** 8400–8407
[4] Huang Z M, Zhang Y Z, Kotaki M and Ramakrishna S 2003 *Compos. Sci. Technol.* **63** 2223–2253

[5] Choi S S, Lee S G, Im S S, Kim S H and Joo Y L 2003 *J. Mater. Sci. Lett.* **22** 891–893
[6] Thavasi V, Renugopalakrishnan V, Jose R and Ramakrishna S 2009 *Mater. Sci. Eng. R-Rep.* **63** 81–99
[7] Thavasi V, Singh G and Ramakrishna S 2008 *Energy Environ. Sci.* **1** 205–221
[8] Xu C Y, Inai R, Kotaki M and Ramakrishna S 2004 *Biomaterials* **25** 877–886
[9] Kim G H, Han H, Park J H and Kim W D 2007 *Polym. Eng. Sci.* **47** 707–712
[10] Bellan L M and Craighead H G 2006 *J. Vac. Sci. Technol. B* **24** 3179–3183
[11] Imaizumi S, Matsumoto H, Suzuki K, Minagawa M, Kimura M and Tanioka A 2009 *Polym. J.* **41** 1124–1128
[12] Rivera R and Pinto N J 2009 *Physica E* **41** 423–426
[13] Pagliara S, Camposeo A, Di Benedetto F, Polini A, Mele E, Persano L, Cingolani R and Pisignano D 2010 *Superlattices Microstruct.* **47** 145–149

Synthesis Conditions and Role of Nickel and Iron Carbides as Intermediate Products for Formation of Carbon Materials

M. Podsiadły, I. Pełech[a], U. Narkiewicz

Institute of Chemical and Environmental Engineering
West Pomeranian University of Technology in Szczecin
Pułaskiego 10, 70-310 Szczecin, Poland

[a] *ipelech@zut.edu.pl*

Carbon fibers, nanotubes and carbon nanoparticles have belonged recently to the most studied carbon materials. In general, catalysts used for their synthesis are based on transition metal particles (Fe, Co, Ni) supported on carriers such as e.g. Al_2O_3, SiO_2, ZrO_2 or MgO. In the present work, unsupported iron and nickel were applied as catalysts prepared from nickel (II) or iron (III) nitrates together with a small amount of calcium and aluminum nitrates. The total content of CaO and Al_2O_3 promoters did not exceed 3.0 wt. % and their role was to protect fine metal particles against sintering at elevated temperatures.

Hydrocarbons were decomposed in a high temperature furnace (HST 12/400 Carbolite). Methane, ethane or ethylene were applied as the carbon source. The processes were performed under atmospheric pressure in the temperature range from 500°C to 700°C for 60 min. The phase composition of the obtained samples was determined using an *X*-ray diffraction (XRD) method (Philips X'Pert).

It was only graphite and nickel phases that were detected in the samples after methane decomposition. The samples obtained under ethylene atmosphere had another phase composition. In addition to the graphite and nickel phases, nickel carbide was also obtained at 500°C under the applied experimental conditions. An increase in the temperature caused a decrease in the peaks intensity ascribed to Ni_3C, and at 700°C, the decomposition rate of Ni_3C was higher than its formation rate.

In the case of an iron catalyst the peaks characteristic for iron, cementite and graphite were identified. The intensity of iron and graphite peaks was greater when the temperature increase, while the intensity of cementite peaks decreased in the same temperature conditions. According to these results, the concentration of iron in the samples increased at higher temperatures.

The role of iron and nickel carbides as intermediate products for formation of carbon materials is discussed.

Nanomaterials Interactions with Biological Systems

P. P. Pompa

Italian Institute of Technology, Center for Bio-molecular Nanotechnologies
Via Barsanti 73010 Arnesano (Lecce) Italy

The interactions between biological systems and nanostructured materials are attracting great interest, due to the possibility to open up novel concepts for the design of smart nano-biomaterials that actively play a functional biological role. On the other hand, the assessment of the potential toxic effects arising from such interactions is gaining increasing attention and a new field known as nanotoxicology is strongly emerging. In this frame, we investigated the response of human neuroblastoma cells line to gold surfaces with different levels of nanoroughness, finding out that neurons are capable to sense and actively respond to these nanotopography features, with a surprising sensitivity to variations of few nanometers. By seeding cells onto micropatterned flat and nanorough gold surfaces, we demonstrated the possibility to realize substrates with cytophilic or cytophobic behavior, simply by fine tuning their surface topography at nanometer scale, inducing a clear self-alignment of neurons. These nanostructured substrates were also investigated to explore the impact of nanoscale topography on genomics and proteomics of adherent bacteria. A multidisciplinary approach (by means of Atomic Force Microscopy, Real Time qPCR and 2D-DIGE) was exploited to characterize bacteria-nanostructured surface interactions, observing that type-1 fimbriae typically disappear in bacteria grown onto nanorough substrates, as opposed to E. coli onto reference glass or flat gold surfaces. We also show the results of several investigations of nanoparticle interactions with *in vitro* and *in vivo* biological systems. In particular, the toxic effects of a wide range of nanomaterials (AuNPs, QDs, SiO_2 NPs) is presented, demonstrating the key role of size, shape and surface coating. Moreover, the peculiar behavior of nanorough and surface engineered nanoparticles is also discussed.

Synthesis and Properties of Nanocrystalline Multiferroic $MnWO_4$

M. Ptak[1a], M. Mączka[1], L. Kępiński[1],
P. E. Tomaszewski[1], J. Hanuza[1,2]

[1] *Institute of Low Temperature and Structure Research*
Polish Academy of Sciences
P.O. Box 1410, 50-950 Wroclaw 2, Poland

[2] *Department of Bioorganic Chemistry*
Faculty of Industry and Economics, University of Economics
Komandorska 118/120, 53-345, Wroclaw, Poland

[a] *m.ptak@int.pan.wroc.pl*

Multiferroic materials, in which magnetic order induces a ferroelectric phase transition, have attracted great attention in recent years. One of such extensively studied materials is simple tungstate $MnWO_4$. [1, 2] This tungstate has also been of great interest due to its electrochemical properties, high ionic conductivity and high sensitivity to humidity changes. [3, 4]

A hydrothermal synthesis of nanocrystalline $MnWO_4$ has been reported in a few papers. [3, 5, 6] These papers have shown that the morphology of crystallites can be controlled using different surfactants and pH values. The published papers have been

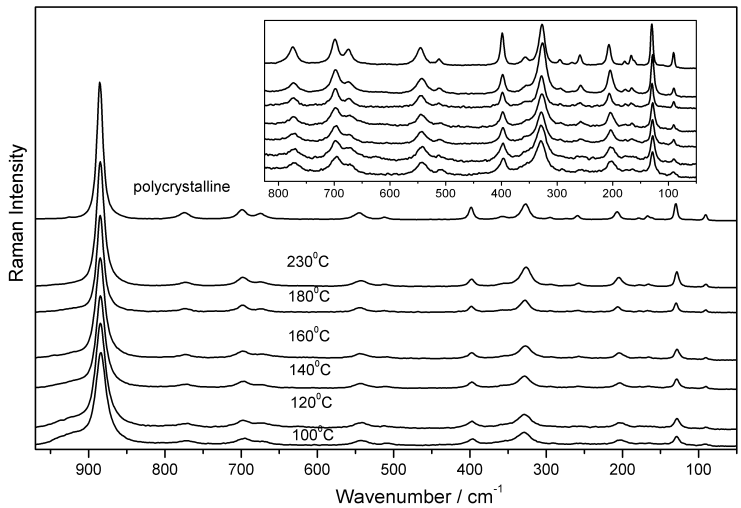

Figure 1: Raman spectra of $MnWO_4$ synthesized at different temperatures; Raman spectrum of polycrystalline sample synthesized by solid state reaction is also shown for the comparison

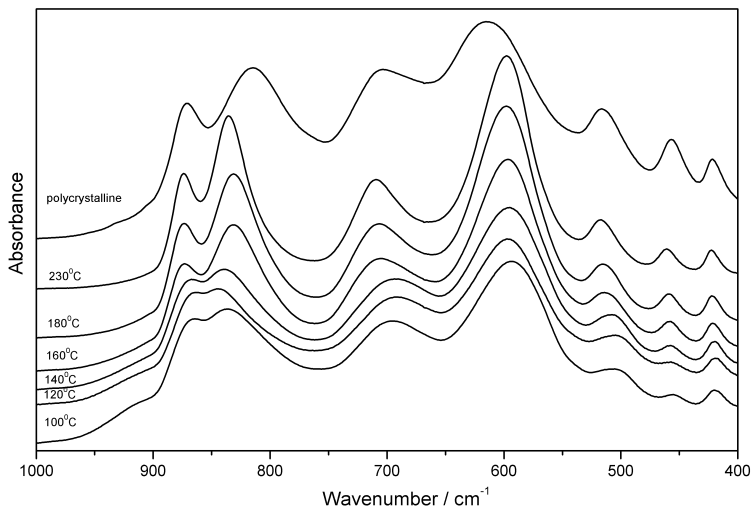

Figure 2: IR spectra of $MnWO_4$ synthesized at different temperatures; IR spectrum of polycrystalline sample synthesized by solid state reaction is also shown for comparison

focused mainly on the synthesis of nanocrystalline $MnWO_4$ but no detailed investigations have been performed on the structural, phonon or magnetic properties of the synthesized samples. Therefore, we decided to undertake a detailed investigation of $MnWO_4$ prepared by the hydrothermal method and solid state reaction in order to obtain information on the relation between various properties and the size of crystallites. In particular, we employed Raman and IR spectroscopes to study the phonon properties of $MnWO_4$ as a function of crystallite size since this technique proved to be very powerful tool in studying of nanomaterials.

Figures 1 and 2 show some representative Raman and IR spectra of the prepared samples. As can be noticed the spectra show pronounced changes with the decreasing particle size. We will discuss the origin of these changes.

References

[1] A. H. Arkenbout, T. T. M. Palstra, T. Siegrist and G. Kimura 2006 *Phys. Rev. B* **74** 184431
[2] T. Taniguchi, N. Abe, H. Sagayama, S. Ohtani, T. Takenobu, Y. Iwasa and T. Arima 2008 *Phys. Rev. B* **77** 064408
[3] L. Zhang, C. Lu, Y. Wang and Y. Cheng 2007 *Mat. Chem. Phys.* **103** 433
[4] J. Maier 2004 *Solid State ionics* **175** 7
[5] S. J. Chen, X. T. Chen, Z. Xue, J. H. Zhou, J. Li, J. M. Hong and X. Z. You 2003 *J. Mater. Chem.* **13** 1132
[6] Y. Xing, S. Song, J. Feng, Y. Lei, M. Li and H. Zhang 2008 *Solid State Sci.* **10** 1299

Binary Alloy Thin Films for MEMS/NEMS Applications

V. Radmilovic

National Center for Electron Microscopy
Lawrence Berkeley National Laboratory, University of California
Berkeley, USA

Silicon and silicon based thin films have been used in fabrication of micro-electromechanical/nano-electromechanical systems MEMS/NEMS [1], despite their low ductility and wear resistance, poor fracture toughness, electrical conductivity and optical reflectivity. Metallic thin films have been considered as potential structural materials for some MEMS/NEMS device applications where their significantly higher electrical conductivity and ductility relative to silicon, oxide or nitride systems are extremely advantageous. Unfortunately polycrystalline metallic films exhibit low strength and hardness, high surface roughness, and significant residual stress making them unusable for these applications. In this presentation we report on synthesis and characterization of amorphous and amorphous-nanocrystalline metallic alloys that overcome these barriers. These alloys are also fairly chemically simple, making them compatible with the usual NEMS/MEMS fabrication routes. The cross sectional transmission electron microscopy shows that the majority of the grains nucleates at the substrate and grow all the way to the surface. The average surface grain diameter, as obtained by AFM, was about 380 nm. The growth mode of $Al_{92}Mo_8$ films is distinctly different from that of pure Al. Although the initial nucleation density at the Si interface is extremely high, most grains do not grow all the way to the surface and are subsumed by either faster-growing or re-nucleated grains. The average surface grain size of 162 nm is less than half of that in the pure Al films. The increase of grain diameters with film thickness is described by the van der Drift model [1]. The film of the $Al_{68}Mo_{32}$ alloy surface is remarkably smooth, characteristic of sputtered amorphous films [2]. The Mo phase, demonstrated to be present in the diffraction pattern, is not visible under bright field conditions. Further investigation revealed that the $Al_{68}Mo_{32}$ microstructure consisted of nanocrystalline Mo islands densely and randomly dispersed in an amorphous Al-rich matrix. In the $Al_{50}Mo_{50}$ sample, tthe microstructure is again crystalline, similar to that of the 8 at % sample, showing a high nucleation density at the substrate interface and significant roughness at the film surface. Careful analysis provided no evidence for the crystalline intermetallic equilibrium phases or non-equilibrium amorphous phases. The microstructure of the $Al_{68}Mo_{32}$ film was strikingly different from that of the other alloy compositions. To elucidate the morphology of the Al-Mo compositions with extremely fine structure we have performed high resolution transmission electron microscopy (HRTEM). HREM reveals that the structure of $Al_{84}Mo_{16}$ film is composed of nanoscale FCC crystallites embedded in

a continuous amorphous matrix, while the structure of the $Al_{68}Mo_{32}$ film is essentially completely amorphous with a small fraction of ordered BCC domains.

A systematic investigation of microstructure and properties as a function of Mo content resulted in an optimum film composition of $Al_{68}Mo_{32}$ with a unique microstructure comprised of a dense distribution of nm-scale Mo crystallites dispersed in an amorphous Al-rich matrix. These films were found to exhibit unusually high nanoindentation hardness and a very significant reduction in roughness compared to pure Al, while maintaining resistivity in the metallic range. A single-anchored cantilever 5 μm long, 800 nm wide and 20 nm thick showed a resonance frequency of 608 kHz, yielding a Young's modulus of 112 GPa, in good agreement with a reduced modulus of 138 GPa measured by nanoindentation. We have fabricated fully released NEMS cantilevers of various geometries from these films. At 4.3 and 20.0 nm thickness, these are the thinnest released metal cantilevers reported in the literature to date.

Acknowledgements
This work is supported by the U.S. Department of Energy under Contract No. DE-AC02-05CH11231.

References
[1] A. Folch et al. 1997 *J. Microelectromech. Syst.*, **6** 303–306
[2] P. Smereka, X. Li, G. Russo, D. J. Srolovitz 2005 *Acta Mater.* **53** 1191

Nanomaterials Can Influence Living Biological Systems with Nanometer Sensitivity

S. Sabella[a], V. Brunetti, G. Maiorano, L. Rizzello, B. Sorce, G. Vecchio, A. Galeone, R. Cingolani, P. P. Pompa

Italian Institute of Technology. Center for Bio-Molecular Nanotechnologies
Via Barsanti, 73010 Arnesano, Lecce, Italy

[a] *stefania.sabella@iit.it*

The interactions between biological systems and nanostructured materials are attracting increasing interest, due to the possibility to open up novel concepts for the design of smart nano-biomaterials that actively play a functional biological role. In this frame we investigated the response of human neuroblastoma cells line (SH-SY5Y) to gold surfaces with different levels of nanoroughness, finding out that neurons are capable to sense and actively respond to these nanotopography features, with a surprising sensitivity to variations of few nanometers [1]. We showed that focal adhesion complexes, that allows cellular sensing, cannot properly assemble onto nanostructured surfaces, leading to a marked decrease in cell adhesion. Moreover, apoptosis/necrosis assays established that nanoscale features induce cell death by necrosis, with a trend directly related to roughness values. Finally, by seeding SH-SY5Y cells onto micropatterned flat and nanorough gold surfaces, we demonstrated the possibility to realize substrates with cytophilic or cytophobic behavior, simply by fine tuning their surface topography at nanometer scale, inducing a clear self-alignment of neurons [1]. These nanostructured substrates were also investigated to explore their use as suitable materials which can prevent bacterial colonization. A multidisciplinary approach (by means of Atomic Force Microscopy, Real Time qPCR and 2-D Differential In Gel Electrophoresis, 2D-DIGE) was exploited to characterize bacteria-nanostructured surface interactions, observing that type-1 fimbriae typically disappear in bacteria adherent onto nanostructured substrates, as opposed to *E. coli* onto reference glass or flat gold surfaces.

References

[1] V. Brunetti, G. Maiorano, L. Rizzello, B. Sorce, S. Sabella, R. Cingolani and P. P. Pompa 2010 *Proc. Natl. Acad. Sci. USA* **107** (14) 6264–6269

Protein Corona Matters: Effects of Cell Culture Media on the Dynamic Formation of Protein-NP Complexes and Influence on the Cellular Response

S. Sabella[a], G. Maiorano, B. Sorce, V. Brunetti, R. Cingolani, P. P. Pompa

Italian Institute of Technology, Center for Bio-Molecular Nanotechnology
Via Barsanti, 73010 Arnesano, Lecce, Italy

[a] *stefania.sabella@iit.it*

Currently, the development of appropriate and universal *in vitro* protocols to assess the potential toxicity of the ever expanding range of nanoparticles (NPs) represents a challenging issue, because of the rapid changes of their intrinsic physicochemical properties (size, shape, reactivity, surface area, etc) upon dispersion in biological fluids. Dynamic formation of protein coating, generally surrounding and hiding nanoparticles surface, has been estimated as a key molecular event, that may strongly impact the biological response in nanotoxicological tests. In such a context, we show here that the dynamics of proteins-NP interactions are differently mediated by different cellular media, which are the liquid environments where NPs encounter cells. To demonstrate this, we used, as a model, spherical NPs (citrate-capped gold nanoparticles, AuNPs) of different sizes (15, 40 and 80 nm). Upon incubation with two widely used cellular media (i.e., DMEM and RPMI, supplemented with fetal bovine serum), we analyzed NPs interactions with serum proteins present in the media, over time, by several spectroscopic techniques (DLS, UV-Vis, PRLS). We found that, while DMEM elicited the formation of a large time-dependent protein corona, RPMI shows different dynamics with a reduced protein coating. Characterization of these nano-bioentietis was also performed out of the medium solutions, after separation by centrifugation. SDS-PAGE and MS results revealed that the strongly bound proteins quantitatively differ depending on the cellular media and that the average composition of protein corona did not reflect the relative abundance of serum proteins. Finally, to evaluate the biological impact of such hybrid bio-nanostructures, comparative viability assays with two model cell lines, namely HeLa and U937, were carried out in the two media in the presence of 15 nm AuNPs. We observed that RPMI induced proteins/NP complexes exerted higher adverse effects on cells viability than those formed in DMEM. Metallic NPs uptake and fate into cells were tracked by label-free 2-photon confocal microscopy. These results show that, beyond an in depth NPs characterization in their synthesis/storage solutions before cellular experiments, a detailed understanding of the effects exerted by cell culture media on NPs is crucial for the development of standardized procedures for nanotoxicity tests.

A Thermomechanical Model for the Thickness, Stiffness and Poisson's Ratio of Carbon Nanotubes and Graphene

L. Boldrin, F. Scarpa, H. X. Peng, C. D. L. Remillat

Advanced Composites Centre for Innovation and Science, University of Bristol
Bristol BS8 1TR, UK

f.scarpa@bris.ac.uk

We present a thermo-mechanical structural model to describe the influence of the temperature over the thickness and stiffness of single wall carbon nanotubes and graphene sheets. The model is based on the equivalence between the stechiometric potential (based on the UFF model) and the mechanical energies associated to stratching, bending and out-of-plane torsion of deep shear Timoshenko beams for the C-C bonds.

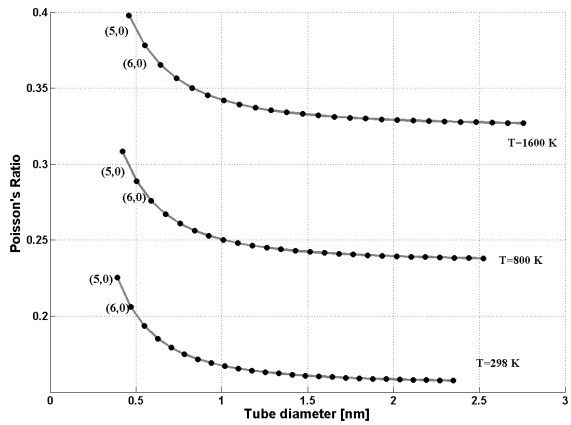

Figure 1: Dependence of the transverse Poisson's ratio in $(n, 0)$ CNTs vs. the tube diameter and temperature

The model allows the identification of the thickness of SWCNTs and graphene for different temperatures, and the derivation of bending and axial force constants in stick-spiral systems [1], taking into account the temperature variation. The results of the model are compared against data from open literature.

References

[1] Chang T, Gao H 2003 *J. Mech. Phys. Solids* **51** (6) 1059–1074

Dopant Concentration Mediated Defects: a Case Study for Activator Dependent Structural and Spectroscopic Properties

P. K. Sharma[1a], G. Żołnierkiewicz[2], N. Guskos[2,3], C. Rudowicz[2], A. C. Pandey[1]

[1] *Nanophosphor Application Centre, University of Allahabad Allahabad 211002, India*

[2] *Institute of Physics, West Pomeranian University of Technology Al. Piastów 17, 70-310 Szczecin, Poland*

[3] *Solid State Physics, Department of Physics, University of Athens Panepistimiopolis, 15 784 Zografos, Athens, Greece*

[a] *prashantnac@gmail.com*

Copper doped ZnO nanoparticles were synthesized by a chemical technique based on a hydrothermal method. The crystallite sizes, estimated by *X*-ray diffraction (XRD), small angle *X*-ray scattering (SAXS) and transmission electron microscopy (TEM) for different doping percentage of Cu^{2+} (1–10%), were found to be in the range of $\approx$ 10–15 nm. Rigaku, RINT2000/PC, a grain size analysis program was used to calculate the size distribution in the samples based on Fankuchen method for the scattering intensity data obtained by SAXS technique. Energy dispersive *X*-rays (EDAX) together with electron paramagnetic resonance (EPR) studies at room temperature (300 K) as well as the temperature dependence of spectra revealed the presence of copper ions in these ZnO nanoparticles, indicating successful doping in the nanocrystals. An analysis of the EPR spectra at room temperature indicated a lower concentration of the isolated Cu^{2+} ions than the Cu nominal one, which could be due to skin depth processes. It appears that some copper (II) ions may form clusters, which would be EPR-silent, so they would strongly influence the reorientation processes of the spin system. The concentration of clusters seems to be the highest for the highest Cu nominal concentration (10%) of the samples. Additionally, the *d*-*d* transitions may influence the spectroscopic properties of the samples. These results are well supported by optical absorption and Fourier transforms infrared (FTIR) studies.

Acknowledgements
Publication of this paper was realised with partial financial support from the budget resources of the West Pomeranian Voivodeship.

Hydrothermal Synthesis and Characterization of $ZnAl_2O_4$ Spinel Doped with Tb^{3+} and Eu^{3+} Obtained in Flow Reactor with Microwave Emission

D. Sibera[1a], E. Wolska[2], R. Jędrzejewski[1], T. Chudoba[3], J. Mizeracki[3], U. Narkiewicz[1], M. Godlewski[2], W. Łojkowski[3]

[1] *Institute of Chemical and Environment Engineering*
West Pomeranian University of Technology
K. Pułaskiego 10, 70-322 Szczecin, Poland

[2] *Institute of Physics, Polish Academy of Sciences*
Al. Lotników 32/46, 02-668 Warsaw, Poland

[3] *Institute of High Pressure Physics, Unipress Polish Academy of Sciences*
Sokołowska 29/37, 01-142 Warsaw, Poland

[a] *dsibera@zut.edu.pl*

Spinels belong to a large family of chemical compounds with a complex structure and important potential application. One of these compounds is zinc – aluminum spinel ($ZnAl_2O_4$) has such interesting properties as: high mechanical resistivity, high thermal stability and low temperature of sintering, which allow it to be used in the ceramic and electronic industry. Interesting physico-chemical properties are attributed to $ZnAl_2O_4$ doped with ions of various chemical elements, mainly transition metals or rare earth elements such as: Co^{+3}, Er^{+3}, Eu^{+3}, Yb^{+3}, Sm^{+3}, Tb^{+3} and Mn^{+3}. Zinc aluminate spinels doped with such elements have excellent luminescence properties. Terbium and europium are some of the most attractive admixtures to powders with luminescent properties.

Nanocrystalline $ZnAl_2O_4$ doped with Tb^{+3} and Eu^{+3} was obtained during a microwave assisted hydrothermal synthesis. Water solutions of $Zn(NO_3)_2 \cdot 6H_2O$, $Al(NO_3)_3 \cdot 9H_2O$, $Tb(NO_3)3 \cdot 5H_2O$ and Eu_2O_3 were used as reactants to synthesize a zinc aluminate spinel. A 2M water solution of KOH was used to precipitate zinc, aluminium and terbium or europium hydroxides. The solution was slowly added until a pH of 10 was reached. The obtained hydroxides were put in a reactor with microwave emission. The microwave assisted synthesis was conducted under a pressure of 3.8 MPa for 30 min. The obtained product was filtered and dried. The phase composition of the samples was determined using *X*-ray diffraction measurements. The XRD analysis confirmed that a $ZnAl_2O_4$ spinel was received. The specific surface area and crystallite size of the nanopowders was determined by the Brunauer-Emmett-Teller (BET) method. The specific surface area of the samples varied from 33 to 204 m^2/g and the mean crystallite size varied from 9 to 60 nm depending on the chemical composition. The morphology of the received materials was characterized using scanning electron microscopy. The photoluminescence effect was examined using a spectrofluorimeter. The measurements were performed in room temperature using the excitation

line of 277 nm. In both series of samples (doped with Tb^{+3} and Eu^{+3}) the $4f$–$4f$ transitions of these ions were observed in the photoluminescence spectra.

Acknowledgements
This work is supported by the European Union within the European Social Fund and the State Budget, in the frame of the project entitled "Investment in knowledge – a driving force of innovation development in the region", coordinated by the Regional Work Office in Szczecin, Poland

The Mini BioArtificiaLiver (BAL): a Cellular Biosensor in the Drug Development Process

F. Somma, D. Berritto, B. Andria,
A. Bracco, N. Landi, R. Grassi

Department of Radiology, Faculty of Medicine and Surgery
Seconda Università degli Studi di Napoli
Napoli, Italy

Purpose: Every year a great amount of financial resources is spent by pharmaceutical companies on unsuccessful Clinical Trials because of poor activity/toxicity ratio, pharmacokinetics and pharmacodinamics accidents, including poor Absorption-Distribution-Metabolism-Excretion/Toxicology profiles.

Considering the key role accomplished by the liver in toxicology and metabolism of drugs, there is a great need for screening tools using hepatocytes. Furthermore the set up of bio-systems using human cells and able to test candidate drugs could be helpful in reducing the use of animals in the experimental testing as well as lowering costs concerning the drug development process.

Methods: In the Center of Biotechnologies of Cardarelli Hospital, in collaboration with the Academic Medical Center of Amsterdam University, we assembled a mini Bioartificial Liver (mini BAL) able to host approximately 300 000 millions of viable human hepatocytes. The mini BAL is a three-dimensional system which resembles the best conditions for hepatocyte culturing and, differently from other monolayer approaches, shows a system-integrated oxygenation addressed to metabolism and respiratory function optimization. Human hepatocytes were obtained by livers discarded from transplantation as well as surgical liver resections. The first steps were aimed to standardize the operating procedures, to set up toxicological protocols and to optimize the biomass in order to ensure homogeneous cell distribution inside the device.

Results: In 2008 a European company gave us the task to study in the miniBAL the hepatotoxicity of a new drug, a conjugated monoclonal antibody, intended for use in multiple myeloma. The miniBAL, charged with 300,000 million viable human hepatocytes (viability $\geq$80%), has been incubated for 6 hours with different molecule's doses and cell function was evaluated up to three days by culturing cells in Williams'E medium.

The hepatotoxicity was evaluated by assessing specific cell functions through urea production, ammonia clearance, oxygen consumption and cell proliferation. We observed a sharp, dose-dependent, decrease in hepatocyte performances with a further restoration of functions. Immunohystological analyses were also performed in order to investigate cell morphology and inflammation or apoptotic indexes.

Conclusions: We propose the use of the mini BAL system as an "hybrid" in the biological scale, between *in vitro* testing and clinical studies of promising compounds for human healthcare.

Finally our report has a paramount significance related to the ethical aspects of preclinical studies. The mini BAL may allow a sensible reduction of the number of animals used in drug testing and a reliable tool for toxicological and pharmacological studies.

7T MRI in Detection of Small Bowel Venous Ischemia: a Rat Model

F. Somma, D. Berritto, C. Cavaliere, S. Russo, N. Landi, R. Grassi

Institute of Radiology, Neurological Sciences Department
Second University of Naples
Piazza Miraglia, 80138, Naples, Italy

Purpose: Acute mesenteric ischemia (AMI) is a potentially fatal vascular emergency with an overall mortality of 60% to 80% and an increasing incidence. The poor prognosis for gut ischemia is partially due to the lack of specific findings, either clinical or radiological, that leads to delayed diagnosis and ineffective treatment. Early diagnosis seems to be the shortest way to reduce the mortality rate. Therefore, the aim of this study is to validate a rat model of acute intestinal ischemia due to a venous occlusion, in which the MR imaging patterns are related to the evolution of intestinal morphodynamism and a histological analysis.

Methods: The study was conducted on 30 *Sprague Dawley* rats. After anaesthesia, a laparotomy was performed and the superior mesenteric vein (SMV) was isolated. Then, the rats were randomly divided into two groups: in the first group ($n = 15$), the "control" animals underwent the SMV occlusion by a tight ligation and, after macroscopical monitoring, the rats were sacrificed at different times and the bowel was removed for a histological analysis; in the second group ($n = 15$), a loop (3-0 gut) was tied loosely around the vessel and the tips were tunnelled from the abdominal cavity through a tube to the posterior cervical area without occluding the vessel. 3 days after surgery, basal MR abdominal scans were collected for each rat using a 7T micro-MR (Bruker Biospec 70/16 US); then the loop was squeezed pulling the external tips in order to occlude the vessel and the MR sessions were repeated after 5 min, 4 and 8 hrs.

Results: The macroscopical monitoring of rats belonging to the first group showed a clear mesenteric vascular congestion at the first time-point (5 min after the ligation of SMV), erosion and frank ulcers with segmental changing in colour and diameter of intestinal loops (*Spastic and Hypotonic Reflex Ileus*) at the second time-point (4 hrs) and worsening of these findings at the third point (8 hrs). Instead, the rats in the second group were scanned using a micro-MR with RARE T2 sequences: no evidence of pathological patterns was detected at the first time-point, while significant bowel wall thickening (>1.5 mm) and mesenteric hyperintensity were found at the following time-points (4 and 8 hrs). After experimentation, the rats were sacrificed and the entire bowel was removed for a histological analysis on hematoxilin-eosin stained sections: vascular congestion in the submucose lamina with no sign of lysis or inflammation was present 5 minutes after ligation (first time-point), while a destruction of

the free portion of the 'villi', the presence of dilated capillaries and inflammatory cells were found at 4 hrs, eventually, a structural destruction of the 'villi' with the sparing of glandular 'criptae', haemorrhage, presence of an inflammatory cell and necrotic material were detected at the third time point.

Conclusion: Compared to the histological analysis and macroscopical evidence, the MR imaging can correctly detect morpho-functional alterations of the ischemic gut. The MR succeeded to identify early the signs of venous mesenteric ischemia already 4 hrs after the SMV occlusion. Its future application in early diagnosis of mesenteric venous ischemia is highly reasonable.

Surface Superconductivity in Electric Field in Two-Band Model

P. Konsin[a], B. Sorkin[b]

Institute of Physics, University of Tartu
Riia 142, 51014 Tartu, Estonia

[a] *konsin@fi.tartu.ee*, [b] *sorkin@fi.tartu.ee*

The influence of the transverse electric field, **E**, on the superconducting transition temperature, T_c, of cuprate films is studied in [1, 2]. The theory [1, 2] considers the bulk properties of superconducting films caused by an external electric field. The surface superconductivity in cuprates in an electric field is investigated [3] on the basis of the one-band Ginzburg-Landau equations in the frames of the BCS theory. The shift of T_c in the electric field in [3] occurs through the DeGennes boundary conditions depending also on the correlation length, ξ, and **E**. The mechanism of high-T_c superconductivity in cuprates is a question of debate. In [4] the two-component theory of superconductivity in cuprates is developed (for a two-band model of superconductivity in MgB_2 see for example [5]) The two-band model is characterized by the two correlation lengths of the Cooper pairs, ξ_1 and ξ_2. These correlation lengths calculated on the basis of various microscopic two-band models [6–8] are real quantities (not imaginary) and $\xi_1 \gg \xi_2$. In our approach the surface superconductivity is considered on the basis of the two-band Ginzburg-Landau equations. The DeGennes boundary conditions in this case depend on ξ_1, ξ_2, **E** and the thickness, L, of films. We have found that T_c lowers or increases in the field **E** (in dependence on the direction of **E**) and can oscillate with thickness L through ξ_2.

Acknowledgements
This work was supported by Estonian Science Foundation Grant No. 7389.

References

[1] P. Konsin, B. Sorkin 1998 *Phys. Rev. B* **58** 5795
[2] P. Konsin, B. Sorkin 2001 *J. Phys. Condens. Mattter* **13** 10031
[3] P. Lipavsky, K. Moravetz et al. 2006 *Phys. Rev. B* **73** 052505
[4] N. Kristoffel, P. Konsin et al. 1994 *Riv. Nuovo Cimento* **17** 1
[5] P. Konsin, B. Sorkin 2004 *Supercond. Sci. Technol.* **17** 1472–1476
[6] Yu. M. Poluektov et al. 1989 *Fiz. Nizkih Temp.* **15** 1259
[7] P. Konsin, B. Sorkin 2006 *Physica C* **435** 16
[8] A. E. Koshelev, A. A. Varlamov et al. 2005 *Phys. Rev. B* **72** 064523

Synthesis and Characterization of New Cadmium and Rare-Earth Molybdato-Tungstates and Their Solid Solutions

E. Tomaszewicz[1a], S. M. Kaczmarek[2], H. Fuks[2]

[1] *Department of Inorganic and Analytical Chemistry*
West Pomeranian University of Technology
Al. Piastów 42, 71-065 Szczecin, Poland

[2] *Institute of Physics, West Pomeranian University of Technology*
Al. Piastów 17,70-310 Szczecin, Poland

[a] *tomela@zut.edu.pl*

Scheelite structure compounds have been of interest because of their luminescent, scintillator and laser host materials. It is well known that $A^{2+}MO_4$ and $A^{1+}A^{3+}(MO_4)_2$ molybdates and tungstates, where $A^{2+} = Ca^{2+}$, Sr^{2+}, Ba^{2+}, Pb^{2+}, Cd^{2+} and Hg^{2+}; $A^{1+} = Li^+$, Na^+, Rb^+ and Cs^+; A^{3+} = rare-earth ion and M = Mo^{6+} or W^{6+} form a scheelite-type tetragonal lattice [1, 2]. In this type of a structure, the A^{1+}, A^{2+} or A^{3+} ions exist as a bisdisphenioid polyhedron with eight oxygen ions, whereas, the molybdenum and tungsten ions are surrounded by four oxygen ions in a tetrahedral site. The similar ionic radii of tetrahedral Mo^{6+} (0.041 nm) and W^{6+} (0.042 nm) may make it possible to prepare solid solutions of the $NaRE(WO_4)_{2-x}(MoO_4)_x$ [3], $LiEu(WO_4)_{2-x}(MoO_4)_x$ type [4].

In our previous papers, we have investigated mutual reactivity in the solid state of cadmium tungstate ($CdWO_4$, a wolframite-type structure) or molybdate ($CdMoO_4$, a scheelite-type structure) with some rare-earth metal tungstates: $RE_2(WO_4)_3$ and $RE_2W_2O_9$ or molybdates: $RE_2(MoO_4)_3$ and RE_2MoO_6 [5–8]. We have synthesized the following scheelite-type compounds and phases: $Cd_{0.25}RE_{0.50}\square_{0.25}WO_4$ [5], $Cd_{0.25}RE_{0.50}\square_{0.25}(MoO_4)_{0.25}(WO_4)_{0.75}$ [8], the $Cd_xRE_{2-2x}(MoO_4)_x(WO_4)_{3-3x}$ solid solutions for $0.50 \leq x < 1.00$ [6] and the $Cd_xRE_{2-2x}(MoO_4)_{2-2x}$ solid solutions for $0.50 \leq x < 1.00$ [7] (Figure 1).

In continuation to our previous studies, we investigated reactivity in the solid state between $CdMoO_4$ and $RE_2W_2O_9$ where RE = Pr, Nd, Sm-Gd. The XRD analysis results of the samples obtained after the last heating cycle of $CdMoO_4/RE_2W_2O_9$ mixtures showed that at the molar ratio of 2 : 1 both reactants reacted to produce a new scheelite-type cadmium and rare-earth metal molybdato-tungstates according to the following equation:

$$2\ CdMoO_{4(s)} + RE_2W_2O_{9(s)} = 4Cd_{0.25}RE_{0.50}\square_{0.25}(MoO_4)_{0.50}(WO_4)_{0.50(s)} + CdO_{(g)}$$

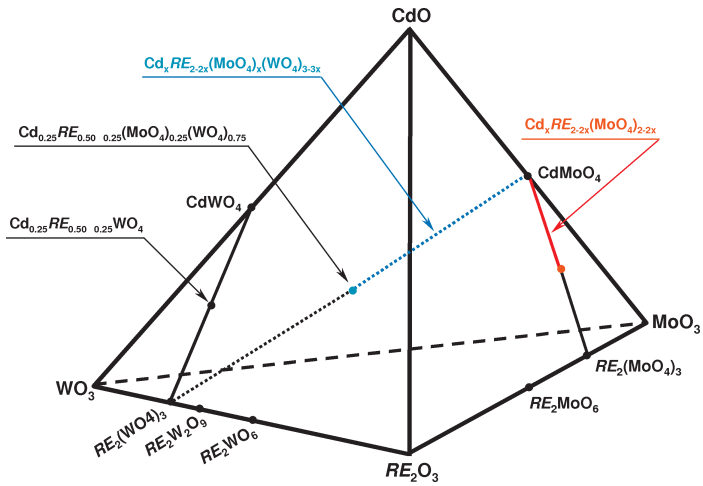

Figure 1: Concentration tetrahedron of CdO-WO_3-RE_2O_3-MoO_3 system

Scheelite-type peaks were found also on powder diffraction patterns of the samples obtained after heating of $CdMoO_4/RE_2W_2O_9$ mixtures comprising initially over 66.67 mol % of $CdMoO_4$. This fact indicated that $Cd_{0.25}RE_{0.50}\square_{0.25}(MoO_4)_{0.50}(WO_4)_{0.50}$ could form scheelite-type solid solutions with $CdMoO_4$. The formula of new solid solutions was $Cd_{9/4x-5/4}RE_{3/2-3/2x}\square_{3/4-3/4x}(MoO_4)_{3/2x-1/2}(WO_4)_{3/2-3/2x}$. The $Cd_{0.25}RE_{0.50}\square_{0.25}(MoO_4)_{0.50}(WO_4)_{0.50}$ phases revealed also a homogeneity region with $RE_2W_2O_9$. This region was located in the range of about 50.00–66.67 mol % of $CdMoO_4$ and its width decreased with a decrease in the RE^{3+} radius. The results of DTA-TG studies showed that the $Cd_{0.25}RE_{0.50}\square_{0.25}(MoO_4)_{0.50}(WO_4)_{0.50}$ phases as well as the obtained solid solutions melted congruently. The obtained phases and some of the solid solutions were characterized by IR, EPR and SEM techniques (Figure 2).

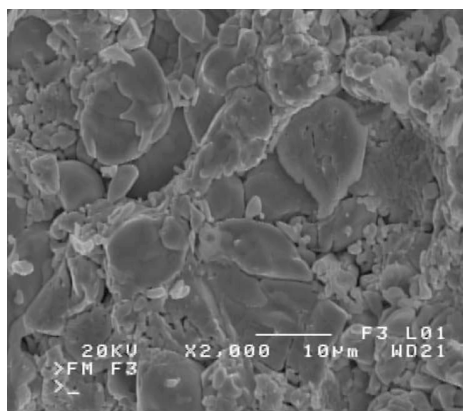

Figure 2: SEM image of the $Cd_{0.25}Gd_{0.50}\square_{0.25}(MoO_4)_{0.50}(WO_4)_{0.50}$ sample

In this study, we explored the thermal expansion of $Cd_{0.25}RE_{0.50}\square_{0.25}(MoO_4)_{0.50}(WO_4)_{0.50}$. The average thermal expansion coefficients along a and c-axes (α_a and α_c) are reported.

Acknowledgements
This work was supported by Research Grant N N209 336937 (2009-2012) from the Polish Ministry of Science and Higher Education.

References

[1] A. A. Kaminskii 1990 *Laser Crystals* Second Ed., Springer, Berlin
[2] A. W. Sleight 1972 *Acta Crystallogr. B* **28** 2899
[3] S. Neeraj, N. Kijima, A. K. Cheetham 2004 *Chem. Phys. Lett.* **387** 2
[4] C. H. Chiu, M. F. Wang, C. S. Lee, T. M. Chen 2007 *J. Solid State Chem.* **180** 619
[5] E. Tomaszewicz, S. M. Kaczmarek, H. Fuks 2009 *J. Rare Earths* **27** 569
[6] E. Tomaszewicz, G. Dąbrowska, S. M. Kaczmarek, H. Fuks *J. Non-Cryst. Solids* under review
[7] E. Tomaszewicz, S. M. Kaczmarek, H. Fuks *Mat. Chem. Phys.* DOI: 10.1016/j.matchemphys.2010.03.052
[8] E. Tomaszewicz, G. Dąbrowska *J. Therm. Anal. Cal.* DOI: 10.1007/s10973-010-0776-y

Electron Paramagnetic Resonance Study of Solid Solutions of MoO_3 in $SbVO_5$

J. Typek[1], E. Filipek[2], G. Żołnierkiewicz[1], N. Guskos[1,3]

[1] *Institute of Physics, West Pomeranian University of Technology*
Al. Piastów 48, 70-311 Szczecin, Poland

[2] *Department of Inorganic and Analytical Chemistry*
West Pomeranian University of Technology
Al. Piastów 42, 71-065 Szczecin, Poland

[3] *Solid State Section, Department of Physics, University of Athens*
Panepistimiopolis, 15 784 Zografos, Athens, Greece

Mixtures of V_2O_5, Sb_2O_4 and MoO_3 oxides as well as other phases formed in the Sb-V-Mo-O system are promising catalysts in selective oxidation of organic compounds, e.g. in the reaction of obtaining acrylonitrile by ammooxidation of propane [1]. In the recent years intensive investigations have been performed aimed at establishing the thermal, electric and other physicochemical properties of these phases [2]. In the present work monophase samples containing a solid solution of MoO_3 in $SbVO_5$ only

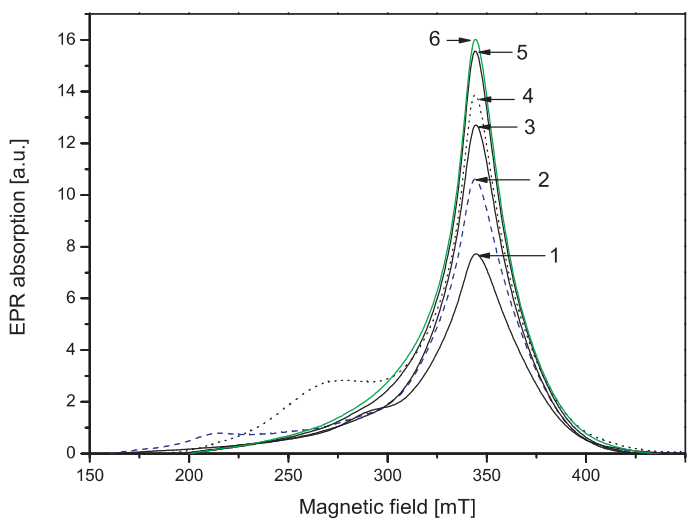

Figure 1: EPR absorption lines registered for samples having the same mass but with different concentration of Mo ions: 1 – 0.73 % mole, 2 – 1.10 % mole, 3 – 1.49 % mole, 4 – 1.89 % mole, 5 – 2.28 % mole, 6 – 2.70 % mole

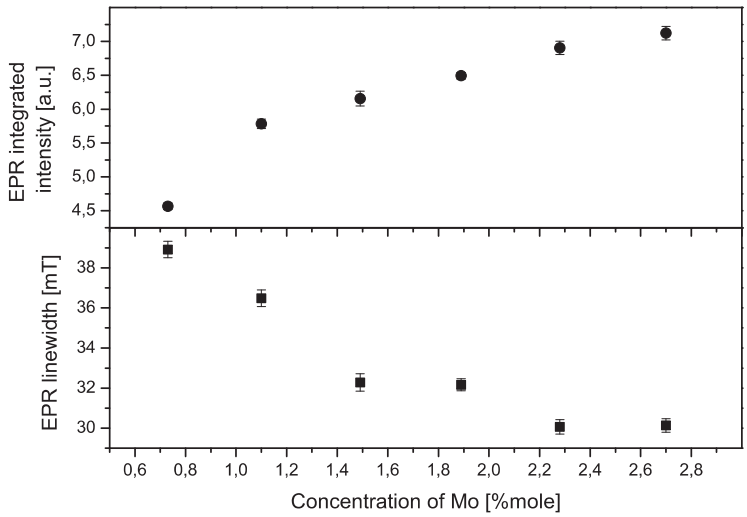

Figure 2: Dependence of EPR integrated intensity (upper panel) and linewidth of unit mass samples (bottom panel) on molar concentration of Mo ions

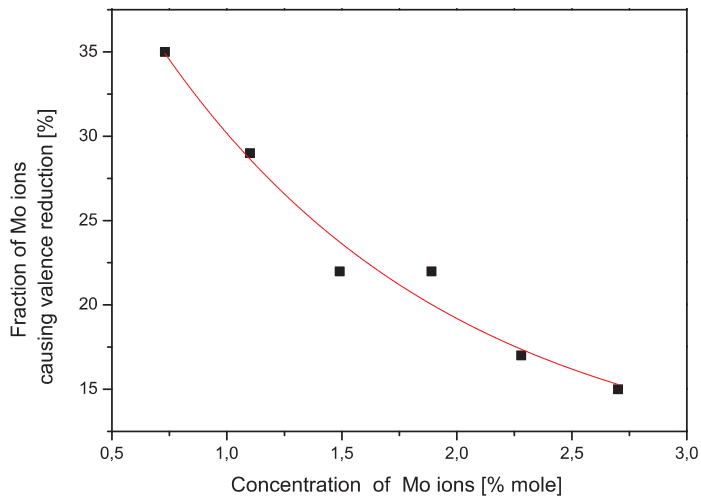

Figure 3: Percentage of Mo ions involved in V^{5+} to V^{4+} valence reduction as a function of total Mo ions concentration in Sb-V-Mo-O solid solution

with the general formula $Sb_{1-6x}\square_x V_{1-6x}\square_x Mo_{10x}O_5$ (for $x = 0.0051$, 0.0077, 0.0104, 0.0132, 0.0159, and 0.018), where $\square$ designates vacancy) were synthesized by using the solid-state reaction method and investigated by the electron paramagnetic resonance (EPR) technique [3].

A recent study has shown that these materials are substitutional solid solutions in which the Mo^{6+} ions are incorporated into the crystal lattice of $SbVO_5$ at both Sb^{5+} and V^{5+} sites, and the compensation of an excessive positive charge occurs mostly through the formation of cationic vacancies at the Sb^{5+} and V^{5+} sites in proportion 1:1 [2]. The EPR study of these compounds aims at detecting V^{4+} and Mo^{5+} paramagnetic ions and calculating their amount in order to discuss the possibility of charge compensation by valence reduction of nominally V^{5+} ions in the $SbVO_5$ lattice. As could be seen in Figures 1 and 2 the EPR signal intensity, attributed to V^{4+} and Mo^{5+} ions and clusters increases with the concentration of Mo ions what is a clear sign of the presence of valence reduction.

A comparison with a reference sample of $VOSO_4 \cdot 5H_2O$ allowed calculating the number of spin centers participating in the resonance and thus estimating the ratio of the Sb^{5+} and V^{5+} vacancies to the V^{4+} paramagnetic centers.

It has been calculated that the percentage of Mo ions involved in the V^{5+} to V^{4+} valence reduction decreases with the total content of Mo ions in the Sb-V-Mo-O solid solution (see Figure 3). This dependence might be roughly described by a decreasing exponential function (solid line in Figure 3).

Acknowledgements
We gratefully acknowledge the financial support of the West Pomeranian Region Office.

References

[1] N. Ballarini, F. Cavani, D. Ghisletti, R. Catani, U. Cornaro 2003 *Catal. Today* **78** 237
[2] E. Filipek 2006 *Solid State Sciences* **8** 577
[3] T. Gron, E. Filipek, H. Duda, S. Mazur, A. W. Pacyna, T. Mydlarz 2009 *J. All. Compd.* **480** 16

Implementation of Method of Fundamental Solutions for Solving Torsion Problem of Rod Made of Functionally Graded Material

A. Uściłowska[a], A. Fraska

Institute of Applied Mechanics, Poznan University of Technology
Piotrowo 3, 60-965 Poznań, Poland

[a] *anita.uscilowska@put.poznan.pl*

This paper describes the application of the Method of Fundamental Solutions to the solution of the torsion of functionally graded rods with hollows. The considered problem is a boundary value problem with a linear second order partial differential equation with variable coefficients and boundary conditions. The proposal of the paper is to solve the problem by a numerical procedure which is combined with the Method of Fundamental Solutions (MFS), approximation by Radial Basis Functions (RBF) and Picard iterations.

From MEMS to Smart Sensors

B. Vigna

STMicroelectronics

The breathtaking growth of the implementation of MEMS into high volume consumer applications, like Mobile Phones, Digital Still Cameras, Gaming Controllers, Laptops, has created a strong and unprecedented demand for smaller, ultra-low power consumption and more advanced system solutions of these sensors.

To meet this demand, the major MEMS suppliers have started to offer systems on a board, systems in a package and integrated single die solutions. iNEMO^{TM} is an STMicroelectronics trademark to mean exactly a smart sensor. The integration of multiple sensors into a package offers a number of advantages including reduced design cycle, increased degrees of freedom enabling a larger number of applications, shorter application development time, reduced number of external components required, higher performance and reliability, reduced cost, easy assembly decreasing the failure rate during the assembly, and smaller size. It also simplifies the supply chain and this represents a big advantage for the customers.

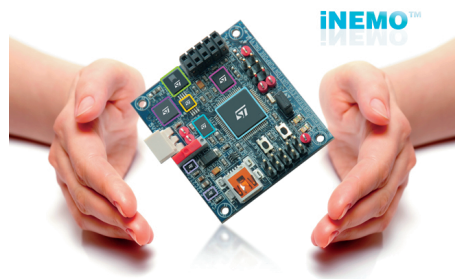

Figure 1: iNEMO

The integrated system solutions in a package can include various components such as accelerometers, gyroscopes, compasses, pressure sensors, temperature sensors, microphones, microcontrollers, interface IC, and connectivity components to wirelessly interface with the outside world. This complexity, however, requires a higher degree of sensor and application expertise to enable the developers to implement the target applications in a timely manner, but also strong manufacturing expertise, especially at assembly and testing level

The integration of multiple sensors into a system allows exciting applications in portable devices, remote controllers, personal navigation systems, advanced video

games, automotive, unmanned aerial vehicles and service robots. But it also enables the wide market adoption of "MEMS around the Human Body".

This presentation discusses the sensor integration starting with a system-on-a-board solution, some of the currently available system-in-a-package solutions, and the trends for future smart sensor system solutions, with a key focus on the market application needs.

First Principle Calculations of Structure and Properties of Small Platinum Clusters

S. Winczewski[1], J. Rybicki[1a,2]

[1] *Department of Solid State Physics, Faculty of Applied Physics and Mathematics*
Gdansk University of Technology
Narutowicza 11/12, 80-233 Gdansk, Poland

[2] *Institute of Mechatronics, Nanotechnology and Vacuum Techniques*
Koszalin University of Technology
Racławicka 5–17, 75-620 Koszalin, Poland

[a] *ryba@pg.gda.pl*

Extensive studies on the structure and properties of small platinum clusters were performed on the basis of the Density Functional Theory. Employing the hybrid search technique, mainly based on a genetic algorithm, numerous stable configurations of clusters consisting of $N = 2$–15 atoms were found. In addition, highly stable structures reported by other authors were carefully reinvestigated.

Small clusters were found to prefer distorted geometries. The postulated magnetism of the investigated systems was confirmed. A quantitative relation between the structure and electrochemical properties of the clusters was established suggesting that the characteristics varied in a fluxional manner. An extensive comparison of our results with those obtained by other groups is presented.

Acknowledgements
The calculations were performed at the TASK Computer Centre (Gdansk, Poland). The work was sponsored by the Polish Ministry of Higher Education and Research, under Grant No. N N519 577838.

Structure and Structural Degradation of Pt and PtCo Nano-Catalysts Supported on Carbon during PEM Fuel Cell Operation: In Situ XAFS

A. Witkowska[1a], G. Greco[2], S. Dsoke[3,4], E. Principi[2], A. Di Cicco[2,5], R. Marassi[3]

[1] *Department of Solid State Physics, Gdansk University of Technology Narutowicza 11/12, 80-233 Gdańsk, Poland*

[2] *School of Science and Technology, Physics Division, University of Camerino via Madonna delle Carceri 9, Camerino (MC), Italy*

[3] *School of Science and Technology, Chemistry Division, University of Camerino via S. Agostino 1, Camerino (MC), Italy*

[4] *ZSW-Zentrum für Sonnenergie und Wasserstoff-Forschung, Helmholtzstraße 8, D-89081 Ulm, Germany (present address)*

[5] *IMPMC-CNRS, Universitè P.et M. Curie, 140 rue de Lourmel, 75015 Paris, France*

[a] *agnieszka@mif.pg.gda.pl*

Understanding the structure and dynamics of nanomaterials as well as their physicochemical properties is currently regarded as a challenging research activity having crucial consequences in the material design for various novel applications. Among them it is nanoparticles of close-packed metals that attract particularly huge interest. Especially, our interest has been focused on the supported metal nanoparticles of a platinum and platinum-based alloy which, due to their catalytic activity, are widely used in the fuel cell technology (especially in a polymer electrolyte membrane fuel cell, PEMFC) [1].

Typical materials for this application are modest quantities (from μg to mg) of nano-particles of a typical size even below 3 nm embedded in a matrix. Therefore, detailed studies of their micro/nanoscopic properties are still relatively difficult to perform, especially when they are under real operating conditions. Therefore, *X*-rays have been recognized as the most suitable probe for *in situ* studies. In particular, *X*-ray absorption spectroscopy (XAS) provides useful complementary information concerning the subtle structural and electronic changes caused by various factors [2], e.g. the electrocatalyst preparation method, FC working conditions, working time (ageing). However, a sophisticated experimental XAS FC set-up is needed to obtain *in situ* high-quality data (for a wide range of *X*-ray energies and metal loading), which could be then safely used for an advanced multiple-scattering extended *X*-ray absorption fine structure (MS EXAFS) analysis, without the risk of data misinterpretation.

In the contribution we present a methodology for an MS EXAFS data-analysis of nanocrystalline [3], applied to high-quality data collected *in situ*, using a specially modified commercial single fuel cell [4]. Detailed results for a few Pt-based electrocatalysts working under various conditions are presented and discussed to demonstrate the efficiency of the XAS FC set-up and correctness of the data analysis [5, 6]. However, the main aim of the present work is to contribute to the shedding light on the processes which govern the structural degradation of carbon supported Pt and PtCo catalysts, one of the factors which strongly limit FC durability [7]. We tested which changes in the microstructure, oxidation and morphology are induced by prolonged use of catalysts in fuel cells. The present study included an accelerated durability test (repetitive step-like potential cycling OCV-0.6 V at 80°C by 50, 100, 150 and 300 hours) as applied for aging the Pt and PtCo catalysts working on the oxygen side in a single PEM FC. Detailed results of combined XRD/HRTEM and multiple-scattering XAFS data analysis (accounting for the degeneracy of two and three-body configurations and the chemical disorder) were used to obtain a robust model of the local structure in a Pt and PtCo nano-alloy as a function of working time. The results revealed that there was an increase in the continuous agglomeration and mean size of particles for the pure Pt catalyst. Whereas, only slight cobalt dissolution and the Pt skin formation during the first aging stage was noted for the PtCo nanocatalyst corroborating higher structural stability of this Pt-based alloy electrocatalyst than pure Pt.

Acknowledgements
We gratefully acknowledge the support of the European Synchrotron Radiation Facility (Grenoble, France) and the Synchrotron Light Laboratory ELETTRA (Trieste, Italy). We would like to thank the BM29 (ESRF) and XAFS 11.1 (ELETTRA) beamlines staff members for assistance during the experiments.

This research has been carried out within the NUME Project "Development of composite proton membranes and of innovative electrode configurations for polymer electrolyte fuel cells" (MIUR, FISR 2003).

References

[1] V. Metha, J. Smith Cooper 2002 *J. Power Sources* **114** 32
[2] A. E. Russell, A. Rose 2004 *Chem. Rev.* **104** 4613
[3] A. Witkowska, A. Di Cicco, E. Principi 2007 *Phys. Rev. B* **76** 104110
[4] E. Principi, A. Di Cicco, A. Witkowska, R. Marassi 2007 *J. Synchr. Rad.* **14** 276–281
[5] A. Witkowska, et al. 2008 *J. Non-Cryst. Solids* **354** 4227–4232
[6] A. Witkowska, et al. 2008 *J. Power Sources* **178** (2) 603–609
[7] R. L. Borup, et al. 2007 *Chem. Rev.* **107** 3904–3951

Nanocrystalline Iron – Thermal Stability and Tuning of Crystallite Size Distribution

R. J. Wróbel

Institute of Chemical and Environment Engineering
West Pomeranian University of Technology
Pułaskiego 10, 70-322 Szczecin, Poland

rwrobel@zut.edu.pl

Nanocrystalline iron was obtained by reduction at 773 K of magnetite doped with structural promoters and characterized by a variety of methods (BET, XRD, TGA, ICP). The crystallite size distribution was determined according to the novel method based on a phenomenon unique for nanomaterials, i.e. the crystallite phase transition dependence on size (Figure 1).

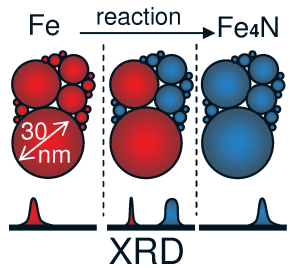

Figure 1: Schematic representation of crystallite phase transition dependence on size. The influence on the XRD peak broadening is presented. The influence on intensity has been neglected

Thermal treatment of nanocrystalline iron under a hydrogen atmosphere at 1073 K revealed that such iron was not thermally stable. The lognormal crystallite size distribution parameters were $d_0 = 15.3$ nm, $\sigma = 0.35$ and $d_0 = 23.5$ nm, $\sigma = 0.17$ for iron treated at 773 K and 1073 K, respectively. The corresponding average crystallite sizes determined from the Scherrer formula were 18 and 24 nm, respectively. The size distributions of the sintered materials clearly showed that thermal stability was a function of the crystallite sizes, i.e. the smallest the crystals, the least thermally stable they were. However, an increase in the contribution of crystallites above 35 nm was not observed. The application of this phenomenon combined with measurement of the crystallite size distribution gives a possibility of fine tuning of the crystallite size distribution.

Sub-Micron Particle based Structures as Reconfigurable Photonic Devices Controllable by External Photonic and Magnetic Fields

A. Shahmoon, Z. Zalevsky

School of Engineering, Bar-Ilan University
Ramat-Gan 52900, Israel

Sub-micron metallic as well as superparamagnetic particles that are incorporated into special structures, may exhibit various interesting properties that may be used for sensing as well as for information manipulation when interacted with photonic radiation. Thus, being applicable as part of reconfigurable photonic devices [1]. It is well known, that at nano scale, materials behave differently compared to larger scale. The resonance wavelength of excitation [2, 3, 4] of nanoparticles strongly depends on their size, geometry, internal morphology, aspect ratio and their dielectric constant. A slight change in the aspect ratio of the nanorod may change dramatically the resonance wavelength of excitation.

In this paper we focus on two types of devices configurations. The first involves metallic nano particles or nano rods incorporated into a semi conducting structured matrix that exhibits strong plasmonic resonance which is dependent on the power of external photonic radiation that is being absorbed by the semiconducting matrix. This spectral shifting of the resonance allows the realizing of (photonic) intensity controllable spectral reflecting structure capable of reflecting another, low power, incident photonic radiation. One example for such fabricated device is demonstrated in Figure 1 (top view SEM image obtained after FIB operation) where the fabrication itself included several stages. At first we evaporated 15 nm of silicon on top of a silica

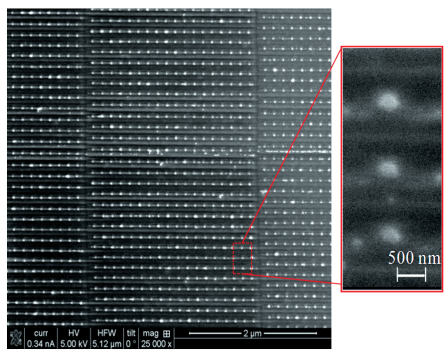

Figure 1: SEM image of the fabricated device

wafer. Right after, 10nm of Au was evaporated again on top of the silicon layer. The next stage was to etch the surface in such a way that an array of nano rods that are made out of two layers (i.e. Au on top of a silicon layer) was generated. Photonic illumination that is being absorbed by the semiconductor varies the effective aspect ratio of the nanorods and thus modifies the resonance wavelength of the excitation. The demonstrated property can be used for the realization of reconfigurable photonic waveguides acting as spectral filters or WDM multiplexers in optics communication links.

The second type of structures that are being described in this paper involve usage of sub-micron superparamagnetic particles embedded into proper structuring grid where, this time, the intensity of an external magnetic field is the one to control the reflectance properties of an incident photonic radiation. Figure 2 presents the superparamagnetic particles while Figure 2a shows the initial state of the magnetic microparticles in the absence of external magnetic field while in Figures 2b and 2c we present the change of their spatial periodicity as function of increased external magnetic field (the field in Figure 2c is 8 times larger than the one of Figure 2b), which directly affects the wavelength being reflected from the structure when illuminated by photonic illumination. Once again the proposed device can be used as photonic reconfigurable filters or WDM multiplexers that are being controlled and reconfigured by external magnetic field.

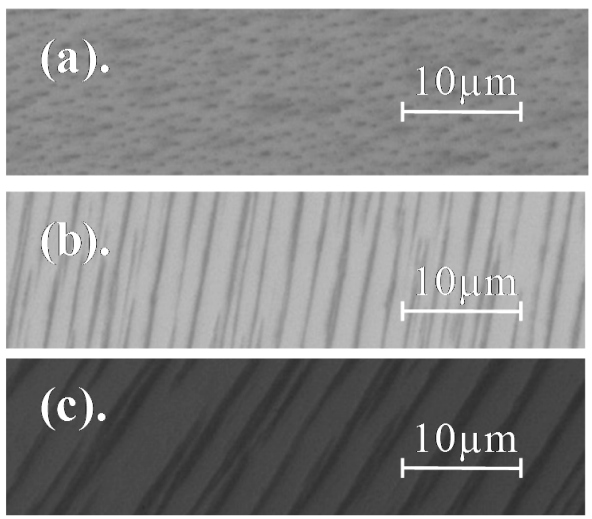

Figure 2: Superparamagnetic micro particles: (a) Microparticles in absence of external magnetic field; (b) and (c) Structure of the microparticles under the influence of increasing external magnetic field

Both types of sub-micron particles based devices can be used for sensing while for the metallic particles structure it is the sensing of photonic radiation and for the case of the superparamagnetic particles based device it is the sensing of external magnetic field.

References

[1] Shahmoon A, Birenboim M, Frydman A and Zalevsky Z, 2010 *Journal of Nanotechnology* **2010** 953212
[2] Eustis S and El-Sayed M A, 2006 *ChemInform* **37** 209–217
[3] Jain P K, Eustis S and El-Sayed M A, 2006 *The Journal of Physical Chemistry* **B 110** 18243–18253
[4] Murphy C J, Gole A M, Hunyadi S E, Stone J W, Sisco P N, Alkilany A, Kinard B E and Hankins P, 2008 *Chemical Communications* **5** 544–557

The Road Ahead for Nanophotonics

N. I. Zheludev

Optoelectronics Research Centre & Centre for Photonic Metamaterials
University of Southampton, Southampton, SO17 1BJ, UK

niz@orc.soton.ac.uk

The next stage of photonic technological revolution will be the development of active, controllable and nonlinear metamaterials surpassing natural media as platforms for optical data processing and quantum information applications.

Metamaterials are artificial media structured on a scale smaller than the wavelength of external stimuli. Conventional materials derive an origin for their electromagnetic characteristics in the properties of atoms and molecules – metamaterials enable us to design our own 'atoms' and thus access new ground breaking functionalities such as invisibility and imaging with unlimited resolution.

The next stage of this technological revolution will be the development of active, controllable and nonlinear metamaterials surpassing natural media as platforms for optical data processing and quantum information applications [1]. Metamaterials are expected to have an impact across the entire range of technologies where electromagnetic radiation is used, and provide a flexible platform for modelling and mimicking fundamental physical effects as diverse as superconductivity and cosmology and for templating electromagnetic landscapes to facilitate observations of otherwise difficult to detect phenomena.

We report an overview on our recent results on achieving new functionalities in nanostructured photonic metamaterials containing nonlinear and active media such as switchable chalcogenide glass, carbon nanotubes, graphene, semiconductor quantum dots and report on exciting plasmonic properties of superconducting metamaterials.

References

[1] N. I. Zheludev 2010 *Science* **328** 582

Herniating Chain Translocation: Approximate Versus Exact Techniques

S. Żurek, M. Kośmider, A. Drzewiński

Institute of Physics, University of Zielona Gora
prof. Szafrana 4a, 65-516 Zielona Góra, Poland

The analysis of polymer translocation through a nanopore is a process that can be modelled with the Rubinstein-Duke [1, 2] rules for hopping reptons along the lattice. The model provides an insight into the chain dynamics where one of the important relations to find is the translocation time dependency on the polymer length (the scaling law). The exact approach to the problem [3] requires evaluation of sparse matrices of enormous sizes (Figure 1) and can be done efficiently only for short chains (a dozen of reptons). On the other hand, approximate Monte Carlo methods [4] allow for an analysis of long chains, however, the conformity of this method and the exact approach have not been reported. The aim of this paper is to compare the MC

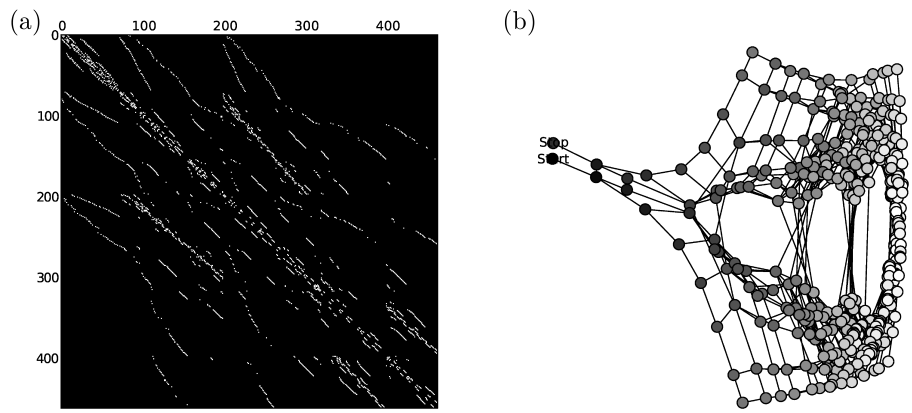

Figure 1: An exact analysis of chain translocation through the pore requires evaluation of the stochastic matrix that holds information on the chain state transitions. Each transition (connection between two chain states) has a probability rate assigned and it is represented in the matrix as a non-zero value.
(a) Sparse stochastic matrix evaluated during translocation time calculations. The plot is made for a chain of length 6. The matrix sparsity factor is 0.01 – the white dots mark non-zero values.
(b) Graph of chain state connections in example chain build of 6 links. Each connection is represented by a transition with a proper probability rate: there are 2562 transitions linking 462 chain configurations in this plot

simulation accuracy to the exact model evaluation for a one- and two-dimensional polymer translocation process.

References

[1] Rubinstein M. 1987 *Phys. Rev. Lett.* **59** 1946–1949
[2] Duke T. A. J. 1989 *Phys. Rev. Lett.* **62** 2877–2880
[3] A. Drzewiński, J. M. J. van Leeuwen 2006 *Phys. Rev. E* **73** 051801
[4] A. van Heukelum, G. T. Barkema 2003 *J. Chem. Phys.* **119** 8197

PART 2

The International Symposium on Trends in Continuum Physics TRECOP 2010

16–20 July 2010, Malta

Modeling and Control of Timing and Spatial-Timing Chaos Using Ordinary and Partial Differential Equations

J. Awrejcewicz

Technical University of Lodz, Department of Automatics and Biomechanics
Stefanowskiego 1/15, 90-924 Łódź, Poland

awrejcew@p.lodz.pl

Lumped and mass distributed mechanical systems governed by nonlinear ordinary differential equations (ODEs) and partial differential equations (PDEs) were studied. In the first case, numerical investigations of ODEs governing the dynamics of a triple physical pendulum with and without rigid limiters of its motion were carried out [1]. Although a single or double pendulum is quite often studied both numerically and experimentally, the triple physical pendulum moving in a plane is rather rarely investigated. There are two aspects of interest in the pendulum dynamics. The first case is that a single pendulum, and in particular coupled pendulums, serve as very rich sources of many interesting phenomena of non-linear dynamics. The second aspect regards the possibility of modeling various natural and technical objects using a system of coupled pendulums. An experimental rig of the triple pendulum with the first body driven periodically was built. A mathematical model composed of three second order strongly non-linear ODEs was derived, and the friction in the pendulum joints was modeled as a composition of dry (Coulomb-like) friction and viscous damping. The model parameters were estimated by matching the output signals from the model and the experiment. Good agreement between both the numerical simulation results and the experimental measurements was obtained and presented. A few chaotic zones were detected and well confirmed by the experiment. The experiment verified positively the boundaries of the particular chaotic windows as well as some qualitative features of chaotic solutions such as performing (or not) full chaotic rotations by individual links. It led to the conclusion that the used triple pendulum mathematical model with its estimated parameters could be applied as a tool for quick searching for various phenomena of nonlinear dynamics exhibited by a real pendulum as well as for explanation of its rich dynamics. It should be noted that due to the way of applying the parameter estimation, the model parameter values were not optimal in the sense of best approximation of real physical values, but rather in the meaning of the best matching of output signals from the model pendulum and the real one.

In the second part of the lecture chaotic and bifurcational vibrations of closed cylindrical shells of an infinite length and circular cross section subject to a transversal local load are studied within the frame of the classical non-linear theories [2]. A transition from PDEs to ODEs was carried out using a higher order Bubnov-Galerkin approach

and the Fourier representation. On the other hand, the Cauchy problem was solved applying the fourth-order Runge-Kutta method. The first static problems of the theory of closed cylindrical shells were studied. The reliability and validity of the obtained results were verified by a comparison with the already published results. Secondly, the stability, bifurcation and chaos of closed cylindrical shells were analyzed. In particular, the influence of the harmonic external load and the control parameters such as the magnitude of pressure measured by an angle of the acting loads, relative linear shell dimension, frequency and amplitude of external transversal load on the shell's non-linear dynamics were studied. This research part presents both a novel approach to analyze the bifurcation and chaos exhibited by vibrated flexible cylindrical shells as well novel results associated with the stability, bifurcation and spatial-timing chaos of the analyzed shells. Particular attention is paid to the verification of the reliability of results while using a higher order Bubnov-Galerkin approach and the Fourier representation. The dynamic stability loss of cylindrical shells is widely described with an emphasis put on the associated problems, which have not been solved appropriately so far and which are related to this important question for both pure and applied scientists. In the case of investigations of closed cylindrical shells subjected to transversal sinusoidal loading it was found that the character of the investigated shell vibrations depended essentially on the loading angle. For small values of the loading angle the total chaos surface was high, whereas an increase in the loading of the cylindrical shell yielded a decrease in the space of chaos, which was shifted into low and middling frequencies. For a large surface of the external load (pressure) the chaotic areas were concentrated on the whole parameters plane (chart) but the largest part was located more in the vicinity of the excitation frequency than in the shell fundamental frequency. The corresponding total surface of the chaotic zone was essentially high. Both the local and global stability loss of the investigated shells was illustrated by numerous figures and tables, and discussed. New scenarios of the transition of the studied shell from harmonic to chaotic ones were detected and illustrated. In addition, passive control of chaotic zones was applied and illustrated.

References

[1] J. Awrejcewicz, B. Supeł, C.-H. Lamarque, G. Kudra, G. Wasilewski, P. Olejnik 2008 *Int. J. Bifurcation and Chaos* **18** (10) 2883–2915
[2] V. A. Krysko, J. Awrejcewicz, N. E. Saveleva 2008 *Int. J. Mech. Sci.* **50** 247–274

Forces Across Sternotomy Closures After Cardiac Surgery

A. Casha[1], A. Manche[1], M. Gauci[1],
M. T. Camilleri Podesta[1], Z. Sant[2], B. Ellul[3], J. N. Grima[3]

[1] *Faculty of Medicine and Surgery, University of Malta*
Msida MSD 2080, Malta

[2] *Faculty of Engineering, University of Malta*
Msida MSD 2080, Malta

[3] *Faculty of Science, University of Malta*
Msida MSD 2080, Malta

auxetic@um.edu.mt

Heart operations require access through an incision in the midline of the chest, called a sternotomy. High pressures within the chest caused by coughing can lead to sternotomy closures breaking down, leading to significant risks of mortality and morbidity. This paper discusses how maximal forces across a sternotomy during coughing can be modelled by considering the chest as a pressure vessel of an ellipsoid shape. Hoop stresses were calculated at different levels of the chest and correlated with differing bone thickness of the sternum at these levels. Computed tomography data of the sternum shows the presence of ridges on the bone. The reduction in the forces in sternotomy closure wires consequent on placement of wires in alternative areas of the sternal bone is discussed. The modelling of the chest as a pressure vessel is discussed in the context of comparative anatomy.

Continuum Models of Binary Systems

J. Burak[1a], Y. Chaplya[1b,2c], M. Cieszko[2d]

[1] *Centre of Mathematical Modeling of Y. S. Pidstryhach Institute of Applied Problems of Mechanics and Mathematics of Ukrainian NAS 15 J. Dudayev Str., 79005 Lviv, Ukraine*

[2] *Institute of Mechanics and Applied Informatics of Kazimierz Wielki University in Bydgoszcz Kopernika 1, 85-064, Bydgoszcz, Poland*

[a] *burak@cmm.lviv.ua,* [b] *chaplia@cmm.lviv.ua,* [c] *czapla@ukw.edu.pl,* [d] *cieszko@ukw.edu.pl*

When describing the mechanical behavior of multi-component solids under certain conditions it is possible to neglect the diffusion migration of body component particles, but it is necessary to take into account their reciprocal local displacements which are considered to be elastic. This situation is characteristic of binary solid solutions where deformation, elastic polarization and heat conductivity are considered. The relative particle displacement of different solution components will be interpreted as elastic polarization.

Two-velocity approach. To each body component at a macroscopic description corresponds a continuum. The law of mass conservation and the balance equation of the components' momentum are given as:

$$\frac{\partial \rho_i}{\partial \tau} + \vec{\nabla} \cdot (\rho_i \vec{v}_i) = 0, \quad \frac{\partial (\rho_i \vec{v}_i)}{\partial \tau} + \vec{\nabla} \cdot (\rho_i \vec{v}_i \otimes \vec{v}_i) = \vec{\nabla} \cdot \hat{\sigma}_i + \rho_i \vec{g}_i + (-1)^i \vec{P}, \quad (i = \overline{1,2}), \quad (1)$$

where ρ_i is the density, $\vec{v}_i$ is the velocity, $\hat{\sigma}_i$ is the Cauchy stress tensor [3]; $\vec{g}_i = -\vec{\nabla}\psi_i$ is the bulk force ($\partial\psi_i/\partial\tau = 0$), ψ_i is the potential; $\vec{P}$ is the interaction force between the continua; $\vec{\nabla}$ is the Hamilton operator, '$\otimes$' is the symbol of tensor product, while the scalar product is designated by a dot.

The balance equations for potential and kinetic energy are derived from equation (1). If they are used in the total energy conservation law, the balance equation of internal energy is obtained in the following form:

$$\frac{\partial (\rho_i u_i)}{\partial \tau} + \vec{\nabla} \cdot (\rho_i u_i \vec{v}_i) = -\vec{\nabla} \cdot \vec{J}_{Qi} + \hat{\sigma}_i : \vec{\nabla} \otimes \vec{v}_i - (-1)^i \vec{P} \cdot \vec{v}_i + (-1)^i e, \quad (i = \overline{1,2}), \quad (2)$$

where u_i is the mass density of internal energy, $\vec{J}_{Qi}$ is the heat flow, e is the energy exchanged locally between the components.

The equilibrium state of a small element is determined by the parameters $T_i - s_i$, $\hat{\tilde{\sigma}}_i - \hat{g}_i$, where T_i is the absolute temperature, s_i is the mass specific entropy, $\hat{\tilde{\sigma}}_i$ and $\hat{g}_i$ are the stress tensor in equilibrium and the metric tensor ($i = \overline{1,2}$), respectively. If

to take into account that in the limit case of $\vec{v}_i \to 0$: $ds_i = dq_{ci}/T_i$ and $\rho_i d_i q_{ci}/d\tau = -\vec{\nabla}\cdot\vec{J}^c_{Qi}$, then, from equation (2) we obtain:

$$\rho_i \frac{d_i u_i}{d\tau} = T_i \rho_i \frac{d_i s_i}{d\tau} + \frac{1}{2}\hat{\tilde{\sigma}}_i : \frac{d_i \hat{g}_i}{d\tau}, \tag{3}$$

where dq_{ci} is the heat obtained by the i^{th} subsystem of a small element, $\vec{J}^c_{Qi}$ is the heat flux, $d_i/d\tau = \partial/\partial\tau + \vec{v}_i\cdot\vec{\nabla}_i$ is the material derivative and $\vec{\nabla}_i$ is the Hamilton operator determined using the kinetic characteristics of component i.

From equations (2) and (3) one obtains the Gibbs' equation [1] and the entropy balance equation:

$$\begin{gathered} du_i = T_i ds_i + \tfrac{1}{2\rho_i}\hat{\tilde{\sigma}}_i : d\hat{g}, \\ \tfrac{\partial(\rho_i s_i)}{\partial\tau} + \vec{\nabla}\cdot(\rho_i s_i \vec{v}_i) = -\vec{\nabla}\cdot\left(\tfrac{\vec{J}_{Qi}}{T_i}\right) + \vec{J}_{Qi}\cdot\vec{\nabla}\left(\tfrac{1}{T_i}\right) - (-1)^i \vec{P}\cdot\tfrac{\vec{v}_i}{T_i} + (-1)^i \tfrac{e}{T_i}. \end{gathered} \tag{4}$$

where $\hat{\sigma}_i = \hat{\tilde{\sigma}}_i$, i.e. non-equilibrium processes related to relaxation of mechanical stress are not considered.

For a physically small element as a whole the entropy balance equation reads as follows:

$$\frac{\partial}{\partial\tau}(\rho_1 s_1 + \rho_2 s_2) + \vec{\nabla}\cdot(\rho_1 s_1 \vec{v}_1 + \rho_2 s_2 \vec{v}_2) = -\vec{\nabla}\cdot\vec{J}_s + \sigma_s, \tag{5}$$

where $\vec{J}_s = \sum_i \vec{J}_{si}$ and $\vec{J}_{si} = \vec{J}_{Qi}/T_i$ are the total entropy flux and entropy fluxes in the subsystems, $\sigma_s = \sum_i \vec{J}_{Qi}\cdot\vec{X}_{Qi} + \vec{P}\cdot\vec{X}_p + eX_T \geq 0$ is the entropy production, $\vec{X}_{Qi} = \vec{\nabla}T_i^{-1}$, $\vec{X}_p = \vec{v}_1 T_1^{-1} - \vec{v}_2 T_2^{-1}$, $X_T = T_2^{-1} - T_1^{-1}$ are the thermodynamic forces conjugated with the flows $\vec{J}_{Qi}$ $(i = \overline{1,2})$, $\vec{P}$ and e. The positive sign of the entropy production is a consequence of the second law of thermodynamics.

The equations of state and kinetic correlations close the set of equations. The state equations are inferred from Gibbs' equation assuming concrete dependence of internal energy $u_i(s_i, \hat{g}_i)$. The kinetic correlations are written down as functional dependences of thermodynamic flows $\vec{J}_{Qi}$ $(i = \overline{1,2})$, $\vec{P}$ and e upon forces $\vec{X}_{Qi}$, $\vec{X}_p$ and X_T, taking into account Onsager and Curie correlations [2].

Single-continuum approach. First of all, as definitions of intercomponent interaction characteristics pose a certain problem, and the properties of the body as a whole or one of its components are often of practical interest, it is also expedient to formulate single-continuum variants of the thermodynamic process description.

In the centroid approximation $\rho\vec{v} = \rho_1\vec{v}_1 + \rho_2\vec{v}_2$, where $\vec{v}$ is the velocity of its points, $\rho = \rho_1 + \rho_2$ is the total density. Then, the laws of mass conservation for separate components and the momentum balance equation can be written as follows:

$$\frac{\partial\rho}{\partial\tau} + \vec{\nabla}\cdot(\rho\vec{v}) = 0, \;\; \rho\frac{dC_1}{d\tau} = -\vec{\nabla}\cdot(\rho_1\vec{w}_1); \;\; \rho\frac{d\vec{v}}{d\tau} = \vec{\nabla}\cdot\hat{\sigma}^* + \rho\vec{g}, \tag{6}$$

where $C_i = \rho_i/\rho$ are the component concentrations $(C_1 + C_2 = 1)$; $\vec{w}_i = \vec{v}_i - \vec{v}$ are the relative component velocities $(i = \overline{1,2})$; $\hat{\sigma}^* = \sum_i \left(\hat{\sigma}_i - \rho_i \vec{w}_i \otimes \vec{w}_i\right)$ is the effective Cauchy stress tensor, $\rho\vec{g} = \sum_i \rho_i \vec{g}_i$ is the total force; $d/d\tau = \partial/\partial\tau + \vec{v}\cdot\vec{\nabla}$ is the material derivative which is defined using the kinematic characteristics of continuum centroid.

The balance equation of internal energy and the corresponding Gibbs' equation are written down in a similar way

$$du = Tds + \frac{1}{\rho}\left(\sigma_1' + \sigma_2'\right) : d\left(\vec{\nabla}_0 \otimes \vec{r}\right)^T + \frac{1}{\rho}\sigma_1' : d\left(\vec{\nabla}_0 \otimes \vec{u}_1\right)^T + \frac{1}{\rho}\sigma_2' : d\left(\vec{\nabla}_0 \otimes \vec{u}_2\right)^T, \quad (7)$$

where $\rho u = \rho_1 u_1 + \rho_2 u_2$ is the specific internal energy, $\sigma_i' = \left(\vec{\nabla} \otimes \vec{r}_0\right)^T \cdot \sigma_i^*$ is the stress tensor having the structure of Piola-Kirchhoff ($i = \overline{1,2}$), $\vec{\nabla}$ and $\vec{\nabla}_0$ are the Hamilton operators in the actual and initial configurations; $\vec{u}_i = \vec{r}_i - \vec{r}$ is the displacement of continuum i particles relative to the points of the centroid continuum.

The values $\vec{r}$, $\vec{u}_1$ and $\vec{u}_2$ are interconnected by the conditions $C_1\vec{u}_1 + C_2\vec{u}_2 = 0$. Choosing new variables $\vec{r}$ and $\vec{w} = \vec{r}_2 - \vec{r}_1$ ($\vec{w}_1 = -C_2\vec{w}$, $\vec{w}_2 = C_1\vec{w}$), the entropy balance equation obtains the following form:

$$\rho\frac{ds}{d\tau} = -\vec{\nabla} \cdot \vec{J}_s + \sigma_{cs}, \quad (8)$$

where $\vec{J}_s = \vec{J}_Q/T$ is the entropy flow, $\vec{J}_Q = \vec{J}_{Q1} + \vec{J}_{Q2} + \sum_i \rho_i u_i \vec{w}_i$ is the resulting heat flux, $\sigma_{cs} = \vec{J}_Q \cdot \vec{X}_Q - \vec{P} \cdot \vec{X}_p \geq 0$ is the entropy production, $\vec{X}_Q = \vec{\nabla}T^{-1}$, $\vec{X}_p = \vec{w}T^{-1}$ are the thermodynamical forces.

It follows from the momentum balace equation for the body components that:

$$\rho\frac{d\vec{w}}{d\tau} = C_2^{-1}\vec{\nabla} \cdot \sigma_2 - C_1^{-1}\vec{\nabla} \cdot \sigma_1 + \rho\left(\vec{g}_2 - \vec{g}_1\right) + \vec{f}_w, \quad (9)$$

where $\vec{f}_w = \rho\vec{w} \cdot \left[\vec{\nabla} \otimes \vec{v} - C_1\vec{\nabla} \otimes (C_1\vec{w}) + C_2\vec{\nabla} \otimes (C_2\vec{w})\right]$ is the force proportional to the displacement velocity $\vec{w}$.

Equation (9) for vector $\vec{w}$ completes the system of correlations necessary for finding all the introduced values. In a similar way the model correlations are obtained in the case when the first component is taken as the basic one and the condition $\rho_1 \gg \rho_2$ is fulfilled.

References

[1] Gibbs J.W., The Collected Works of J.W. Gibbs, v. 1, *Yale University Press*, New Haven, 1948.
[2] Gyarmati I., Non-equilibrium Thermodynamics, *Springer-Verlag*, New York, 1970.
[3] Eringen A.C., Mechanics of Continuum, *John Wiley and Sons*, New York, 1967.

Semi-Analytical Method to Solve an Inverse Problem for Heat Conduction Equation

M. Ciałkowski[a], A. Maćkiewicz[b],
J. A. Kołodziej[c], A. Frąckowiak[d]

Poznan University of Technology
Piotrowo 3a, Poznań, Poland

[a] *michal.cialkowski@put.poznan.pl,* [b] *andrzej.mackiewicz@put.poznan.pl*
[c] *jan.kolodziej@put.poznan.pl,* [d] *andrzej.frackowiak@put.poznan.pl*

The current control of thermal stresses, particularly with significant thermal loading changes, has big influence on the life time of steam turbine casing elements and other power machines. The heat exchange boundary conditions for determining the temperature field are not always known. In such cases we use a measured temperature distribution in chosen points and in chosen times steps. Determining unknown boundary conditions from additional data is an inverse problem in heat conduction. Inverse problems are generally ill-conditioned and require regularization. An important problem is the investigation of the inverse problem stability which permits to determine the propagation of measured errors. In this paper the method of integration of a matrix form of heat equations with respect to time is presented. The number of measured temperature points is limited to two due to the notch phenomenon connected with the construction of a thermoelement. In consequence, one of the dimensional inverse heat condition problems is solved (for a steam turbine casing it corresponds to the real case).

A comparison of the numerical results with the exact solutions will be made in the paper. The influence of different positions of the measured points on the inverse problem stability will be investigated.

Acknowledgements

This work was carried out within the frame of Grant 3143/T02/2007 from the Polish Ministry of Higher Education.

Modeling of Two-Phase Flow in Porous Materials

M. Cieszko

Institute of Mechanics and Applied Computer Science, Kazimierz Wielki University
Kopernika 1, 85-074 Bydgoszcz, Poland

cieszko@ukw.edu.pl

A new macroscopic description of capillary transport of liquid and gas in porous materials is presented in the paper. A three component model is proposed for which the balance equations of mass, linear momentum and energy are formulated. The constitutive relations are derived basing on the balance inequality of the mechanical internal energy and the Langrange multipliers method.

Introduction. In the paper a new macroscopic description of capillary transport of liquid and gas in porous materials is presented. The main point of the theoretical consideration is the refusal of the assumption, commonly accepted in modeling of fluid flow in unsaturated porous materials that, local content of liquid is a unique function of the capillary pressure. The new approach allows description of the inhomogeneity of liquid distribution in quasi static processes. Such approach radically changes description of fluid motion in unsaturated porous materials and their parametric characteristics. Theoretical considerations are based on the concepts of multiphase continuum mechanics. A three component model is proposed for which the balance equations of mass, linear momentum and internal mechanical energy are formulated. Additional equation is obtained as mass balance of liquid in the pressure-space. The constitutive relations are derived basing on the balance inequality of the mechanical internal energy for the whole system and on the Langrange multipliers method.

Basic assumptions and balance equations. It was assumed that liquid and gas filling rigid porous material form continuum composed of four constituents: skeleton, gas, mobile liquid and capillary liquid. The division of liquid into two continua is justified both from kinematical and energetic point of view. The capillary liquid is contained in the thin layer of its internal contact surface with the skeleton. This liquid gathers the whole capillary energy of fluid and is immoveable. It can, however, exchange the mass with the mobile liquid in the vicinity of meniscus surfaces. The mass exchange appears only during their motion in the pore space. The mobile liquid is located in the internal area of liquid surrounded by its internal surface and surfaces of meniscus. Each constituent is characterized by the mass densities and their distributions are defined by parameters of volume content.

The local balance equations of mass and linear momentum for gas, mobile and capillary liquids read as follows:

$$\frac{\partial \bar{\rho}_g}{\partial t} + \operatorname{div}(\bar{\rho}_g \mathbf{v}_g) = 0, \quad \frac{\partial \bar{\rho}_m}{\partial t} + \operatorname{div}(\bar{\rho}_m \mathbf{v}_m) = -\bar{q}, \quad \frac{\partial \bar{\rho}_k}{\partial t} = \bar{\mathbf{q}},$$

$$\bar{\rho}_g \frac{D_g \mathbf{v}_g}{Dt} = \operatorname{div}(\bar{\mathbf{T}}_g) + \pi_g + \bar{\rho}_g g, \quad \bar{\rho}_m \frac{D_m \mathbf{v}_m}{Dt} = \operatorname{div}(\bar{\mathbf{T}}_m) + \pi_m + \bar{\rho}_m g - \bar{q}(\mathbf{w} - \mathbf{v}_m),$$

$$\mathbf{0} = \operatorname{div}(\bar{\mathbf{T}}_k) + \pi_k + \bar{\rho}_k g + \bar{q}\mathbf{w},$$

where $\bar{\rho}_g = f_v \theta_g \rho_g$, $\bar{\rho}_m = f_v \theta_m \rho_m$, $\bar{\rho}_k = f_v \theta_k \rho_k$ and f_v is the volume porosity, whereas θ_g, θ_m, θ_k $(\theta_g + \theta_m + \theta_k = 1)$ stand for volume contents of gas, mobile and capillary liquids in the pore space, respectively. Vector $\mathbf{w}$ denotes velocity of the exchanged mass between mobile and capillary liquids.

Additional balance equation is obtained for quasi static processes of capillary liquid transport in unsaturated porous media. The balance of mass is formulated in the pressure-space taking into account that in such processes capillary pressure plays the similar role as time in the no stationary processes. It takes the form

$$\frac{\partial \theta_k}{\partial p} + \operatorname{div}(\mathbf{q}) = r,$$

where flux $\mathbf{q}$ and source r are constitutive quantities. This equation allows introducing into the model the mechanism of motion of capillary surfaces.

Constitutive relations. The constitutive relations for quantities describing mechanical processes in unsaturated porous materials are derived basing on the balance inequality for the mechanical internal energy of the three-component system. The new approach is proposed similar to that used in the rational thermodynamics based on the entropy inequality analysis and the Lagrange multipliers method. In this approach balance equations of the system are used as constraints imposed on independent constitutive quantities. It was assumed that internal energy of gas, mobile and capillary liquids are unique functions of their mass densities and that content of capillary liquid is a unique function of mobile liquid content.

The obtained constitutive relations are:

- for stress tensors in gas and mobile liquid

$$\bar{\mathbf{T}}_g = -f_v \theta_g p_g \mathbf{I} + \sigma_g(\mathbf{L}_g), \quad \bar{\mathbf{T}}_m = -f_v \theta_m p_m \mathbf{I} + \sigma_m(\mathbf{L}_m);$$

- for volume interaction of gas and mobile liquid with constituents

$$\pi_g = f_v p_g \mathbf{grad}(\theta_g) - R_g \mathbf{v}_g, \quad \pi_m = f_v \big((p_m - p_g) - \beta \frac{D_m \theta_m}{Dt}\big) \mathbf{grad}(\theta_m) - R_m \mathbf{v}_m;$$

- for energies exchanged between mobile and capillary liquids

$$\frac{p_m}{\rho_m} + u_m - \frac{p_k}{\rho_k} - u_k = \alpha \frac{\partial \rho_k}{\partial t}, \quad p_m - p_g + \frac{d\theta_k}{d\theta_m}\big((p_k - p_g) + \alpha \rho_k \frac{\partial \rho_k}{\partial t}\big) = \beta \frac{D_m \theta_m}{Dt}.$$

The parameters α and β are positively definite and characterize dissipation of mechanical energy during the mass exchange between both type of liquids.

For the flux $\mathbf{q}$ modeling mechanism of capillary surfaces motion it is assumed that is proportional to the gradient of capillary liquid content

$$\mathbf{q} = -C(\theta_k, p_k) \mathbf{grad}(\theta_k).$$

Rayleigh Type Wave Propagation in Auxetic Dielectric

A. Drzewiecki

Poznan University of Technology, Institute of Applied Mechanics
Piotrowo 3, 60-965 Poznań, Poland

andrzej.drzewiecki@put.poznan,pl

The problem geometry is shown in Figure 1.

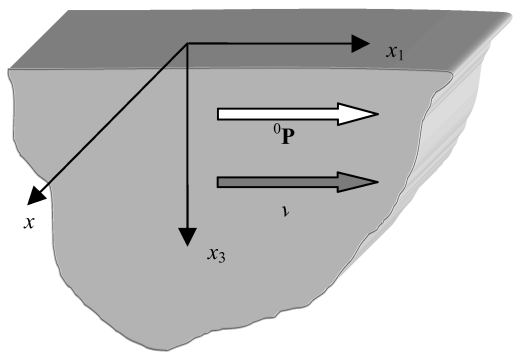

Figure 1: Problem geometry

Initial uniform electric polarization ^{0}P has the direction of the x_1 axis. The propagation of a Rayleigh type surface wave in the same direction is considered:

$$\begin{aligned}\{u_1, u_3, P_1, P_3, B_2\} &= \{\tilde{u}_1(x_3), \tilde{u}_3(x_3), \tilde{P}_1(x_3), \tilde{P}_3(x_3), \tilde{B}_2(x_3)\}\exp[i\gamma(vt - x_1)],\\ \{e_1, e_3, b_2\} &= \{\tilde{e}_1(x_3), \tilde{e}_3(x_3), \tilde{b}_2(x_3)\}\exp[i\gamma(vt - x_1)],\end{aligned} \tag{1}$$

where the symbols used in (1) stand for:

γ – wave number;
v – phase velocity;
u_α – displacement;
P_α – small correction to initial polarization;
B_2 – magnetic induction;
e_α, b_2 – electric field strength and magnetic induction in vacuum.

In this paper the equations of a statistical model (according to K. Hutter and A. Van de Ven classification) of interactions between mechanical and electromagnetic

fields and the method of linearization with respect to some intermediate state were chosen. For editorial reasons (paper volume) it was not possible to present the basic equations of the problem. In Figure 2 the dependence of the dimensionless phase velocity $\sqrt{f}$ ($f = v^2/c_2^2$) on the dimensionless external electric field strength $\sqrt{g}$ ($g = v^2/c_2^2$, $v^2 = P_0^2/\big(\rho_0\varepsilon_0\kappa(1+\kappa)\big)$) for a conventional material is presented.

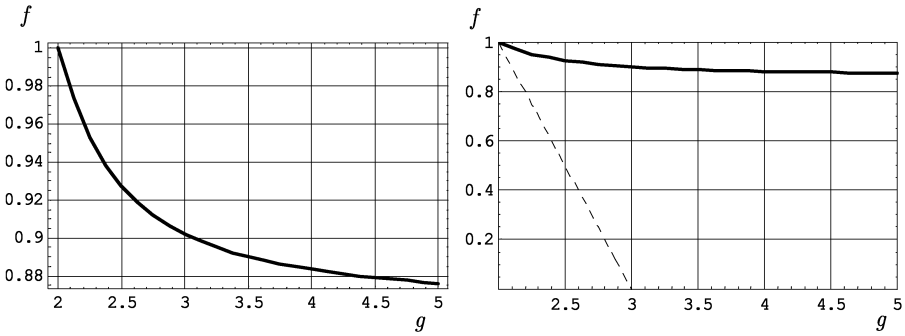

Figure 2: $a = c_1^2/c_2^2 = 3$; conventional material; strong external electric field

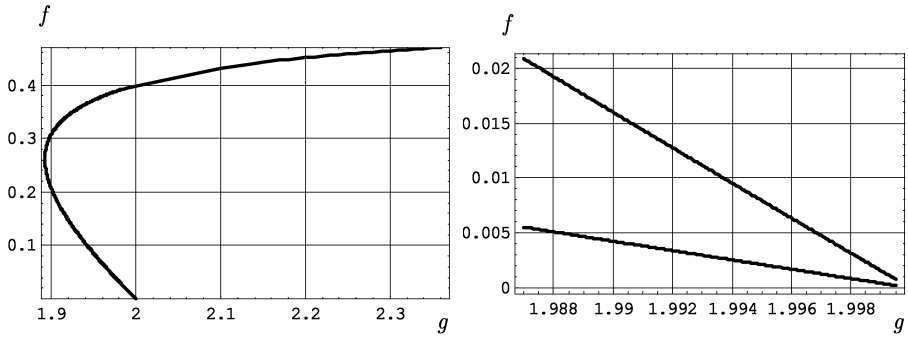

Figure 3: $a = c_1^2/c_2^2 = 1.5$; auxetic material; strong external electric field

A similar dependence for an auxetic is shown in Figure 3. There are three modes of the wave for a strong, external electric field.

Equilibrium Condition in Quotient Space

J. Jankowski

Poznan University of Technology
Piotrowo 5, 60-965 Poznań, Poland

janusz.jankowski@put.poznan.pl

It is necessary to apply forces as a model of interactions. We adopt load as a model of interactions putting against the body [1]. The sum of loads is also the load. Nevertheless, a local character of the load introduces dependence of the sum on the place (point of application) [2]. That is why we suggest a new concept named action. This is an abstraction class in mathematical load quotient space. It allows introducing an equilibrium condition as the balance law in a global form. The local shape can be received by selection of some elements from abstraction classes. It gives new possibilities of applications in engineering problems.

Model of duration. Interval $(0,\tau)$ in space E^1 of real numbers with the Euclidean norm is called the time.

Model of universe. Cartesian product E^3 with the Euclidean norm is called the space.

Model of body. Open set $\Omega \subset E^3$, elements $A \in \Omega$ of which are places, is the region. The set difference $\bar{\Omega}\backslash\Omega$ is called constraints, $\partial\Omega$, while $E^3\backslash\bar{\Omega}$ is called the surroundings, Ω'.

Model of region. If the distance between two places $A, B \in \Omega$ is a constant function of actual instant $t \in (0,\tau)$ and the places do not change the orientation between them at all the region is called a rigid body.

Model of interactions. Load ${}^{A}\langle F, M\rangle$ is defined as a function from the region Ω to a Cartesian product, E^6, where ${}^{A}\mathbf{F}$ is a force and ${}^{A}\mathbf{M}$ is a moment [3].

The sum ${}^{C}\langle H, V\rangle$ of loads ${}^{A}\langle F, M\rangle$ and ${}^{B}\langle G, N\rangle$ is given by:

$$ {}^{C}\mathbf{H} \equiv {}^{A}\mathbf{F} \oplus {}^{B}\mathbf{G}, \quad {}^{C}\mathbf{V} \equiv {}^{A}\mathbf{M} \oplus {}^{B}\mathbf{N} \oplus \mathbf{CA} \times {}^{A}\mathbf{F} \oplus \mathbf{CB} \times {}^{B}\mathbf{G} \tag{1} $$

where the sign $\oplus$ means the vector addition operation. The operation load addition is signed as:

$$ {}^{C}\langle H, V\rangle \equiv {}^{A}\langle F, M\rangle \overset{C}{\longleftrightarrow} {}^{B}\langle G, N\rangle, \quad C \in \Omega \tag{2} $$

The equivalent relation in the load set, Y, is characterized as:

$$ \begin{aligned} &{}^{C}\langle H, V\rangle \Psi {}^{D}\langle H, V\rangle \Leftrightarrow \\ &\qquad {}^{C}\langle H, V\rangle = {}^{A}\langle F, M\rangle \overset{C}{\longleftrightarrow} {}^{B}\langle G, N\rangle \wedge {}^{D}\langle H, V\rangle = {}^{A}\langle F, M\rangle \overset{D}{\longleftrightarrow} {}^{B}\langle G, N\rangle \end{aligned} \tag{3} $$

This relation defines a division of some classes $[H, V]$ named **plots** on the set, Y, of loads. Set $Y_{\langle\rangle}$ of plots is the quotient space [4] with a plot addition operation:

$$ [H, V] = [F, M] \otimes [G, N] \Leftrightarrow {}^{C}\langle H, V\rangle = {}^{A}\langle F, M\rangle \overset{C}{\longleftrightarrow} {}^{B}\langle G, N\rangle \tag{4} $$

Opposite load. For the load, ${}^{A}\langle F,M\rangle$, a load ${}^{B}_{\_}\langle F,M\rangle \equiv {}^{B}\langle P,N\rangle$ is defined that fulfils:

$$ {}^{A}\langle F,M\rangle \overset{C}{\longleftrightarrow} {}^{B}\langle P,N\rangle = {}^{C}\langle 0,0\rangle, \quad C\in\Omega \tag{5}$$

The opposite load has to belong to the plot, $[F,M]$:

$$ {}^{A}\langle F,M\rangle \overset{C}{\longleftrightarrow} {}^{B}\langle P,N\rangle = {}^{C}\langle 0,0\rangle = {}^{B}\langle P,N\rangle \overset{C}{\longleftrightarrow} {}^{D}\langle H,U\rangle, \quad C\in\Omega \tag{6}$$

The plot, $_{\_}[F,M]=[P,N]$, opposite to the $[F,M]$ plot, is defined as a set of loads satisfying (5):

$$ [0,0] = [F,M]\otimes {}_{\_}[F,M] \tag{7}$$

The plot, $_{\_}[F,M]$, is called the **respond** (on plot $[F,M]$).

The sum of the surroundings loads is called the **active load,** the sum of the intersection loads in cut off from constraints, is called the **constraints load,** and the sum of constraints loads is called the **passive load**. The **sub-plot** $[F,M]$ includes active loads as elements, the **constraints plot** includes constraints loads as elements. The sum of the actions of constraints is called the **passive plot**.

Equilibrium condition – global balance

$$ [F,M]\otimes[R,U] = [0,0] \tag{8}$$

The sum of active and passive plots have to be a zero plot. The global equilibrium condition does not depend on the place in the region. It is not only the place but the whole body that is in an equilibrium state. However, the balance law does not contain any integrals. That is why the transition to the local form of the balance law does not require any adoption of an arbitrary small sub-body and continuity of density functions in integrals [5].

Equilibrium condition – local balance

$$ {}^{A}\langle F,M\rangle \overset{C}{\longleftrightarrow} {}^{B}\langle R,U\rangle = {}^{C}\langle 0,0\rangle, \quad C\in\Omega \tag{9}$$

The sum of active and passive loads have to be a zero load. Formally, equation (9) depends on the place in the region. However, the zero load is not susceptible to a change of place. Hence, the local equilibrium condition does not depend on the place in the region. The local form differs from the common static condition in the notation only.

When the body meets with the surroundings on Ω, then there are two passive plots only:

$$ [P,V]\otimes[Q,W] = [0,0] \tag{10}$$

This is an equilibrium condition for the action-reaction law defined on a special kind of the region.

References

[1] J. Jankowski 2004 *Proc. XXI Symp. Vibrations in Physical Systems*, Poznań-Kiekrz
[2] S. Banach 1956 *Mechanika*, PWN Warsaw (in Polish)
[3] J. Jankowski 2003 *Statyka techniczna*, Wyd. Politechniki Poznańskiej, Poznań (in Polish)
[4] K. Maurin 1973 *Analiza*, part I, Elementy, Wydanie drugie, PWN Warsaw (in Polish)
[5] W. Kosiński 1981 *Wstęp do teorii osobliwości pola i fal* PWN Warsaw-Poznań (in Polish)

Impact of Discretization of Rope on Solution Quality

P. Fritzkowski[a], H. Kamiński[b]

Institute of Applied Mechanics, Poznan University of Technology
Piotrowo 3, 60-965 Poznań, Poland

[a] *pawel.fritzkowski@gmail.com,* [b] *henryk.kaminski@put.poznan.pl*

Ropes and other similar bodies (e.g. whips, chains) are usually modelled as continuous systems. This approach seems very natural, however, it leads to a relatively complicated mathematical formulation [1]. On the other hand, a discrete model can be developed by applying methods of analytical mechanics.

In this paper, dynamics of a rope with rheonomic constraints is considered. A discrete elastic-dissipative model with an arbitrary number of members is presented. In some numerical experiments the following problem is analysed: how the discretization density affects the model's behaviour.

We consider the two-dimensional motion of a rope fixed at one end (Figure 1). The system consists of n identical members – rigid prismatic rods of length l and mass m. They are connected by non-ideal joints, involving elasticity and damping. As can be seen, a spring and a viscous damper are combined and placed in every joint. Assuming that all the springs are identical and have stiffness k_T; similarly, the damping coefficient, c, refers to all the dampers.

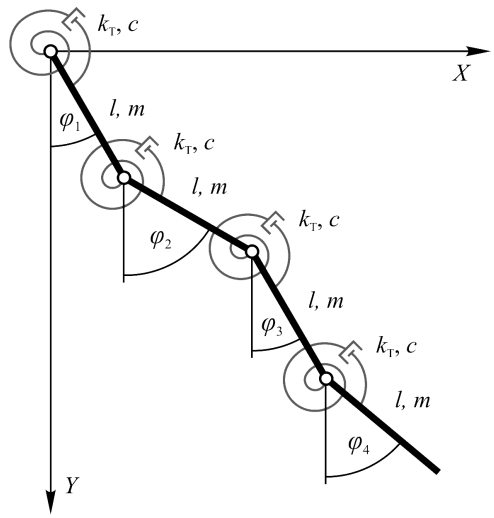

Figure 1: Discrete elastic-dissipative model of rope

In general, the system may be subjected to rheonomic constraints, so that the position of the support depends explicitly on time:

$$x_0 = x_0(t), \quad y_0 = y_0(t).$$

Using the angular generalized coordinates, φ_i $(i = 1, 2, \ldots, n)$, and applying the Lagrange formulation, one can obtain the following equations of motion:

$$\sum_{j=1}^{n} a_{ij}\ddot{\varphi}_j \cos(\varphi_i - \varphi_j) + \sum_{j=1}^{n} a_{ij}\dot{\varphi}_j^2 \sin(\varphi_i - \varphi_j) + \frac{b_i}{l}(\ddot{x}_0 \cos\varphi_i - \ddot{y}_0 \sin\varphi_i) = \frac{1}{ml^2}(Q_i^G + Q_i^T + Q_i^D), \quad i = 1, 2, \ldots, n\,,$$

where a_{ij} and b_i are real coefficients; moreover, Q_i^G, Q_i^T and Q_i^D are the generalized forces resulting from gravity, transverse elasticity and dissipation, respectively [2–4].

In case of a discrete model, the number of elements is crucial. In particular, one could expect that the rope's behaviour converges as the number of segments n is increased. It can be examined in several numerical simulations performed for various values of n.

We focus on a system whose motion is enforced by means of function $x_0(t)$. Due to certain periodic excitation, the elastic-dissipative model can experience quasi-periodic vibrations, which leads to a relatively simple analysis of the dynamics. Differences between a pair of solutions may be evaluated in a finite number of points which are located uniformly along the rope in both cases. Thus, performing numerical experiments for varying n, we are able to assess how the discretization density impacts the quality of motion by comparing the positions of the points, their velocities, etc.

References

[1] Gatti-Bono C., Perkins N. C. 2002 *J. Sound. Vibr.* **255** 555–577
[2] Fritzkowski P., Kaminski H. 2008 *J. Mech. Mater. Struct.* **3** 1059–1075
[3] Fritzkowski P., Kaminski H. 2009 *10th Conference on Dynamical Systems – Theory and Applications* Łódź, 905–912
[4] Fritzkowski P., Kaminski H. 2009 *10th Conference on Dynamical Systems – Theory and Applications* Łódź, 913–918

An Approach to Electromagnetic Wave Propagation in Magnetodielectric Superlattices

J. Kapelewski[a], A. Kawalec

Military University of Technology
S. Kaliskiego, 00-908 Warsaw, Poland

[a] *jerzy.kapelewski@wel.wat.edu.pl*

A phenomenological approach using a modified Green's function method is proposed to polarized electromagnetic (EM) wave propagation in a superlattice composed of piezoelectric and magnetodielectric planar layers. The magnetodielectric (ME) coupling between dielectric and magnetic layers is mediated by mechanical forces.

Acknowledgements
This paper is financed from sources for science in the years 2007-2010 in the frame of ordered scientific project PBZ-MNiSW-DBO-04/I/2007.

Solitary Wave Collisions in Auxetics

P. Kołat[1], B. T. Maruszewski[1a], K. W. Wojciechowski[2]

[1] *Poznan University of Technology, Institute of Applied Mechanics*
Piotrowo 3, 60-965 Poznań, Poland

[2] *Institute of Molecular Physics, Polish Academy of Sciences*
Smoluchowskiego 17, 60-179 Poznań, Poland

[a] *bogdan.maruszewski@put.poznan.pl*

The aim of the paper are computer simulations of solitary wave collisions in auxetic materials. The main property of auxetics is a negative Poisson's ratio.

While colliding with one another during propagation, solitary waves conserve their pulse shape and velocity. They are suitable to be used in nondestructive testing techniques, particularly for heterogeneous and/or composite materials. The paper deals with an analysis of computer simulations of solitary wave collisions.

Method of Fundamental Solutions for Stationary Flow through Fibrous Filter

J. A. Kołodziej[a], P. Fritzkowski[b]

Institute of Applied Mechanics, Poznan University of Technology
Piotrowo 3, 60-965 Poznań, Poland

[a] *jan.kolodziej@put.poznan.pl,* [b] *pawel.fritzkowski@gmail.com*

Liquid filtration and purification systems are widely used in many branches of engineering. Filters can be designed for various types of media: water, oil, fuel, etc. A filter pack which fills the filter housing, plays a key role. In many practical applications, the pack is comprised of some fibrous material.

In this paper, a problem of steady-state incompressible flow through a cylindrical filter is considered. The Laplace type governing equation is solved by means of the Method of Fundamental Solutions (MFS) which provides an approximation of the pressure field. Hence, it is easy to obtain the velocity of the fluid flow and evaluate the total discharge.

We consider a filter whose internal geometry forms a cylinder with radius c and height h (see Figure 1). The filter inlet and outlet size is specified by the radii a and b, respectively. Assume that the fluid is incompressible. It is exposed to pressure p_{in} at the inlet and flows past the fibrous medium within the filter. Finally, the outlet pressure equals p_{out}.

One can treat the fibrous material as an isotropic porous medium and specify the filtration velocity according to Darcy's law in terms of fluid pressure p:

$$q = -\frac{\kappa}{\mu}\,\text{grad}\,p,$$

where κ is the permeability of the medium and μ is the dynamic viscosity of the fluid. Consequently, a continuity equation reduces to the Laplace's equation for p in the cylindrical coordinate system $(r,\,\varphi,\,z)$. Introducing the non-dimensional variables:

$$R = \frac{r}{c}, \quad Z = \frac{z}{c}, \quad A = \frac{a}{c}, \quad B = \frac{b}{c}, \quad H = \frac{h}{c}, \quad P = \frac{p - p_{\text{out}}}{p_{\text{in}} - p_{\text{out}}},$$

and considering the axial symmetry of the problem, the governing equation can be written as:

$$\frac{\partial^2 P}{\partial R^2} + \frac{1}{R}\frac{\partial P}{\partial R} + \frac{\partial^2 P}{\partial Z^2} = 0 \text{ in } \Omega.$$

Additionally, the following conditions must be imposed on the unknown function $P(R,Z)$ on the boundary Γ (see Figure 1): $P=1$ at the inlet, $P=0$ at the outlet, zero normal derivative on the walls and a symmetry condition on the vertical axis (zero normal derivative).

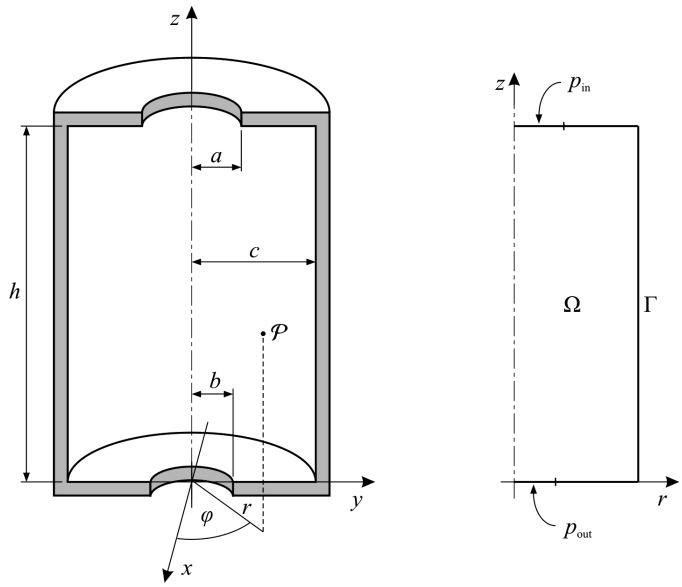

Figure 1: Filter geometry

The resulting boundary value problem is solved by using the MFS. Thus, the pressure field is approximated by a linear combination of the fundamental solutions for the axisymmetric Laplace equation, which are expressed in terms of complete elliptic integrals (see [1, 2]). The combination coefficients are determined simply to ensure fulfilment of the boundary conditions at the selected collocation points. Then, it is easy to evaluate the dimensionless field of pressure and velocity.

To calculate the dimensional quantities, such as p, q or the total discharge, it is necessary to specify the porous medium permeability. Assuming that the arrangement of fibres is random and the porosity coefficient $0.4 \leq \varepsilon \leq 0.8$, one can apply the experimental formula provided by Rahli *et al.* [3].

Special attention is paid to the optimal location of the source points lying on some pseudo-boundary, outside the solution domain. As proposed in [4], the location is determined by numerical minimization of the maximum absolute boundary error.

References

[1] Karageorghis A., Fairweather G. 1999 *Int. J. Numer. Meth. Engng.* **44** 1653–1669
[2] Ramachandran P. A., Gunjal P. R. 2009 *Engineering Analysis with Boundary Elements* **33** 704–716
[3] Rahli O., Tadrist L., Miscevic M. 1996 *AIChE Journal* **42** 3547–3549
[4] Karageorghis A. 2009 *Adv. Appl. Math. Mech.* **1** 510–528

Inverse Determination of Volume Fraction of Fibers in Unidirectionally Reinforced Composite for Given Effective Thermal Conductivity Coefficient

J. A. Kołodziej[a], M. Mierzwiczak[b]

Poznan University of Technology
Piotrowo 3a, Poznań, Poland

[a] *jan.kolodziej@put.poznan.pl*, [b] *magdalena.mierzwiczak@wp.pl*

In the literature the following problems are considered to be classical inverse heat conduction problems: (i) determination of heat sources i.e. [1], (ii) determination of heat transfer coefficient, i.e. [2], (iii) Cauchy problem, i.e. [3], (iv) determination of temperature dependent thermal conductivity, i.e. [4]. The above mentioned problems usually apply to the homogeneous media. In the case of composite materials (nonhomogeneous media) other practically important issues might have to be considered. One of them is the inverse problem of determination of volume fractions of constituents in order to obtain the appropriate effective thermal conductivity.

Let us consider a unidirectional fibrous composite with a regular arrangement of fibers (Figure 1a). If the thermal conductivity coefficients of the constituents and their volume fractions are known, then the composite can be treated as a homogeneous region for which effective thermal conductivity can be determined as a function of known parameters. Currently there are many papers in which the effective thermal conductivity coefficient is determined for a regular arrangement of fibers for given thermal conductivity of constituents and volume fraction of fibers (direct problem). The method of determination is usually based on the solution of heat transfer equation at a microstructure level in a repeated element of an array, i.e. [5].

Our goal is to propose an analytic-numerical algorithm for the determination of the volume fraction of fibers in order to obtain a given value of transverse effective thermal conductivity λ_z (inverse problem). The proposed method is useful for any ratio of thermal conductivity of fibers λ_f to thermal conductivity of matrix λ_m labeled as $F = \lambda_f/\lambda_m$. The fibers are arranged in a regular way according to a square array for which the volume fraction of fibers is given by $\varphi = \pi E^2/4$, where $E = a/b$, a is the radius of fibers and $2b$ is the distance between the center of the neighboring fibers. The perfect thermal contact between the fibers and the matrix is assumed and the steady heat flow is perpendicular to the direction of the fibers.

A unit-cell approach is used to determine the volume fraction of fibers, i.e. the heat flow in the repeated element which consists of one fiber in the matrix is considered. This leads to a 2-D linear boundary value problem in the matrix and fiber regions, with the formulation presented in Figure 1b, where T_f and T_m are the temperature fields in the fiber and matrix regions, respectively. The boundary collocation method

is used [6] to solve this boundary value problem. The approximate solution of the boundary value problem in the fiber and matrix regions, respectively, is assumed in the forms:

$$T_f = 1 + \sum_{k=1}^{N} w_k R^{(2k-1)} \cos[(2k-1)\theta],$$

$$T_m = 1 + \sum_{k=1}^{N} \frac{w_k}{2} \left[(1+F) R^{(2k-1)} + (1-F) \frac{E^{2(2k-1)}}{R^{(2k-1)}} \right] \cos[(2k-1)\theta],$$

where R, θ are the polar coordinates, w_k are the temporary unknown constants, N is the assumed integer.

The assumed forms of solutions not only exactly fulfill the governing equations but also some of the boundary conditions – the conditions marked by the solid lines in Figure 1b.

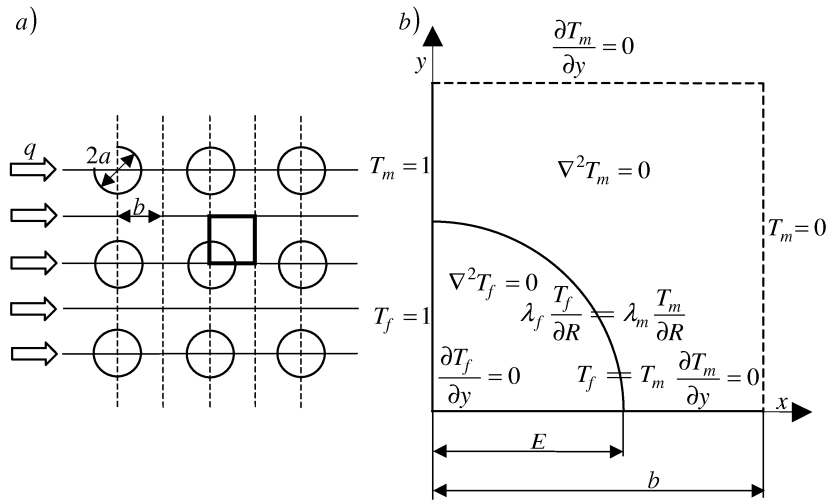

Figure 1: Unidirectionally reinforced fibrous composite with square array fiber arrangement: a) general view, b) formulation boundary value problem in repeated element

Using the boundary condition, $T_m = 0$ for $X = 1$, in the boundary collocation manner in M collocation points (R_j, θ_j) we obtain:

$$F_j(w_k, E) = 1 + \sum_{k=1}^{N} \frac{w_k}{2} \left[(1+F) R_j^{2k-1} + (1-F) \frac{E^{2(2k-1)}}{R_j^{2k-1}} \right] \cos[(2k-1)\theta_j] = 0,$$
$$j = 1, 2, \ldots, M.$$

Similarly, using the boundary condition $\frac{\partial T_m}{\partial Y} = 0$ for $Y = 1$ in M collocation points (R_l, θ_l) we have:

$$F_l(w_k, E) = \sum_{k=1}^{N} \frac{w_k}{2}(2k-1)\left[(1+F)R_l^{2(k-1)}\sin[2(k-1)\theta_l] + (1-F)\frac{E^{2(2k-1)}}{R_l^{2k}}\sin[2k\theta_l]\right] = 0,$$
$$l = 1, 2, \ldots, M.$$

Knowing the value of the effective thermal conductivity we obtain an additional equation:

$$F_{2M+1}(w_k, E) = \sum_{k=1}^{N} \frac{w_k}{2}(-1)^{k+1}\left[(1+F) + (F-1)E^{2(2k-1)}\right] - \frac{\lambda_z}{\lambda_m} = 0.$$

In this way we end up with a system of nonlinear equations with the unknown values of w_1, w_2, …, w_N, E. Choosing $N+1 = 2M+1$ this system is solved by the Newton method and the unknown volume fraction of fibers is determined. The numerical experiments show that this solution provides a very accurate determination of the volume fraction.

References

[1] Yan L., Fu C. L., Yang F. L. 2008 *Engineering Analysis with Boundary Elements* **32** 216–222
[2] Hon Y. C., Wei T. 2004 *Engineering Analysis with Boundary Elements* **28** 489–495
[3] Marin L. 2005 *Int. J. Solids and Structures* **42** 4338–4351
[4] Chantasiriwan S. 2002 *Int. Commun. in Heat and Mass Transfer* **29** 811–819
[5] Han L. S., Cosner A. A. 1981 *J. Heat Transfer* **103** 387–392
[6] Kołodziej J. A., Zieliński A. P. 2009 *Boundary Collocation Techniques and their Application in Engineering* WIT Press, Southampton

Local Gradient Theory of Dielectrics with Polarization Inertia and Irreversibility of Local Mass Displacement

V. Kondrat[a], O. Hrytsyna[b]

Center of Mathematical Modeling
Institute of Applied Problems of Mechanics and Mathematic NASU
15 Dudajev Str., L'viv, 79005 Ukraine

[a] *kon@cmm.lviv.ua,* [b] *gryt@cmm.lviv.ua*

Non-local theories of dielectrics which predict the constitutive relations of an integral type or take into account the body state dependence on the strain gradients, polarization gradient, electric field gradients or higher electric moments, are well known in the literature [1–3]. A new local gradient theory of dielectrics which takes into account the process of local displacement of mass has been proposed in [4]. The irreversibility of the process of local mass displacement has been taken into account in [5]. This work is devoted to the development of the aforementioned theory taking into account the polarization inertia [1] and the irreversibility of processes of local mass displacement and polarization.

Conservation of mass according to [4] can be written as: $\partial\rho/\partial t + \vec{\nabla}\cdot(\rho\vec{v}_* + \vec{J}_{ms}) = 0$, where ρ is the mass density, $\vec{v}_*$ is the velocity of convective mass transport, $\vec{J}_{ms} = \partial\vec{\Pi}_m/\partial t$, $\vec{\Pi}_m$ is the vector of local mass displacement, t is the time. The velocity vector $\vec{v}$ of the center of mass is defined by the relation $\vec{v} = \rho^{-1}(\rho\vec{v}_* + \partial\vec{\Pi}_m/\partial t)$ [3, 4]. Then, the mass balance equation has a typical form: $\partial\rho/\partial t + \vec{\nabla}\cdot(\rho\vec{v}) = 0$.

Assume that the total energy of the system "solid-electromagnetic field" is the sum of internal energy, kinetic $\rho\vec{v}^2/2$ energy, electromagnetic field energy and polarization kinetic energy $\rho d_E(\dot{\vec{p}})^2/2$ [1]. Here $\vec{P} = \rho\vec{p}$ is the polarization vector, d_E is the scalar related to inertia of the polarization process [1] and the dot above the symbol denotes the total time derivative. The total energy change is a result of the convective energy transport through the surface, the work of the surface forces $\hat{\sigma}\cdot\vec{v}$, the heat flux $\vec{J}_q$, the electromagnetic energy flux, the work $\mu\vec{J}_m$ related to the mass transport relative to the center of the body mass, the work $\mu_\pi\partial\vec{\Pi}_m/\partial t$ related to the structure change, and the action of the mass forces and the distributed heat sources. Here $\hat{\sigma}$ is the Cauchy's stress tensor, $\vec{J}_m = \rho(\vec{v}_* - \vec{v})$, μ is the chemical potential, μ_π is the energy measure of the mass displacement influence on the internal energy. Taking into account the mass balance equations, the electromagnetic field entropy and energy, from the balance equation of the total energy we obtain: (i) the following Gibbs equation for generalized Helmholtz free energy f, (ii) the relation for the entropy production σ_s, and (iii) the equation that relates the vectors $\vec{E}^L$, $\vec{E}^r_*$ and $\vec{p}$:

$$df = -sdT + \rho^{-1}\hat{\sigma}_* : d\hat{e} - \vec{p}\cdot d\vec{E}L + \mu'_\pi d\rho_m + \vec{\pi}_m\cdot d(\vec{\nabla}\mu'_\pi)^r, \tag{1}$$

$$\sigma_s = \vec{J}_{e*}\cdot\vec{E}_*T^{-1} - \vec{J}_q\cdot(\vec{\nabla}T)T^{-2} + \rho\dot{\vec{p}}\cdot\vec{E}^i_*T^{-1} - \rho\dot{\vec{\pi}}_m\cdot(\vec{\nabla}\mu'_\pi)^iT^{-1},\ \ \vec{E}^r_* - \vec{E}^L = d_E\ddot{\vec{p}}. \quad (2)$$

Here s is the specific entropy, T is the absolute temperature, $\hat{e}$ is the strain tensor, $\vec{J}_{e*}$ is the electric current density, $\vec{E}^L$ is the local electric field vector [1], $\vec{E}^r_*$, $(\vec{\nabla}\mu'_\pi)^r$ are the reversible and $\vec{E}^i_*$, $(\vec{\nabla}\mu'_\pi)^i$ are the irreversible components [5] of the electric field vector, $\vec{E}_*$, and the vector, $\vec{\nabla}\mu'_\pi$, $\mu'_\pi = \mu_\pi - \mu$, $\vec{\pi}_m = \vec{\Pi}_m/\rho$, $\rho_m = -(\vec{\nabla}\cdot\vec{\Pi}_m)/\rho$, is the specific value of the induced mass density [3], $\hat{\sigma}_* = \hat{\sigma} - \rho(\vec{E}_*\cdot\vec{p} - \rho_m\mu'_\pi - \vec{\pi}_m\cdot\vec{\nabla}\mu'_\pi)\hat{\mathbf{I}}$. Note that equation (2_2) is known as the "balance equation of the intermolecular force" [1]. The constitutive relations are obtained from equations (1) and (2). In particular, for the determination of vectors $\vec{p}$ and $\vec{\pi}_m$ we have such rheological relations as $L^p_d\ddot{\vec{p}} - \rho\dot{\vec{p}} + L^p_p\vec{p} + L^p_\pi\vec{\pi}_m = L^p_T\vec{\nabla}T + L^p_\varphi\vec{\nabla}\varphi + L^p_\mu\vec{\nabla}\mu'_\pi$, $L^\pi_d\ddot{\vec{p}} - \rho\dot{\vec{\pi}}_m + L_{\pi\pi}\vec{\pi}_m + L_{p\pi}\vec{p} = L^\pi_T\vec{\nabla}T + L^\pi_\varphi\vec{\nabla}\varphi + L^\pi_\mu\vec{\nabla}\mu'_\pi$, where φ is the electric potential, other values are the material constants. If we eliminate the local mass displacement vector from these equations we will obtain a differential equation for the polarization vector that will also contain first, second and third time derivatives of the polarization vector: $\mathbf{L}\vec{p} = \mathbf{L}_T\vec{\nabla}T + \mathbf{L}_\varphi\vec{\nabla}\varphi + \mathbf{L}_\mu\vec{\nabla}\mu'_\pi$. Here $\mathbf{L} = \left(L^p_d\frac{d^2}{dt^2} - \mathbf{L}_p\right)\mathbf{L}_\pi + \frac{L^p_\pi L^\pi_p}{\rho_0}\left(\frac{d^2}{dt^2} + 1\right)$, $\mathbf{L}_T = L^p_T\mathbf{L}_\pi + L^\pi_T\frac{L^p_\pi}{\rho_0}$, $\mathbf{L}_\varphi = L^p_\varphi\mathbf{L}_\pi + L^\pi_\varphi\frac{L^p_\pi}{\rho_0}$, $\mathbf{L}_\mu = L^p_\mu\mathbf{L}_\pi + L^\pi_\mu\frac{L^p_\pi}{\rho_0}$, $\mathbf{L}_\pi = \frac{d}{dt} - \frac{1}{\tau_\pi}$, $\mathbf{L}_p = \frac{d}{dt} - \frac{1}{\tau_p}$, τ_p and τ_π are the times of relaxation of the polarization processes and local mass displacement [5]. Therefore, the equations obtained here can be effective for studying quick-change processes.

References

[1] Maugin G. A. 1988 *Continuum Mechanics of Electromagnetic Solids* North-Holland, Amsterdam
[2] Yang J. 2006 *Appl. Mech. Rev.* **59** 335–345
[3] Kondrat V., Hrytsyna O. 2009 *Physico-Mathematical Modelling and Inform. Techn.* **9** 7–46 (in Ukrainian)
[4] Burak Ya., Kondrat V., Hrytsyna O. 2008 *J. Mech. Mat. and Struct.* **3** (6) 1037–1046
[5] Kondrat V. F., Hrytsyna O. R. 2009 *J. Math. Sci.* **160** 492–502

Local State Thermodynamics of Porous Media

J. Kubik[1a], Y. Chaplya[1b,2c], M. Cieszko[1d]

[1] *Institute of Mechanics and Applied Informatics of Kazimierz Wielki University in Bydgoszcz Kopernika 1, 85-064, Bydgoszcz, Poland*

[2] *Centre of Mathematical Modeling of Y. S. Pidstryhach Institute of Applied Problems of Mechanics and Mathematics of Ukrainian NAS 15 J. Dudayev Str., 79005 L'viv, Ukraine*

[a] *kubik@ukw.edu.pl*
[b] *czapla@ukw.edu.pl*, [c] *chaplia@cmm.lviv.ua*
[d] *cieszko@ukw.edu.pl*

Theoretical models of multiphase and multicomponent bodies in the description of processes of deformation, thermal conductivity and diffusion are based, as a rule, on space averaged equations for the balance of mass, impulse and energy and they use applicable constitutive relations.

In most cases, among constitutive relations, there are state equations connecting reciprocally conjugated parameters which give the local body state as well as kinetic equations which connect reciprocally the conjugated thermodynamic force and fluxes [1]. Such a division makes it possible to use concrete dependencies for separate medium phases as well as the known physical laws at formulating the explicit form of constitutive relations for multiphase media.

In this work their analogue was found for a saturated porous consolidated medium, proceeding from the known Gibbs and Euler equations for solid and liquid phases and on the basis of the internal energy additivity. The expressions connected with the porosity change were distinguished in the change of the internal energy of a body as a whole in an explicit form. The linear state equations were obtained and their generalizations for the case of non-linear dependence of the phase concentration was proposed.

At tha macroscopic description the concerned phases are treated as thermodynamical subsystems. We assume that the equilibrium thermodynamical state of separate phases in an element is determined by the following conjugated parameters for the solid phase: $T^s \div \delta S^s$, $\sigma_s^{\alpha\beta} \div \varepsilon^s_{\alpha\beta}$, $\mu^s \div \delta m^s$ and for the liquid phase: $T^f \div \delta S^f$, $P^f \div \delta V^f$, $\mu^f \div \delta m^f$. Here, T^j is the absolute temperature, δS^j is the entropy of phase j; $\sigma_s^{\alpha\beta}$ are the components of the symmetric Cauchy stress tensor, $\varepsilon^s_{\alpha\beta}$ are the deformation tensor components $(\alpha, \beta = \overline{1,3})$; P^f is the pressure in the liquid phase; μ^j are the chemical potentials of j-phase particles $(j = \overline{s,f})$. The conditions $\delta V = \delta V^s + \delta V^f$, $\delta m = \delta m^s + \delta m^f$ are fulfilled for the volume and the mass of this element where δm, δm^j is a mass being in the δV, δV^j volume.

Let us assume that the Gibbs and Euler equations are fulfilled for separate phases [2]. We treat the Gibbs equation as a differential 1-form connecting infinitesimally small

changes of both internal energy δU^j and entropy δS^j at physically small changes of deformation tensor components and separate phases masses while the Euler equation is concerned as an extensive condition of a thermodynamic system.

The following Gibbs equation takes place for the solid phase of the body element which is in a physically small region and the Euler equation is:

$$dU^s = T^s dS^s + \delta V^s \sigma_s^{\alpha\beta} d\varepsilon_{\alpha\beta}^s + \mu_v^s dm^s, \quad \delta U^s = T^s \delta S^s + \frac{\sigma_s}{3}\delta V^s + \mu^s \delta m^s, \qquad (1)$$

where $\mu_v^s = \mu^s + \sigma_s \bar{v}^s/3$ is the chemical potential of particles in the solid phase, σ_s is the first invariant of the Cauchy stress tensor $\hat{\sigma}_s$, $\bar{v}^s = 1/\bar{\rho}^s$ is the true specific volume, $\bar{\rho}^s$ is the true density. It should be noted that a summation is taken with respect to the repeated Greek symbols in all the formulae.

Accordingly, the Gibbs and Euler equation for the liquid phase of the body element is as follows:

$$dU^f = T^f dS^f - P^f dV^f + \mu^f dm^f, \quad \delta U^f = T^f \delta S^f - P^f \delta V^f + \mu^f \delta m^f. \qquad (2)$$

The contribution to the internal energy of particles on the interphase surface is neglected for the infinitesimally small body element. Let us assume that the internal energy, δU, is the sum of internal energies of both phases. Simultaneously, taking into account that the equality of temperatures $T^s = T^f \equiv T$ takes place under thermodynamical equilibrium conditions, we obtain the Gibbs and Euler equations:

$$dU = TdS - P^s dV^s - P^f dV^f + \delta V^s \sigma_d^{\alpha\beta} d\varepsilon_{\alpha\beta}^s + \mu_v^s dm^s + \mu^f dm^f, \qquad (3)$$

$$\delta U = T\delta S - P^s \delta V^s - P^f \delta V^f + \mu^s \delta m^s + \mu^f \delta m^f, \qquad (4)$$

where δS is the entropy for the body element, P^s is the pressure in the solid phase, $\sigma_d^{\alpha\beta}$ is the component of the stress tensor deviator, $\mu_v^s = \mu^s - P^s \bar{v}^s$ is the chemical potential of solid phase particles.

Then, we can introduce the porosity in the explicit form, $\gamma = \lim\limits_{\delta V \to 0} \left(\delta V^f / \delta V\right)$. Taking into account the fact that $\delta V^s = (1-\gamma)\delta V$, $\delta V^f = \gamma \delta V$, $\delta m^s = \bar{\rho}^s \delta V^s = (1-\gamma)\bar{\rho}^s \delta V$, $\delta m^f = \bar{\rho}^f \delta V^f = \gamma \bar{\rho}^f \delta V$, then the equations (3) and (4) are presented as:

$$\begin{gathered} dU = TdS - PdV + \tilde{f}_v \delta V d\gamma + (1-\gamma)\delta V \sigma_d^{\alpha\beta} d\varepsilon_{\alpha\beta}^s + (1-\gamma)\delta V \mu_v^s d\bar{\rho}^s + \gamma \delta V \mu^f d\bar{\rho}^f, \\ \delta U = T\delta S - P\delta V, \end{gathered} \qquad (5)$$

where $P = (1-\gamma) f_v^s + \gamma f_v^f$ is a parameter conjugated to the volume change; $\tilde{f}_v = f_v^s - f_v^f$ is a parameter conjugated to the porosity change; $f_v^s = P^s - \mu^s \bar{\rho}^s$, $f_v^f = P^f - \mu^f \bar{\rho}^f$ are parameters that can be treated as the densities of Helmholtz free energies for the separate phase ($f_v^s = u_v^s - T s_v^s$, $f_v^f = u_v^f - T s_v^f$).

We define the densities of internal energy u_v and entropy s_v of the body element according to the expressions:

$$du_v = T ds_v + \tilde{f}_v d\gamma + (1-\gamma)\sigma_d^{\alpha\beta} d\varepsilon_{\alpha\beta}^s + (1-\gamma)\mu_v^s d\bar{\rho}^s + \gamma \mu^f d\bar{\rho}^f, \quad u_v = T s_v - P. \qquad (6)$$

It should be noted that the magnitude, $-P$, from the last equation (6) can be treated as the density of the Helmholtz free energy for a whole body.

If we define densities for internal energy, u, of the element of two-phase body and entropy s per unit mass, then the equations are:

$$du = Tds - Pdv + v\tilde{f}_v d\gamma + (1-\gamma)v\sigma_d^{\alpha\beta} d\varepsilon^s_{\alpha\beta} + (1-\gamma)v\mu_v^s d\bar{\rho}^s + \gamma v\mu^f d\bar{\rho}^f, \qquad u = Ts - Pv, \tag{7}$$

where $v = 1/\rho$ is the specific volume.

Let the Helmholtz free energy for the medium be f_v by relationship $f_v = u_v - Ts_v$. If it is accepted that $f_v = f_v(T, \gamma, \varepsilon^s_{\alpha\beta}, \bar{\rho}^s, \bar{\rho}^f)$, then we obtain state equations from equations (6) in the form:

$$-s_v = \frac{\partial f_v}{\partial T}, \quad \tilde{f}_v = \frac{\partial f_v}{\partial \gamma}, \quad (1-\gamma)\sigma_d^{\alpha\beta} = \frac{\partial f_v}{\partial \varepsilon^s_{\alpha\beta}}, \quad (1-\gamma)\mu_v^s = \frac{\partial f_v}{d\bar{\rho}^s}, \quad \gamma\mu^f = \frac{\partial f_v}{\partial \bar{\rho}^f}. \tag{8}$$

Assuming the analytical relationship of the Helmholtz free energy from its natural independent arguments we obtained linear state equations and their generalization for non-linear dependence on the concentrations of separate phases (the free energy depends logarithmically on the masses of separate body parts). These equations connect the temperature, porosity, deformation and true phase densities changes and their conjugate parameters, i.e. entropy, interphase difference of specific free energy of phases, stresses and chemical potentials.

References

[1] De Groot S. R., Mazur P. 1962 *Non-Equilibrium Thermodynamics* North-Holland Publ. Comp., Amsterdam

[2] Gibbs J. W. 1982 *Thermodynamics. Statistical mechanics* Nauka, Moscow (in Russian)

On the Strain Dependent Properties of Auxetic Mechanisms

E. Manicaro, E. Chetcuti, J. N. Grima

Faculty of Science, University of Malta
Msida MSD 2080, Malta

Auxetics are materials that have a negative Poisson's ratio i.e. exhibit the unusual characteristic of getting fatter when stretched and thinner when compressed. Several analytical models to explain this behaviour have been proposed whereby the Poisson's ratio as a function of some model parameter for example the hinging angle is derived. Unfortunately this is not in conformity with the Poisson's ratio obtained experimentally whereby the Poisson's ratio as a function of strain is obtained. Here, we propose a numerical method to obtain the Poisson's ratio as a function of strain for analytical models. In particular, we discuss the Poisson's ratio as a function of the model parameters and as a function of strain for different initial configurations of three analytical models.

Waves in Finite Extent Superconductors

B. T. Maruszewski[a], A. Drzewiecki[b], R. Starosta[c]

Poznan University of Technology
Piotrowo 3a, Poznań, Poland

[a] *bogdan.maruszewski@put.poznan.pl,* [b] *andrzej.drzewiecki@put.poznan.pl,*
[c] *roman.starosta@put.poznan.pl*

A magnetic field enters the type – II superconducting body along a discrete arrangement of magnetic vortex lines. In the dynamic case when the magnetic field varies in time, a supercurrent flows around each such a line. Thus, the vortices interact with one another with the help of the Lorentz force forming in this way a new mechanical field of elastic properties. Moreover, those lines arrange themselves in a triangular or quadratic lattice. Such a set is observed, if the intensity of the magnetic field applied to the material is close to its lower limiting value.

The paper aims at investigating the dispersion and amplitude distributions of magnetoelastic waves propagating solely in the vortex field of the superconducting structures: halfspace, layer on halfspace and layer. Our attention was focused on the surface waves and on the influence of the layer thickness on the dispersion features and amplitudes for various wave velocities. The vortex field consists only of soft vortices (the superconducting crystal is free of lattice defects). Some anomalous properties of the vortex dynamics were discussed.

Solving Inverse Unsteady Heat Conduction Problem with Unknown Strength of Continuous Heat Sources

M. Mierzwiczak[a], J. A. Kołodziej[b]

Poznań University of Technology
Piotrowo 3a, Poznań, Poland

[a] *magdalena.mierzwiczak@wp.pl,* [b] *jan.kolodziej@put.poznan.pl*

The method of fundamental solutions (MFS), as one version of the Trefftz method, has become increasingly popular over the last two decades. The majority of applications of this method pertain to elliptic problems. However, some different versions of the method used for parabolic heat transfer problems have appeared in recent years. This paper deals with the inverse determination of the sources function in a 2D transient heat conduction problem. The following 2D boundary-initial-value problem in the square rectangular region, Ω, with the boundary, $\partial\Omega$, is considered:

$$\frac{\partial T}{\partial F}(X,Y,F) = \nabla^2 T(X,Y,F) + b(X,Y,F) \text{ in } \Omega, \tag{1}$$

$$T(X,Y,0) = G(X,Y) \text{ in } \Omega, \tag{2}$$

$$a \cdot Tt(X_B,Y_B,F) + b \cdot \frac{\partial T(X_B,Y_B,F)}{\partial n} = c \text{ on } \partial\Omega, \tag{3}$$

where $T(X,Y,F)$ is the dimensionless temperature, $\nabla^2(\ldots) = \frac{\partial^2(\ldots)}{\partial X^2} + \frac{\partial^2(\ldots)}{\partial Y^2}$ is the Laplace operator, F is the Fourier number, $b(X,Y,F)$ is the unknown dimensionless sources function, $G(X,Y)$ is the specified dimensionless initial temperature distribution, X_B, Y_B are the coordinates of boundary points, n is the outward normal to the boundary, a, b, c are the specified functions of the position.

As the sources function $b(X,Y,F)$ is unknown, the problem given by the equations (1–3) is an inverse problem and requires an additional condition. This extra condition is created by knowing the value of temperature in a few points placed inside the domain:

$$T(X_i,Y_i,F) = T_i, \quad i = 1,2,\ldots,M \text{ in } \Omega. \tag{4}$$

Taking the Laplace transform of the governing equation we obtain a new differential equation in the Laplace transfer domain (the s-domain) which is an inhomogeneous modified Helmholtz equation. This inhomogeneity includes the unknown sources function and the temperature function known from the initial condition. The solution of the modified Helmholtz equation is the sum of the homogeneous solution and the particular solution. The solution of the homogeneous equations is a linear combination of fundamental solutions of the modified Helmholtz equation with unknown coefficients. For the solution of inhomogeneous equations the right hand side function must be interpolated by RBF and polynomials with unknown coefficients. The particular solution has the form of a linear combination particular solution for

RBF and polynomials. The unknown coefficients are determined from a collocation of boundary and additional conditions at each s value. The transformed solution of temperature and of sources must be inverted back to the time domain for each inner point for which we would like to know the temperature. We utilize a relatively accurate method which states that the function of time, $g(t)$, may be approximated by following formula [1]:

$$g(t) = A + B \cdot t + \sum_{j=1}^{N} C_j \cdot e^{-D_j \cdot t} \tag{5}$$

The A, B, C_j, D_j coefficients are evaluated by taking the Laplace transform of Equation (5) and comparing it to the value of the solution for the temperature and the source in the s-domain. In a real domain the temperature $T(X,Y,F)$ and the strength of the source equation $b(X,Y,F)$ are expressed by formula (5) with the obtained adequate value of coefficients.

In order to validate the discussed numerical method, some 2D numerical examples in unit square $\Omega = [0,1] \times [0,1]$, with exact solutions known from literature, are carried out. The simulated experimental data, needed for an inverse analysis to compensate for the unknown conditions, are generated by adding random errors to the exact temperature for the interior of the plate which simulates the measurement error, $U_{\text{meas.}} = U_{\text{ana.}}(1 + \langle -1, 1\rangle \cdot \Delta U)$, where ΔU is the disturbance coefficient. The method accuracy is checked by calculating the maximal relative error $\delta_{\text{MAX}} = \max\{|T_{\text{ana.}} - T_{\text{num.}}|\}/T_{\text{ana.MAX}}$ and the root mean squared relative error $\delta_{\text{SQR}} = \dfrac{1}{T_{\text{ana.MAX}} \cdot NN} \sqrt{\sum_{i=1}^{NN} \left(T_{i,\text{ana.}} - T_{i,\text{num.}}\right)^2}$ for the source and field of temperature in the inner control points.

The proposed algorithm is very accurate when data without measurement errors is considered. The influence of measurement errors of the temperature and source function was investigated in this work, as well. The negative impact of the measurement error can be reduced by using the Tikhonov regularization method based on the SVD with L-curve criterion [2] for choosing the regularization parameter.

References

[1] B. Davies, B. Martin 1979 *J. Comput. Phys.* **33** 1–32
[2] P. Ch. Hansen, D. P. O'Leary 1993 *SIAM J. Comput.* **14** 1487–1503

Hybrid Quantum/Classical Approach for Atomistic Simulation of Metallic Systems

J. Dziedzic[1], M. Bobrowski[1,2], J. Rybicki[1,2,3]

[1] *Faculty of Technical Physics and Applied Mathematics*
Gdansk University of Technology
Narutowicza 11/12, 80-233 Gdansk, Poland

[2] *TASK Computer Centre, Gdansk University of Technology*
Narutowicza 11/12, 80-233 Gdansk, Poland

[3] *Institute of Mechatronics, Nanotechnology and Vacuum Techniques*
Koszalin University of Technology
Racławicka 5–17, 75-620 Koszalin, Poland

The Learn-on-the-Fly (LOTF) method [1] serves to seamlessly embed quantum-mechanical computations within a molecular-dynamics frame-work by continual local re-tuning of the potential's parameters so that it reproduces the quantum-mechanical forces. In its current formulation it is suitable for systems where the interaction is short-ranged, such as covalently bonded semiconductors. We propose a substantial extension of the LOTF scheme to metallic systems, where, due to electronic delocalization, the interaction range is longer and the many-body nature of the potential makes the original LOTF technique impossible to apply. We propose to realize the force optimization stage in a divide-and-conquer fashion and give detailed analysis of the difficulties encountered and the means to overcome them. We show how the technique, which we have termed Divide and Conquer Learn-on-the-Fly (DCLOTF), can be parallelized to utilize several tens of processors. Finally, we present the results of an application of the proposed scheme (utilizing tight-binding for the quantum-mechanical part) to nanoindentation and nanoscratching of copper.

References

[1] G. Csányi et al. 2004 *Phys. Rev. Lett.* **93** 175503

Analysis of the Stress-Strain Distribution within the Spinal Segment

M. Cauchi[1a], Z. Sant[1b], M. Spiteri[2c]

[1] *Department of Mechanical Engineering*
Faculty of Engineering, University of Malta
Msida MSD 2080, Malta

[2] *Mater Dei Hospital, Msida, Malta*

[a] *mcau0010@um.edu.mt,* [b] *zdsant@eng.um.edu.mt,* [c] *michellesp@waldonet.net.mt*

The interest in spine research changed its direction from military based problem to problems related to treatment of various spinal disorders and problems related to degenerative disease or trauma. Various studies have listed pain related to spinal structures as that constituting the majority of the problems when compared to headaches, abdominal pain and chest pain. A recent EU Commission study also suggests that 67 million people suffered pain in their lower or upper back in the week previous to the conducted survey.

The degenerative process accompanying the ageing causes changes in the form and composition of spinal tissues. This results in the back pain particularly in cases such as internal disruption of intervertebral disc or the stress shielding. In case of stress shielding the damaged tissue has decreased ability to resist loading, and tend to be protected by adjacent healthy tissue, as it occur in the lumbar spine.

The spine has a non-linear, elastic behaviour so at lower loads it provides little resistance while to increased load it responds with augmented resistance Therefore, the stability of spine provided by the intervertebral discs, surrounding ligaments and muscles together with the geometry of the vertebral body must be preserved at any situation.

In some situations, the patients would need to undergo surgical treatment which might involve the implantation of a biomedical device. The design of such devices prompts the need for the prior development of reliable computer models together with analytical approaches to investigate the biomechanical deficiencies of pathological spinal segments since the required information are very difficult if not impossible to obtain via *in vivo* measurements. The generation of finite element computational models seems to be the best way to assist the proper understanding of the role played by each anatomical structure of the system and in the same time via computer simulation the prediction of the biomechanical feedback to the designed device can be achieved.

The motion segment consists of two adjacent vertebrae L3 and L4, two phase structure of intervertebral disc and the cartilages at the facet joints modelled as a single-phase structure connective tissue. The material properties of intervertebral disc comprising of annulus fibrousus and nucleus pulpous were varied thus simulating different level of degeneration.

Bilayer and Multilayer Graphene: Mechanical Static and Vibration Properties

F. Scarpa[1], R. Chowdhury[2], S. Adhikari[2]

[1] *NSQI, University of Bristol*
BS8 1TR Bristol, UK

[2] *Multidisciplinary Nanotechnology Centre, Swansea University*
Swansea, UK

We describe the static and dynamic (vibration) properties of bilayer and multilayer graphene sheets simulated using atomistic-continuum models for the C-C bonds and Lennard-Jones potentials of the graphene sheets.

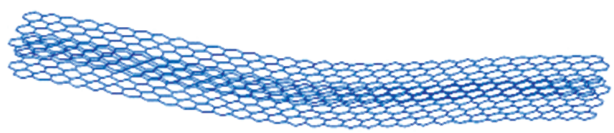

Figure 1: Bilayer graphene sheet under 3-point loading

The bilayer and multilayer sheets are modeled using a hybrid FE approach developed by the Authors in [1]. We extend this approach to predict the coefficients of the 2nd order stress-strain tensor for graphene with multiple layers (from two to eight), and the vibration spectrum of bilayer and multiple layers sheets carrying out a modal analysis using novel condensation techniques validated through a Molecular Mechanics model [2]. The results are benchmarked against data in open literature.

References

[1] Scarpa F, Adhikari S, Chowdhury R, 2010 *Phys. Lett. A* **374** (19–20) 2053
[2] Scarpa F, Chowdhury R, Adhikari S, Kam K, Ruzzene M 2010 *Nanotechnology* (submitted)

Trefftz Functions for Three-Dimensional Wave Equation

M. Sokała

Kielce University of Technology
Faculty of Management and Computer Modelling
Al. Tysiąclecia Państwa Polskiego 7, 25-314 Kielce, Poland

sokala@tu.kielce.pl

It is crucial to the Trefftz method variant presented here to find a system of functions which satisfy the three-dimensional wave equation. Additionally, they can be used as base functions in a modified FEM. An approximate solution of the considered problem is represented in the form of a linear combination of the Trefftz functions. Unknown coefficients of this approximation are calculated by minimization of the functional fitting of the approximate solution to the pre-set conditions. In the paper we present two methods to obtain the Trefftz functions for the three-dimensional wave equation. The first method is connected with a generating function, and leads to recurrent formulas for polynomials and their derivatives [1]. The second method is based on the Taylor series expansion, and uses additionally an inverse Laplace operator [2, 3]. This leads to other forms of the Trefftz wave functions which can be used in the modified FEM.

Consider the dimensionless wave equation:

$$\frac{\partial^2 u}{\partial x^2}+\frac{\partial^2 u}{\partial y^2}+\frac{\partial^2 u}{\partial z^2}=\frac{\partial^2 u}{\partial t^2} \tag{1}$$

One of the concepts of generating the Trefftz functions for equation (1) is based on the Taylor series expansion for function $u(x,y,z,t)$ satisfying (1), namely:

$$u(x,y,z,t)=u(x_0,y_0,z_0,t_0)+\sum_{n=0}^{N}\frac{d^n u(x_0,y_0,z_0,t_0)}{n!}+R_{N+1} \tag{2}$$

Using (1) we transform the right hand side of (2) to eliminate $\frac{\partial^2 u}{\partial t^2}$ and then group other partial derivatives in a specific way. This leads to a sum the coefficients of which are functions satisfying the equation (1). These functions are constructed by inverting the Laplace operator of harmonic functions.

The functions obtained by the above presented method can be transformed to a system of other coordinates by proper, commonly known substitutions.

A general solution of a non-homogeneous wave equation:

$$\frac{\partial^2 u}{\partial x^2}+\frac{\partial^2 u}{\partial y^2}+\frac{\partial^2 u}{\partial z^2}+Q(x,y,z,t)=\frac{\partial^2 u}{\partial t^2} \tag{3}$$

is given by:

$$u(x,y,z,t) = L^{-1}(0) + L^{-1}(Q), \quad L = \frac{\partial^2 u}{\partial t^2} - \frac{\partial^2 u}{\partial z^2} - \frac{\partial^2 u}{\partial y^2} - \frac{\partial^2 u}{\partial x^2} \tag{4}$$

A general solution, $L^{-1}(0)$, of a homogeneous equation is sought as a linear combination of the Trefftz wave functions with unknown coefficients. They are determined by minimization of the functional describing the approximation adjustment (in the mean square sense) to the given boundary and initial conditions. The particular solution is given as a linear combination of polywave functions, obtained by the acting operator, L^{-1}, on the Trefftz wave functions. The formula for $L^{-1}(x^k y^l z^m t^n)$ is given in [1].

The effectiveness of the presented method is tested on simple examples describing the direct and inverse problems under the three-dimensional wave equation. They show good accuracy for an approximate solution with the Trefftz functions as the base functions. Moreover, an unquestionable advantage of wave polynomials is the fact that they do not yield any restrictions for the shape of the area, thus, the method can be applied to more complicated shapes.

References

[1] Maciąg A. 2005 *Mathematical Problems in Engineering* **5** 583–598
[2] Ciałkowski M., Frąckowiak A. 2003 *Współczesne Problemy Techniki. Studia i Materiały* Wydawnictwo Uniwersytetu Zielonogórskiego, Zielona Góra **3** 7–69 (in Polish)
[3] Sokała M. 2004 *Doctoral thesis* Poznań (in Polish)

Kinematically Excited Dynamical Systems Near Resonances – Asymptotic Analysis

R. Starosta[1a], G. Sypniewska-Kamińska[1b], J. Awrejcewicz[2c]

[1] *Poznan University of Technology*
Piotrowo 3a, 60-965 Poznań, Poland

[2] *Technical University of Lodz, Department of Automatics and Biomechanics*
Stefanowskiego 1/15, 90-924 Łódź, Poland

[a] *roman.starosta@put.poznan.pl*
[b] *grazyna.sypniewska-kaminska@put.poznan.pl,* [c] *awrejcew@p.lodz.pl*

Nonlinear dynamical problems are solved numerically by most researchers due to their complexity. The application of such techniques allows obtaining the time history of the system, however, in this way, we cannot ask for its qualitative changes, such as resonance conditions, modulations etc. During last years many authors have developed some analytical methods adequate to those problems [1, 2]. It is especially asymptotic methods that are suitable to treat nonlinear systems, also near resonances [3]. The paper concerns investigations of nonlinear dynamics of two-degree of freedom systems with kinematic excitation. And it is particularly their behaviour near resonances that is tested.

We adopt an asymptotic method of a multiple scale in order to perform analytical calculations. The tested model is a spring pendulum hanged on a moving point. The point is moving harmonically and independently in two mutually perpendicular directions. It causes its motion along the Lissayou curve.

The system studied is presented in Figure 1a. The motion is planar, and X and φ are the generalized co-ordinates. The pendulum is loaded by the external force, $F(t) = F_0 \cos\Omega_1 t$, and the moment, $M(t) = M_0 \cos\Omega_2 t$. Moreover, linear viscous damping is assumed.

The governing equations of the system in the non-dimensional form are as follows:

$$\ddot{z}(\tau) + c_1\dot{z}(\tau) - \big(1+z(\tau)\big)\big(\dot{\varphi}(\tau)\big)^2 + z(\tau) + w^2\big(1-\cos(\varphi(\tau))\big) - r\,p^2\cos(\tau\,p - \varphi(\tau)) = f_1\cos(p_1\tau), \tag{1}$$

$$\big(1+z(\tau)\big)^2\ddot{\varphi}(\tau) + \big(c_2 + 2\big(1+z(\tau)\big)\,\dot{z}(\tau)\big)\,\dot{\varphi}(\tau) + w^2\sin(\varphi(\tau))\big(1+z(\tau)\big) - r\,p^2\big(1+z(\tau)\big)\sin(\tau\,p - \varphi(\tau)) = f_2\cos(p_2\tau), \tag{2}$$

where $L = L_0 + \frac{mg}{k}$, $z = \frac{Z}{L}$, $r = \frac{R}{L}$, $\omega_1^2 = \frac{k}{m}$, $w = \frac{\omega_2}{\omega_1}$, $\omega_2^2 = \frac{g}{L}$, $c_1 = \frac{B_1}{m\omega_1}$, $c_2 = \frac{B_2}{mL^2\omega_1}$, $f_1 = \frac{F_0}{mL\omega_1^2}$, $f_2 = \frac{M_0}{mL^2\omega_1^2}$, $p_1 = \frac{\Omega_1}{\omega_1}$, $p_2 = \frac{\Omega_2}{\omega_1}$, $p = \frac{\Omega}{\omega_1}$, $\tau = \omega_1 t$.

L denotes the length of the statically stretched pendulum at $\varphi = 0$, m is its mass, k denotes the spring stiffness, g is the gravitational acceleration, B_1 and B_2 are the

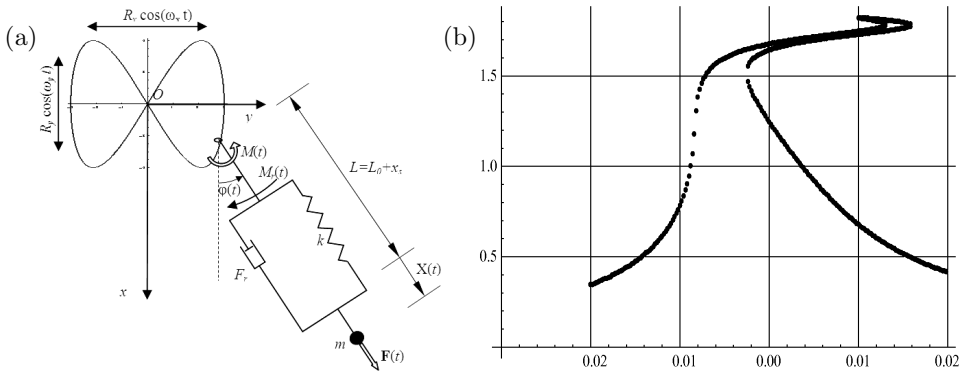

Figure 1: (a) Two degree of freedom system with kinematic excitation; (b) Frequency response function for two co-existing resonances, for chosen parameters

viscous coefficients. The equations (1)–(2) should be supplemented by adequate initial conditions.

The dimensionless equations of motion were introduced and successfully solved with the multiple scale method. General solutions, including the third order of approximation, were achieved in an analytical form. Dimensionless solutions are universal and valid for many systems of the same scale of similarity. Frequency response functions are obtained for various kinds of simultaneously occurring resonances. The example of an amplitude curve versus the detuning parameter is presented in Figure 1b.

References

[1] Gendelman O. V., Gorlov D. V., Manevitch L. I., Musienko A. I. 2005 *J. Sound Vib.* **286** 1–19
[2] Zhu S. J., Zheng Y. F., Fu Y. M. 2004 *J. Sound Vib.* **271** 15–24
[3] Awrejcewicz J., Starosta R. 2010 *MESA* **1** (1) 81–90

Asymptotic Solutions and Resonance Responses for 3-DOF Planar Physical Pendulum

G. Sypniewska-Kamińska[1a], R. Starosta[1b], J. Awrejcewicz[2c]

[1] *Poznan University of Technology*
Piotrowo 3, 60-965 Poznań, Poland

[2] *Technical University of Lodz*
Stefanowskiego 1/15, 90-924 Łódź, Poland

[a] *grazyna.sypniewska-kaminska@put.poznan.pl*
[b] *roman.starosta@put.poznan.pl,* [c] *awrejcew@p.lodz.pl*

The dynamical behaviour of a harmonically excited and linear damped 3-dof system is investigated in the paper. The system consists of a rigid body of mass, m, suspended at point A on a massless and linear spring, whose other end is fixed at point O as is shown in Figure 1. The point C is the mass centre of the body. Let $S = AC$ denote the eccentricity. The dynamical extension of the spring, Z, and the angles, φ and ψ, are used as the generalized coordinates. The external excitations, i.e. the force, $F(t) = F_0 \cos(\Omega_1 t)$, the moment, $M_\varphi(t) = M_2 \cos(\Omega_2 t)$, and the moment, $M_\psi(t) = M_3 \cos(\Omega_3 t)$ are taken into consideration. The pendulum motion is damped by the viscous force, $C_1 \dot{Z}$, and two linear moments, $C_1 \dot{\varphi}$ and $C_3 \dot{\psi}$.

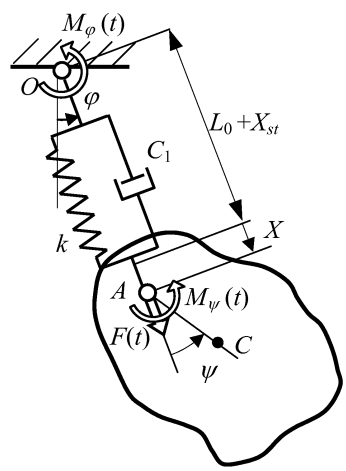

Figure 1: Physical spring pendulum

Applying the Lagrange equations we obtain the motion equations. They have the following dimensionless form:

$$\ddot{z}(\tau)+c_1\dot{z}(\tau)+w_1^2 z(\tau)+1-\cos\big(\varphi(\tau)\big)-\big(1+z(\tau)\big)\big(\dot{\varphi}(\tau)\big)^2+s\sin\big(\varphi(\tau)-\psi(\tau)\big)- s\cos\big(\varphi(\tau)-\psi(\tau)\big)\big(\psi(\tau)\big)^2=f_1\cos(p_1\tau),$$

$$\big(1+z(\tau)\big)^2\ddot{\varphi}(\tau)+c_2\dot{\varphi}(\tau)+\big(1+z(\tau)\big)\Big(\sin\big(\varphi(\tau)\big)+2\dot{z}(\tau)\dot{\varphi}(\tau)\Big)+ s\big(1+z(\tau)\big)\Big(\sin\big(\varphi(\tau)-\psi(\tau)\big)\big(\dot{\psi}(\tau)\big)^2+\cos\big(\varphi(\tau)-\psi(\tau)\big)\ddot{\psi}(\tau)\Big)=f_2\cos(p_2\tau),$$

$$\ddot{\psi}(\tau)+c_3\dot{\psi}(\tau)+w_3^2\sin\big(\psi(\tau)\big)+ w_3^2\big(1+z(\tau)\big)\Big(\sin\big(\varphi(\tau)-\psi(\tau)\big)+\cos\big(\varphi(\tau)-\psi(\tau)\big)\ddot{\varphi}(\tau)\Big)- w_3^2\big(1+z(\tau)\big)\sin\big(\varphi(\tau)-\psi(\tau)\big)\big(\dot{\varphi}(\tau)\big)^2+2w_3^2\cos\big(\varphi(\tau)-\psi(\tau)\big)\dot{z}(\tau)\dot{\varphi}(\tau)= f_3\cos(p_3\tau),$$

where $L=L_0+mg/k$, k denotes the spring stiffness, L_0 is its length, when it is unstretched, g is the gravitational acceleration, $\omega_1^2=k/m$, $\omega_2^2=g/L$, $\omega_3^2=Sg/I_A^2$, I_A is the radius of the body inertia with respect to the axis, which passes through point A and is perpendicular to the plane of motion:

$$z=Z/L,\quad s=S/L,\quad \tau=\omega_2 t,\quad w_1^2=\omega_1^2/\omega_2^2,\quad w_3^2=\omega_3^2/\omega_2^2,$$

$$c_1=\frac{C_1}{m\omega_2},\quad c_2=\frac{C_2}{Lm\omega_2},\quad c_3=\frac{C_3S}{I_A^2Lm\omega_2},\quad f_1=\frac{F_0}{Lm\omega_2^2},\quad f_2=\frac{M_2}{L^2m\omega_2^2},\quad f_3=\frac{M_3}{m\omega_2^2I_A^2},$$

$$p_1=\frac{\Omega_1}{\omega_2},\quad p_2=\frac{\Omega_2}{\omega_2},\quad p_3=\frac{\Omega_3}{\omega_2}.$$

The above presented equations describing the dynamical behaviour of the pendulum are solved by the multiple scales method (MSM).

The behaviour of the nonlinear system can be very complicated, especially near the resonance, when several resonances will occur simultaneously. The MSM application allows determining the condition under which external and internal resonances occur in the system. The differential equations of amplitude and phase modulation were obtained for several combinations of simultaneously occurring external resonances. The equations were solved numerically due to their very complex form. The amplitude responses as function of detuning parameters were received taking into account the steady-state conditions.

References

[1] Lee W. K, Park H. D. 1997 *Nonlinear Dynamics* **14** 211–229
[2] Sado D., Gajos K. 2008 *J. of Theoretical and Applied Mechanics* **46.1** 141–156
[3] Starosta R., Sypniewska-Kamińska G., Awrejcewicz J. 2009 *Dynamical Systems Theory and Applications – 10^{th} Conference* 581–588

Mesh-Free Method Based Numerical Experiment for Estimation of Torsional Stiffness of Long Bone

A. Uściłowska[a], A. Fraska[b]

Poznan University of Technology
Piotrowo 3, Poznań, Poland

[a] *anita.uscilowska@put.poznan.pl,* [b] *agnieszka.fraska@put.poznan.pl*

The external loads acting on the long bone could cause fractures in the bone. A fracture is any break in the bone or in the cartilage. It is usually a result of trauma but can be due to an acquired bone disease such as osteoporosis or abnormal bone formation in a congenital disease of the bone such as osteogenesis imperfecta.

Fractures are classified by their nature and location. Examples of the classification include "spiral fracture of the femur," "greenstick fracture of the radius," "impacted fracture of the humerus," "linear fracture of the ulna," "oblique fracture of the metatarsal," "compression fracture of the vertebrae," and "depressed fracture of the skull." A "comminuted fracture" is a fracture in which the bone is broken into a number of pieces, as distinguished from a "compound fracture" in which the bone sticks through the skin. The problem discussed in this paper is the twisting of the lone bone which can cause a spiral fracture of the long bone (see Figure 1).

Figure 1: Spiral fracture (Ref. [3])

There are some papers in the literature treating the problem of torsional stiffness of the long bone. Comparative studies of the long bone biomechanics in primates frequently use the polar moment of inertia as a variable reflecting the overall mechanical rigidity, average bending rigidity, or resistance to torsional shear stresses. The authors of [1] show that while the use of this variable for characterizing the first two properties is appropriate, it is potentially a highly misleading measure of the torsional resistance. The theoretical and experimental results of the research show that the use of the polar moment of inertia for estimating long bone torsional rigidity should be restricted to samples of relatively invariant and/or cylindrical geometry. The subject of the paper is the open section effect in the long bone with a longitudinal defect [2]. The authors of [2] say that a longitudinal defect dramatically alters the stress distribution within the long bone. For the applied torsion, the defect interrupts the normal shear flow around the bone. The problem is solved by Finite Element Method.

The bone in a living animal consists of both the living tissue and non-living substances. There are blood vessels, nerves, collagen, and living cells including: osteoblasts (cells that help form the bone), and osteoclasts (cells that help eat away the old bone) in the "living bone".

In addition, the bone contains cells called osteocytes which are mature osteoblasts that have ended their bone-forming careers. The nonliving, but very important substances in the bone are minerals and salts. In addition to the metabolically active cellular portion of the bone tissue, the bone is also made up of a matrix (bonding of multiple fibers and chemicals) of different materials, including primarily collagen fibers and crystalline salts. The crystalline salts deposited in the bone matrix are composed principally of calcium and phosphate which are combined to form hydroxyapatite crystals. In particular, it is the collagen fibers and the calcium salts that help to strengthen the bone. In fact, the collagen fibers of the bone have great tensile strength (the strength to endure the stretching forces), while calcium salts, which are similar in terms of physical properties to marble, have great compressional strength (the strength to endure the squeezing forces). These combined properties, plus the degree of bondage between the collagen fibers and the crystals, provide a bony structure that has both extreme tensile and compressional strength.

Due to such a complicated structure the bone is treated as an object made with a Functionally Graded Material (FGM). FGMs are materials with continuously varying material properties designed for specific engineering and bioengineering applications.

An algorithm based on the method of Fundamental Solution is proposed as a procedure for solving the considered problem. The results of the numerical experiment and the discussion will be presented in the full text version and during the Symposium presentation.

References

[1] Daegling D. J. 2002 *J. Human Evolution* **43** 229–239
[2] Elias J. J., Frassica F. J., Chao E. Y. S. 2000 *J. Biomechanics* **33** 1517–1522
[3] Pierce M. C., Bertocci G. E., Vogeley E., Moreland M. S. 2004 *Child Abuse and Neglect* **28** 505–524

Objective Gradient Elasticity

P. Ván

Department of Theoretical Physics, KFKI, RIPNP
1525 Budapest, Konkoly Thege Miklós u. 29–33., Hungary

Department of Energy Engineering
University of Technology and Economics
Budapest, Hungary

MONTAVID Thermodynamic Research Group
Budapest, Hungary

vpet@rmki.kfki.hu

A constitutive theory of continuum physics is a theoretical approach to find macroscopic material models. The two most important basic principles are the frame independence of constitutive functions – material frame indifference – and the Second Law of thermodynamics. At the same time these are the most problematic and discussed concepts of material modelling.

Our spacetime model based investigations led to an improved formulation of the objectivity (compared to the classical formulation of Noll) [1–3], and a representation of finite deformation kinematics that is unique and based on evolutionary differential equations.

In a parallel and related research we developed a method to understand the thermodynamic compatibility of gradient (weakly nonlocal) extensions of classical field theories. Our method is based on the Liu procedure [4] and applied to gradient elasticity in the Noll objective Piola-Kirchoff framework [5].

In this presentation we show, how these developments can be combined to form a theory of finite deformation continuum mechanics, where the consequences of the Second Law are derived with the help of an objective Liu procedure, where material frame indifference is automatically fulfilled.

References

[1] Frewer M. 2009 *Acta Mechanica* **202** 213–246
[2] Matolcsi T., Ván P. 2006 *Phys. Lett. A* **353** 109–112
[3] Matolcsi T., Ván P. 2007 *J. Math. Phys.* **48** 053507–19
[4] Ván P. 2005 *Periodica Polytechnica Ser. Mechanical Engineering* **49/1** 79–94
[5] Ván P., Papenfuss C. 2010 – under publication in *Proceedings of the Estonian Academy of Sciences*

Application of Mechanical Model of Cervical Spine Assessing Changes Caused by Degenerative Disease

T. Walczak[1a], B. T. Maruszewski[1b], R. Jankowski[2c], M. Chudzicka-Adamczak[3d]

[1] *Institute of Applied Mechanics, Poznan University of Technology*
Piotrowo 3, 60-965 Poznań, Poland

[2] *Clinic of Neurosurgery and Neurotraumatology*
Poznań University of Medical Sciences
Przybyszewskiego 49, 60-355 Poznań, Poland

[3] *Polytechnic Institute, Higher Vocational State School in Piła*
Podchorążych 10, 64-920 Piła, Poland

[a] *bogdan.maruszewski@put.poznan.pl*, [b] *tomasz.walczak@put.poznan.pl*
[c] *klinikanch@op.pl*, [d] *martachudzicka@wp.pl*

A degenerative disease consists of faster usage and degeneracy of tissues creating a joint. It usually appears with elderly people, however, it may also happen to younger people. This disease leads to an improper conformation of the spine what leads to a wrong distribution of loads, and finally, to pain, deformation of vertebrae or neurological deficits.

In the paper, the authors focused on the cervical spine and examining the basic mechanical parameters of the bone structure of the spine subject to improper loads caused by the degenerative disease.

The object of the study are appropriately parameterised cervical spines of patients affected by a degenerative disease after intervertebral disc removal. The influence of the conformation change on the load changes and, in effect, on the distribution of tensions and displacements in the vertebra body occurring with patients who were operated is analysed.

The data used for the analysis comes from X-ray photos. It is a basis to create an individualized mechanical model of a cervical spine considering the patient's weight, vertebra geometry and spinal conformation. There are different approaches possible as the vertebra body is made of two substances. In the paper, the authors applied a model which is the closest to reality which means that they treated the body as heterogeneous and, as has been already mentioned, as consisting of two substances. A simplification was also introduced which meant omitting the trabecular bone transferring a tiny part of the loads in comparison to the cortical bone of the body. This model was used to determine the field of the stress fields for the anterior and posterior surfaces of the bodies of the vertebrae from C_2 to C_7. Every vertebra was treated as an elliptical beam with an elliptical hollow.

In the paper, the values of normal tensions on the anterior and posterior surfaces of the bodies of the vertebrae from C_2 to C_7 measured in the middle of the heights of the vertebrae bodies for two cervical spine conformations for a group of 30 patients before and after cage stabilization are presented. The parameters such as vertebrae body centre coordinates, vertebrae body diameters (characteristic measurements) were taken from the X-ray images of the patients. What is more, the value of force S (the vertical component force of the net force of muscles) was determined based on the data considering the moment of the cervical muscle forces [4–6], while the material parameters of the bone tissue were taken from the literature. It can be noticed that owing to the changes in the geometry, the distribution of tensions in the vertebrae bodies changed.

References

[1] Mrozowski J., Awrejcewicz J. 2004 *Fundamentals of Biomechanics* Wydawnictwo Politechniki Łódzkiej, Łódź (in Polish)
[2] Gzik M. 2007 *Biomechanics of Human Spine* Wydawnictwo Politechniki Śląskiej, Gliwice (in Polish)
[3] Zielnica J. 1996 *Strength of Materials* Wydawnictwo Politechniki Poznańskiej, Poznań (in Polish)
[4] Harrison D. E., Harrison D. D., Janik T. J., Jones E. W., Cailliet R., Normand M. 2001 *Clinical Biomechanics* **16** 276–284
[5] de Zee M., Falla D., Farina D., Rasmussen J. 2007 *J. Biomechanics* **40**
[6] Vasavada A. N., Li S., Delp S. L. 1998 *Spine* **23** 412–422
[7] Burden R. L., Faires J. D. 1988 *Numerical Analysis* PWS-KENT Publishing Company, Boston
[8] Ogawaai Y., Chiba K., Matsumoto M., Nakamura M., Takaishi H., Toyama Y. 2006 *J. Neurosurgery Spine* **5** 483–487
[9] Harrison D. E., Harrison D. D., Janik T. J., Jones E. W., Cailliet R., Normand M. 2001 *J. Manipulative and Physiological Therapeutics* **16** 276–284
[10] Harrison D. E., Jones E. W., Janik T. J., Harrison D. D. 2002 *J. Manipulative and Physiological Therapeutics* **25** 391–401
[11] Harrison D., Harrison D., Haas J., Janik T. 2003 *J. Manipulative and Physiological Therapeutics* **26** 608–612

Application of Meshfree Methods in Cervical Spine

T. Walczak[1a], B. T. Maruszewski[1b], R. Jankowski[2c], M. Chudzicka-Adamczak[3d]

[1] *Institute of Applied Mechanics, Poznan University of Technology*
Piotrowo 3, 60-965 Poznań, Poland

[2] *Clinic of Neurosurgery and Neurotraumatology*
Poznań University of Medical Sciences
Przybyszewskiego 49, 60-355 Poznań, Poland

[3] *Polytechnic Institute, Higher Vocational State School in Piła*
Podchorążych 10, 64-920 Piła, Poland

[a] *tomasz.walczak@put.poznan.pl*, [b] *bogdan.maruszewski@put.poznan.pl*
[c] *klinikanch@op.pl*, [d] *martachudzicka@wp.pl*

The Method of Fundamental Solutions belongs to the meshfree numerical methods serving to solve differential equations describing many engineering issues. It has already been used in problems of heat conduction, theory of elasticity, plasticity and fluid mechanics. Its main advantage is its relatively easy computer implementation and very little complexity of calculations, in comparison to other methods.

In the MFS, the problem solution (differential equation + boundary condition) is approximated by a linear combination of the fundamental solutions of the governing equation. The fundamental solutions are the source point functions occurring outside the examined area.

In order to obtain a solution of the examined problem in a given area, it is enough to define one algebraic linear equation system in which the coefficients standing before the fundamental solutions in their linear combination are unknown. These linear coefficients are determined based on the boundary conditions. It allows estimating easily the calculation and approximation error thanks to the standard tools of linear algebra.

An example of the method application is determining the stress patterns in a model implant of an intervertebral disc. The chosen object has a homogeneous structure, therefore, the classical Cauchy-Navier equations were used to describe the fundamental mechanical parameters (stresses, displacements, strains).

The Method of Fundamental Solutions was shown in the example of the problem of determining the tension distribution in the vertebra bodies of the cervical spine in humans (Figure 1).

The maximum tensions were examined in the vertebra bodies of patients suffering from the cervical degenerative spine disease. The maximum tensions were determined for two spine conformations, before and after cage stabilization. The loads constituted only the mass forces and the vertebra body geometry was determined based on the

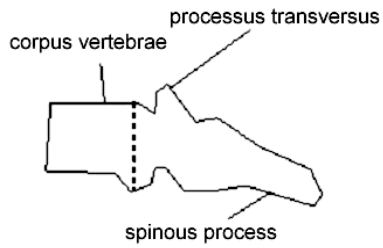

Figure 1: Structure of spinal vertebra (C_3-C_6)

X-ray images of patients. However, the parameters of bone tissue were taken from the literature [8].

References

[1] Berger J. R., Karageorghis A. 2001 *Engineering Analysis with Boundary Elements* **25** 877–886
[2] Fairweather G., Karageorghis A. 1998 *Advances in Computational Mathematics* **9** 69–95
[3] Poullikas A., Karageorghis A., Georgiou G. 2002 *Computers & Structures* **80** 365–370
[4] Redekop D., Cheung R. S. W. 1987 *Computers & Structures* **26** 703–707
[5] Redekop D., Thompson J. C. 1983 *Computers & Structures* **17** 485–490
[6] Tsai C. C.2007 *Engineering Analysis with Boundary Elements* **31** 586–594
[7] Mrozowski J., Awrejcewicz J. 2004 *Fundamentals of Biomechanics* Wydawnictwo Politechniki Łódzkiej, Łódź (in Polish)
[8] Gzik M. 2007 *Biomechanics of Human Spine* Wydawnictwo Politechniki Śląskiej, Gliwice (in Polish)
[9] Zhang Q. H., Teo E. C. 2008 *Medical Engineering & Physics* **30** 1246–1256

PART 3

3rd International Conference and 7th International Workshop on Auxetics and Related Systems

19–23 July 2010, Gozo & Malta

Negative Thermal Expansion Induced by Cold Deformation of β-Type Ti-Alloys

M. Abdel-Hady[1,2a], M. Niinomi[1], M. Nakai[1], M. Morinaga[3]

[1] *Institute for Materials Research, Tohoku University*
Sendai 980-8577, Japan

[2] *Department of Metal Technology, Central Metallurgical R&D Institute*
El-Tabbin, 87-Helwan, Egypt

[3] *Department of Materials Science and Engineering*
Graduate School of Engineering, Nagoya University
Nagoya, 464-8603, Japan

[a] *geprell@yahoo.com*

Low coefficient of thermal expansion (CTE) found in the invar alloys is related to the negative thermal expansion (NTE) induced by the magnetic transition from paramagnetic to ferro-magnetic or anti-ferromagnetic phase. The CTE is given as a total value of the normal and the negative thermal expansion terms [1]. Accordingly, most of the invar alloys are limited to the applications where no interference is present between its ferromagnetism and the operating conditions. Here we present different Ti-alloys with controllable CTE to achieve zero thermal expansion through the careful

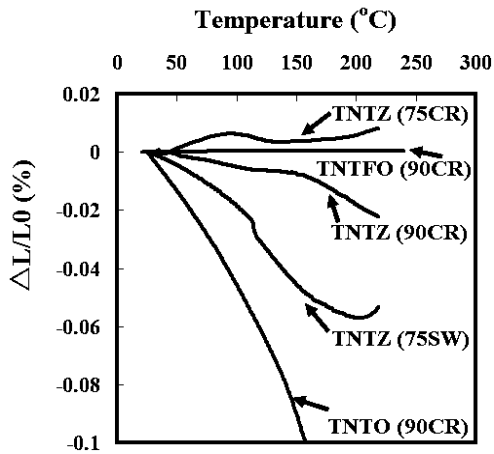

Figure 1: Change in specimen length with temperature, $\Delta L/L_0$, showing the effect of cold deformation and alloy composition, of $Ti_{72}Nb_{20.1}Ta_{4.6}Zr_{3.3}$, TNTZ, $Ti_{76}Nb_{17}Ta_6O_1$, TNTO, and $Ti_{75}Nb_{17}Ta_6Fe_1O_1$, TNTFO alloys after 75 and 90% cold rolling, CR, and after 75% cold swaging, SW

selection of alloying elements and the proper thermomechanical treatments. This will give a lot of room for the new invar alloys to be used for many applications without the former restrictions.

We propose here that NTE factors are enhanced by the cold deformation of those alloys which possess elastic softening [2], presented by low tetragonal shear, $C' = (C_{11} - C_{12})/2$, and large elastic anisotropy presented by $A = C_{44}/C'$.

Cold drawing, swaging, and rolling are tools to introduce oriented microstructures to these alloys including stress induced phase transformation [3, 4]. These oriented microstructures, with specific orientation relationship with the parent phase, β-phase, becomes the origin of the NTE through a fully reversible reaction in heating-cooling cycles within a considerable temperature range.

As shown in Figure 1, the idea is applied to three kinds of Ti-alloys such as Ti-Nb-Ta-Zr (TNTZ), Ti-Nb-Ta-O, and Ti-Nb-Ta-Fe-O. The amount of the unique oriented microstructure can be controlled through alloy composition, deformation method, degree of cold deformation, and subsequent heat treatments.

References

[1] Y. Nakamura 1978 *Physics and Engineering Applications of Invar Alloys* Maruzen, Tokyo
[2] M. Abdel-Hady, K. Henoshita, M. Morinaga 2006 *Scripta Mater.* **55** 477
[3] M. Nakai, M. Niinomi, T. Akahori, H. Tsutsumi, X. Feng, M. Ogawa 2009 *Mater. Trans.* **50** 423
[4] M. Abdel-Hady, M. Morinaga 2009 *Scripta Mater.* **61** 825

Developments in Auxetic Foams

A. Alderson, K. L. Alderson

University of Bolton, Institute for Materials Research and Innovation
Deane Road, Bolton BL3 5AB, UK

A.Alderson@bolton.ac.uk

Auxetic foams have potential in a range of applications [1] including, but not limited to, filtration, packaging, acoustic damping, cushions and mattresses, personal protective equipment and apparel. To deliver the potential of auxetic foams in such applications requires improvements in fabrication and control over form, structure and properties of the final product. At previous conferences in this series [2–4] and elsewhere [5, 6], work at Bolton and collaborating partners on variations of the original compression/heat treatment foam production method of Lakes [7], in the form of the effects of triaxial, biaxial and uniaxial compression/stretching on the foam structure, properties and deformation mechanisms, has been presented. This presentation will report recent work extending the previous investigations to consider the production of auxetic foam in alternative forms to the monolithic cuboidal/cylindrical samples usually considered, including an assessment of the spatial distribution of structure and properties within the product.

References

[1] Evans K. E., Alderson A. 2000 *Advanced Materials* **12** (9) 617
[2] Alderson A. 2006 *1st International Conference on Auxetics and Related Systems* Exeter
[3] McDonald S. 2009 *6th International Workshop on Auxetics and Related Systems* Bolton
[4] McDonald S., Ravirala N., Withers P., Alderson A. 2009 *Script. Mater.* **60** 232
[5] Alderson A., Alderson K. L., Davies P. J., Smart G. M. 2005 *American Society of Mechanical Engineers, Aerospace Division (Publication) AD* **70** AD; 2005 *Proceedings of the ASME Aerospace Division* 503
[6] Grima J. N., Alderson A., Evans K. E. 2005 *J. Phys. Soc. Jpn.* **74** 1341
[7] Lakes R. S. 1987 *Science* **235** 1038

Trapping Double Negative Particles in Optical Tweezers

L. A. Ambrosio

School of Electrical and Computer Engineering (FEEC)
University of Campinas (Unicamp), Department of Microwave and Optics (DMO)
13083-970 – Campinas/SP, Brazil

leo@dmo.fee.unicamp.br

Gradient forces on optical trapping are presented for left-handed or double negative (DNG) particles in optical tweezers. Based on a recent work, the analysis first includes simple geometric optics considerations, where force calculations are performed for a single ray and then theoretically extended to an arbitrary incident beam. New trapping characteristics arise from Snell's law inversion due to the negative refractive index of the particle, and they are confirmed using full electromagnetic theory. Theoretical and numerical results reveal interesting potentialities of these DNG particles that could be successfully exploited in biomedical optics in the near future.

Acknowledgements

The author thanks FAPESP (Fundação de Amparo à Pesquisa e ao Ensino do Estado de São Paulo) and CNPq (Conselho Nacional de Desenvolvimento Científico e Tecnológico) for supporting this work.

Modelling of Honeycombs Exhibiting Zero Poisson's Ratio

J. N. Grima[1], D. Attard[1], L. Oliveri[2], B. Ellul[1], R. Gatt[1], G. Cicala[2], G. Recca[2]

[1] *Faculty of Science, University of Malta*
Msida MSD 2080, Malta

[2] *Faculty of Engineering, Department of Physical and Chemical Methodologies for Engineering, University of Catania*
Viale A. Doria No 6, 95125 Catania, Italy

auxetic@um.edu.mt

Zero Poisson's ratio materials are those which do not exhibit changes in transverse directions when uniaxially loaded. A detailed analytical model for novel hexagonal honeycomb structures, composed of alternate layers of re-entrant and non re-entrant features is presented, showing that in such honeycombs, deformation from hinging, flexure and/or stretching of the cell walls can lead to zero Poisson's ratios, a property which is highly desirable in niche applications. Various hypothetical polyphenylacetylene networks designed to mimic the geometry of these hexagonal honeycombs are also analysed for their mechanical behaviour, in particular the main molecular level deformation mechanism(s) taking place in response to uniaxial stresses.

Acknowledgements
This work is financed by the Malta Government Scholarship Scheme awarded to D. Attard.

Giant Poisson Ratios for Superelastic Carbon Nanotube Muscles Providing Giant Strokes and Giant Stroke Rates from 0 to 1900 K

A. Aliev, J. Oh, M. Kozlov, A. Kuznetsov, S. Fang, A. Fonseca, R. Robles, M. Lima, M. Haque, Y. Gartstein, M. Zhang, A. Zakhidov, R. Baughman

The Alan G. Mac Diarmid NanoTech Institute, University of Texas Dallas, TX 75083, USA

We have developed a fundamentally new type of artificial muscle, which operates in air to generate giant strokes and stroke rates of 220% and $3.7 \cdot 10^4$%/s, respectively. Charge-driven resonant and dc linear actuation result for volt to kilovolt drive voltages, and temperatures from below 80 K to above 1900 K. Using mechanical and electrical resonances, these carbon-nanotube-based artificial muscles provided ±30% oscillatory actuation at a kHz when driven by 10 V_{RMS}. In the high modulus sheet direction, where actuator stroke is a few percent, stress generation was 32-fold higher than the sustainable value for natural skeletal muscle. Actuation in this direction differs in sign from that in sheet width and thickness directions. We theoretically explain this sign reversal using giant observed Poisson's ratios of up to 15, which provide a negative linear compressibility for the sheets. The observed dependence of actuation on boundary constraints, applied voltage, and sheet thickness are also theoretically explained.

On the Mechanical Properties of 2D Models Made from Rigid Rotating Triangles

J. N. Grima[1], E. Chetcuti[1], E. Manicaro[1],
D. Attard[1], M. Camilleri[1], K. E. Evans[2]

[1] *Faculty of Science, University of Malta*
Msida MSD 2080, Malta

[2] *College of Engineering, Mathematics and Physical Sciences*
Harrison Building, University of Exeter
Exeter, EX4 4QF, UK

In this paper, we propose an analytical model to describe the mechanical properties of a 2D system made from connected rigid triangles constructed from two sets of different shaped and sized scalene triangles. In this model it is assumed that when the structure is mechanically loaded, the triangles cannot change their shape or size, but, can rotate relative to each other in the plane of the structure. We show that such systems can exhibit mechanical properties which are dependent on the shape and size of the triangles and the angles between them. We also show that such systems can exhibit negative Poisson's ratio, i.e. have the ability to expand or contract in both the loading and the transverse direction, a property which can be useful in many practical applications. The density profile of such system is also considered.

Finally, in view of the fact that micrograph images of cross-sections of cell struts indicate that cell struts of auxetic foams have a Plateau border geometry which may be simplified as triangular shaped struts, and, in view of recent work by Grima et al. and Alderson et al., we show that our model can be used to model the mechanical properties of auxetic foams. This is the first attempt to represent in an analytical model some degree of irregularity which is characteristic of auxetic foams.

Composites with Needle and Coin Shaped Inclusions Exhibiting Negative Thermal Expansion

B. Ellul, D. Attard, J. N. Grima

Faculty of Science, University of Malta
Msida MSD 2080, Malta

auxetic@um.edu.mt

In this work simple cylindrical structures with either stiff needle-like inclusions or stiff coin-shaped inclusions embedded within a much softer matrix are presented and analysed with the aim of obtaining systems with tuneable thermal expansion properties and/or negative thermal expansion. It is shown that by the correct combination of the shape, thermal and mechanical properties of the matrix and inclusion, it is possible to design systems which can be tailormade to exhibit particular values of the coefficient of thermal expansion (CTE) in the radial and axial directions. Negative thermal expansion (NTE) is also exhibited in some directions. This work is complemented by simple analytical models to explain some of these effects.

On the Effect of Disorder on the Mechanical Properties of Hexagonal Honeycombs

B. Ellul, R. Gatt, D. Attard, J. N. Grima

Faculty of Science, University of Malta
Msida MSD 2080, Malta

auxetic@um.edu.mt

A system which has been extensively studied from the point of view of its Poisson's ratio is the highly symmetric hexagonal honeycomb structure which is known to be capable of exhibiting in-plane Poisson's ratios ranging from $+\infty$ to $-\infty$. This model has also been used to explain the magnitude of the Poisson's ratio in various cellular materials, most notably those of conventional and auxetic foams.

Here we discuss the results of finite elements simulations which were performed on a large number of imperfect honeycombs in an attempt to analyse how the degree of such defects affects the Poisson's ratio and Young's modulus. In particular, we show that the Poisson's ratio of the systems considered is significantly affected by these imperfections with the effect being most pronounced on systems which in their ordered form would have very high positive or very high negative Poisson's ratio (in both cases the magnitude of the Poisson's ratio decreases). This may offer a better explanation for the observed properties in real auxetic materials such as foams which can be described as highly irregular cellular solids. We also suggest that a 'disorder correction factor' may need to be introduced to correlate better the properties predicted by the existing highly symmetric models and real experimental data.

On the Use of Auxetic Materials for the Manufacture of Pressure Vessel Heads

B. Ellul, J. N. Grima

Faculty of Science, University of Malta
Msida MSD 2080, Malta

auxetic@um.edu.mt

Auxetic materials exhibit the unusual property of expanding when stretching in the direction normal to an applied uniaxial tension and vice versa when compressed, i.e. exhibit negative Poisson's ratios. This phenomenon is known to result in many beneficial effects in the performance of materials in various practical situations. In particular it has long been suggested that spherical shells made from isotropic materials having Poisson's ratio less than -0.5 exhibit enhanced resistance to buckling as a result of externally applied normal pressure.

This work makes predictions on the properties pressure vessel heads constructed from auxetic materials. Finite elements modelling is used to assess the behaviour of various spherical, torispherical and ellipsoidal shells when they are subjected to external (in all cases) or internal (in the case of torispherical and ellipsoidal shells) pressures. We find that to a first approximation, the critical buckling pressures scale linearly with $(1-\nu^2)^{-1/2}$ thus suggesting that the critical buckling pressures tends to infinity as ν tends to -1, this being in accordance to what was known for spherical shells [1]. We also find that the Poisson's ratio has an effect on the amplitude and the number of buckling wavelengths that occur when the shells buckle.

References

[1] B. Ellul, M. Muscat and J. N. Grima 2009 *Phys. Stat. Sol. (b)* **246** (9) 2025–2032

Auxetic Properties of Iron-Gallium Alloys

H. M. Schurter[1], Y.-N. Zhang[2], R.-Q. Wu[2], A. Flatau[1a]

[1] *Department of Aerospace Engineering, University of Maryland College Park, MD 20742, USA*

[2] *Department of Physics & Astronomy, University of California Irvine, CA 92697-4575, USA*

[a] *aflatau@umd.edu*

Large auxetic properties of iron-gallium alloys have been investigated with both theoretical and experimental approaches. Tensile tests of single-crystal iron-gallium alloys with compositions of 12–25% gallium were conducted to determine the composition dependent values of the Poisson's ratio. These alloys are believed to be one of the first of the class of structural auxetic alloys, in that they are materials with a high-modulus, with $E_{[110]} \approx 100$ GPa for $Fe_{75}Ga_{25}$, and they exhibit significant molecular auexticity, with a Poisson's ratio of -0.7 for $Fe_{75}Ga_{25}$. Systematic density functional calculations revealed a simple correlation between the Poisson's ratio and tetragonal shear modulus. The key factor for producing elastic anisotropy, and subsequently the auxetic behavior of these alloys, is attributed to an unlikely distribution pattern of Ga and Al atoms within the Fe lattice, in which these atoms need to be far apart from each other.

Further Modelling Studies on the Negative Poisson's Ratio in α-Cristobalite

R. Gatt[1], A. Alderson[2], J. N. Grima[1]

[1] *Faculty of Science, University of Malta*
Msida MSD 2080, Malta

[2] *Institute for Materials Research & Innovation, University of Bolton*
Deane Road, Bolton BL3 5AB, United Kingdom

auxetic@um.edu.mt

Auxetic materials exhibit the unusual property of getting fatter when uniaxially stretched and thinner when compressed, i.e. exhibit a negative Poisson's ratio. A particularly interesting auxetic material is α-cristobalite, a naturally occurring silicate which is known to be exhibit a high degree of auxeticity at ambient conditions to the extent that auxeticity is not limited to particular directions in its crystalline form, but is also predicted to be present in the polycrystalline aggregate.

In this paper, we will attempt to obtain a better picture of the behaviour of α-cristobalite by simulating the deformations that occur when α-cristobalite is loaded in directions of maximum auxeticity which are not in the (100) and (010) planes and attempt to explain these in terms of the rotating rectangles model. In fact, we will show that auxetic behaviour of α-cristobalite in the planes passing through the [001] direction can be explained in terms of simple 2D models involving semi-rigid rotating rectangles which rectangles are the projections in the (100) and (010) planes of a more complex 3D model involving semi-rigid rotating tetrahedral. Moreover we will also discuss the behaviour of such systems as the tetrahedra become progressively more rigid.

Anomolous Anelasticity in Some Liquid Crystalline Networks: Mechanically Induced Strains Ratio as a Mechanistic Probe

W. Ren, W. M. Kline, P. J. McMullan, A. C. Griffin[a]

School of Polymer, Textile and Fiber Engineering
Georgia Institute of Technology
Atlanta, GA 30332-0295 USA

[a] *anselm.griffin@ptfe.gatech.edu*

For some smectic liquid crystalline networks a pronounced lack of rapid reversibility (anelasticity) is seen in film specimens when the loading force is removed and the film is allowed to undergo free recovery. This behavior is observed at temperatures significantly above the glass transition temperature yet far below the liquid crystal – isotropic transition temperature. In an effort to elucidate the origins of this anelasticity, we have examined a series of smectic liquid crystalline network polymer films by subjecting them to a large uniaxial stress at temperatures far below the clearing temperature. As expected, the dimensional recovery is anelastic showing substantial retained strain. The uniaxial strain produces a polydomain-to-monodomain transition in the film and the monodomain thus produced is temporally stable.

Upon heating this monodomain film, recovery of the original film dimensions can occur. The recovery curves show a pronounced curvature as the temperature approaches the smectic-isotropic temperature. We have obtained accurate strain (length) vs. temperature plots for these films and have also simultaneously recorded the corresponding specimen width changes as well. An interesting consequence of obtaining both length and width data is that the mechanically induced strains ratio (MISR) for the film can be calculated as a function of temperature; i.e., a 'Poisson's ratio' under zero tensile force, as the elevated temperature causes the original film shape and dimensions to be recovered in this 'shape memory' polymeric material. It is proposed that nanosegregation of netpoints in the smectic structure is responsible for the anelasticity and that the temperature dependence of the shape recovery is consistent with a balance between enthalpic and entropic forces with temperature. A mechanically induced strains ratio (MISR) was observed on heating these pre-stressed films. Loss of the monodomain structure near the isotropization temperature is postulated to rationalize the shape of the MISR curves.

Acknowledgements
The authors thank the National Textile Center (M04-GT21) for financial support.